NMR Applications in Soft Materials Science: Correlation of Structure, Dynamics, and Transport

Ying Chen

Dissertation submitted to the faculty of the Virginia Polytechnic Institute and State University in partial fulfillment of the requirements for the degree of

Doctor of Philosophy
In
Chemistry

Louis A. Madsen (Chair)
Brian M. Tissue
John R. Morris
Harry C. Dorn
Sungsool Wi

(June 24th, 2015)
Blacksburg, VA

Keywords: Solid-state NMR
PFG diffusometry
Imaging
Spin relaxation
Diffusion
Ionic liquids
Polymer
Supramolecular assembly
Nanoparticle

NMR Applications in Soft Materials Science: Correlation of Structure, Dynamics, and Transport

Ying Chen

ABSTRACT

This dissertation aims to investigate and correlate structure, dynamics and transport properties of several novel soft materials systems using multiple Nuclear Magnetic Resonance (NMR) methodologies, including solid-state NMR (SSNMR), diffusometry, and imaging, and with the help of X-ray scattering.

First, we report the investigation of structure and dynamics of three polymeric membranes: hydroxyalkyl-containing imidazolium homopolymers, poly(arylene ether sulfone) segmented copolymers, and disulfonated poly(arylene ether sulfone) random copolymers using a wide array of SSNMR techniques, including: 1) ^{13}C cross-polarization magic angle spinning (CPMAS) with varying cross-polarization (CP) contact time, 2) ^{13}C single-pulse magic angle spinning (MAS) with varying delay time, 3) ^{23}Na single-pulse MAS, 4) two dimensional phase-adjusted spinning sideband (2D PASS), 5) proton spin−lattice relaxation (T_1), 6) rotating frame spin−lattice relaxation ($T_{1\rho}$), and 7) center-band-only detection of exchange (CODEX). These various types of SSNMR spectroscopic methods provide a wealth of structural and dynamic information over a wide range of time scales from a few nanoseconds to seconds.

We further present a picture of rich structural and transport behaviors in supramolecular assemblies formed by amphiphilic wedge molecules using a combination of ^{23}Na solid-state NMR, $^{1}H/^{2}H$ PFG NMR diffusion, relaxation and grazing-incidence small-angle X-ray scattering. Our results show that the liquid crystalline domains in these materials undergo a transition from columnar to bicontinuous cubic phases with a simple increase in humidity, while the amorphous domain boundaries consist of individual wedge molecules with a

significant fraction (~ 10%) of total wedge molecules. Multiple-component diffusion of both wedges and water further confirms the structural and dynamic heterogeneity, with the bicontinous cubic phase being able to facilitate much faster water and ion transport than the columnar phase.

We then develop a quantitative approach to probe the migration of two novel "theranostic" polymeric agents (combining "therapeutic" and "diagnostic" functions) into bulk hydrogels using two distinct time-resolved magnetic resonance imaging (MRI) methods. To the best of our knowledge, this is the first work that combines time-resolved MRI experiments to reliably quantify diffusivity of paramagnetic and superparamagnetic nanoparticles in bulk biological media. Our results agree closely with those obtained from fluorescence techniques, yet the capability of our approach allows the analysis of actual nanoparticles diffusion through biogels on mm to cm scales during a range of time periods.

Finally, we employ a combination of NMR techniques to obtain a comprehensive understanding of ion clustering and transport behaviors of ionic liquids inside the benchmark ionic polymer Nafion. Spin relaxation shows that anion relaxation is more influenced by the fixed sulfonate groups than cation relaxation. 2D ^{1}H-^{19}F heteronuclear Overhauser effect spectroscopy (HOESY) and 1D ^{19}F-^{19}F selective nuclear Overhauser effect (NOE) spectroscopy confirm our assumption of the formation of ion clusters at low water content in the ionomer. While we observe non-restricted diffusion behavior for cations, anion diffusion is strongly restricted both between domain boundaries and within domains in the absence of water. The restricted anion diffusion can serve as a reliable probe for detailed multiscale structures of the ionomer.

Acknowledgement

First I have to express my deepest gratitude to my advisor, Dr. Louis A. Madsen. He is a great mentor and a truly nice person. His enthusiasm in science and his generosity in life through his constant discussions with us about science and beyond inspire me to become a better scientist and a better person. He can always find the best in me and gives me great freedom in my research. I may have quit my graduate studies without his generous support during my personal difficulties. He is my role model. I am extremely grateful to Dr. Madsen for his guidance, patience, understanding, encouragement and support in my research and life. This thesis would not be possible without his constant help.

I would like to acknowledge my sincere debt to my previous advisor, Dr. Sungsool Wi. He guided me into the wonderful world of spin dynamics, constantly inspired me with his dedication to NMR, and supported me through my personal difficulties. I would also like to show my sincere appreciation to my committee Dr. Harry C. Dorn, Dr. Brian M. Tissue and Dr. John R. Morris for their valuable advice on my research and their very helpful editing on the thesis. This thesis is much better than it would be without their professional help.

I am very thankful to my lab members Dr. Justin Spano, Dr. Jianbo Hou, Dr. Mark Lingwood, Dr. Zhiyang Zhang, Dr. Mithun Goswami, Cocoa Wang, Bryce Kidd, Ying Wang, Kacey McCreary, and Yongzheng Huang, who shared time, knowledge, happiness, and sometimes frustrations with me in Blacksburg. I want to make a special acknowledgement to Dr. Jianbo Hou, Dr. Mark Lingwood, and Cocoa Wang for tolerating me during our close collaborations. I also want to express my deep thanks to Dr. Diego Troya and Robert Chapleski for their great help in the molecular dynamics simulations project.

Last, I would like to give my gratitude to my parents Qinglu and Caimei, and my husband Xiaosong for their constant love, support and encouragement over the years. I also want to thank my child Isaac for being so sweet and cute.

Attribution

Below I describe the contributions of co-authors who contributed to the chapters in this dissertation.

Chapter 3: For section 3.2, Dr. Michael H. Allen from Prof. Timothy E. Long's group synthesized the material. I contributed to NMR experiment design, data collection, interpretation and writing the NMR section. Dr. Louis Madsen provided valuable advice on the NMR section. For section 3.3, Dr. Bin Zhang from Prof. Richard Turner's group synthesized the material. Dr. Justin Spano contributed to NMR data collection, I contributed to simulations for data fitting, and Dr. Sungsool Wi wrote the final paper. For section 3.4, Dr. Chang Hyun Lee from James E. McGrath's group synthesized the material. I contributed to NMR data collection and interpretation and Dr. Sungsool Wi provided valuable advice and final editing on the NMR section.

Chapter 4: Dr. Heng Zhang from Prof. Xiaomin Zhu's group synthesized the material. Dr. Jaime J Hernandez from Prof. Dimitri A. Ivanov's group collected and analyzed X-ray data, and wrote the X-ray section. Dr. Mark Lingwood collected initial NMR diffusion data and wrote the first draft. I conducted further NMR diffusion experiments, collected data on solid-state and relaxation NMR experiments, reinterpreted results with a new model, and wrote the final paper. Dr. Louis Madsen provided valuable advice and editing.

Chapter 5: Dr. Lian Xue from Theresa M. Reineke's group and Nipon Pothyaee from Prof. Judy S. Riffle's group synthesized the material. Cocoa (Xiaoling) Wang collected all NMR data and wrote the first draft of the manuscript. I conducted all data analysis and helped Cocoa with NMR experimental design, result interpretation and paper editing. Dr. Louis Madsen provided valuable advice and editing.

Chapter 6: Dr. Jianbo Hou started some NMR experiments and provided valuable ideas for data interpretation. I redesigned NMR experiments, collected all NMR data, conducted data analysis and wrote the paper. Dr. Louis Madsen provided valuable advice and editing.

Table of Contents

List of Figures

List of Tables

Chapter 1

Structure, Dynamics and Transport in Soft Materials

1.1 Motivation, strategy and research goals

This thesis concerns detailed studies of soft materials using a wealth of nuclear magnetic resonance (NMR) techniques. The complicated and dynamic nature of soft materials raises a challenge to the analysis methods used for their characterization. A combination of multiple NMR methodologies can provide an expanded scope of information for understanding soft materials structure, dynamics and transport.

The term "soft" materials usually refers to materials with relatively soft macroscopic mechanical properties, in contrast to "hard" materials such as crystalline solids. In other words, soft materials combine properties and behaviors of both solids and liquids. The field of soft materials spans topics in structured liquids, liquid crystals, colloids, foams, gels, granular materials, biological macromolecules, synthetic polymers, as well as supramolecular assemblies. As a primary focus of materials science in the past few decades, soft materials have been developed rapidly and become indispensable in modern life. For example, ion conducting materials based on soft materials have played an essential role in electrochemical energy conversion, storage and transmission devices ranging from batteries, chemical sensors, fuel cells, solar cells to artificial muscle actuators. A common feature of soft materials is their relatively weak but collective intermolecular interactions that are responsible for maintaining a degree of local molecular order but not the well-defined long-range order found in crystalline structures.[1] With intermolecular interaction energies approximately equal to room temperature thermal energy $k_B T$, soft materials are often dynamic and may deform easily at room

temperature.[2] Therefore the structure and dynamics of soft materials are complicated but yet tunable in multi-length and multi-time scales, with their bulk material properties being controlled through the fine modulation of intermolecular interactions.

NMR spectroscopy has been widely used as a powerful analytical tool in chemistry, biology, materials science, and many other fields since its discovery in 1938,[3] and observation in condensed phases in 1946.[4-5] For soft materials, with their complicated and multiscale structures and dynamics, NMR studies are extremely valuable for enabling a whole spectrum of research activities, including chemical composition identification, multi-length-scale structure ormorphology determination, multi-time-scale dynamics observation, transport (diffusion and flow) measurements, as well as *in vitro* and *in vivo* imaging. A major advantage of NMR techniques is that they can report on dynamic and not only static properties, which is essential for studies of soft materials. More importantly, numerous novel NMR strategies and methodologies have been developed and more will be created to understand special and sophisticated properties of soft materials. Besides, NMR spectroscopy is non-destructive (using radiofrequency radiation only) and is highly chemically and physically selective based on specific isotopes, providing more varieties of information on soft materials. In addition to NMR, X-ray and neutron scattering also serve as complementary and powerful probes for static structures of soft materials with sizes ranging from < 1 nm up to 100 nm.

This thesis contains investigations and correlations of structure, dynamics and transport properties of several novel soft materials systems using multiple NMR methodologies, including solid-state NMR, solution NMR, diffusometry, relaxometry, and imaging, with the help of X-ray scattering. This dissertation is organized as follows. Chapter 1 quickly introduces structure and dynamics of three soft materials systems that are the subjects of the

dissertation, as well as some fundamental concepts and models of transport phenomena in porous media. Chapter 2 briefly reviews basic concepts of NMR spectroscopy followed by three distinct NMR methodologies used in the studies of this thesis: high-resolution solid-state NMR (SSNMR), pulsed-field-gradient (PFG) diffusometry, and magnetic resonance imaging (MRI). Following the two introduction sections, in Chapter 3 we report three examples using solid-state NMR methods to investigate structure and dynamics of polymeric membranes: hydroxyalkyl-containing imidazolium homopolymers,[6] poly(arylene ether sulfone) segmented copolymers,[7] and disulfonated poly(arylene ether sulfone) random copolymers.[8] In Chapter 4, we present a picture of rich structural and transport behaviors in supramolecular assemblies formed by amphiphilic wedge molecules using a combination of ^{23}Na solid-state NMR, ^{1}H/^{2}H PFG NMR diffusion, NMR spin relaxation and grazing-incidence small-angle X-ray scattering.[9] In Chapter 5, we develop a quantitative approach to probe the migration of two novel "theranostic" polymeric agents (combining drug delivery and contrast agent functions) into bulk hydrogels using two distinct time-resolved microMRI methods.[10] In Chapter 6, we use the benchmark ionic polymer Nafion as a medium to study nanoscale confinement effects on ion clustering and motions of ionic liquids (ILs) by ^{1}H/^{2}H/^{19}F PFG NMR diffusometry, relaxometry, 2D ^{1}H-^{19}F heteronuclear Overhauser effect spectroscopy (HOESY), and 1D ^{19}F-^{19}F selective NOE spectroscopy. We demonstrate that study of restricted ion diffusion using PFG NMR serves as a reliable probe for detailed multiscale structures in ionomer membranes. Finally, Chapter 7 summarizes current work and provides prospects for future work.

1.2 Structural organization and dynamics in soft materials

Here we introduce three soft materials systems that are the subjects of our studies in later Chapters, including supramolecular assemblies, ionic liquids (ILs), and ionic polymers

(ionomers). The complicated structural and dynamic heterogeneity of these systems greatly influences their macroscopic properties and demands cautious analysis. A critical motivation for studying these materials is to better understand and correlate their water or ion transport properties with their structure and dynamics to provide insight into the design of novel ion-conducting materials. A common feature of ion-conductive materials is the co-existence of "ion transport" and "mechanical support" moieties that phase separate on the nanometer scale to form coexisting networks that serve these two different purposes. The local geometry and tortuosity of the ion transport network plays a key role in determining the conduction performance.

Figure 1.1 shows three examples of structural organization in soft materials with the ion transport portion represented by blue and the mechanical support portion by yellow. In lamellar structures, molecules/ions translate between layers with two-dimensional freedom. In hexagonal columnar structures, a macroscopic channel alignment is required in order to maximize transport along the columnar axis as the single direction. Bicontinuous structures are composed of non-intersecting channel networks organized by multi-armed struts, allowing molecules/ions to move in the highly interconnected labyrinth with three-dimensional freedom. Clearly, lamellar or hexagonal structures afford higher diffusion anisotropy, but bicontinuous structures can usually provide better transport properties in three dimensions.

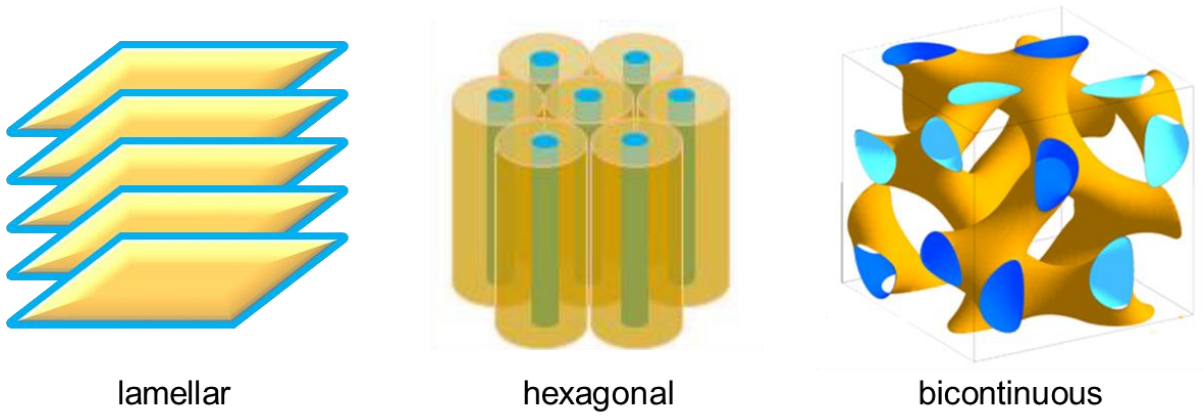

Figure 1.1 Schematic diagrams of topologies of ion or molecular transport channels in soft materials.

Furthermore, due to their relatively fast molecular dynamics, the mesoscopic structures of soft materials (in the range of 1-1000 nm) are sensitive to surrounding environments such as temperature and humidity (for supramolecular assemblies) or to pretreatment processes (for polymers). Therefore, dynamics is interwoven with structure for soft materials. Determining detailed structure – dynamics – transport relationships in soft materials is the main theme of this dissertation.

1.2.1 Supramolecular assemblies

Supramolecular assemblies can arise from molecular building blocks with specifically designed intermolecular interactions, such as hydrogen bonding, ionic interactions, ion-dipole interactions, π-stacking, excluded volume repulsion and shape anisotropy.[11-15] Such assemblies allow for increased degrees of freedom in controlling macroscopic material properties. Many studies have explored liquid crystalline structures formed from supramolecular assemblies for ion conduction applications.[16-21]

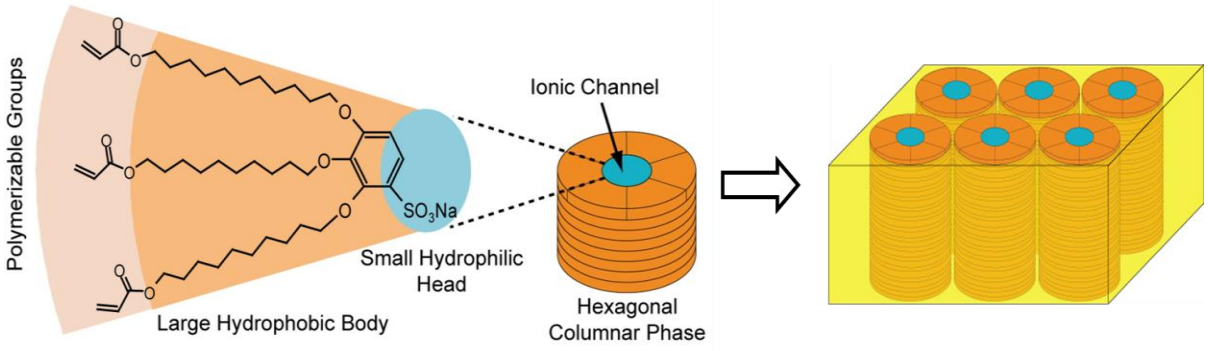

Figure 1.2 Chemical structure of sodium 2,3,4-tris(1,1'-acryloyloxyundecyl-1'-oxy)benzene sulfonate (**A-Na**). Self-assembly of the acrylate sulfonate wedge molecules **A-Na** (left) forms supramolecular disks (middle) and then a classical 2D hexagonal columnar structure (right) with ion conducting channels running along the column axes. Self-standing membranes can be obtained by photo-polymerization of the columnar structures through acrylate groups.[22]

Figure 1.2 shows the chemical structure of wedge molecules **A-Na** (the subject of Chapter 4)[15]and a representative supramolecular self-assembly process to form columnar phases. This wedge-shaped sulfonate amphiphile has a typical design to serve as an ion conductive material: a hydrophilic head that self assembles into ionic channels via electrostatic interactions, a hydrophobic body that forms a mechanical support matrix through π-stacking and shape anisotropy, as well as a polymerizable terminal group to generate stable membranes by covalent crosslinking. Intriguingly, this novel system experiences a drastic phase transition from columnar to bicontinuous phases with a significant increase in ion conductivity when exposed to humid air.[22] In Chapter 4, we report that the real structure of this supramolecular assembly is far more complicated than the neat representation shown in Figure 1.2. We also investigate transport behaviors of both water and wedge molecules, and correlate these with the structure and dynamics at the molecular level.

1.2.2 Ionic liquids

Ionic liquids (ILs) are room temperature molten salts composed entirely of bulky unsymmetrical organic ions, including typical cations such as imidazolium, pyrrolidinium, and quaternary ammoniums as well as typical anions like tetrafluoroborate, halide, hexafluorophosphate, triflate, trifluoroacetate, acetate, and methide.[23-26] Their fluidity at relatively low temperature is the result of their reduced molecular packing efficiency due to their large ion sizes. ILs find wide applications as green solvents and liquid electrolytes due to their unique physicochemical properties such as high ion conductivity, broad electrochemical window, low vapor pressure, non-flammability, high thermal stability, and tunable solubility.[27-29]

Tremendous effort has been devoted to understand the liquid structure of ILs. It is well known that ionic liquid crystals are, *e.g.*, formed if the alkyl side chain length of either cation or anion of ILs increases to a certain length like n-dodecyl, when collective weak interactions such as dipole - dipole interactions, van der Waals interactions, and π - π stacking start to drive liquid crystalline ordering.[30] The wedge molecule **A-Na** mentioned previously can be viewed as a special case of an ionic liquid crystal. Therefore, when the alkyl chain length is not long enough for the formation of liquid crystals, IL local structures lie in between classical liquids and liquid crystals. An intriguing proposal about IL structures that has recently attracted attention is the formation of supramolecular structure composed of polar and nonpolar domains on the nanometer scale, mainly driven by a 3-D cooperative network of hydrogen bonds (H-bonds).[31-33] *Ab initio* simulations demonstrate that a doubly ionic H-bond that forms between a cation and an anion in ILs is bifurcated and chelating, permitting 3-D ion organization, with

the charge on the ions strengthening the H-bond.[34] Figure 1.3a shows an example of IL that form 3-D arrangements.

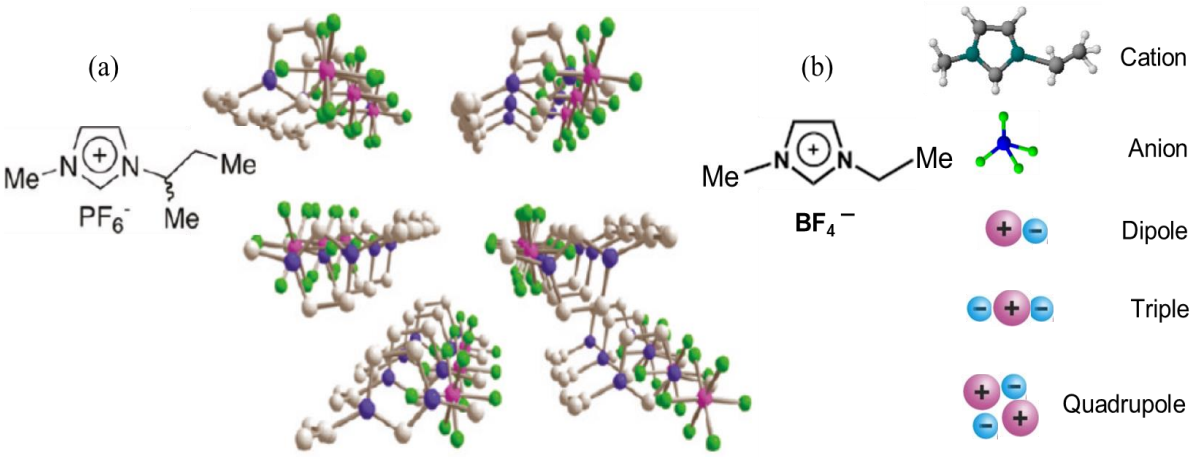

Figure 1.3 Chemical structures and ion organizations of two imidazolium based ILs. (a) 1-(2-butyl)-3-methyl-imidazolium hexafluorophosphate and its low temperature crystal structure showing a 3-D cooperative network of cations and anions connected by hydrogen bonds; (b) 1-ethyl-3-methyl-imidazolium tetrafluoroborate [C_2mim][BF_4] and its possible ion associations.

One of the ongoing mysteries of IL structuring concerns the existence, lifetime, and fraction of ion pairs or larger ion clusters in neat ILs. There is some experimental evidence that supports the existence of ion pairs,[35-36] and their lifetime is estimated to be only a few pico- to nanoseconds.[37-38] The coulombic interaction between cation and anion is the main driving force

for ion aggregates in ILs. The combined properties of ions such as size, asymmetric charge distribution, shape anisotropy, and conformational flexibility determine the formation and types of ion aggregations.[39-40] Figure 1.3b shows chemical structure of 1-ethyl-3-methyl-imidazolium tetrafluoroborate ([C_2mim][BF_4]), the main IL used in Chapter 6, as well as some potential aggregate species like dipole, triple, and quadrupole ions. Comparing the two chemical structures in Figure 1.3, it is clear that [C_2mim][BF_4] is less prone to forming a 3-D organized supramolecular structure due to the shorter alkyl side chain. Previous work of our group reveals that anion-rich triple ions may exist as a prominent mobile species when [C_2mim][BF_4] is soaked into ionic polymer Nafion.[41] In Chapter 6, we will further investigate the confinement effect of an ionic polymer matrix on local IL structures and transport properties.

1.2.3 Ionic polymers

Ionic polymers (ionomers) are polymers containing charged and neutral moieties in their chemical structures, and these moieties often phase separate into hydrophilic and hydrophobic domains. With the hydrophilic domains to allow for ion transport and hydrophobic domains to provide mechanical support, ionic polymers find broad applications in the fields of ion conductors, water purification, gas separation, etc. We will discuss three ionic polymers in this dissertation: a polymerized imidazolium-based ionic liquid (Chapter 3), disulfonated poly(arylene ether sulfone) random copolymers (Chapter 3), and the sulfonated tetrafluoroethylene-based copolymer Nafion® (Chapter 6).

Here we use Nafion as an example to briefly explain the multi-length-scale structures of ionic polymers. Developed by DuPont, Nafion is one of the most studied ionomers and serves as a benchmark material for fuel cell membranes. Despite being exposed to extensive

and close inspection, a complete picture of the morphology of Nafion remains unresolved.[42] Based on the information gathered from X-ray, neutron scattering, and TEM, a wide range of models have been proposed for the morphology of hydrated Nafion, including an interconnected hydrophilic network of inverted micellar spherical ionic clusters,[43] bundles of elongated rod- or ribbon-like polymeric aggregates in a hydrated matrix,[44-46] long and parallel cylindrical water nanochannels in a hydrophobic matrix,[47] alternating polymer-rich and water-rich lamellar layers,[48] locally narrow and flat water films,[49] and a random nanoscale channel-type bicontinuous network.[50] For example, in the model of elongated ribbon-like polymeric aggregates, polymer chains form elongated ribbon-like aggregates of a few hundred nanometers length surrounded by fixed sulfonate groups and counterions, and the aggregates organize into bundles with preferential orientation ordering to construct sub-micron domains which orient randomly in space (Figure 1.4 left).[43-45] In the model of water nanochannels, the sub-micron domains are characterized by interconnected hydrophilic channels formed from aggregates of sulfonate groups (Figure 1.4 right).[46] These models are conceptually distinct, but most of them are compatible by changing our viewing perspectives. For example, when the ribbons of polymeric aggregates are close enough, hydrophilic channels are formed between them. So the polymeric-ribbon model and the hydrophilic-nanochannel model are exchangeable depending on the size of and distance between the polymeric aggregates. The difficulties in unraveling a complete Nafion morphology lie in its complexity and heterogeneity as well as the fact that the sub-micron structures are strongly influenced by pre-treatment and relaxation effect.[49, 51-53] Previous studies of our group have demonstrated that these sub-micron domains can rotate and realign under macroscopic drawing while the alignment within domains and junctions between domains are not affected.[54] However, little

information has been revealed about these domain boundaries and how they affect ion transport. In Chapter 6, we will use restricted ion diffusion studies to probe deeper into the domain structures of Nafion.

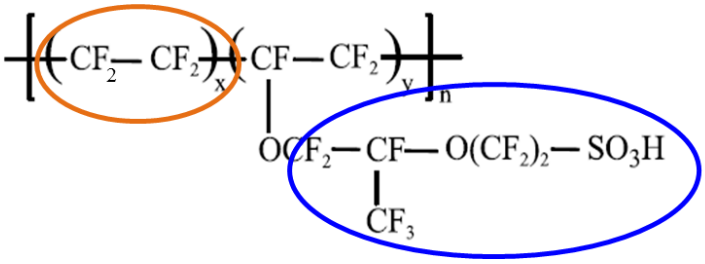

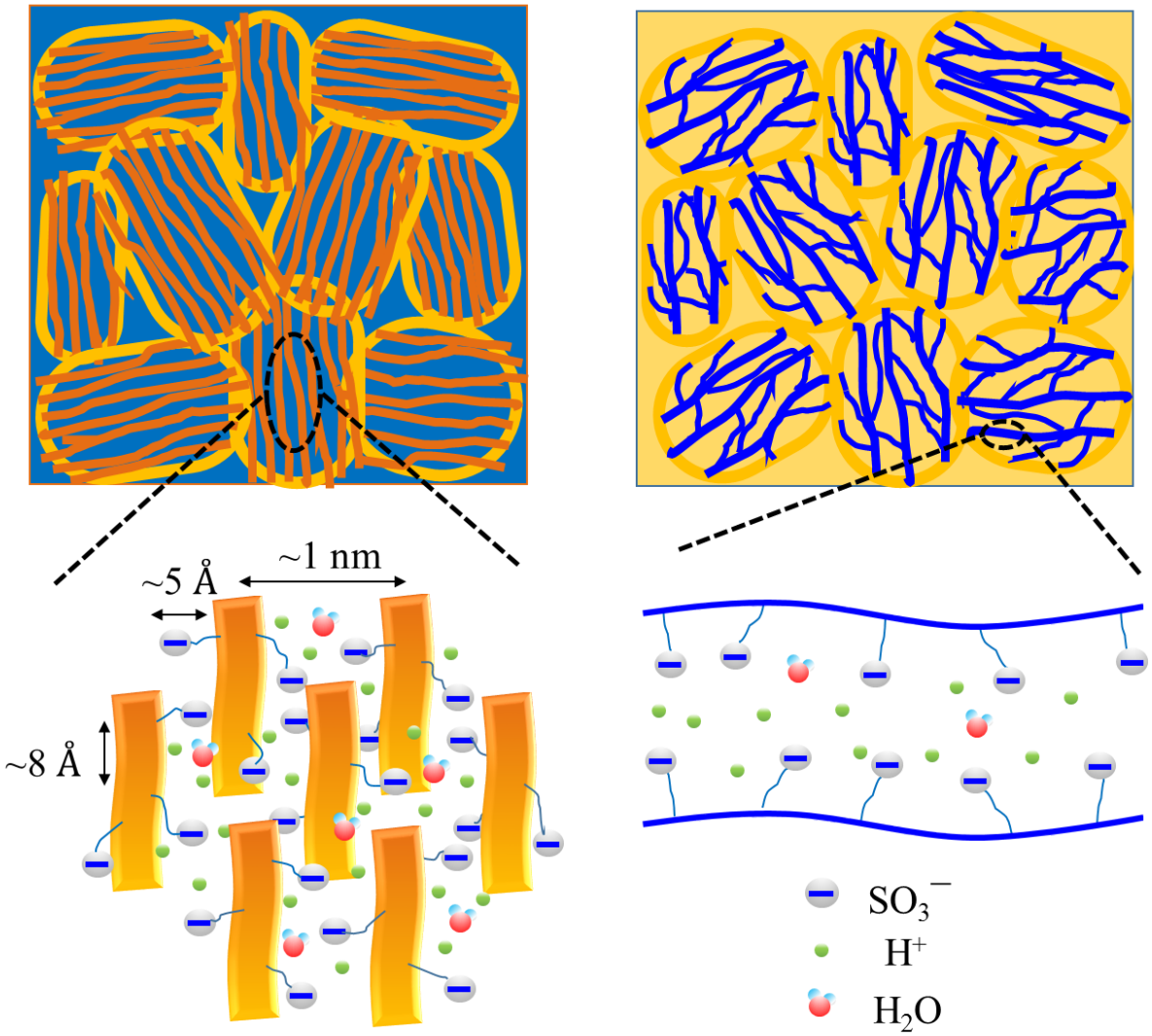

Figure 1.4 Chemical structure of Nafion and schematic illustration of multiple length-scale structures of Nafion swollen with water. The charged and neutral moieties in Nafion chemical structures form hydrophilic (blue) and hydrophobic (yellow) phases, respectively, with the former allowing for transport of ions and water, and the latter providing mechanical and chemical stability. In the polymeric-ribbon model (left), the polymer backbones (yellow) form elongated aggregates that are aligned within sub-micron domains but oriented randomly in the hydrophilic matrix. In the nanochannel model (right), the sub-micron domains of aligned hydriphilic channels (blue) orient randomly in the hydrophobic matrix. These two models are compatible depending on the size of and distance between the polymeric aggregates.

1.3 Transport in soft materials

Molecular transport properties of many materials are essential for their applications. For example, water, gas, and ion diffusion through polymers plays a key role for their applications as water-purification, gas-separation, and ion-conducting membranes, respectively. Many biological processes involving energy or mass transfer are also highly dependent on molecular diffusion. For instance, nanoparticles diffusing into or within tumor tissues is a crucial step for drug delivery.[10] Moreover, structural and dynamic properties of soft materials strongly influence or determine the transport of absorbed molecules, therefore transport studies can in turn reflect and probe structure and dynamics of soft materials in ways that may not be accessible by other analytical tools. In this section, we will introduce some fundamental concepts about diffusion and some models for diffusion in fluids as well as diffusion behaviors within confined geometries in soft materials.

1.3.1 Diffusion: macroscopic and microscopic approach

Generally, transport phenomena include the transfer of thermal energy (heat), mass, momentum, electric charge, etc., based on continuous thermal motion of molecules. Bulk flow may be caused by external forces (eg. pressure, heat) applied on the system, which is important for some applications of soft materials, for example, water permeability through reserve-osmosis membranes driven by external pressure. However, here we only focus on transport phenomena without external physical driving forces, *i.e.*, diffusion. The process of diffusion is evident by a change in an initially formed gradient of concentration, but diffusion can also be viewed as the random walk of particles due to thermal molecular motion. This thesis employs concepts and measurements of diffusion both from the macroscopic perspective (measurable variations in concentration) as well as the microscopic perspective (local self-diffusion).

The empirical or "macroscopic" approach to diffusion is Fick's law.[55-57] For one-dimensional diffusion, Fick's first law describes the relation between the flux J of particles and the gradient of concentration, dc/dx:

$$J = -D\frac{\mathrm{d}c}{\mathrm{d}x} \tag{1.1}$$

The proportionality constant D is called the diffusion coefficient or diffusivity, and the negative sign signifies that the net flow of particles is from regions of high concentration to regions of low concentration. In three dimensions, $\boldsymbol{J}$ is a vector, and $\boldsymbol{D}$ becomes a 3×3 tensor, and Fick's first law then reads:

$$\boldsymbol{J}(\boldsymbol{r},t) = -\boldsymbol{D}\,\nabla c(\boldsymbol{r},t) \tag{1.2}$$

Combined with the law of mass conservation:

$$\frac{\partial c(\boldsymbol{r},t)}{\partial \mathrm{t}} = -\nabla\cdot\boldsymbol{J}(\boldsymbol{r},t) \tag{1.3}$$

Fick's second law or the diffusion equation is derived:

$$\frac{\partial c(\boldsymbol{r},t)}{\partial t} = D\nabla^2 c(\boldsymbol{r},t) \tag{1.4}$$

This diffusion equation describes the change of concentration as a function of spatial position $\boldsymbol{r}$ and time t. For simplicity, we consider the one-dimension diffusion equation:

$$\frac{\partial c(x,t)}{\partial t} = D\frac{\partial^2 c(x,t)}{\partial^2 t} \tag{1.5}$$

Boundary conditions and initial conditions are required to solve this equation. Here we show two solutions to Eq. 1.5 with different initial conditions.

The first example (Figure 1.5a) represents a droplet of dye with a total number of particles of n_0 being deposited at position $x = 0$ at $t = 0$ and spreading out along $\pm x$. With the condition $\int_{-\infty}^{+\infty} c(x,t)dx = n_0$, we easily find[58]

$$c(x,t) = \frac{n_0}{\sqrt{4\pi Dt}}\exp\left(-\frac{x^2}{4Dt}\right). \tag{1.6}$$

The second example (Figure 1.5b) represents a long tube of dye with a concentration of c_0 placed at positon $x = 0$ at $t = 0$ and spreading out along $+x$. With the conditions $c(x \le 0, t) = c_0, c(x > 0, 0) = 0$, we have[55]

$$c(x,t) = c_0\mathrm{erfc}\left(\frac{x}{2\sqrt{Dt}}\right). \tag{1.7}$$

Here erfc(x) is the complementary error function, defined as

$$\mathrm{erfc}(x) = 1 - \mathrm{erf}(x) = \frac{2}{\sqrt{\pi}}\int_x^{\infty} e^{-t^2}\mathrm{d}t. \tag{1.8}$$

Figure 1.5 shows the interesting difference of concentration as a function of displacement and time between the two situations with identical diffusion coefficient and times. In Chapter 5,

we will study the diffusion of imaging contrast agent solution into gels using the second model mentioned here.

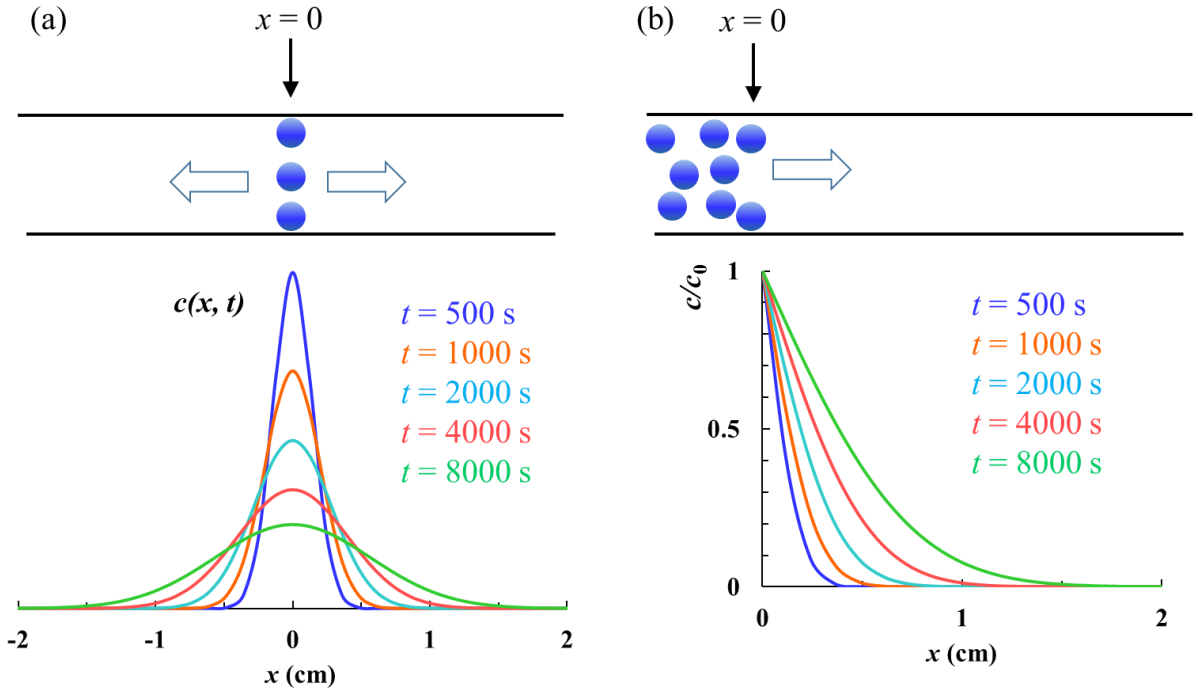

Figure 1.5 Concentration vs. displacement curves as a function of time for particles that (a) begin with initial position x = 0 and initial time $t = 0$ with a constant total particle number over time, with diffusion along $\pm x$, and (b) are maintained at constant concentration c_0 at x = 0 over time and diffuse along + x. Note $D = 2 \times 10^{-9}$ m^2/s and time intervals are the same for both cases.

Apart from Fick's law, an atomistic or "microscopic" approach to diffusion is nonequilibrium statistical mechanics,[55] as originally formulated by Einstein.[59] Diffusion of particles can be computed using the random-walk model. For simplicity, we consider a random "walker" in one dimension along the x direction. The probability $P(m, N)$ is defined that a walk has N total steps with m of them being forward (in the $+x$ direction) and N-m steps being

backward (in the –*x* direction), while the *a priori* probability of a forward step is denoted as *f* and the probability of a backward step is $b = 1 - f$. $P(m, N)$ can be written as[58]

$$P(m,N) = \frac{N!}{m!\,(N-m)!} f^m b^{N-m} \tag{1.9}$$

When $N \to \infty$, $P(m,N)$ is a Gaussian distribution function:

$$P(m,N) = \frac{1}{\sqrt{2\pi Nfb}} e^{-(m-Nf)^2/(2Nfb)} \tag{1.10}$$

$P(m,N)$ reaches a maximum when $m = Nf$. The average distance traveled by a random walker is zero, but the root-mean-square (RMS) displacement is the measure of the width of $P(m,N)$ and is the most important characterization of the average trajectory of a random walker:

$$\langle (m - Nf)^2 \rangle = Nfb \tag{1.11}$$

When considering molecular self-diffusion with free boundary conditions, the conditional probability $P(x, t)$ denotes the probability of a diffusing particle to travel a distance x within the time t: [55, 60]

$$P(x,t) = \frac{1}{\sqrt{4\pi Dt}} \exp\left(-\frac{x^2}{4Dt}\right). \tag{1.12}$$

Then we have

$$\langle x^2 \rangle = 2Dt \tag{1.13}$$

for a one-dimensional random walk, and

$$\langle r^2 \rangle = 6Dt \tag{1.14}$$

for a three-dimensional model. These equations relate the widely accepted concept of the diffusion coefficient with the experimentally measurable mean-square displacement as a function of time.

In conclusion, diffusion can be viewed on the macroscopic scale as the movement of particles by an "effective force" due to a concentration gradient, but statistically (entropically), diffusion down the concentration gradient can be simply explained in that large numbers of particles have more ways to "walk" than small numbers of particles.

1.3.2 Diffusion in porous media

Diffusion in porous media is a common phenomenon observed in many biological, physical, and chemical systems, such as K^+/Na^+ transporting via the K^+ channel of human red blood cells,[61] long-range proton transfer in hydrogen fuel cells,[62-63] or water permeation through reverse osmosis membranes.[64-67] Molecular motions are hindered or facilitated when traveling in the structural labyrinth of the porous matrix. Transport of particles in a porous medium is greatly influenced by many factors, including 1) intermolecular interaction among mobile species, 2) interaction between mobile species and pore surface, 3) local geometry and tortuosity of pores, and 4) dynamics such as chain motions of the porous medium. A better understanding of structure-transport relationships for these complex media will benefit many fields of science.

One of the most effective and simplest way to probe molecular transport is the observation of root-mean-square displacement as a function of diffusion time,[68]

$$\langle (r(t) - r(0))^2 \rangle = ADt^n \tag{1.15}$$

Here *A* is the dimensional factor with values of 2, 4, 6 for diffusion in one-, two- and three-dimensions, respectively. Compared with Eq. 1.13 and Eq. 1.14, this equation has an additional term *n*, which determines the type of diffusion mechanism. *n* = 2, 1, or 1/2 represent ballistic, diffusive (Fickian), or single-file diffusion mechanisms, respectively (Figure 1.6). When *n* = 1, and Eq. 1.15 is identical to Eq. 1.13 or 1.14, diffusion is caused by random thermal motion

of molecules, obeying Fick's law. Pure ballistic motion happens at time scales below where diffusive motion takes place, when molecules have not collided with each other. This usually occurs at very short times for liquids (t < 10 ps) but at longer times for gases, which have a much greater mean free path, and the travel distance $|r^2|$ is equal to v^2t^2 leading to n = 2. Single-file diffusion occurs when molecules can only travel along one dimension and cannot pass each other, usually in a very narrow confined environment, resulting in n = 1/2. For entangled high molecular weight polymers diffusing in viscous solutions, very small n such as n = 1/4 may be observed. The deviation from these n values suggests a change in the diffusion mechanism. For example, for water molecules diffusing in carbon nanotubes, molecular dynamics simulations and experiments have reported single-file diffusion dominates in small nanotubes, while the diffusion mechanism switches from diffusive to ballistic when the observation region switches from the center to the surface of relatively large nanotubes.[9, 69-75] Different diffusion mechanisms may also be observed in porous soft materials such as polymers and supramolecular assemblies. In Chapter 6, we will show that anions of $[C_2mim][BF_4]$ inside Nafion experience a transition from single-file diffusion to 3D diffusive behaviorwith increasing temperature.

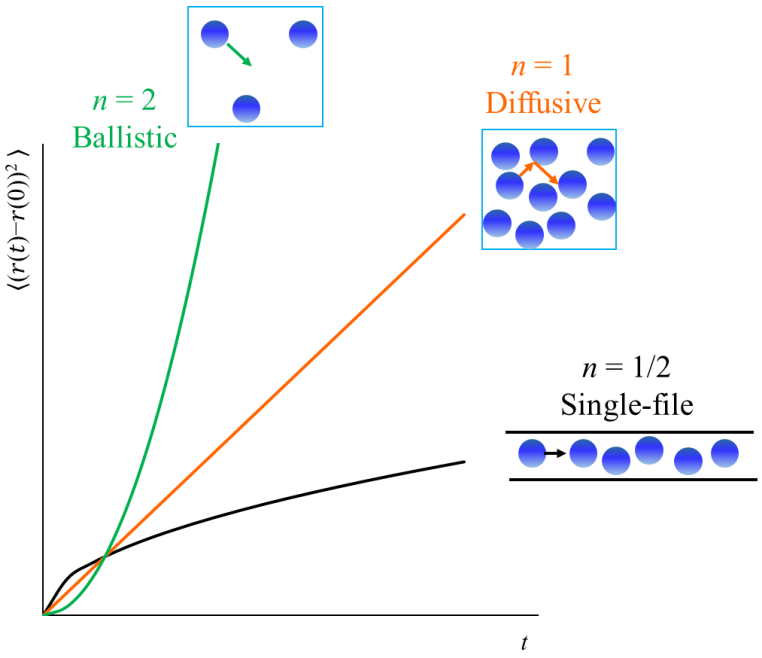

Figure 1.6 Schematic representation of three diffusion mechanisms with their root-mean-square displacement vs. diffusion time.

Sometimes an apparent n = 1 may be observed for molecular diffusion in a porous medium even when diffusion is restricted by pores with an effective size of d and tortuosity $\Im$. In this case, an effective diffusion coefficient D_{eff} can be defined as $D_{\text{eff}} = \langle\left(r(t) - r(0)\right)^2\rangle / 6t$.[68] Diffusion length is defined as $L = \sqrt{\langle\left(r(t) - r(0)\right)^2\rangle}$. Figure 1.7 shows D_{eff} obtained from $\langle\left(r(t) - r(0)\right)^2\rangle$ as a function of diffusion t for three cases. We denote D_0 as the "free" (intrapore or pure liquid) molecular diffusion coefficient. At small diffusion time, the collision between particles and pore surface is rare, therefore $\langle\left(r(t) - r(0)\right)^2\rangle$ vs. time is linear, resulting in $D_{\text{eff}} = D_0$. When increasing diffusion time, the probability for particles to collide with the pore surface increases and therefore the confinement effect of the pore significantly

influences $\langle\left(r(t)-r(0)\right)^2\rangle$, which plateaus at a value of d^2 for isolated pores (Figure 1.7e), resulting in $D_{\text{eff}}(\infty)=0$. For interconnected pores, at long diffusion time, some particles collide with the pore surface while some can travel through the narrow connections between pores, leading to another linear dependence of $\langle\left(r(t)-r(0)\right)^2\rangle$ vs. t with $0 < D_{\text{eff}}(\infty) < D_0$. Therefore, in both isolated and interconnected pores, particle diffusion behaviors coincide with what we observe in the free liquid state only at very small diffusion times. The time-dependent diffusion behavior reflects the size and tortuosity of the confinement. For example, the pore size d can be obtained as the diffusion length L at the plateau for isolated pores, and the tortuosity $\Im$ can be obtained by $\Im = D_{\text{eff}}(\infty)/D_0$. Therefore transport (dynamic) measurements can be employed to provide structural information.

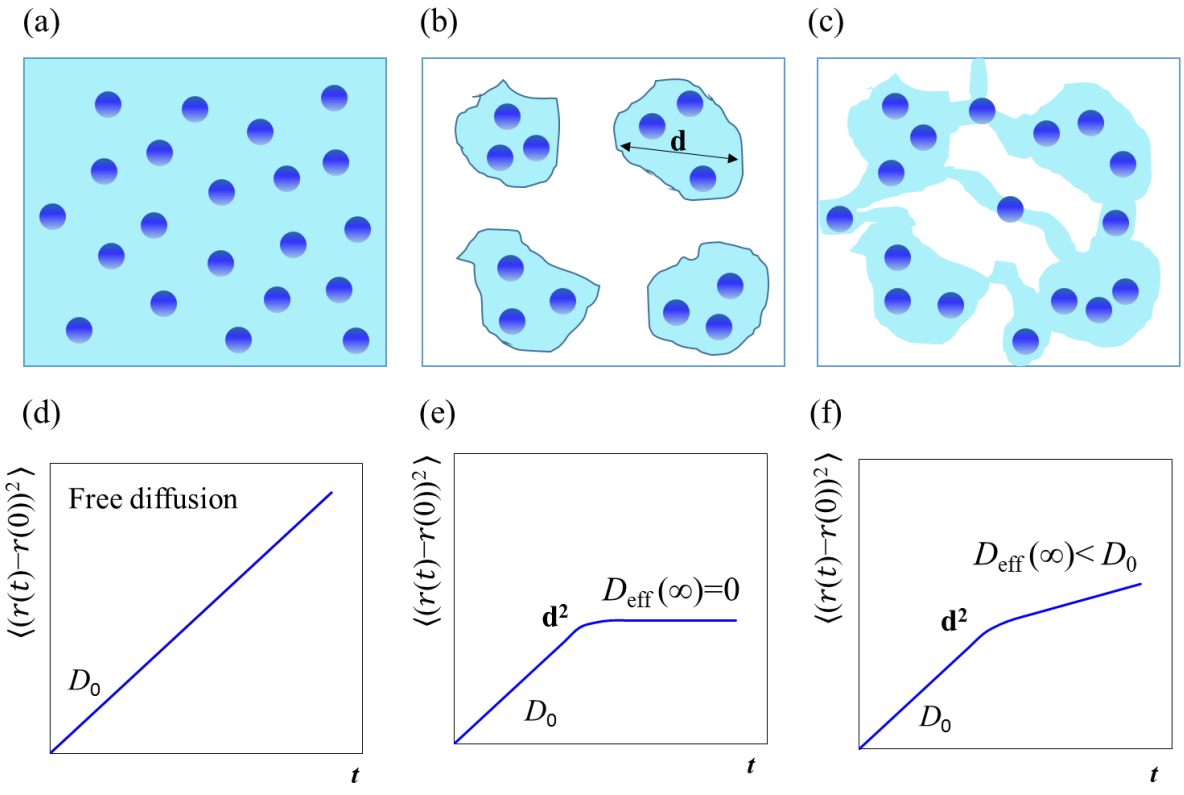

Figure 1.7 Schematic illustration of root-mean-square displacement vs. diffusion time for particles that (a) obey free diffusion, (b) are in isolated pores, and (c) are in an interconnected porous medium.[64]

In summary, this chapter quickly introduces structure and dynamics of three soft materials systems: supramolecular assemblies, ionic liquids and ionic polymers. These three systems are the subjects of Chapter 3, 4 and 6. This chapter also briefly reviews some fundamental concepts of diffusion and diffusion phenomena in porous media, which also appear in Chapter 4, 5 and 6. In Chapter 2, we will introduce relevant concepts of the NMR methodologies used in our studies.

Reference

(1) Hamley, I. W., *Introduction to Soft Matter: Synthetic and Biological Self-Assembling Materials, Revised Edition*. Wiley: England, 2013.
(2) Dutcher, J. R. M., Alejandro G, *Soft Materials; Structure and Dynamics*. Ringgold Inc: Portland, 2005.
(3) Rabi, I. I. Z., J. R.; Millman, S.; Kusch, P. A New Method of Measuring Nuclear Magnetic Moment. *Physical Review* **1938,** *53*, 318-318.
(4) Purcell, E. M.; Torrey, H. C.; Pound, R. V. Resonance Absorption by Nuclear Magnetic Moments in a Solid. *Physical Review* **1946,** *69*, 37-38.
(5) Bloch, F.; Hansen, W. W.; Packard, M. Nuclear Induction. *Physical Review* **1946,** *69*, 127-127.
(6) Allen, M. H.; Wang, S.; Hemp, S. T.; Chen, Y.; Madsen, L. A.; Winey, K. I.; Long, T. E. Hydroxyalkyl-Containing Imidazolium Homopolymers: Correlation of Structure with Conductivity. *Macromolecules* **2013,** *46*, 3037-3045.
(7) Zhang, B.; Spano, J.; Chen, Y.; Turner, R.; Wi, S. Crystallinity and Motional Dynamics Study of a Series of Poly(Arylene Ether Sulfone) Segmented Copolymer Analogues. *The Journal of Physical Chemistry B* **2012,** *116*, 7970-7980.

(8) Lee, C. H.; Lee, K.-S.; Lane, O.; McGrath, J. E.; Chen, Y.; Wi, S.; Lee, S. Y.; Lee, Y. M. Solvent-Assisted Thermal Annealing of Disulfonated Poly(Arylene Ether Sulfone) Random Copolymers for Low Humidity Polymer Electrolyte Membrane Fuel Cells. *RSC Advances* **2012,** *2*, 1025-1032.
(9) Chen, Q.; Wang, Q.; Liu, Y.-C.; Wu, T. The Effect of Hydrogen Bonds on Diffusion Mechanism of Water inside Single-Walled Carbon Nanotubes. *The Journal of Chemical Physics* **2014,** *140*, 214507.
(10) Wang, X.; Chen, Y.; Xue, L.; Pothayee, N.; Zhang, R.; Riffle, J. S.; Reineke, T. M.; Madsen, L. A. Diffusion of Drug Delivery Nanoparticles into Biogels Using Time-Resolved Micromri. *The Journal of Physical Chemistry Letters* **2014,** *5*, 3825-3830.
(11) Lehn, J.-M., *Supramolecular Chemistry: Concepts and Perspectives*. Wiley-VCH Verlag GmbH & Co. KGaA: Weinheim, FRG, 1995.
(12) Nakanishi, T., *Supramolecular Soft Matter: Applications in Materials and Organic Electronics*. John Wiley & Sons, Inc.: Hoboken, New Jersey, 2012.
(13) Dong, B.; Sakurai, T.; Honsho, Y.; Seki, S.; Maeda, H. Cation Modules as Building Blocks Forming Supramolecular Assemblies with Planar Receptor–Anion Complexes. *J. Am. Chem. Soc.* **2013,** *135*, 1284-1287.
(14) Ye, X.; Chen, J.; Engel, M.; Millan, J. A.; Li, W.; Qi, L.; Xing, G.; Collins, J. E.; Kagan, C. R.; Li, J.; Glotzer, S. C.; Murray, C. B. Competition of Shape and Interaction Patchiness for Self-Assembling Nanoplates. *Nat Chem* **2013,** *5*, 466-473.
(15) Chen, Y.; Lingwood, M. D.; Goswami, M.; Kidd, B. E.; Hernandez, J. J.; Rosenthal, M.; Ivanov, D. A.; Perlich, J.; Zhang, H.; Zhu, X.; Möller, M.; Madsen, L. A. Humidity-Modulated Phase Control and Nanoscopic Transport in Supramolecular Assemblies. *The Journal of Physical Chemistry B* **2014,** *118*, 3207-3217.
(16) O'Neill, M.; Kelly, S. M. Liquid Crystals for Charge Transport, Luminescence, and Photonics. *Adv. Mater.* **2003,** *15*, 1135-1146.
(17) Kishimoto, K.; Yoshio, M.; Mukai, T.; Yoshizawa, M.; Ohno, H.; Kato, T. Nanostructured Anisotropic Ion-Conductive Films. *J. Am. Chem. Soc.* **2003,** *125*, 3196-3197.
(18) Yoshio, M.; Mukai, T.; Ohno, H.; Kato, T. One-Dimensional Ion Transport in Self-Organized Columnar Ionic Liquids. *J. Am. Chem. Soc.* **2004,** *126*, 994-995.
(19) Shimura, H.; Yoshio, M.; Hoshino, K.; Mukai, T.; Ohno, H.; Kato, T. Noncovalent Approach to One-Dimensional Ion Conductors: Enhancement of Ionic Conductivities in Nanostructured Columnar Liquid Crystals. *J. Am. Chem. Soc.* **2008,** *130*, 1759-1765.
(20) Ichikawa, T.; Yoshio, M.; Hamasaki, A.; Kagimoto, J.; Ohno, H.; Kato, T. 3d Interconnected Ionic Nano-Channels Formed in Polymer Films: Self-Organization and Polymerization of Thermotropic Bicontinuous Cubic Liquid Crystals. *J. Am. Chem. Soc.* **2011,** *133*, 2163-2169.
(21) Yeh, M.-C.; Su, Y.-L.; Tzeng, M.-C.; Ong, C. W.; Kajitani, T.; Enozawa, H.; Takata, M.; Koizumi, Y.; Saeki, A.; Seki, S.; Fukushima, T. Amphiphilic Design of a Discotic Liquid-

Crystalline Molecule for Dipole Manipulation: Hierarchical Columnar Assemblies with a 2d Superlattice Structure. *Angew. Chem. Int. Ed.* **2013,** *52*, 1031-1034.
(22) Zhang, H.; Li, L.; Möller, M.; Zhu, X.; Rueda, J. J. H.; Rosenthal, M.; Ivanov, D. A. From Channel-Forming Ionic Liquid Crystals Exhibiting Humidity-Induced Phase Transitions to Nanostructured Ion-Conducting Polymer Membranes. *Adv. Mater.* **2013,** *25*, 3543-3548.
(23) Tokuda, H.; Hayamizu, K.; Ishii, K.; Susan, M.; Watanabe, M. Physicochemical Properties and Structures of Room Temperature Ionic Liquids. 1. Variation of Anionic Species. *J. Phys. Chem. B* **2004,** *108*, 16593-16600.
(24) Tokuda, H.; Hayamizu, K.; Ishii, K.; Susan, M. A.; Watanabe, M. Physicochemical Properties and Structures of Room Temperature Ionic Liquids. 2. Variation of Alkyl Chain Length in Imidazolium Cation. *J Phys Chem B* **2005,** *109*, 6103-10.
(25) Tokuda, H.; Ishii, K.; Susan, M. A. B. H.; Tsuzuki, S.; Hayamizu, K.; Watanabe, M. Physicochemical Properties and Structures of Room-Temperature Ionic Liquids. 3. Variation of Cationic Structures. *The Journal of Physical Chemistry B* **2006,** *110*, 2833-2839.
(26) MacFarlane, D.; Forsyth, S.; Golding, J.; Deacon, G. Ionic Liquids Based on Imidazolium, Ammonium and Pyrrolidinium Salts of the Dicyanamide Anion. *Green Chemistry* **2002,** *4*, 444-448.
(27) Galinski, M.; Lewandowski, A.; Stepniak, I. Ionic Liquids as Electrolytes. *Electrochimica Acta* **2006,** *51*, 5567-5580.
(28) Forsyth, S.; Pringle, J.; MacFarlane, D. Ionic Liquids-an Overview. *Australian Journal of Chemistry* **2004,** *57*, 113-120.
(29) Tokuda, H.; Tsuzuki, S.; Susan, M. A. B. H.; Hayamizu, K.; Watanabe, M. How Ionic Are Room-Temperature Ionic Liquids? An Indicator of the Physicochemical Properties. *The Journal of Physical Chemistry B* **2006,** *110*, 19593-19600.
(30) Binnemans, K. Ionic Liquid Crystals. *Chemical Reviews* **2005,** *105*, 4148-4204.
(31) Gozzo, F. C.; Santos, L. S.; Augusti, R.; Consorti, C. S.; Dupont, J.; Eberlin, M. N. Gaseous Supramolecules of Imidazolium Ionic Liquids: "Magic" Numbers and Intrinsic Strengths of Hydrogen Bonds. *Chemistry – A European Journal* **2004,** *10*, 6187-6193.
(32) Dupont, J. From Molten Salts to Ionic Liquids: A "Nano" Journey. *Accounts of Chemical Research* **2011,** *44*, 1223-1231.
(33) Corvo, M. C.; Sardinha, J.; Menezes, S. C.; Einloft, S.; Seferin, M.; Dupont, J.; Casimiro, T.; Cabrita, E. J. Solvation of Carbon Dioxide in [C4mim][Bf4] and [C4mim][Pf6] Ionic Liquids Revealed by High-Pressure Nmr Spectroscopy. *Angewandte Chemie International Edition* **2013,** *52*, 13024-13027.
(34) Hunt, P. A.; Ashworth, C. R.; Matthews, R. P. Hydrogen Bonding in Ionic Liquids. *Chemical Society Reviews* **2015,** *44*, 1257-1288.
(35) Tokuda, H.; Hayamizu, K.; Ishii, K.; Susan, M. A. B. H.; Watanabe, M. Physicochemical Properties and Structures of Room Temperature Ionic Liquids. 2. Variation of Alkyl Chain Length in Imidazolium Cation. *The Journal of Physical Chemistry B* **2005,** *109*, 6103-6110.

(36) Gebbie, M. A.; Valtiner, M.; Banquy, X.; Fox, E. T.; Henderson, W. A.; Israelachvili, J. N. Ionic Liquids Behave as Dilute Electrolyte Solutions. *Proceedings of the National Academy of Sciences* **2013,** *110*, 9674-9679.
(37) Weingärtner, H. Understanding Ionic Liquids at the Molecular Level: Facts, Problems, and Controversies. *Angewandte Chemie International Edition* **2008,** *47*, 654-670.
(38) Gabl, S.; Steinhauser, O.; Weingärtner, H. From Short-Range to Long-Range Intermolecular Noes in Ionic Liquids: Frequency Does Matter. *Angewandte Chemie International Edition* **2013,** *52*, 9242-9246.
(39) Wang, H. Y.; Wang, J. J.; Zhang, S. L.; Pei, Y. C.; Zhuo, K. L. Ionic Association of the Ionic Liquids [C(4)Mim][Bf4], [C(4)Mim][Pf6], and [C(N)Mim]Br in Molecular Solvents. *ChemPhysChem* **2009,** *10*, 2516-2523.
(40) Tsuzuki, S.; Tokuda, H.; Hayamizu, K.; Watanabe, M. Magnitude and Directionality of Interaction in Ion Pairs of Ionic Liquids: Relationship with Ionic Conductivity. *J Phys Chem B* **2005,** *109*, 16474-81.
(41) Hou, J.; Zhang, Z.; Madsen, L. A. Cation/Anion Associations in Ionic Liquids Modulated by Hydration and Ionic Medium. *The Journal of Physical Chemistry B* **2011,** *115*, 4576-4582.
(42) Mauritz, K. A.; Moore, R. B. State of Understanding of Nafion. *Chemical Reviews* **2004,** *104*, 4535-4586.
(43) Gierke, T. D.; Munn, G. E.; Wilson, F. C. The Morphology in Nafion Perfluorinated Membrane Products, as Determined by Wide- and Small-Angle X-Ray Studies. *Journal of Polymer Science: Polymer Physics Edition* **1981,** *19*, 1687-1704.
(44) Rubatat, L.; Rollet, A. L.; Gebel, G.; Diat, O. Evidence of Elongated Polymeric Aggregates in Nafion. *Macromolecules* **2002,** *35*, 4050-4055.
(45) Rubatat, L.; Gebel, G.; Diat, O. Fibrillar Structure of Nafion: Matching Fourier and Real Space Studies of Corresponding Films and Solutions. *Macromolecules* **2004,** *37*, 7772-7783.
(46) Gebel, G.; Diat, O. Neutron and X-Ray Scattering: Suitable Tools for Studying Ionomer Membranes. *Fuel Cells* **2005,** *5*, 261-276.
(47) Schmidt-Rohr, K.; Qiang, C. Parallel Cylindrical Water Nanochannels in Nafion Fuel-Cell Membranes. *Nature Materials* **2008,** *7*, 75-83.
(48) Dura, J. A.; Murthi, V. S.; Hartman, M.; Satija, S. K.; Majkrzak, C. F. Multilamellar Interface Structures in Nafion. *Macromolecules* **2009,** *42*, 4769-4774.
(49) Kreuer, K.-D.; Portale, G. A Critical Revision of the Nano-Morphology of Proton Conducting Ionomers and Polyelectrolytes for Fuel Cell Applications. *Advanced Functional Materials* **2013,** *23*, 5390-5397.
(50) Allen, F. I.; Comolli, L. R.; Kusoglu, A.; Modestino, M. A.; Minor, A. M.; Weber, A. Z. Morphology of Hydrated as-Cast Nafion Revealed through Cryo Electron Tomography. *ACS Macro Letters* **2015,** *4*, 1-5.
(51) Li, J.; Wilmsmeyer, K. G.; Madsen, L. A. Hydrophilic Channel Alignment Modes in Perfluorosulfonate Ionomers: Implications for Proton Transport. *Macromolecules* **2008,** *41*, 4555-4557.

(52) Li, J.; Wilmsmeyer, K. G.; Madsen, L. A. Anisotropic Diffusion and Morphology in Perfluorosulfonate Ionomers Investigated by Nmr. *Macromolecules* **2009,** *42*, 255-262.
(53) Park, J. K.; Li, J.; Divoux, G. M.; Madsen, L. A.; Moore, R. B. Oriented Morphology and Anisotropic Transport in Uniaxially Stretched Perfluorosulfonate Ionomer Membranes. *Macromolecules* **2011,** *44*, 5701-5710.
(54) Li, J.; Park, J.K.; Moore, R. B.; Madsen, L. A. Linear Coupling of Alignment with Transport in a Polymer Electrolyte Membrane. *Nature Materials* **2011,** *10*, 507-511.
(55) Crank, J., *The Mathematics of Diffusion*. Oxford University Press: Oxford, 1975.
(56) Hunter, R. J., *Foundations of Colloid Science*. Oxford University Press: Oxford, 1986.
(57) Arfken, G., *Mathematical Methods for Physicists*. Academic Press: New York, 1995.
(58) Dill, K. A.; Bromberg, B. *Molecular Driving Forces*. Garland Science: New York, 2011.
(59) Einstein, A. Über Die Von Der Molekularkinetischen Theorie Der Wärme Geforderte Bewegung Von in Ruhenden Flüssigkeiten Suspendierten Teilchen. *Annalen der Physik* **1905,** *322*, 549-560.
(60) Kärger, J.; Heink, W. The Propagator Representation of Molecular Transport in Microporous Crystallites. *Journal of Magnetic Resonance (1969)* **1983,** *51*, 1-7.
(61) Vestergaard-Bogind, B.; Stampe, P.; Christophersen, P. Single-File Diffusion through the Ca2+-Activated K+ Channel of Human Red Cells. *J. Membrain Biol.* **1985,** *88*, 67-75.
(62) Kreuer, K.-D.; Paddison, S. J.; Spohr, E.; Schuster, M. Transport in Proton Conductors for Fuel-Cell Applications: Simulations, Elementary Reactions, and Phenomenology. *Chemical Reviews* **2004,** *104*, 4637-4678.
(63) Weber, A. Z.; Newman, J. Modeling Transport in Polymer-Electrolyte Fuel Cells. *Chemical Reviews* **2004,** *104*, 4679-4726.
(64) Paul, D. R. Reformulation of the Solution-Diffusion Theory of Reverse Osmosis. *Journal of Membrane Science* **2004,** *241*, 371-386.
(65) Geise, G. M.; Lee, H.-S.; Miller, D. J.; Freeman, B. D.; McGrath, J. E.; Paul, D. R. Water Purification by Membranes: The Role of Polymer Science. *Journal of Polymer Science Part B: Polymer Physics* **2010,** *48*, 1685-1718.
(66) Geise, G. M.; Freeman, B. D.; Paul, D. R. Sodium Chloride Diffusion in Sulfonated Polymers for Membrane Applications. *Journal of Membrane Science* **2013,** *427*, 186-196.
(67) Geise, G. M.; Paul, D. R.; Freeman, B. D. Fundamental Water and Salt Transport Properties of Polymeric Materials. *Progress in Polymer Science* **2014,** *39*, 1-42.
(68) Callaghan, P. T., *Translational Dynamics & Magnetic Resonance: Principles of Pulsed Gradient Spin Echo Nmr*. Oxford University Press: Great Clarendon Street, Oxford, 2011.
(69) Striolo, A. The Mechanism of Water Diffusion in Narrow Carbon Nanotubes. *Nano Letters* **2006,** *6*, 633-639.
(70) Cheng, C.-Y.; Bowers, C. R. Observation of Single-File Diffusion in Dipeptide Nanotubes by Continuous-Flow Hyperpolarized Xenon-129 Nmr Spectroscopy. *ChemPhysChem* **2007,** *8*, 2077-2081.

(71) Barati Farimani, A.; Aluru, N. R. Spatial Diffusion of Water in Carbon Nanotubes: From Fickian to Ballistic Motion. *The Journal of Physical Chemistry B* **2011,** *115*, 12145-12149.
(72) Kipper, A. C.; da Silva, L. B. Water Filling of Carbon Nanotubes Membranes: Porosity and Temperature Effects. *Chemical Physics Letters* **2012,** *552*, 84-87.
(73) Hughes, Z. E.; Shearer, C. J.; Shapter, J.; Gale, J. D. Simulation of Water Transport through Functionalized Single-Walled Carbon Nanotubes (Swcnts). *The Journal of Physical Chemistry C* **2012,** *116*, 24943-24953.
(74) Fasano, M.; Chiavazzo, E.; Asinari, P. Water Transport Control in Carbon Nanotube Arrays. *Nanoscale Research Letters* **2014,** *9*, 559.
(75) Liu, L.; Patey, G. N. Simulations of Water Transport through Carbon Nanotubes: How Different Water Models Influence the Conduction Rate. *The Journal of Chemical Physics* **2014,** *141*, 18C518.

Chapter 2

Multi-Modal NMR Methodologies for Soft Materials

In this chapter, we will turn to the major tools, based on NMR, used for our soft materials studies.[1-2] We will first quickly review some basic NMR concepts and interactions, followed by three distinct NMR methodologies: high-resolution solid-state NMR (SSNMR), pulsed-field-gradient (PFG) diffusometry, and magnetic resonance imaging (MRI). These methods provide comprehensive and unique ways to investigate and correlate the structure, dynamics and transport properties of soft materials.[3-6]

2.1 Basic NMR concepts and interactions

Spin angular momentum or simply referred to as "spin" is an intrinsic property of atomic nuclei, parameterized using the nuclear spin quantum number I.[7] While nuclei with I = 0 are NMR inactive and not observable with NMR spectroscopy, there are more than 100 NMR-active nuclear isotopes with $I > 0$, including ~79 elements.[8] Nuclear spin is closely related to magnetism, with the spin magnetic moment $\hat{\boldsymbol{\mu}}$ proportional to spin angular momentum $\hat{\boldsymbol{I}}$:[7]

$$\hat{\boldsymbol{\mu}} = \gamma \hat{\boldsymbol{I}} \tag{2.1}$$

The gyromagnetic ratio γ is unique for each isotope, for example, $\gamma(^2\text{H})$ and $\gamma(^{13}\text{C})$ are only ~ 1/7 and ~ 1/4 of $\gamma(^1\text{H})$, respectively. One theoretical basis of NMR spectroscopy is that this magnetic moment interacts with the external (spectrometer-generated) and internal (molecular- or material-based) magnetic fields. In addition to magnetic interactions, a quadrupolar nucleus with $I > ½$ such as ^{2}H and ^{23}Na has a non-spherical electric charge distribution, which interacts with the surrounding electric potential, thereby reflecting local electric field gradient. Spin I = ½ nuclei such as ^{1}H and ^{13}C are spherical and free from electric interactions.

Basically, in NMR experiments, various external magnetic fields are applied to manipulate nuclear spins, then the interactions of the spins with these external magnetic fields as well as the interactions between spins and and their local environments within the NMR sample are recorded. Thus, NMR signals reveal important information about the structures and motions of the sample, and this information can span the atomic scale (spectroscopy) up to the meter scale (MRI). In other words, NMR reports both the external and internal interactions of nuclear spins under user-controlled external magnetic fields. According to quantum mechanics, the spin state evolution of nuclei can be described by the time-dependent Schrödinger equation:[9]

$$\frac{\mathrm{d}}{\mathrm{d}t}\left|\psi_{\mathrm{spin}}(t)\right\rangle = -\mathrm{i}\hat{\mathcal{H}}_{\mathrm{spin}}\left|\psi_{\mathrm{spin}}(t)\right\rangle. \tag{2.2}$$

$|\psi_{\mathrm{spin}}(t)\rangle$ is the wave function representing the spin states and $\hat{\mathcal{H}}_{\mathrm{spin}}$ is the nuclear spin Hamiltonian, containing all NMR interaction terms. Figure 2.1 briefly summarizes the most important NMR interactions.[9] The total spin Hamiltonian can be written as the sum of Hamiltonians accounting for each NMR interaction:[9]

$$\hat{\mathcal{H}}_{\mathrm{spin}} = \hat{\mathcal{H}}_{\mathrm{Z}} + \hat{\mathcal{H}}_{\mathrm{RF}} + \hat{\mathcal{H}}_{\mathrm{G}} + \hat{\mathcal{H}}_{\mathrm{Q}} + \hat{\mathcal{H}}_{\mathrm{D}} + \hat{\mathcal{H}}_{\mathrm{CS}} + \hat{\mathcal{H}}_{\mathrm{J}} + \hat{\mathcal{H}}_{\mathrm{SR}} \tag{2.3}$$

where the Hamiltonians on the right side are attributed to the Zeeman interaction ($\hat{\mathcal{H}}_{\mathrm{Z}}$), applied radio-frequency (RF) field ($\hat{\mathcal{H}}_{\mathrm{RF}}$), applied magnetic field gradient ($\hat{\mathcal{H}}_{\mathrm{G}}$), quadrupolar couplings ($\hat{\mathcal{H}}_{\mathrm{Q}}$), dipole-dipole coupling ($\hat{\mathcal{H}}_{\mathrm{D}}$), chemical shift ($\hat{\mathcal{H}}_{\mathrm{CS}}$), J-coupling ($\hat{\mathcal{H}}_{\mathrm{J}}$), and spin rotation ($\hat{\mathcal{H}}_{\mathrm{SR}}$), respectively.

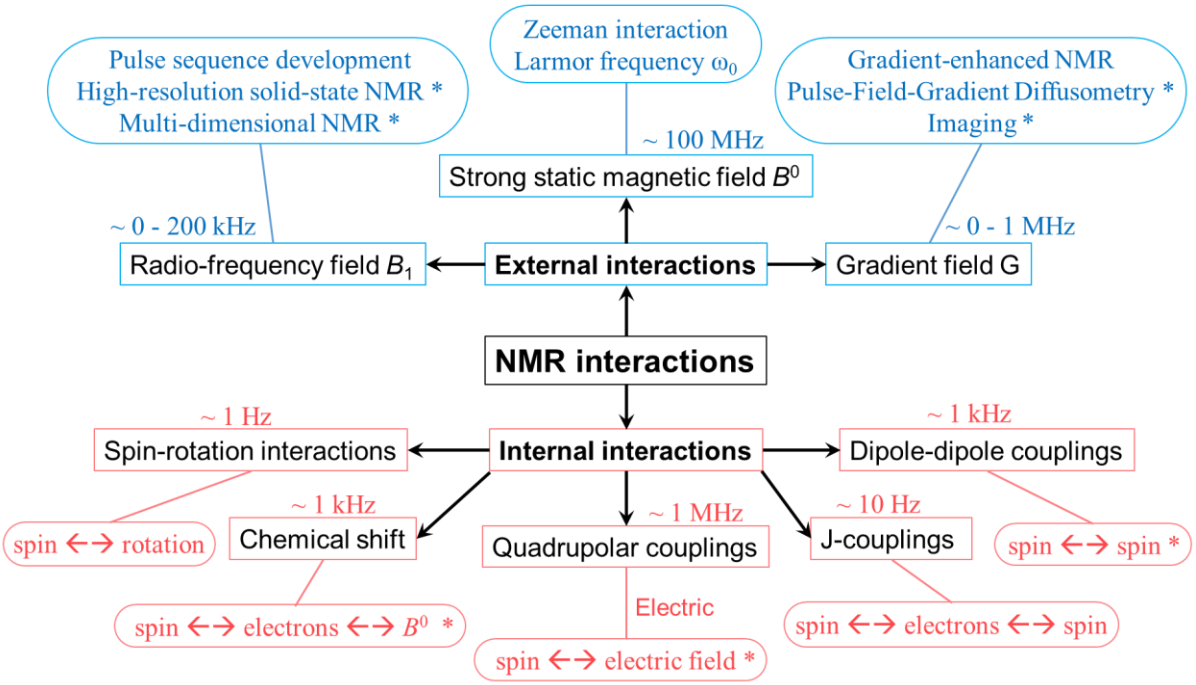

Figure 2.1 Summary of NMR interactions. The value above each box indicates the typical relative magnitude of each interaction. Note that all interactions are magnetic except quadrupolar couplings which is electric. The terms with * are the subjects of studies in the later chapters of this dissertation. Basically, our strategy is to manipulate external NMR interactions through a variety of NMR techniques in order to reveal details of subtle internal NMR interactions, which uncover structure, dynamics and transport information in soft materials.

As emphasized by Malcohm H. Levitt in his remarkable book *Spin Dynamics*,[9] we want to highlight the point that makes NMR different from all other spectroscopies. In NMR, external interactions are orders of magnitude higher (Zeeman interaction) or comparable (RF pulse and gradient pulse) to internal interactions, therefore a huge variety of techniques including extraordinary pulse sequences can be employed to "tailor" internal (spin Hamiltonian) interactions and "edit" NMR spectra to extract specific information of interest.

2.1.1 External NMR interactions

External NMR interactions are determined by external magnetic fields applied by an NMR spectrometer, usually including a very strong static magnetic field $\boldsymbol{B}^0$ ranging from 0.1 T to 30 T, an oscillating radio-frequency (RF) field $\boldsymbol{B}_1(t)$, and a magnetic field gradient $\boldsymbol{G}(r,t)$. The spin interaction with $\boldsymbol{B}^0$ is called the nuclear Zeeman interaction, and its spin Hamiltonian reads[9]

$$\hat{\mathcal{H}}_Z = -\hat{\boldsymbol{\mu}} \cdot \boldsymbol{B}^0 = -\gamma B^0 \hat{I}_z = -\omega_0 \hat{I}_z \tag{2.4}$$

Here $\omega_0 \equiv \gamma B^0$ is the Larmor frequency, generally ranging from 10 MHz to 1 GHz for ^{1}H in different spectrometers. According to quantum theory of angular momentum, a spin with quantum number I has $2I+1$ Zeeman eigenstates with eigenvalues $-I, -I+1, -I+2, \ldots +I$. Any spin state can be represented as a superposition of these eigenstates. Taking a spin-½ nucleus ^{1}H as an example, when placed in a static magnetic field $\boldsymbol{B}^0$, the Zeeman interaction splits the degenerate spin energy levels to "spin up" and "spin down" levels with the energy (frequency) difference ω_0 between them, as shown in Figure 2.2. The population distribution between the two energy levels is given by the Boltzmann distribution:

$$\frac{n_{\text{down}}}{n_{\text{up}}} = \exp\left(\frac{-\Delta E}{kT}\right) = \exp\left(\frac{-\hbar\omega_0}{kT}\right) \tag{2.5}$$

The population difference $n_{\text{up}} - n_{\text{down}}$ yields the net spin polarization M_z along z-direction, which determines NMR signal intensity. Furthermore, due to the significant difference in gyromagnetic ratio γ for different nuclei as well as the fact that the Zeeman interaction is several orders of magnitude larger than other interactions, the Zeeman interaction is usually used to identify various types of nuclear isotopes, while other interactions serve to gather more detailed structural and motional information of interest.

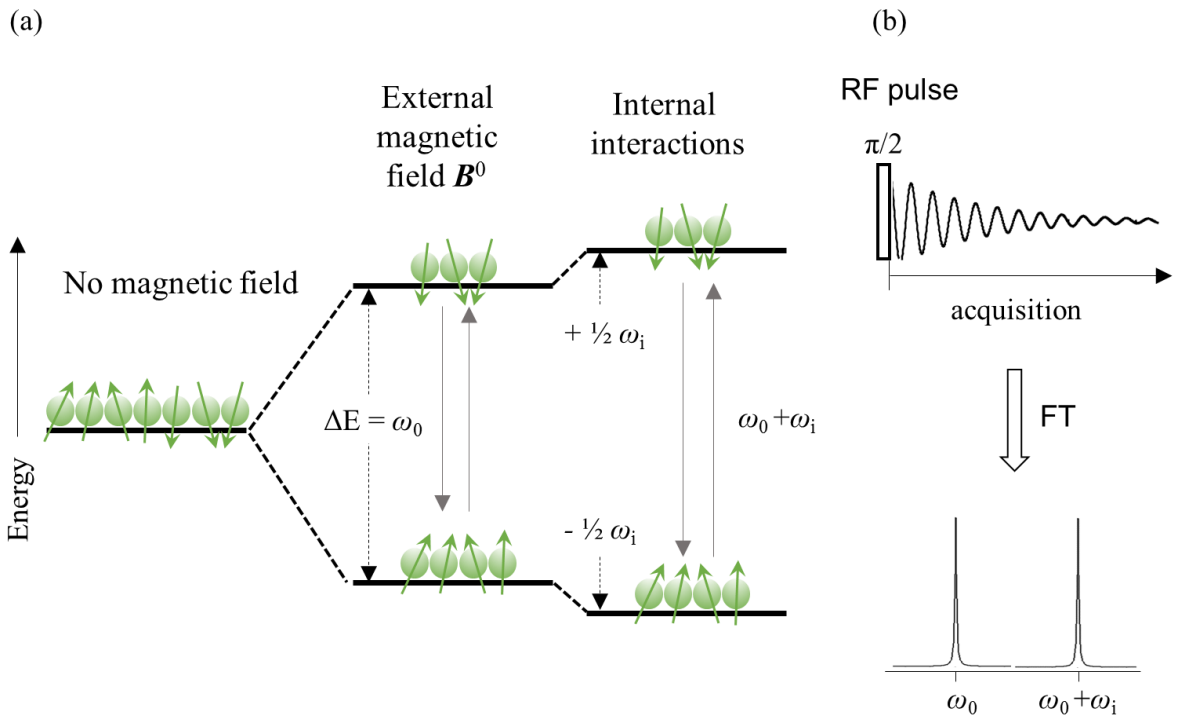

Figure 2.2 (a) Energy level diagram and population distribution of spin states for spin ½ nuclei under no magnetic field (left), the external static magnetic field $\boldsymbol{B}^0$ (middle) and with internal interactions (right). In zero field, spin states are degenerate. Under $\boldsymbol{B}^0$, Zeeman interaction leads to an energy level splitting and population difference between the two spin states. Intermolecular interactions slightly elevate, lower or further split energy levels, causing a shift in the resonance position of an NMR spectral transition. While Zeeman interaction is used for isotope identification, internal interactions can be considered as *perturbations* to it (called the secular approximation). (b) Single-pulse experiment and Fourier transform of time domain signal into a frequency domain spectrum that encodes NMR internal interactions.

A radio-frequency (RF) pulse $\boldsymbol{B}_1(t)$ is provided by an RF coil, characterized by: 1) the tilt angle θ – the angle between the RF field and the static field $\boldsymbol{B}^0$, 2) the spectrometer reference or carrier frequency ω_{ref} (close to the Larmor frequency ω_0), 3) the pulse duration τ, 4) the

phase $\emptyset$, and 5) the nutation frequency $\omega_{\mathrm{nut}} \equiv |\frac{1}{2}\gamma B_1 \sin\theta|$ with magnitude 1 – 200 kHz. [9-11] Usually the RF field is perpendicular to $\boldsymbol{B}^0$, θ = 90^0, but in some cases, such as in high-resolution SSNMR, θ = 54.7^0 for magic angle sample spinning. The pulse duration τ is normally kept short ~ 1 - 1000 μs to avoid sample and coil heating. The spin Hamiltonian can be written as

$$\hat{\mathcal{H}}_{\mathrm{RF}}(t) \cong -\omega_{\mathrm{nut}}\{\cos(\omega_{\mathrm{ref}}t + \emptyset)\,\hat{I}_{\mathrm{x}} + \sin(\omega_{\mathrm{ref}}t + \emptyset)\,\hat{I}_{\mathrm{y}}\} \quad \text{during } 0 < t < \tau. \quad (2.6)$$

Simply put, the RF pulse rotates the net spin magnetization M_z about the *x*- or *y*-axis by the flip angle determined by $\omega_{\mathrm{nut}}\tau$. For example, a π/2 ($90^0$) pulse rotates M_z to the *xy* plane and therefore equalizes the spin population while creating coherence (spin precession); a π (180^0) pulse rotates M_z to the -*z* direction and therefore inverts the spin population. RF pulses are amazing ways to manipulate nuclear spins and play a key role in high resolution SSNMR and multi-dimensional NMR. In fact, nearly all NMR methodology development involves pulse sequence programming.

A magnetic field gradient pulse $\boldsymbol{G}(\mathbf{r},t)$ is generated by gradient coils, and depends on the position **r** and time *t*. The gradient may be set along *x*-, *y*- or *z*-axis. The spin Hamiltonian for the gradient along *z*-axis reads:

$$\hat{\mathcal{H}}_{\mathrm{G}}(t) = -\gamma G_z(t) z \hat{I}_{\mathrm{z}} \quad (2.7)$$

Gradient pulses further manipulate nuclear spins as well as encode and report on the spin positions and/or displacements. They are the fundamental basis for gradient-enhanced NMR, PFG NMR diffusometry, and imaging.

2.1.2 Single-pulse experiment

The most basic experiment in typical NMR is the single-pulse experiment, as shown schematically in Figure 2.2b. This simple experiment involves three steps: 1) build up a

longitudinal spin polarization along the *z*-axis by the external static magnetic field $\boldsymbol{B_0}$, 2) "rotate" the spin polarization to the transverse plane using a $\pi/2$ pulse generated by the external RF field $\boldsymbol{B}_1$, 3) detect the oscillating electric currents in the transverse plane created by NMR samples as a free induction decay (FID), which is then Fourier transformed to the frequency domain to generate a spectrum.[9] The FID signal is encoded with internal NMR interactions whose tensor values directly reflect molecular structure and dynamics information of an NMR sample.

2.1.3 Internal NMR interactions

As shown in Figure 2.1, internal NMR interactions are orders of magnitude smaller than external interactions, spanning from ~1 Hz (spin-rotation interactions) to ~ 1 MHz (quadrupolar couplings), therefore it is impossible to cover all interactions in a single spectrum. In the gas and liquid states, due to fast rotational and translational motions of molecules, quadrupolar, dipolar and chemical shift anisotropy are averaged out, and so only J-couplings and isotropic chemical shifts remain, providing well-resolved symmetric peaks. On the contrary, in the solid state, due to highly restricted motions and large variations in configurational distributions, quadrupolar, dipolar and chemical shift anisotropy dominate the spectra with broad asymmetric overlapping peaks, while J-couplings and spin-rotational interactions are negligible.

Generally, internal interactions are anisotropic and can be represented by second-rank Cartesian tensor $\mathbb{A}$. The complete Hamiltonian is given as a bilinear product[10-11]

$$\widehat{\mathcal{H}}_{\text{int}} = \hat{\boldsymbol{I}} \cdot \mathbb{A} \cdot \hat{\boldsymbol{S}} = \begin{pmatrix} \hat{I}_{\text{x}} & \hat{I}_{\text{y}} & \hat{I}_{\text{z}} \end{pmatrix} \begin{pmatrix} A_{xx} & A_{xy} & A_{xz} \\ A_{yx} & A_{yy} & A_{yz} \\ A_{zx} & A_{zy} & A_{zz} \end{pmatrix} \begin{pmatrix} \hat{S}_{\text{x}} \\ \hat{S}_{\text{y}} \\ \hat{S}_{z} \end{pmatrix} \tag{2.8}$$

Here $\hat{\boldsymbol{S}}$ can be spin angular momentum operators of a second or the same spin in the cases of dipolar or quadrupolar couplings, or $\hat{\boldsymbol{S}}$ can describe the Cartesian vector of the static magnetic field in the case of chemical shift. Here we use chemical shift anisotropy (CSA) as an example to demonstrate how internal interactions are dealt with in SSNMR. We will discuss the static CSA spectrum in this section and how CSA is averaged under magic angle sample spinning (MAS) in the next section, then we will demonstrate the reintroduction of CSA information by two-dimensional phase-adjusted spinning sideband (2D-PASS) experiments in Chapter 3.

The chemical shift interaction is the most sensitive NMR interaction for structure determination. Chemical shifts result from the indirect magnetic interactions between a nuclear spin and the external magnetic field B^0 through the electron cloud surrounding the spin.[12] The external field generates a small magnetic field around the nucleus via circulating currents of electrons and therefore changes the effective field the nuclear spin experiences as well as its resonance frequency. In the liquid state, when molecular motions are very fast, isotropic chemical shift is the key to chemical structure identification for most organic and biological chemistry. In the solid state or other situations where motional averaging is not fast enough relative to the spin interactions, chemical shift is highly orientation dependent, or anisotropic, because the electron density around a nucleus from bonds, *p*- or π- orbitals are not symmetric but are orientation dependent. As shown in Figure 2.3a and b, different resonance positions in a NMR spectrum correspond to different orientations of phospholipids versus the external static magnetic field. The line shapes and positions provide information about the structural organization of phospholipids, such as a bilayer with a specific orientation or an isotropic liposome.

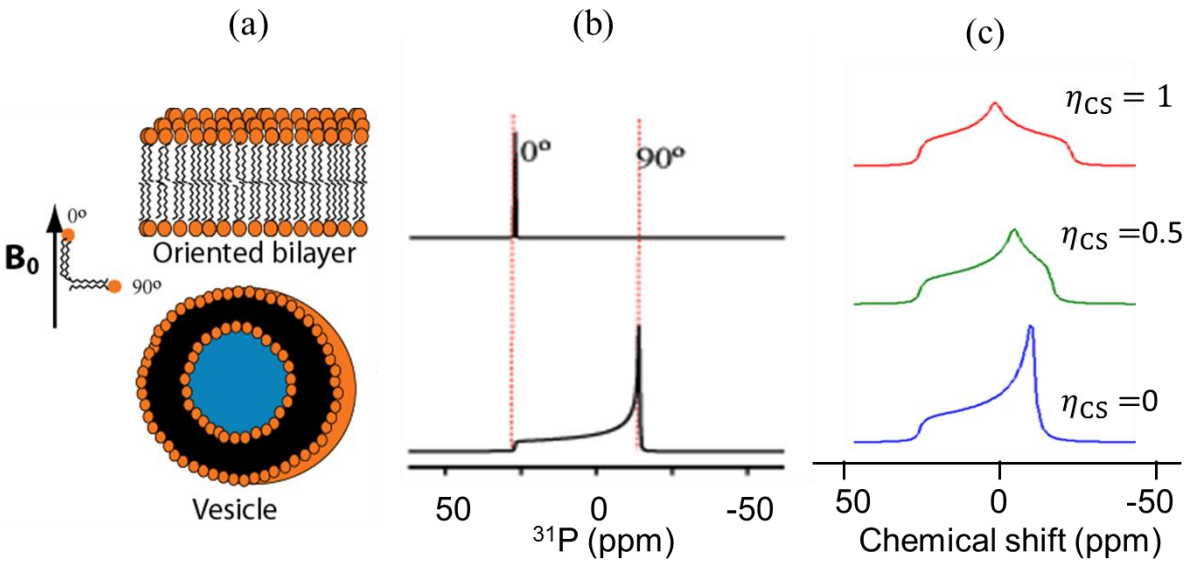

Figure 2.3 (a) schematic illustration of the orientation of a phospholipid vs. the external static field as well as the structure of a bilayer and vesicle formed from phospholipid, (b) ^{31}P static spectra of the two structures, (c) simulated static powder line shapes of chemical shift anisotropy with varying asymmetry parameter (η_{CS}) values.

In order to understand internal NMR interactions, a reference frame is chosen such that only the diagonal elements of the internal interaction tensor $\mathbb{A}$ are non-zero. This reference frame is called the Principal Axis System (PAS), where $\mathbb{A}$ is symmetric and the non-zero diagonal elements are the principal values. For example, in the PAS frame, the chemical-shift tensor $\boldsymbol{\sigma}_{CS}$ can be expressed using only three terms (principal components), σ_{xx}^{PAS}, $\sigma_{yy}^{PAS}$and σ_{zz}^{PAS}, characterizing the chemical shielding effect when the *x*, *y*, or *z* shielding axis of the PAS is aligned with B^0, respectively.[12-13]

This chemcial shift Hamiltonian can be expressed as the coupling of nuclear spin $\boldsymbol{I}$ with the external magnetic field $\gamma\boldsymbol{B}^0$ ($\boldsymbol{B}^0 = [0, 0, B^0]$) through a chemical shift tensor $\boldsymbol{\sigma}_{CS}$:

$$\widehat{\mathcal{H}}_{\mathrm{CS}} = \hat{\boldsymbol{I}} \cdot \boldsymbol{\sigma}_{\mathrm{CS}} \cdot \gamma \boldsymbol{B}^0 = \gamma B^0 \left(\hat{I}_{\mathrm{x}} \sigma_{xz}^{\mathrm{LF}} + \hat{I}_{\mathrm{y}} \sigma_{yz}^{\mathrm{LF}} + \hat{I}_{\mathrm{z}} \sigma_{zz}^{\mathrm{LF}} \right) \cong \omega_0 \hat{I}_{\mathrm{z}} \sigma_{zz}^{\mathrm{LF}} . \tag{2.9}$$

Here the secular (perturbative) approximation masks the two component $\hat{I}_{\mathrm{x}} \sigma_{xz}^{\mathrm{LF}}$ and $\hat{I}_{\mathrm{y}} \sigma_{yz}^{\mathrm{LF}}$, and only $\hat{I}_{\mathrm{z}} \sigma_{zz}^{\mathrm{LF}}$ remains. $\sigma_{\alpha\beta}^{\mathrm{LF}}$ indicates that the chemical-shift tensor is expressed in the laboratory-frame representation. After performing coordinate transformation $\mathrm{PAS} \xrightarrow{(\phi,\theta,0)} \mathrm{LAB}$, where $(\phi, \theta, 0)$ are Euler angles related to the rotation of the PAS frame to the LAB frame, the chemical shift Hamiltonian can be rewritten as:

$$\widehat{\mathcal{H}}_{\mathrm{CS}} = \left\{ \sigma_{\mathrm{iso}} + \frac{\delta_{\mathrm{csa}}}{2} [3\cos^2\theta - 1 + \eta_{\mathrm{cs}} \sin^2\theta \cos 2\phi] \right\} \omega_0 \hat{I}_{\mathrm{z}} \tag{2.10}$$

Here $\sigma_{\mathrm{iso}} \equiv (\sigma_{xx}^{\mathrm{PAS}} + \sigma_{yy}^{\mathrm{PAS}} + \sigma_{zz}^{\mathrm{PAS}})/3$ is the isotropic chemical shift, *i.e.*, the center of gravity of the static powder line shapes. σ_{iso} is orientation independent and survives in the liquid state. $\delta_{\mathrm{csa}} \equiv \sigma_{zz}^{\mathrm{PAS}} - \sigma_{\mathrm{iso}}$ is the anisotropy parameter, indicating the maximum separation in the line shapes from the center of gravity. $\eta_{\mathrm{cs}} \equiv (\sigma_{xx}^{\mathrm{PAS}} - \sigma_{yy}^{\mathrm{PAS}})/\delta_{\mathrm{csa}}$ is the asymmetry parameter, indicating the deviation from an axially symmetric tensor where $\sigma_{xx}^{\mathrm{PAS}} = \sigma_{yy}^{\mathrm{PAS}}$ and hence $\eta_{\mathrm{cs}} = 0$.

A solid-state powder sample involves random orientations, therefore the powder line shapes can be obtained by performing the angle averages for θ and ϕ $\int_0^{2\pi} \int_0^{\pi} \omega(\theta, \phi) \sin\theta \, \mathrm{d}\theta \mathrm{d}\phi$ to take all possible orientations into consideration.[13] Figure 2.3c gives the static powder spectra with varying η_{CS}values. With $\eta_{\mathrm{CS}} = 0$, the line shape fits well with the spectrum for the liposome, suggesting a symmetric spherical organization of phospholipids. Therefore chemical shift can be used for structure determination of solid-state samples if well-defined CSA line shapes can be extracted from SSNMR experiments. This is usually difficult due to the highly reduced sensitivity and resolution, except for some orientated liquid crystals with relatively fast motions. Fortunately, SSNMR has developed outflanking

tactics to remove CSA for high resolution and then reintroduce CSA through delicately designed pulse sequences.

Apart from chemical shift, dipolar and quadrupolar interactions are the other two most important interactions in SSNMR. While two spins can communicate with each other directly through dipole-dipole interactions, the additional electric quadrupole moment possessed by quadrupolar nuclei with spin $I > ½$ has an electrostatic interaction with the electric field gradient of surrounding electrons. Both can be used to extract structural and motional information of materials under consideration. Details can be found in many references.[9-14]

2.2 High-resolution solid-state NMR (SSNMR)

As mentioned above, the peaks are usually so broad and overlapping in NMR spectra for solid-state samples that little useful information can be obtained. Fortunately, two techniques serve as the foundation to achieve enhanced resolution and sensitivity for SSNMR spectra, magic angle spinning (MAS)[14-15] and cross polarization (CP).[13, 16]

2.2.1 Magic angle spinning (MAS)

Looking at the Hamiltonians in Equation 2.10, in order to completely remove the anisotropy of chemical shift, we need to 1) set $(3\cos^2\theta - 1)/2 = 0$, and 2) rotate infinitely fast to make the time average of the trigonometric terms vanish. Therefore the solution is to locate a sample system in a rotor which rotates rapidly about an axis titled by the angle $\theta = \arccos(1/\sqrt{3}) = 54.74°$ with respect to the static magnetic field B^0 (z-axis).[17] Figure 2.4a shows that the three axes x, y and z are completely symmetric when looking along the space diagonal of a cube. Fast spinning of a sample (relative to the spin interaction frequencies) around this axis lets the sample experience the time and space average of NMR interactions, therefore CSA, dipolar interactions and first-order quadrupole interactions are removed, and

only the isotropic chemical shift σ_{iso} and partial second-order quadrupole interactions remain. Figure 2.4b shows the line shapes of CSA under magic angle sample spinning with varying spinning rates ω_r. The spinning (frequency modulated) side bands resulting from trigonometric terms are equally distributed by ω_r and eventually disappear when ω_r is significantly greater than the internal interactions that broaden the spetrum. Therefore MAS elevates both resolution and sensitivity of SSNMR spectra.[14-15, 18] In Chapter 3 and 4, MAS is employed for SSNMR studies of several polymer membranes and a supramolecular assembly.

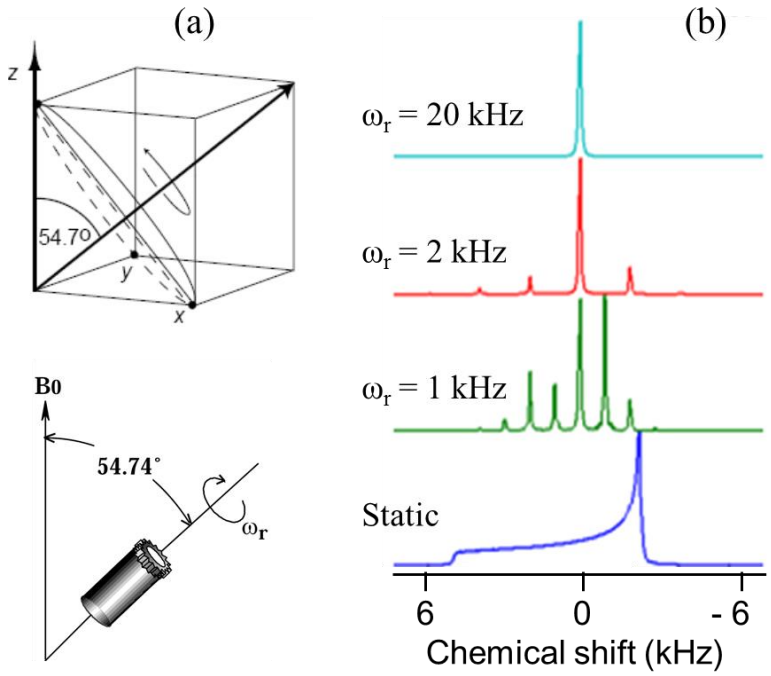

Figure 2.4 (a) The magic angle is the angle between the space diagonal of a cube with any of its axes. (b) MAS line shapes with varying sample spinning speed ω_r compared to CSA static powder line shapes.

2.2.2 Cross polarization (CP)

Cross polarization (CP) is an experiment designed to enhance signals for low-γ nuclei such as ^{13}C and ^{15}N. The major problem with direct detection of low-γ spins even with ^{1}H decoupling is low signal intensity caused by 1) low isotopic abundances, *e.g.*, 1.08% natural abundance for ^{13}C, 2) low spin polarization, *e.g.*, $\gamma(^{13}\mathrm{C})$ is only ~ 1/4 of $\gamma(^{1}\mathrm{H})$, and 3) long spin-lattice relaxation time T_1 leading to a dramatic increase in experimental time (5 T_1 for a single scan), *e.g.*, $T_1(^{13}\mathrm{C})$ is ~ 20 s but can be as long as ~100 s in some samples while $T_1(^{1}\mathrm{H})$ is ~ 3 s in water and much shorter in solid samples. A smart way to conquer this problem is to transfer spin magnetization from high-γ abundant nuclei (such as ^{1}H or ^{19}F) to low-γ rare nuclei. This method works on both liquid-state or solid-state samples, but with different pulse sequences utilizing different internal interactions. In solution NMR, the magnetization is often initially generated for ^{1}H, then transferred to neighboring ^{13}C via J-couplings, and then transferred back to ^{1}H for detection (also via J-couplings), leading to a significant increase in signal intensity and thus a dramatic decrease in experimental time.[19-21] In solid-state NMR, this technique is called cross polarization (CP), and is used to transfer magnetization from protons to neighboring low-γ rare nuclei through dipolar couplings.[16]

Figure 2.5a (upper) shows a Hartmann-Hahn[22] CP pulse sequence where initially a π/2 pulse applied to ^{1}H spins transfers proton magnetization to *xy*-plane, immediately followed by simultaneous application of two continuous RF pulses on both channels, which makes so-called "CP contact" between the two spins and transfers magnetization from ^{1}H to ^{13}C, and finally ^{13}C signal is detected directly under ^{1}H decoupling. During the CP contact time, the two RF pulses have distinct reference frequencies ω_{ref} but identical nutation frequency ω_{nut} (Section 2.1.1), for example, $\omega_{\mathrm{ref}}(^{1}\mathrm{H})$ = 400 MHz, $\omega_{\mathrm{ref}}(^{13}\mathrm{C})$ = 100 MHz, $\omega_{\mathrm{nut}}(^{1}\mathrm{H})$ =

ω_{nut}(^{13}C) = 100 kHz. So the two spins oscillate rapidly at their own Larmor resonance frequencies while rotating independently around the RF field direction at the same nutation frequency. A simple analogy is two planets rotating rapidly around their own axes with distinct rates but traveling around a sun with the same speed. If dipole-dipole interaction exists between the two spins, a "flow" of magnetization is created from highly polarized spin (^{1}H) to poorly polarized spin (^{13}C). Therefore the strength of ^{1}H-^{13}C dipolar interaction is a determining factor for polarization transfer efficiency. For example, carbons with more protons directly attached to them are faster to build up polarization, while unprotonated carbons are less efficiently coupled during CP contact and need longer CP time. However, T_1 relaxation also occurs during CP contact so the polarization build-up starts to decrease after a certain time. Therefore by changing CP contact time or comparing NMR spectra obtained from CP-pulsed and single-pulsed experiments, one can determine the protonation degree of carbon atoms. Moreover, the relaxation delay required for repeating scans is determined by T_1(^{1}H) instead of T_1(^{13}C) for CP pulse, further decreasing experimental time.

Figure 2.5b shows an example to demonstrate the signal enhancement effect caused by Hartmann-Hahn CP pulse sequence (upper) comparing to a single-pulse experiment (lower), both with MAS.[23] Due to the high sensitivity and short relaxation time of ^{1}H compared to ^{13}C, a ~ 45× signal enhancement can be obtained for ^{13}C in this sample. The combination of CP and MAS is usually called CPMAS and become a routine operation for low-γ or rare nuclei in SSNMR.[24-25] All experiments in Chapter 3 are based on CPMAS.

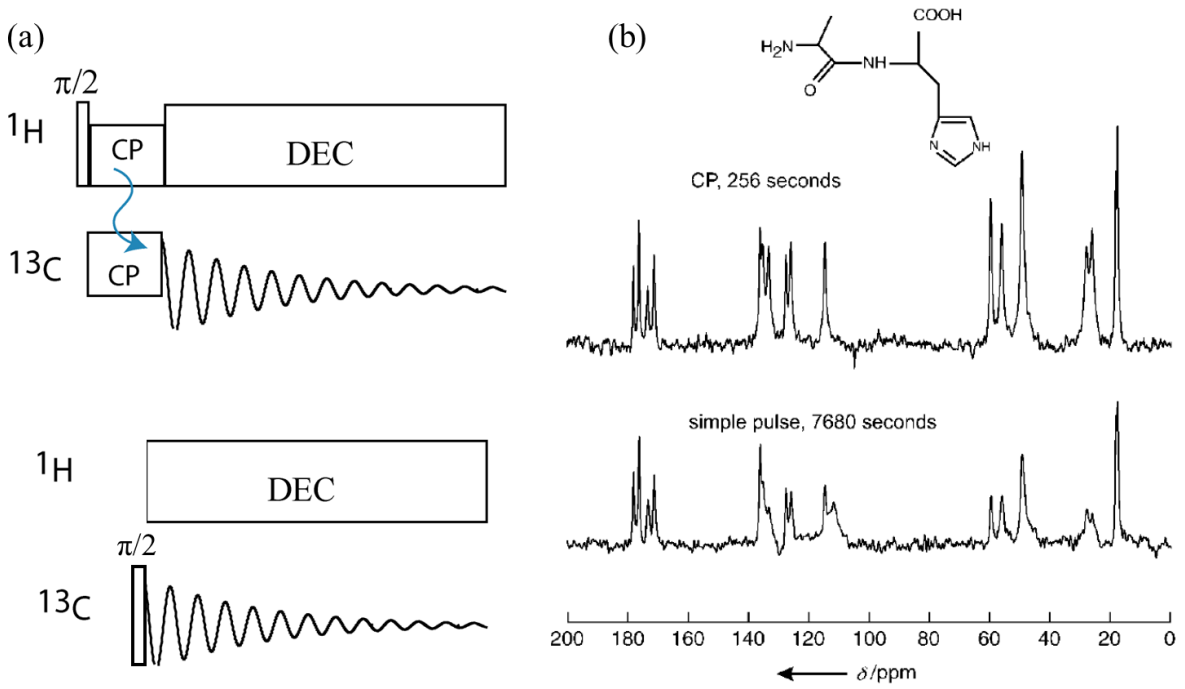

Figure 2.5 (a) Hartmann ─ Hahn CP pulse sequence of ^{13}C by ^{1}H with ^{13}C detection under ^{1}H decoupling (upper) and ^{13}C single-pulse experiment with ^{1}H decoupling (lower), (b) ^{13}C MAS spectra (spinning speed = 12 kHz) of unlabeled alanyl histidine powder: with CP enhancement (upper) and in a single-pulse experiment (lower). The recycle delay was 2 s for the CP experiment, but 60 s for the single-pulse experiment, leading to ~ 45× enhancement in terms of signal per unit of time.[23]

2.3 Pulsed-Field-Gradient (PFG) NMR

Magnetic field gradients, by definition, are spatially varying magnetic fields and can be used to encode spin spatial positions.[26] They are the fundamental tools for two important techniques: PFG diffusometry and MRI. The main function of a gradient $\boldsymbol{G}(\mathbf{r},t)$ is to generate spatially distributed Larmor frequency $\omega_0(\mathbf{r})$ along with its associated phase shift $\omega_0(\mathbf{r})t$, which can be detected to yield spatial (position) information in MRI or to provide translation motion (displacement) measurement in PFG diffusometry. For simplicity, we consider a single

gradient applied along the *z*-axis with magnitude g and duration δ. Phase shift $\emptyset(z,t)$ of a spin at position *z* and time *t* can be written as:

$$\emptyset(z,t) = \omega_0(z)t = \gamma B_0 t + \gamma z g t \qquad \text{during } 0 < t < \delta\,. \tag{2.11}$$

To better understand the effect of magnetic field gradient, we introduce a concept: isochromat, which is a collection or aggregate of "like" spins. Spins are "alike" if they are of the same isotopic species and in the same chemical and physical (net magnetic field) environment. In an inhomogeneous field, an isochromat is large on the atomic scale, containing a sufficient number of spins to obey well-defined statistical averages. When an external (usually pulsed) gradient is applied, the size of an isochromat is determined by the gradient strength and the spatial resolution of the measuring technique. The typical length scale of an isochromat is ~ 1 μm in MRI, but only ~ 1 nm under a high gradient applied in PFG diffusometry.[27]

Figure 2.6 schematically illustrates how molecular self-diffusion is measured using a typical PFG experiment.[27-28] PFG methods form the basis of many of the experiments described in Chapters 4 and 6 in this thesis. In a pulsed-gradient spin echo (PGSE) sequence (Figure 2.6a upper), the first 90 °pulse rotates the net magnetization from the *z*-direction to the *xy*-plane. Immediately after the RF pulse, all spins precess with the same frequency $\omega_0 = \gamma B_0$ under the static magnetic field $\boldsymbol{B}_0$, so before the first (linear) gradient pulse, isochromats at different positions are in phase. When the first gradient pulse is applied, isochromats precess with position-dependent angular frequency $\omega_0(z) = \gamma B_0 + \gamma z g$, leading to a spatially distributed phase angle $\emptyset(z) = \gamma B_0 \delta + \gamma z g \delta$ at the end of the gradient pulse with duration δ. $\emptyset(z)$ varies continuously and linearly in space and forms a helix profile along the gradient direction. Such a process is called *phase encoding* since it establishes a relationship between

phase angle and molecular position. If molecules with spins are fixed in position during the time period Δ (the delay between the first and second gradient pulses) the 180 °RF pulse inverts the helix phase, and the second gradient pulse of the same strength, duration and sign perfectly rewinds the helix, producing a maximum echo signal when all the spin isochromats come into phase again, with a signal intensity denoted as I_0. If there are translational molecular motions during the time period Δ, a distribution of phases encoded with the history of the motions disturbs the complete refocus of the spin isochromats after the second gradient pulse, leading to a loss of magnetization phase coherence and thereby a decrease in NMR signal intensity (denoted as I).

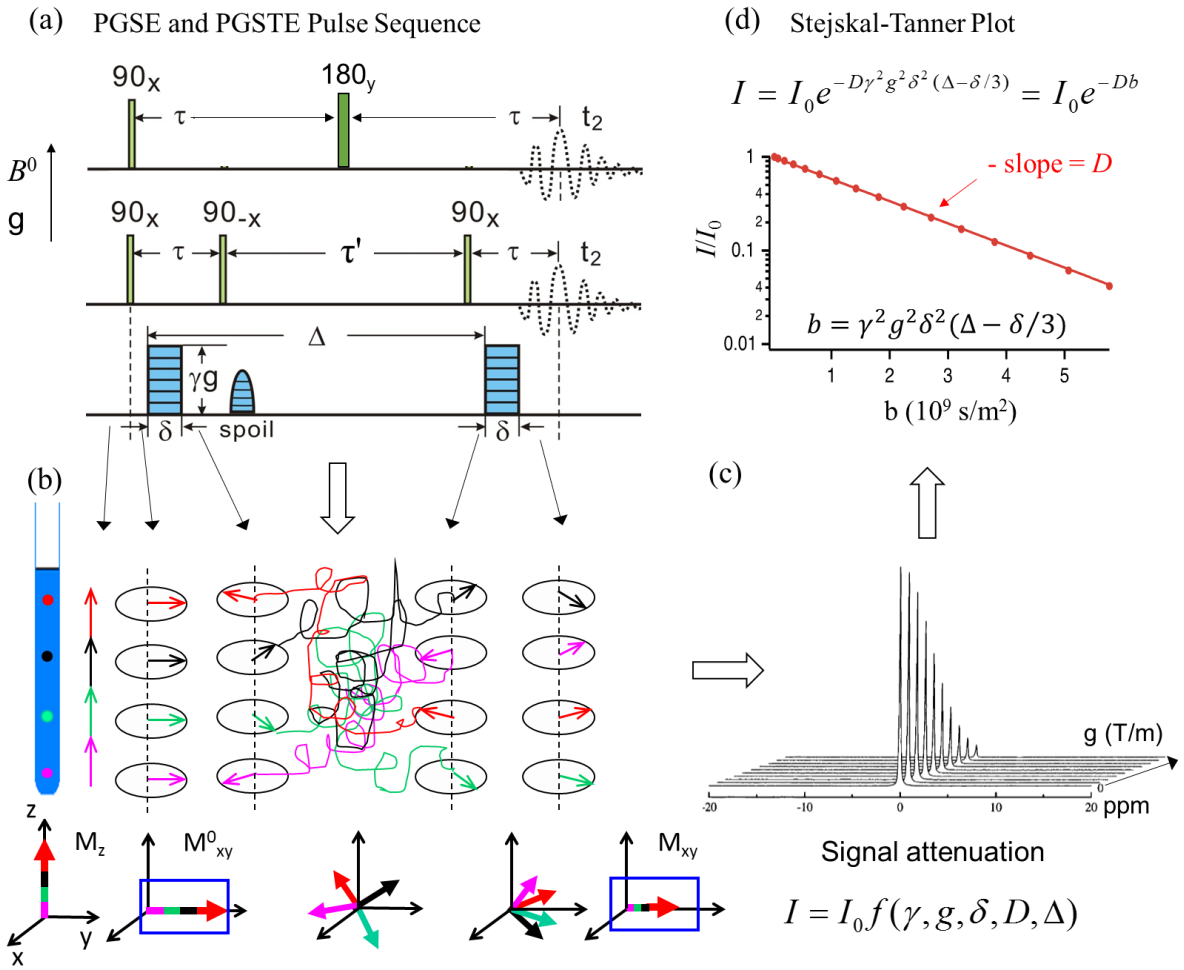

Figure 2.6 Gathering diffusion information from PFG experiments. (a) Pulse timing schemes of PGSE (upper), PGSTE (middle) RF pulse sequences and gradient pulses (lower). (b) Illustration of molecular diffusion during the PFG pulse sequence. Dots with different colors represent spin isochromats at different positions along the vertically placed NMR tube. The colored arrows represent net spin magnetization of each isochromat. The first magnetic field gradient encodes the spin positions and the second gradient decodes the positions. If molecular diffusion happens during mixing time Δ, phase coherence over the whole sample is partially lost due to the change in spin positions, leading to a diffusion-dependent signal attenuation. (c) Signal intensity decreases as the gradient strength increases due to diffusion.[28] Signal attenuation is a function of gyromagnetic ratio γ, gradient strength g, gradient duration δ, diffusion time Δ, and diffusion coefficient *D*. (d) Stejskal-Tanner equation for free diffusion and fitting experimental data to obtain *D* from signal attenuation.[26, 29]

Considering signal decay due to the spin relaxation during the pulse sequence, if the signal intensity right after the first 90 °RF pulse is defined as S_0, for PGSE pulse sequence, we have[30]

$$I_0 = S_0 \exp(-2\tau/T_2) \quad \text{with } 2\tau > \Delta\,. \tag{2.12}$$

In some cases, especially in soft materials, T_2 is very short, for example, $T_2(^1\text{H})$ of some ionic liquids soaked into ionic polymers is ~ 1 ms, while $T_1(^1\text{H})$ is ~ 1 s. In this case, diffusion time Δ can only be set to very short values and so PGSE is often impractical (insufficient I_0) considering the necessary gradient duration and post-gradient stabilization time. Fortunately, an alternative, pulsed-gradient stimulated echo (PGSTE) sequence (Figure 2.6a, middle), works better than PGSE for many soft materials, with a second 90 ° pulse storing the

magnetization along the *z* direction to allow increased gradient pulse delay Δ and relaxation under T_1 instead of T_2 before the third 90 °pulse:[30]

$$I_0 = S_0 \exp(-2\tau/T_2 - \tau'/T_1) \quad \text{with } \tau + \tau' > \Delta\,. \tag{2.13}$$

For soft materials with $T_1 \gg T_2$, PGSTE supports measurements with much longer diffusion times and produces much better signal intensity than PGSE.

In PFG experiments, what is directly measured is the displacement along the gradient axis that happens during the diffusion time Δ. More precisely in statistical language, PGSE and PGSTE measure the conditional probability of finding a spin at position $\mathbf{r}_1$ after time period *t* with an initial position $\mathbf{r}_0$, $P(\mathbf{r}_0, \mathbf{r}_1, t)$, which depends on the net dynamic displacement $\mathbf{R} = \mathbf{r}_1 - \mathbf{r}_0$. Here we will not discuss the details about how to obtain $P(\mathbf{r}_0, \mathbf{r}_1, t)$ and diffusion information, but simply show the results. For free and isotropic diffusion, the Stejskal-Tanner equation gives the signal intensity[26, 29]

$$I = I_0 \exp(-D\gamma^2 g^2 \delta^2 (\Delta - \delta/3)) = I_0 \exp(-Db) \tag{2.14}$$

with Stejskal-Tanner paramter $b = \gamma^2 g^2 \delta^2 (\Delta - \delta/3)$. Usually in PFG experiments, signal attenuation I/I_0 is measured as a function of the gradient strength g, and the self-diffusion coefficient *D* can be obtained directly from the slope of fitting $\ln(I_0/I)$ vs. b using the Stejskal-Tanner equation (Figure 2.6d).

2.4 Magnetic resonance imaging (MRI).

MRI is the youngest but the most popular and well-known technology in the NMR family. MRI has been developed extraordinarily quickly since its discovery,[31] due to its high power and demand in medicine. Chapter 4 of this thesis relies on time-resolved MRI to track drug delivery agents in simulated tissue. A remarkable difference of MRI from NMR techniques is its intricate and widespread use of magnetic field gradients. Figure 2.7a shows

the conventional spin-echo pulse sequence for MRI,[32-33] with three orthogonal linear gradients required for 3-D image reconstruction. The RF pulse sequence is a basic spin-echo sequence with a "soft" (frequency bandwidth-selective) 90 ° pulse to generate transverse magnetization and a 180 ° pulse to reverse all the phases of spin precession to form a signal echo. Slice selection is achieved by the combination of 1) a gradient which provides a linearly varying magnetic field with Larmor frequency $\omega_0(z) = \gamma B_0 + \gamma z g$ directly related to slice location, and 2) the soft RF pulse that only excites a specific frequency band corresponding to a specific spatial slice of a sample. Therefore only spins in a selected 2D region (slice) can be excited by the soft 90 ° RF pulse and be imaged. In the phase encoding direction, the pulsed gradient is applied with its magnitude incremented after each repetition of the experiment. Fourier transform of a complete set of phase encoded signals (repetitions) provides spatial information along this direction. In the frequency encoding direction, the gradient is applied during the readout of the echo, directly linking spatial location to frequency. Here we will not look into the details about how these gradients work to construct 3D images, but focus on the different signal contrast, or intensity variation, obtained in MRI images.

Contrast is probably the most fundamental characteristic of an image. In medical imaging such as X-ray radiography and ultrasound, contrast is created by the differential interactions between the radiation and the body tissues. X-ray imaging contrast is dependent on differences in electron density, and ultrasound imaging contrast on differences in acoustic impedance. On the contrary, MRI allows for "manipulation" or "editing" of contrast in images to optimize visualization of one tissue or another, using a huge variety of NMR techniques that selectively emphasize a certain contrast mechanism. In spin echo imaging, the most important

contrast mechanisms include spin relaxation (T_1 and T_2), spin density, diffusion, flow, etc. Here we will focus on spin relaxation weighted contrast.

There are two important time parameters TE and TR in the spin-echo pulse sequence. TE is the echo time between the 90 °pulse and the refocused echo, during which T_2 relaxation is active. TR is the repetition time, the total length of time between repetitive scans, including the acquisition time and delay time during when T_1 relaxation is active. Therefore signal intensity from a conventional spin-echo MRI can be expressed as:

$$S = S_0(1 - e^{-TR/T_1})e^{-TE/T_2} \tag{2.15}$$

Here S_0 is the signal intensity immediately after the first 90 °pulse, and can be linked directly to proton density. To obtain T_1-weighted images, TE is short (< 40 ms) to minimize the T_2 effect and TR is short (< 750 ms) to emphasize differences in T_1 (Figure 2.7d). Spins with shorter T_1 create brighter regions in the image. For T_2–weighted images, TR is long (> 2000 ms) to minimize the T_1 effect and TE is long to emphasize differences in T_2 (Figure 2.7e). Spins with longer T_2 create brighter regions in the image. For example, tissues with increased water amount have relatively long proton T_1 and T_2 and therefore show as dark regions in T_1-weighted images but bright in T_2-weighted images, while fat-based tissues have relatively short T_1 and T_2 and therefore show as bright regions in T_1-weighted images but dark in T_2-weighted images. Another commonly used method is to keep TE short and TR long to minimize the effect of both T_1 and T_2, therefore the contrast directly reflects proton density. Note that differences in T_1 may be completely eliminated if TR is long enough, but the T_2 effect can only be diminished to a certain level because TE has to be long enough to accommodate all the gradients. These aspects of weighting are used explicitly in Chapter 5 of this thesis.

Another spin relaxation weighting technique prepends a 180 ° pulse to the spin-echo pulse sequence (Figure 2.7f) with a delay time TD that can selectively destroy the signal from a tissue.[34] As shown in Figure 2.7c, the 180 ° pulse inverses spin magnetizations of all species from the z to $-z$ direction, which recover to equilibrium according to their respective T_1 relaxation, with zero signal obtained at time $TD = T_1 \cdot \ln 2$ for a given species. Signal intensity from this inversion-recovery spin-echo MRI is given by:

$$S = S_0\left(1 - e^{-TR/T_1}\right)e^{-TE/T_2}\left(1 - 2e^{-TD/T_1}\right) \tag{2.16}$$

This sequence is exploited for fat suppression clinically, and is used in the agent-tracking experiments of Chapter 5.

In medical imaging, contrast agents are usually used to enhance the visibility of certain body tissues or structures temporarily, such as barium-sulfate compounds used in X-ray radiography. MRI contrast agents can shorten T_1 or T_2 of surrounding water to provide better contrast in T_1- or T_2-weighted images and these are called T_1 or T_2 relaxation agents, respectively. A simple relationship between the relaxation times and the concentration of contrast agents reads:

$$\frac{1}{T_1} = \frac{1}{T_{1,\,0}} + r_1 c \tag{2.17a}$$

$$\frac{1}{T_2} = \frac{1}{T_{2,\,0}} + r_2 c \tag{2.17b}$$

Here $T_{1,0}$ and $T_{2,0}$ are the natural relaxation times of water or other solvents without contrast agent, r_1 or r_2 are molecular relaxivity. Higher r_1 or r_2 indicates less contrast agent is required to obtain the same contrast enhancement. In Chapter 5, we will use the experimental setup shown in Figure 2.7b to study the diffusion process of contrast agents into biogels by the

different relaxation weighting techniques mentioned above, some examples of their images shown in Figure 2.7d, e and f.

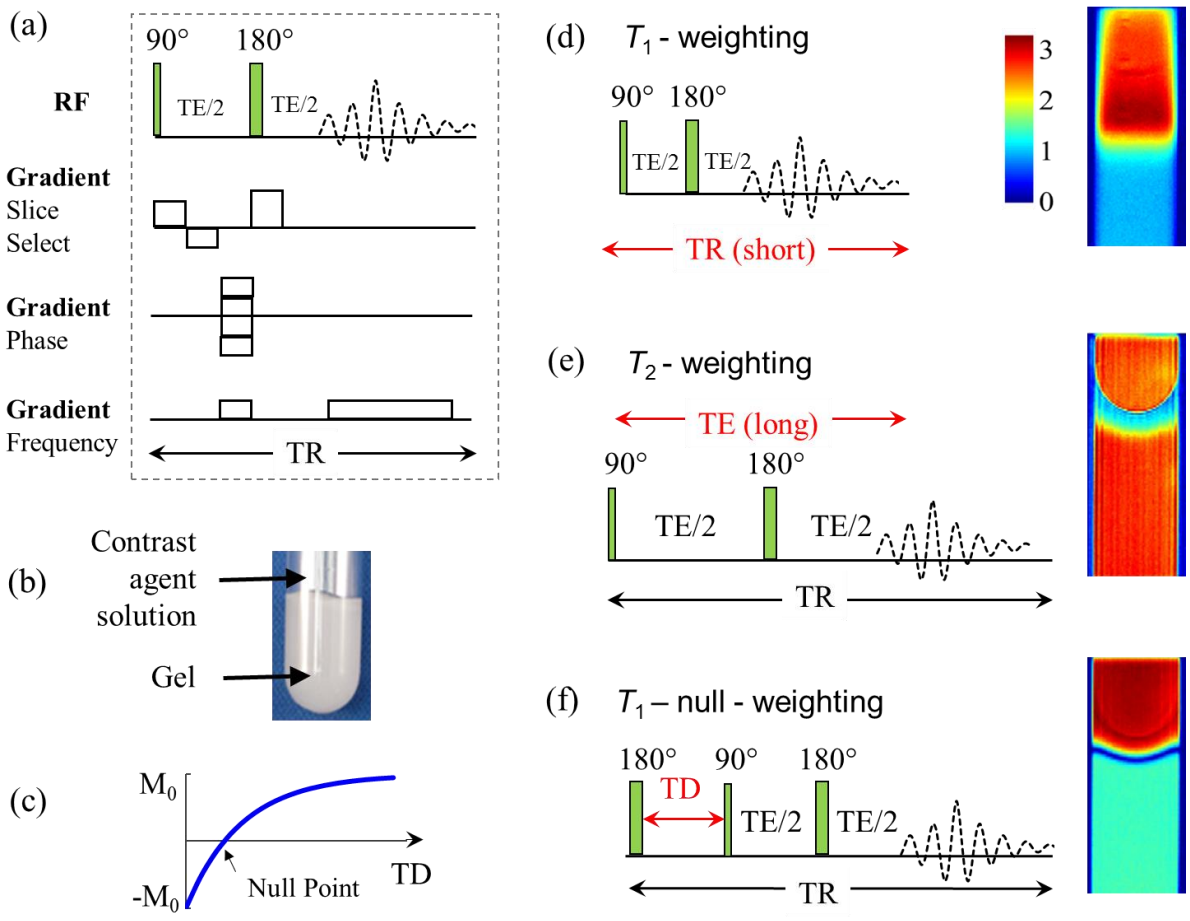

Figure 2.7 (a) Spin echo imaging sequence with two important time parameters TE (echo time) and TR (repetition time).[31] (b) Experimental setup with an imaging contrast agent solution diffusing into a gel, an example used to demonstrate the difference in three imaging techniques, with their RF pulse sequences and images displayed in (d) T_1-weighting, (e) T_2-weighting and (f) T_1-null-weighting. (c) Determination of TD (delay time) used for pulse sequence in (f).

In summary, this Chapter quickly reviews basic NMR external (user applied) and internal (molecular) interactions, and introduces three distinct NMR methodologies: high-

resolution SSNMR, PFG diffusometry, and MRI. SSNMR will be employed in Chapter 3 for structure and dynamics studies of polymer membranes. PFG diffusometry will be the major method for transport studies of supramolecular assemblies (Chapter 4) and the ionic polymer Nafion (Chapter 6). Time-resolved MRI will be the main tool to investigate nanoparticles diffusing into biogels in Chapter 5. These various NMR techniques provide comprehensive ways to investigate and correlate the structure, dynamics and transport properties of soft materials.

Reference

(1) Purcell, E. M.; Torrey, H. C.; Pound, R. V. Resonance Absorption by Nuclear Magnetic Moments in a Solid. *Physical Review* **1946,** *69*, 37-38.
(2) Bloch, F.; Hansen, W. W.; Packard, M. Nuclear Induction. *Physical Review* **1946,** *69*, 127-127.
(3) Schmidt-Rohr, K. S., Hans Wolfgang, *Multidimensional Solid-State NMR and Polymers* Academic Press: London, 1994.
(4) Cheng, H. N. A., Tetsuo; English, Alan D., *NMR Spectroscopy of Polymers: Innovative Strategies for Complex Macromolecules*. American Chemical Society: Washington, DC, 2011.
(5) Brown, S. P.; Spiess, H. W. Advanced Solid-State NMR Methods for the Elucidation of Structure and Dynamics of Molecular, Macromolecular, and Supramolecular Systems. *Chemical Reviews* **2001,** *101*, 4125-4156.
(6) Pons, M.; North Atlantic Treaty Organization. Scientific Affairs, D., *NMR in Supramolecular Chemistry*. Kluwer Academic Publishers: Dordrecht; Boston, 1999; Vol. 526; no. 526.
(7) Abragam, A., *Principle of Nuclear Magnetism*. Oxford University Press: Oxford 1985.
(8) Weber, U.; Thiele, H., *NMR-Spectroscopy: Modern Spectral Analysis*. Wiley: 2008.
(9) Levitt, M. H., *Spin Dynamics : Basics of Nuclear Magnetic Resonance* John Wiley & Sons Ltd: England, 2008.
(10) Duer, M. J., *Introduction to Solid-State NMR Spectroscopy*. Blackwell Publishing: Malden, 2004.
(11) Keeler, J., *Understanding NMR Spectroscopy*. John Wiley & Sons: West Sussex, 2005.

(12) Mehring, M., *Principles of High Resolution NMR in Solids*. Springer Berlin Heidelberg: New York, 1983.
(13) Haeberlen, U., *High Resolution NMR in Solids Selective Averaging*. Academic Press: New York, 1976.
(14) Lowe, I. J. Free Induction Decays of Rotating Solids. *Physical Review Letters* **1959,** *2*, 285-287.
(15) Maricq, M. M.; Waugh, J. S. NMR in Rotating Solids. *The Journal of Chemical Physics* **1979,** *70*, 3300-3316.
(16) Pines, A.; Gibby, M. G.; Waugh, J. S. Proton‐Enhanced NMR of Dilute Spins in Solids. *The Journal of Chemical Physics* **1973,** *59*, 569-590.
(17) Andrew, E. R.; Bradbury, A.; Eades, R. G. Nuclear Magnetic Resonance Spectra from a Crystal Rotated at High Speed. *Nature* **1958,** *182*, 1659-1659.
(18) Man, P. P. Second-Order Quadrupole Effects on Hahn Echoes in Fast-Rotating Solids at the Magic Angle. *Physical Review B* **1997,** *55*, 8406-8424.
(19) Cavanagh, J. P., A. G.; Fairbrother, W. ; Skelton, N. , *Protein NMR Spectroscopy: Principles and Practice*. Academic Press: San Diego, 1996.
(20) Derome, A. E., *Modern NMR Techniques for Chemistry Research*. Pergamon: Oxford, 1987.
(21) Claridge, T. D. W., *High-Resolution NMR Techniques in Organic Chemistry*. Elsevier: Amsterdam; London, 2009; Vol. 27.; 27.
(22) Hartmann, S. R.; Hahn, E. L. Nuclear Double Resonance in the Rotating Frame. *Physical Review* **1962,** *128*, 2042-2053.
(23) Laws, D. D.; Bitter, H.-M. L.; Jerschow, A. Solid-State NMR Spectroscopic Methods in Chemistry. *Angewandte Chemie International Edition* **2002,** *41*, 3096-3129.
(24) Stejskal, E. O.; Schaefer, J.; Waugh, J. S. Magic-Angle Spinning and Polarization Transfer in Proton-Enhanced NMR. *Journal of Magnetic Resonance (1969)* **1977,** *28*, 105-112.
(25) Schaefer, J.; Stejskal, E. O. Carbon-13 Nuclear Magnetic Resonance of Polymers Spinning at the Magic Angle. *Journal of the American Chemical Society* **1976,** *98*, 1031-1032.
(26) Stejskal, E. O.; Tanner, J. E. Spin Diffusion Measurements: Spin Echoes in the Presence of a Time-Dependent Field Gradient. *Journal of Chemical Physics* **1965,** *42*, 288-292.
(27) Callaghan, P. T., *Translational Dynamics & Magnetic Resonance: Principles of Pulsed Gradient Spin Echo NMR*. Oxford University Press: Great Clarendon Street, Oxford, 2011.
(28) Price, W. S. Pulsed-Field Gradient Nuclear Magnetic Resonance as a Tool for Studying Translational Diffusion: Part 1. Basic Theory. *Concepts in Magnetic Resonance* **1997,** *9*, 299-336.
(29) Tanner, J. E. Use of the Stimulated Echo in NMR Diffusion Studies. *Journal of Chemical Physics* **1970,** *52*, 2523-2526.
(30) Kimmich, R., *NMR: Tomography, Diffusometry, Relaxometry*. Springer: New York; Berlin, 1997.

(31) Lauterbur, P. C. Image Formation by Induced Local Interactions: Examples Employing Nuclear Magnetic Resonance. *Nature* **1973,** *242*, 190-191.
(32) Kumar, A.; Welti, D.; Ernst, R. R. NMR Fourier Zeugmatography. *Journal of Magnetic Resonance (1969)* **1975,** *18*, 69-83.
(33) Edelstein, W. A.; Hutchison, J. M. S.; Johnson, G.; Redpath, T. Spin Warp NMR Imaging and Applications to Human Whole-Body Imaging. *Physics in Medicine and Biology* **1980,** *25*, 751.
(34) Callaghan, P. T., *Principles of Nuclear Magnetic Resonance Microscopy*. Oxford Science: Oxford, England, 1991.

Chapter 3

Solid-state NMR Studies of Polymeric Membranes

Section 3.2, 3.3 and 3.4 are adapted from the NMR sections of the following references: M. Allen, S. Wang, S. Hemp, Y. Chen, L. A. Madsen, K. I. Winey, and T. E. Long. *Macromolecules* **2013**, *46*, 3037 ©2013, American Chemical Society; B. Zhang, J. Spano, Y. Chen, R. Turner, and S. Wi. *J. Phys. Chem. B* **2012**, *116*, 7970 ©2012, American Chemical Society; and C. H. Lee, K.S. Lee, K. S. Lee, O. Lane, J. E. McGrath, Y. Chen, S. Wi, S. Y. Lee, and Y. M. Lee. *RSC Adv.* **2012**, *2*, 1025 ©2012, Royal Society of Chemistry, respectively. Section 3.4 also includes further studies based on the published work.

3.1 Introduction

Polymers have played an essential role in our modern life. In order to better design and develop novel polymeric systems with desired properties, we have to understand their structure and dynamics at molecular level. Due to highly disordered and dynamic nature of polymeric materials, a choice of appropriate characterization methods is crucial. Solid-state NMR (SSNMR) has been proven a powerful technique to investigate multiscale structure and dynamics of polymers.[1-3] In this chapter, we demonstrate SSNMR applications in polymer characterization on three novel polymer systems synthesized by other research groups.[4-6] The SSNMR techniques applied here include: ^{13}C CPMAS with varying CP contact time, ^{13}C single-pulse MAS with varying delay time, ^{23}Na single-pulse MAS, two dimensional phase adjusted spinning sideband (2D PASS), proton spin−lattice (T_1), rotating frame spin−lattice relaxation time ($T_{1\rho}$), and the center-band-only detection of exchange (CODEX).

As the basic SSNMR technique, CPMAS can provide valuable information about polymer structures in some cases, especially with varying times between pulses and compared

with single-pulse MAS experiments.[7-8] As a quadrupolar nucleus with spin I = 3/2, ^{23}Na is a powerful probe of the local environment around the nucleus in various materials,[9-13] as the quadrupolar interaction is very sensitive to atomic bonds of the nucleus, the structure and composition of nearby molecules, and the symmetry of the surrounding charges.[14] ^{13}C CSA information obtained from 2D PASS experiment aids understanding not only the local electronic structures but the local mobility of molecular segments.[15-16] T_1 is affected by motions on the order of MHz regime,[17-20] whereas $T_{1\rho}$ is sensitive to the dynamic processes on the order of kHz regime.[17, 19, 21-22] CODEX is powerful to investigate slow segmental reorientations of the polymer backbone ranging from a few seconds to a few milliseconds with a high sensitivity and resolution.[23-24] The key information available from CODEX experiments are the amplitude and correlation time of segmental motions as well as, in some favorable cases, the geometry and number of exchanging sites involved in the motion. Therefore together these measurements help to understand polymer structures as well as the motions of polymer chains over a wide range of time scales from a few nanoseconds to seconds.

3.2 Structure and dynamics of hydroxyalkyl-containing imidazolium homopolymers[6]

3.2.1 Motivation and materials studied

Motivation. Polymerization of ionic liquid monomers enables the design of conductive membranes suitable for electroactive devices,[25-26] gas separation,[27-28] and microwave-absorbing materials.[29] In polymerized ionic liquids (PILs), the cation or anion remains covalently bound to the macromolecule, thus restricting its mobility. The mobility restriction advantageously prevents leakage of liquid electrolytes in electrochemical devices; however, the reduction in ionic conductivity proves problematic. Anion selection remains a highly researched component of cationic PILs to improve macromolecular ionic conductivity.[30-37]

Materials studied. Dr. Michael H. Allen from Prof. Timothy E. Long's group synthesized for the first time vinylimidazolium (VIM) ionic liquid monomers functionalized with various hydroxyalkyl groups and investigate the impact of functional substituents on PVIM thermal properties, morphology, and ionic conductivity. Here SSNMR complemented the X-ray results by providing quantitative ratios of nanophase-separated versus disordered components as well as providing local molecular dynamics information. The chemical structures of the polymerized 1-ethyl-3-vinylimidazolium bis(trifluoromethane)sulfonamide (EVIM-Tf_2N), 1-hydroxyethyl-3-vinylimidazolium Tf_2N (HEVIM-Tf_2N), 1-hexyl-3-vinylimidazolium Tf_2N (HVIM-Tf_2N), and 1-hydroxyhexyl-3-vinylimidazolium Tf_2N (HHVIM-Tf_2N) are shown at the top of Figure 3.1.

3.2.2 NMR experimental section

NMR experiments were performed on a Bruker Avance II-300 wide bore spectrometer operating at 300.13 MHz for ^{1}H and 75.47 MHz for ^{13}C. Polymer samples were tightly packed into 4 mm ZrO_2 rotors which were used for ^{1}H-^{13}C cross-polarization magic-angle spinning(CP-MAS) probe. The MAS spinning speed was set at 6.25 kHz, CP contact time 1 ms, recycle delay 5s and signal averaging 2048 scans for most experiments. A pulse sequence known as TOSS (total suspension of spinning sidebands) at an rf field strength of 85 kHz was combined with all CP-MAS experiments to obtain sideband-free ^{13}C spectra. Small phase incremental alternation with 64 steps (SPINAL-64) decoupling sequence at 62.5 kHz was used during ^{13}C detection for proton decoupling.

^{13}C single pulse excitation (SPE) experiment with a recycle time of 1s and two more CP-MAS experiments with varying contact times (50 us and 4 ms) were performed to assistin ^{13}C resonancesassignment. Proton spin-lattice relaxation times in the rotating frame $T_{1\rho}(^{1}H)$

were measured by a standard proton spin-lock sequence followed by CP, TOSS and ^{13}C detection with SPINAL-64 decoupling, with varying proton spin-lock time from 0.001 to 9 ms in 16 steps for poly(EVIM-Tf_2N) and poly(HEVIM-Tf_2N), and from 0.001 to 18 ms in 16 steps for poly(HVIM-Tf_2N) and poly(HHVIM-Tf_2N).

3.2.3 NMR results and discussion

Locally ordered vs. disordered morphology. Here we use SSNMR to unravel the molecular associations and morphological phase separations present in these novel polymer systems. SSNMR investigated the molecular associations and the local morphology present in these novel polymer systems. Figure 3.1a shows standard ^{13}C CP-MAS spectra of poly(EVIM-Tf_2N), poly(HEVIM-Tf_2N), poly(HVIM-Tf_2N) and poly(HHVIM-Tf_2N). The resonances from the backbone carbons consisted of the methylene (C2) centered at 40.7 ppm as well as the methine (C1) at 56.2 and 53.6 ppm. Upon changing alkyl chain length or hydroxyl group incorporation to the terminus of the substituent chain, significant changes were not observed in the chemical shifts of methylene carbons. However, the resonance line became relatively sharper for poly(HEVIM-Tf_2N) and poly(HHVIM-Tf_2N) compared to poly(EVIM-Tf_2N) and poly(HVIM-Tf_2N). This indicated a faster motion for the main-chain carbon with a more polar side chain.

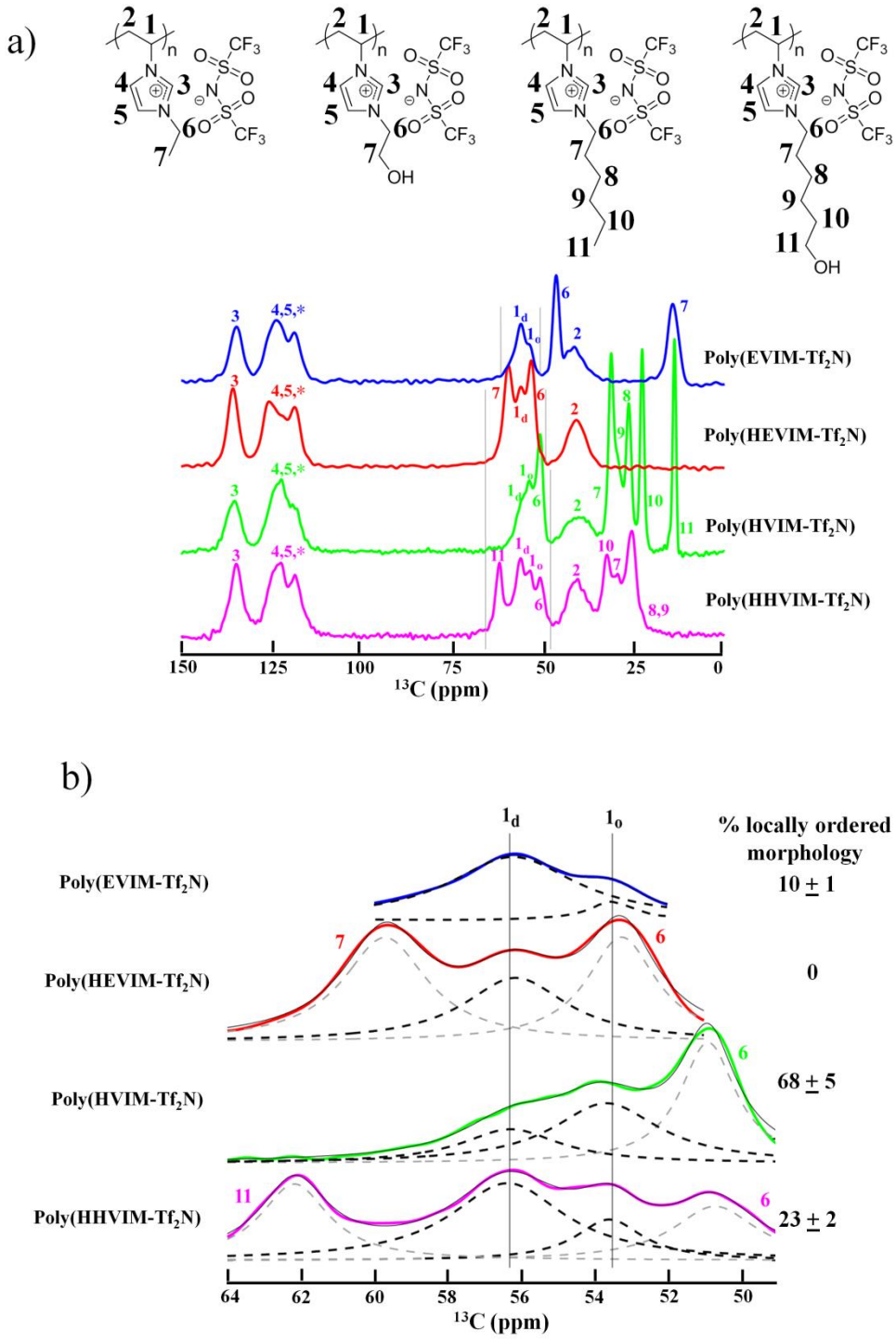

Figure 3.1 (a) ^{13}C CP-MAS spectra of poly(EVIM-Tf_2N), poly(HEVIM-Tf_2N), poly(HVIM-Tf_2N) and poly(HHVIM-Tf_2N). Assignments of peaks and their linewidths provide information about local polymer molecular associations and dynamics. (b) Deconvolution of

resonances between 64 - 49 ppm where 1_d and 1_o represent the backbone methine carbons in homogenously disordered and locally ordered morphologies, respectively. Thus, SSNMR enables the determination of the percent locally ordered morphology in each sample through spectral deconvolution (shown at right of each spectrum).

Unlike methylene carbons, methine carbon resonances exhibit remarkable differences (Figure 3.1b). For all samples the methine carbons correspond to the resonances at 56.2 ppm and 53.6 ppm, except for poly(HEVIM-Tf_2N) where the 53.6 ppm peak remains absent. These two resonances for the methine carbons provide strong evidence of two distinct chemical environments. In a nanophase-separated morphology, the Tf_2N^- anions reside away from nonpolar side chain aggregates and closely bind to imidazolium cations. Consequently, the backbone methine carbons experience a more negative chemical environment compared to a phase-mixed morphology where anions are more homogeneously distributed in the polymer matrix. Therefore, the upfield resonance at 53.6 ppm was assigned to the nanophase-separated, locally ordered region, and the downfield 56.2ppm to a more disordered region. Assuming similar cross-polarization efficiencies in the two morphologies, the amount of phase separation was quantified through deconvolution of the peaks between 64-49 ppm (Figure 3.1b). The locally ordered fraction increased from 10% to 68% with increasing alkyl chain length from n = 2 to n = 6; addition of the hydroxyl group to the side chain terminus decreased the locally ordered fraction from 10% to 0% for n = 2 and from 68% to 23% for n = 6. This ordering trend strongly agrees with and amplifies results from WAXS where the q_b peak becomes less intense and broader with hydroxyl group incorporation.

^{13}C spectra assignments. The backbone carbons are assigned by comparing standard cross-polarization magic angle spinning (CP-MAS) (Figure 3.1) and single pulse excitation

(SPE)-MAS spectra (Figure 3.2). SPE-MAS with a short recycle time 1s reveal resonances with short T_1, which are mobile carbons of the polymer samples. The rotation of backbone carbons are more hindered compared to side chain carbons, therefore the contribution of backbone carbons are significantly reduced in SPE spectra. One major difference between Figure 3.1a and Figure 3.2 is the resonances missing from Figure 3.2 between 64-49 ppm and 45-33 ppm; therefore, these missing peaks are assigned to backbone methine and methylene carbons, respectively. The other difference between 100-140 ppm is caused by two factors: 1) the rotation of imidazolium carbons are restricted so the resonances at 136 ppm (C3) and between 120-130 ppm (C4 and C5) decrease in intensity and 2) the two sharp peaks at 118 ppm and 122 ppm are probably caused by mobile Tf_2N^-anions.

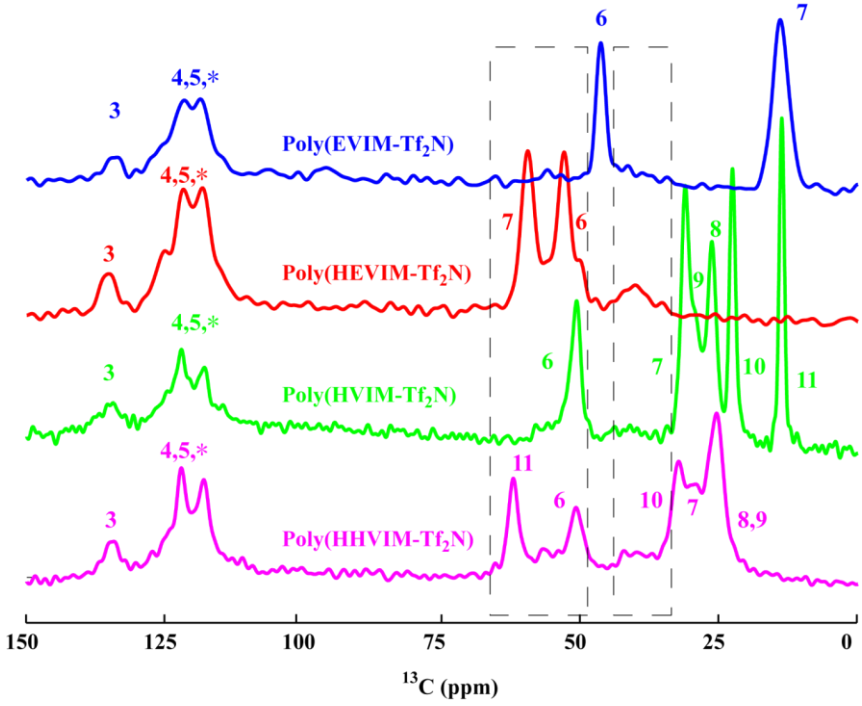

Figure 3.2 ^{13}C SPE-MAS spectra of poly(EVIM-Tf_2N), poly(HEVIM-Tf_2N), poly(HVIM-Tf_2N) and poly(HHVIM-Tf_2N). The resonances missing within the two dash boxes compared to the standard CP-MAS spectra are assigned to backbone methine and methylene carbons,

respectively. The rotation of backbone carbons are more hindered compared to side chain carbons and the resultant longer T_1 values prevent these carbons showing in the SPE spectra with only a short recycle time of 1s.

In order to distinguish the anion carbons in CP-MAS spectra, different cross polarization contact time (50 us, 4 ms) were used. Figure 3.3 shows the resonance between 100-150 ppm with 50 μs and 4 ms contact time. The carbons located in the Tf_2N^- anion lack protons, the intermolecular ^1H-^{13}C cross polarization from polymer matrix protons to anions carbons depends strongly on close proximity and rigidity. Theoretically, no intermolecular CP would occur at short contact time such as 50 μs. By increasing contact time to 4 ms, anion carbons can form dipolar interactions with more remote protons and produce stronger signals (the two sharp peaks at 118 ppm and 122 ppm) as a result while other carbons decrease in intensity due to both $T_{1\rho}(^1H)$ and $T_{1\rho}(^{13}C)$ decay during the long contact time. Therefore in the standard CP-MAS (1 ms contact time), the resonances between 110-130 ppm have contributions from both imidazolium and anion carbons. Further studies on these intermolecular cross polarization signals may offer valuable information about how anions locate and move in the polymer matrix and how the interaction between anions and polymer matrix affects the ionic transport properties.

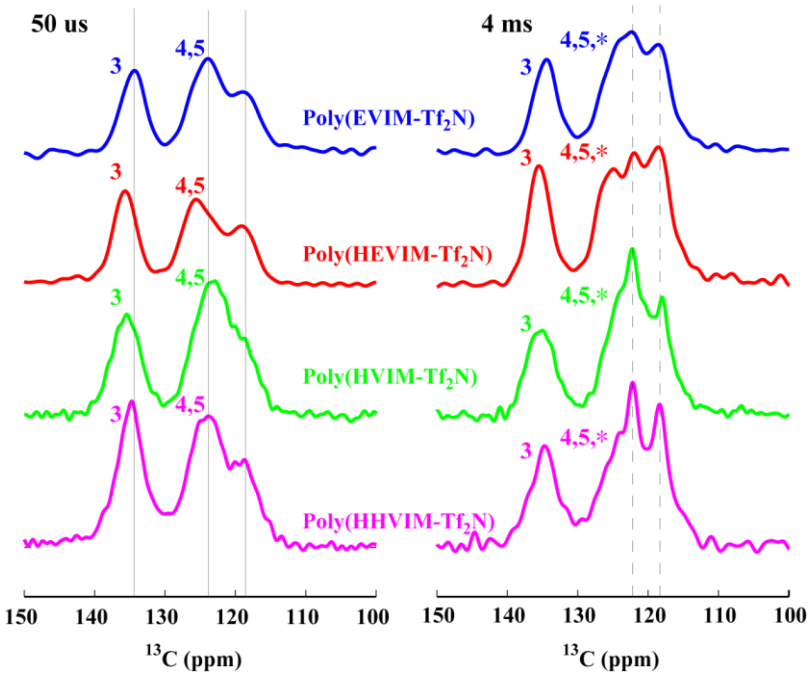

Figure 3.3 ^{13}C CP-MAS spectra of poly(EVIM-Tf_2N), poly(HEVIM-Tf_2N), poly(HVIM-Tf_2N) and poly(HHVIM-Tf_2N) with different CP contact time: 50 μs (left), and 4 ms (right). The two sharp peaks appearing at 4 ms are assigned to the anion carbons because at longer (4 ms) CP contact time the quaternary anion carbons produce stronger signals as a result of dipolar interactions with more remote (intermolecular) protons. All other carbons decrease in intensity due to both $T_{1\rho}(^1H)$ and $T_{1\rho}(^{13}C)$ decay during the long (4 ms) contact time.

By close examination of the spectra with only imidazole carbons signals (Figure 3.3) where anion carbons signals are eliminated by short contact time, we can see C3 is less downfield shift than C4 and C5 by adding a hydroxyl group to the side chain for n = 2, while for n = 6, C4 and C5 are slightly downfield shifted, but C3 is slightly upfield shifted. These shifts suggest some amount of intra- or inter-molecular hydrogen bonding between C3 and hydroxyl group or anions. The assignment for the peak at 118 ppm is still unknown, but it might be caused by the arrangement of imidazolium rings in a disordered morphology.

Proton spin-lattice relaxation time in the rotating frame $T_{1\rho}$ (^{1}H) analysis. Normally for a single-component homogenous polymer or a multi-component polymer with intimate mixing (nanoscale), one $T_{1\rho}(^1H)$ value would be found for all protons due to rapid spin diffusion throughout a given sample. Figure 3.4 shows the $T_{1\rho}(^1H)$ decay of carbon resonances between 60-52 ppm for poly(EVIM-Tf_2N), poly(HEVIM-Tf_2N), poly(HVIM-Tf_2N) and poly(HHVIM-Tf_2N). The experimental data were least-squares fitted to a linear equation $\ln(M(\tau)/M(0)) = -\tau/T_{1\rho}(^1H)$ to extract $T_{1\rho}(^1H)$. For poly(EVIM-Tf_2N) and poly(HEVIM-Tf_2N) with n=2, $T_{1\rho}(^1H)$ detected by backbone and side-chain carbons differ by less than 5%. However for poly(HVIM-Tf_2N) and poly(HHVIM-Tf_2N) with n = 6, $T_{1\rho}(^1H)$ detected from side-chain alkyl carbons are slightly smaller than $T_{1\rho}(^1H)$ from main-chain and imidazole carbons. All $T_{1\rho}(^1H)$ values are presented in Table 3.1, the alkyl chain $T_{1\rho}(^1H)$ being indicated in the brackets.

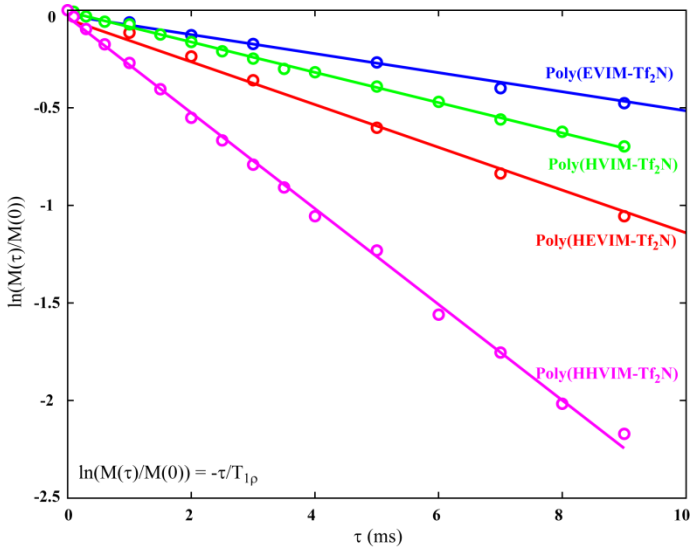

Figure 3.4 $T_{1\rho}(^1H)$ relaxation measurements. Normalized carbon magnetization $\ln(M(\tau)/M(0))$ is plotted versus spin-lock time τ for the four samples, focusing on the methine carbon resonances between 60-52 ppm. The slope of a least-square fit provides the $T_{1\rho}(^1H)$ value. All

$T_{1\rho}(^1H)$ decays are single component and are the same for backbone and imidazole carbon resonances within one polymer system, indicating similar motional timescale for these molecular subunits.

Table 3.1 $T_{1\rho}(^1H)$ relaxation analysis

Sample	$T_{1\rho}$ at 62.5 kHz (ms)	$T_{1\rho}$ at 100 kHz (ms)	$\langle\delta_{HH}\rangle$ (Hz)	$\langle r_{HH}\rangle$ (Å)	τ_C (μs)
p(EVIM-Tf_2N)	19.7	26.1	100	11	4.1
p(HEVIM-Tf_2N)	8.42	11.7	150	9.1	4.6
p(HVIM-Tf_2N)	13.2 (12.6)	18.2 (17.1)	121 (126)	10 (9.9)	4.5 (4.4)
p(HHVIM-Tf_2N)	4.26 (3.11)	6.19 (4.82)	210 (230)	8.4 (8.0)	5.1 (5.6)

$T_{1\rho}(^1H)$ relaxation mechanism is usually dominated by ^1H-^1H homonuclear dipolar coupling for polymers under T_g, because the contribution of ^1H-^{13}C dipolar interaction is relatively small and negligible due to low natural abundance of ^{13}C (1.08%). For the spin-lattice relaxation in the on-resonance rotating frame, the relaxation rates can be described by

$$\frac{1}{T_{1\rho}} = \frac{1}{2}\langle\delta_{HH}\rangle^2\left\{\frac{2\tau_c}{1+4\omega_0^2\tau_c^2}+\frac{5\tau_c}{1+\omega_0^2\tau_c^2}+\frac{3\tau_c}{1+4\omega_1^2\tau_c^2}\right\} \quad (3.1)$$

Here $\langle\delta_{HH}\rangle$, τ_c, ω_0, and ω_1 represent the effective ^1H-^1H homonuclear dipolar coupling strength at the measurement site, the segmental motion correlation time, Larmor frequency of proton (300.13 MHz), and the field strength of spin-lock pulse, respectively. By measuring $T_{1\rho}(^1H)$ at two different ω_1 (62.5 kHz and 100 kHz), both $\langle\delta_{HH}\rangle$ and τ_c can be solved from this equation by Newton-Raphson algorism. The average inter-proton distance can be obtained by

$\langle r_{HH} \rangle = (122\ \text{kHz}/\langle \delta_{HH} \rangle)^{1/3}$(Å) because the dipolar coupling strength is 122 kHz for ^{1}H-^{1}H with a distance of 1 Å.

3.3 Local structure and segmental motions of poly(arylene ether sulfone) copolymer[5]

3.3.1 Motivation and materials studied

Motivation. One polymer system of industrial importance that has been highly researched is thermoplastic polyarylethers.[38-39] In particular, poly(arylene ether sulfone)s (PAES) are known to have excellent thermal and mechanical properties.[40] However, PAES copolymers possess limited applications due to their poor solvent resistance and unacceptable thermal dimensional changes near the glass transition temperature (Tg). One way that these disadvantages can be addressed is by incorporating aliphatic segmental blocks, such as 1,4-cyclohexylene ring units, into the polymer backbone.[41] It is well-known that incorporation of cyclohexylene rings into a sequence can enhance the mechanical properties and crystallization rate of the polymer system.5 Cyclohexylene ring containing polyesters, such as poly(1,4-cyclohexylenedimethylene 1,4-cyclohexanedicarboxylate) (PCCD), poly(butylene 1,4-cyclohexanedicarboxylate) (PBCHD), and poly(1,4-cyclohexane dimethylene terephthalate) (PCT), have been widely reported in the literature; however, to the best of our knowledge, little efforts have been done with cyclohexylene ring containing PAESs.

Materials studied. Dr. Bin Zhang from Prof. Richard Turner's group synthesized a series of modified poly(arylene ether sulfone)s (PAES) copolymer sequences with short ester links for improving their thermal and mechanical properties, chemical structures shown in Figure 3.5.

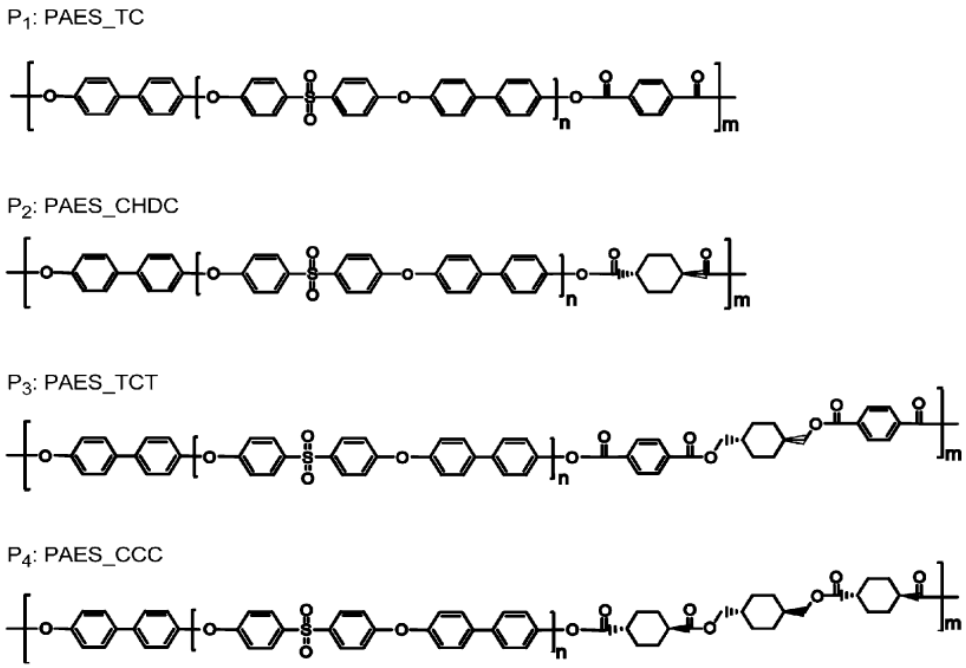

Figure 3.5 Structures of cyclohexylene ring containing PAES samples investigated (Pl, P2, P3, and P4). The *n* and *m* values of each copolymer are 3 or 4.

3.3.2 NMR experimental section

Polymer samples in powdered form were packed into 4 mm rotors for magic-anglespinning (MAS) ^{13}C SSNMR measurements using a Bruker Avance II-300 wide bore NMR spectrometer (7.05 T) operating at ^{13}C and ^{1}H Larmor frequencies of 75.47 and 300.13 MHz, respectively. The chemical shift anisotropy (CSA) of carbon sites was measured site-specifically by analyzing the spinning sideband patterns, which are separated by order, of a 2D PASS experiment employing a slow magic-angle spinning (MAS) condition (1.5 kHz). Successive rows of a 2D PASS spectrum were sheared along the indirect frequency domain so as to align all sidebands positioning at the same frequency position. A slice obtained at a specific frequency position provides the CSA sideband pattern of a ^{13}C site under investigation.

Numerical simulations were carried out by employing a home-built program written by the Matlab programming language to extract CSA tensor parameters from the experimental spectra.

All of these experiments utilize a ^{13}C-detection mode based on the Hartman-Hahn 1H–^{13}C cross-polarization (CP) scheme for obtaining enhanced signal intensity.[7, 42] The Hartman-Hahn 1H–^{13}C CP scheme utilizes a relatively short relaxation delay (2−5 s) that is governed by the shorter 1H T_1 relaxation time rather than by the longer ^{13}C T_1 relaxation time. A pulse sequence known as the total suppression of spinning sidebands (TOSS)[43] that consists of a train of four π-pulses with appropriate delay times was combined with each of our NMR pulse sequences to obtain sideband free ^{13}C MAS spectra. The signal averaging was achieved by adding 2048 scans with a 5 s acquisition delay time. 1Hand ^{13}C π/2 pulse lengths were 4 and 5 μs, respectively. Small phase incremental alternation with 64 steps (SPINAL-64)[44] decoupling sequence at 75 kHz power was used for proton decoupling during the direct ^{13}C signal detection in each experiment.

3.3.3 NMR results and discussion

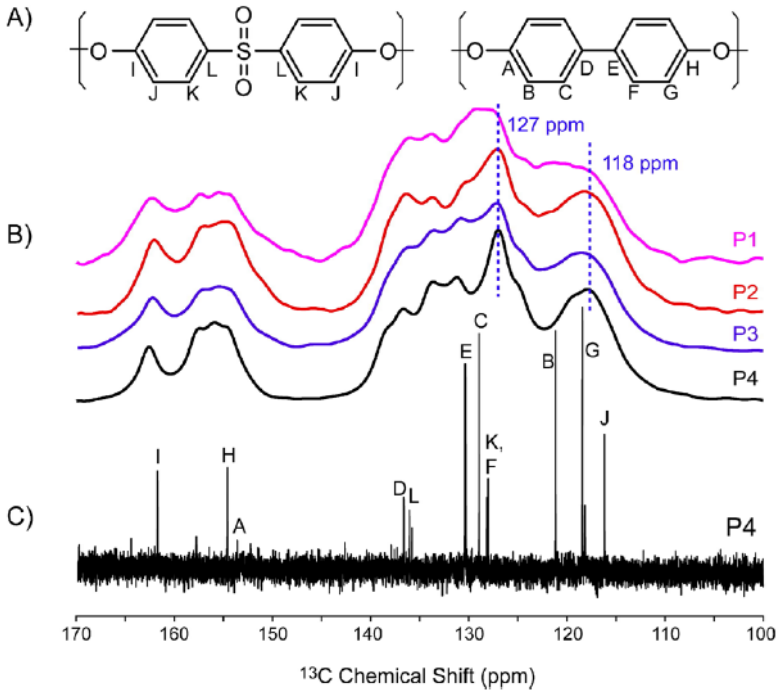

Figure 3.6 Details of NMR peak assignments. The aromatic segments from the polymers focused on in our SSNMR experiments are exhibited, with different ^{13}C sites labeled by letters (A). Example ^{13}C MAS spectra for each of the polymer samples (B) are shown atop a solution ^{13}C spectrum of P4 (C). The letter-labeled peaks in the solution spectrum (C) correspond to the ^{13}C sites of the aromatic rings (A). Dashed vertical lines in B represent frequency positions employed for CSA and CODEX experiments and show how the broad peaks in the MAS spectra at 127 and 118 ppm match up to the peaks in the solution spectrum. Additionally, a quaternary peak located at position H (136 ppm) is considered for CODEX experiments.

The ^{13}C spectra of the PAES copolymers investigated in this study are shown in Figure 3.6. In the experiments mentioned herein, methine groups in the aromatic phenylene rings indicated at B, C, F, G, J, and K sites (Figure 3.6A) were utilized for various types of SSNMR experiments for monitoring molecular motions. Shown below the ^{13}C MAS spectra of P1−P4

(Figure 3.6B) is a solution ^{13}C NMR spectrum of P4 (Figure 3.6C) for guiding peak assignments. The solution-state ^{13}C NMR spectrum had been assigned for sites A−L and served to aid in assigning peaks in the SSNMR spectra. The ^{13}C SSNMR peaks centered at 127 and 118 ppm were chosen for analysis since these peaks correspond to the aromatic methine ^{13}C sites in phenylene rings: C, F, and K (127 ppm) and B, G, and J (118 ppm). Sites B, G, and J correspond to ^{13}C sites that are adjacent to the ^{13}C that is directly bonded to oxygen. Sites C and F are three bonds away from the ether oxygen, and site K is adjacent to the ^{13}C that is directly bonded to the sulfone group.

Signal overlaps due to the convolution of several peaks in the frequency regions of 127 and 118 ppm may prevent site-resolved SSNMR data interpretation. In many cases, however, this potential limitation can be lifted or, at least, alleviated in a multidimensional correlation spectroscopy or in a technique that does not necessitate a fully resolved 1D spectrum. For instance, a fully resolved, site-specific NMR spectrum is not a prerequisite for measuring ^{1}H T_1 relaxation time in solid state. Protons in a bulk hydrocarbon sample system in solid-state form an equilibrium state via forming a strong ^{1}H–^{1}H dipolar coupling network. Therefore, protons involved in a common spin network share a uniform T_1 value, not necessitating the spectra of fully resolved peaks for ^{1}H T_1 measurements. In ^{13}C SSNMR spectroscopy, meaningful structural and/or motional dynamics information can also be obtained even from overlapped ^{13}C sites if spectra of samples possessing a similar type of structures are compared.

Chemical shift anisotropies (CSAs) of ^{13}C sites in the PAES blocks were analyzed to investigate the influence of the segmented aliphatic blocks on the local electronic structures and motions. Shown in Figure 3.7A is, for example, the 2D PASS spectrum of P2. The central band and multiple spinning sidebands of each ^{13}C site in a 2D PASS spectrum are separated by

the order along the indirect frequency domain in such a way that the frequency position of a spinning sideband is shifted by $v_r \times$ SD/SW from a band that is located a step below it, where SD, v_r, and SW are the spectral data point, the spinning speed (1.5 kHz), and the spectral width of the spectrum, respectively. All of the central and sidebands from a ^{13}C site must be aligned at the same frequency position in the direct acquisition domain to extract a 1D projection for obtaining MAS sideband spectrum. For this purpose, a shearing transformation was applied to the 2D PASS spectrum shown in Figure 3.7A by shifting each row by $-k$ ($v_r \times$ SD/SW), where k (= 1, 2, ...) is the order of spinning sideband.

Table 3.2 CSA Parameters of ^{13}C Sites Measured on 136 and 127 ppm

	P_1		P_2		P_3		P_4	
peak position	δ^a	η^b	δ	η	δ	η	δ	η
136 ppm	88[c]	0.7[d]	88	0.6	90	0.6	92	0.5
127 ppm	92	0.5	94	0.6	88	0.6	94	0.6

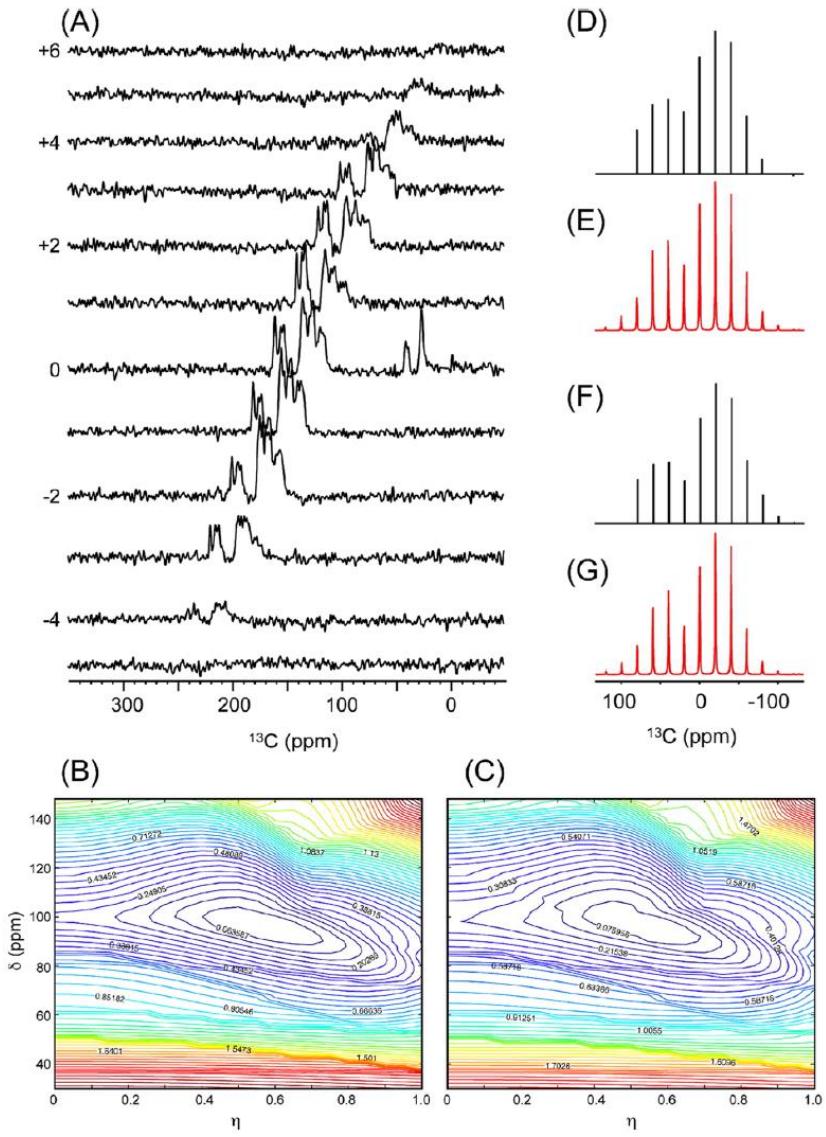

Figure 3.7 Two-dimensional ^{13}C PASS spectrum of P2 (A). The ω1 slices are sorted according to the order of the sidebands. The MAS spinning speed used was 1500 Hz. rms statistic as a function of the CSA parameters δ and η of P2 (B) and P4 (C) that are measured on the ^{13}C peak at 127 ppm. Experimental (D and F) and simulated (E and G) CSA spinning sideband bars obtained for P2 (D and E) and P4 (F and G) are shown.

An experimental 1D MAS sideband pattern extracted from the sheared 2D PASS spectrum was normalized in such a way that the intensity of the biggest line was set to be 1

and the intensities of other lines were adjusted according to the relative intensity ratios with respect to the biggest line. Numerical simulations were carried out to find the best-fit spectrum and tensor parameters for each data set by employing a home-built program written in Matlab programming language. The root-mean-square variance, $(\Sigma(E_i - S_i)^2)^{1/2}$, where E_i and S_i are the line intensity of experimental and simulated 1D MAS spectra of order i, was calculated for each data point on a two-dimensional grid map formed by varying trial tensor parameters, δ and η. Figure 3.7, panels B (P2) and C (P4), are the contour maps, thus obtained, that show the calculated variances, considering the MAS sideband spectrum taken at 127 ppm of each 2D PASS spectrum. Regions of the minimum variance are visible in both contour maps. The position of the minimum variance corresponds to the optimal δ and η parameters that provide the best-fit simulation. Panels D and F in Figure 3.7 are the experimental 1D MAS sideband spectra of P2 and P4, respectively, that are taken at 127 ppm. Panels E and G in Figure 3.7 are the corresponding best-fit simulations of P2 and P4, employing CSA tensor parameters found from panels B and C in Figure 3.7 (δ = 94 $\pm$5 ppm; η = 0.6 $\pm$0.1). Table 3.2 summarizes CSA values of P1−P4 samples thus obtained from ^{13}C sites at 136 and 127 ppm. As can be seen in the table, the range of CSA tensor parameters obtained at the common block are all very similar, regardless of the type of segmented copolymer structures. This invariance implies that the changes in the intermolecular packing order, ultimately the crystallinity of the polymeric matrix, due to the introduction of aliphatic segments span over long distances involving a few adjacent segmented domains. The aromatic PAES segments may form local structural domains that are isolated from the aliphatic segments on the nanoscopic scale.

Slow Segmental Reorientation Dynamics. Figure 3.8 shows ^{13}C CODEX NMR data measured on P1 (B−C) and P4 (C−F) detected at 154, 127, and 34 ppm and the corresponding

best-fit simulations to extract the correlation times of the slow reorientational dynamics of polymers. We have chosen only two extreme examples P1 and P4 to extract the influence of the aliphatic segmental blocks on the chain dynamics of aromatic PAES block. Demonstrated in Figure 3.9A are the pure exchange CODEX spectra ($\Delta S = S_0 - S$) of P4 sample recorded at several exchange mixing times, tm's, under a fixed CSA recoupling time, t_{CSA} = 0.32 ms (N = 4; $t_{CSA} = 2\tau_r$). Peaks shown in the pure exchange CODEX spectra are those ^{13}C sites that undergo conformational reorientations during the CODEX mixing time. Shown on the bottom of Figure 3.9A for comparison is the CPMAS spectrum that shows all the carbon sites regardless of the relative mobility of conformational reorientations. Plotted in Figure 3.9B−F are pure CODEX exchange signal intensities, $\Delta S = (S_0 - S)$, of P1 and P4 samples recorded at 154, 127, and 34 ppm that are normalized by S0, where S0 is the signal intensity recorded by switching t_m and t_z in the CODEX pulse sequence to compensate signal loss due to the T_1 and T_2 relaxations. As the mixing time tm increases, the spectral intensity of $\Delta S/S_0$ increases as expected.

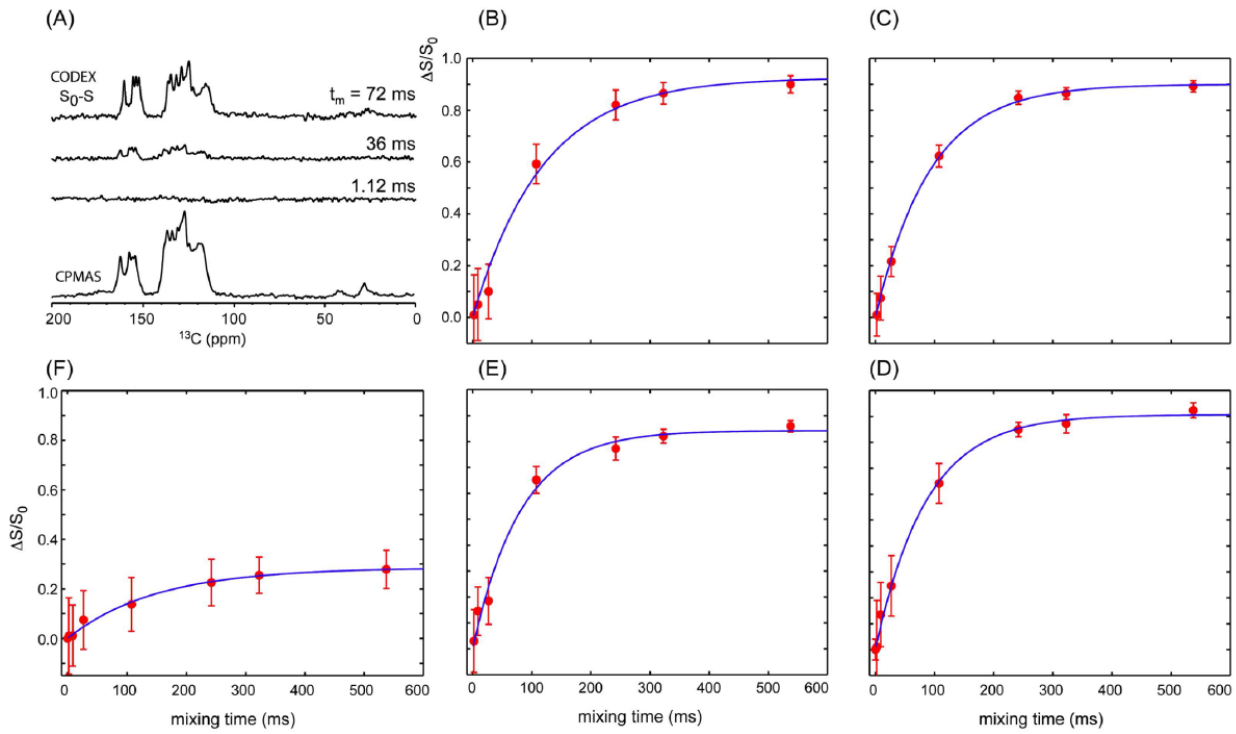

Figure 3.8 CODEX NMR data of P1 and P4. Pure exchange CODEX spectra of P4 (A) recorded by varying tm with t_{CSA} = 0.32 ms and t_z = 1.12 ms. The normalized tm-dependent CODEX dephasing intensities (B−C: P1 and D−F: P4) measured on the ^{13}C peaks at 154 (B and D), 127 (C and E), and 34 ppm (F). Error bars are obtained by calculating the signal-to-noise ratio (SINO) of both signal (S) and reference (S_0) spectra according to $\delta(S/S_0) = (S/S_0)[(1/SINO)_{S0} + (1/SINO)_S]$. Aromatic methine groups with (P4) and without (P1) aliphatic, segmented copolymer blocks demonstrate different motional correlation times in CODEX experiments. A long aliphatic, segmented copolymer block included in the common aromatic block has resulted in slower motional reorientations for both quaternary and methine carbon sites in the common aromatic segments.

Filled, red circles with error bars in each graph in Figure 3.8B−F were used to designate the experimental $\Delta S/S_0$ intensities recorded at 154 [B (P1) and D (P4); aromatic quaternary carbons], 127 [C (P1) and E (P4); aromatic methine sites], and 34 ppm [F (P4); aliphatic carbon

sites], respectively. Our experimental CODEX data were fitted to a stretched exponential function, $A[1 - \exp(-(t_m/\tau_0)^{\beta})]$[45], where A ($0 < A < 1$) is a value to which the $\Delta S/S_0$ signal intensity approaches asymptotically at a long mixing time and β and τ_0 are the stretched exponential coefficient and the center of the correlation time, respectively. The β coefficient is related to the width of the correlation time distribution.[46] Then, the mean correlation time, $<\tau_c>$, for the segmental reorientational motion, for instance, of phenylene ring-flips is related to $<\tau_0>$ and β values by $<\tau_c> = (\tau_0/\beta)\Gamma(1/\beta)$, where Γ is the gamma function. The mean correlation times and the stretched exponential coefficients thus obtained from the curve fitting are summarized in Table 3.3.

Table 3.3 Mean correlation times and stretched exponential coefficients obtained from the t_m-dependent CODEX data.

	P_1		P_4		
	154 ppm	127 ppm	154 ppm	127 ppm	34 ppm
A	0.877	0.891	0.925	0.844	0.37
τ_0 (ms)	102 ± 3	90. ± 3	91 ± 3	81 ± 3	385 ± 20
β	1.40 ± 0.05	1.07 ± 0.05	0.904 ± 0.02	0.990 ± 0.02	0.72 ± 0.10
$\langle\tau_c\rangle$ (ms)	93 ± 3	88 ± 3	95 ± 3	82 ± 3	475 ± 20

As can be seen in Table 3.3, the best-fit CODEX simulation data obtained employing the stretched exponential function model have provided a correlation time within the range of 82 (±3) to ~88 (±3) ms for the aromatic methine sites and virtually invariant values (93 [±3] to ~95 [±3] ms) for the aromatic quaternary carbon sites. Although the $<\tau_c>$ values for the aromatic methine sites with and without aliphatic segmentation are not significantly different, the difference is at least beyond the error bound detected (±3 ms), indicating that the aliphatic segmentation in the *m*-blocks speeds up the rotational reorientations of aromatic pheneylene rings present in the *n*-blocks. Thus, an inclusion of the aliphatic blocks in the copolymer sequence had resulted in an increase in the rate of the segmental reorientation motion of

aromatic methine site, while maintaining a virtually invariant rate for quaternary sites. This implies that an inclusion of the aliphatic, segmented block in the polymer sequence may have resulted in an overall increase of the free volume in the polymer matrix, making the ring-flip motions of aromatic rings more favorable. The correlation time of the aliphatic chain motions observed at 34 ppm of P4 was much more slower (475 ± 20 ms) than those of aromatic sites. The reorientational motion of aliphatic segments would be less favorable than the aromatic phenylene rings, which can undergo much easier ring-flip motions around the positions where they are located, because aliphatic segments would encounter more restrictions from the nearby chains against their reorientational rotations or translations. The slow reorientational dynamics of polymer chains would possess multiple motional modes with a distribution in the magnitude of correlation times because the inhomogeneous nature of the solid matrices include both crystalline and amorphous regions.

Another experimentally observed feature is that the line width of peaks in the CODEX spectra is narrower than those peaks in the CPMAS NMR spectrum (Figure 3.8A). This feature would be attributed to the difference in the relaxation times (both T_1 and T_2) of the amorphous and crystalline regions. The ^{13}C sites in the amorphous regions would possess shorter relaxation times. Therefore, ^{13}C signals in CODEX spectra are mainly from the crystalline regions in the polymer matrix because peaks from the amorphous regions might have underwent more signal decays during the periods of relatively long CODEX mixing times. As can be seen in Figure 3.8A, the pure exchange CODEX spectra are indeed sharper than the CPMAS spectrum, indicating that the motional characteristics revealed in the CODEX spectra are mainly from the crystalline domains in the polymer matrix.

3.4 Thermal annealing of disulfonated poly(arylene ether sulfone) random copolymers[4]

3.4.1 Motivation and materials studied

Motivation. Polymer electrolyte membrane fuel cells (PEMFCs) are ecofriendly alternative power sources with high energy efficiency, fuel flexibility (e.g., hydrogen, and methanol) and zero pollutant emission.[47-48] Appropriately controlling membrane preparation conditions may enhance the physicochemical properties (e.g., proton conductivity) of polymer electrolyte membranes, particularly those made up of sulfonated hydrocarbon materials. Most of sulfonated hydrocarbon materials used for PEMs are amorphous glassy polymers in the non-equilibrium state. Thus, the thermal history during membrane preparation may influence the packing density of their polymer chains and may change the hydrophilic and hydrophobic domain characteristics, such as size and phase separated morphologies.[49] Thermal annealing is a simple route for stabilizing glassy polymers via the densification of their polymer chains and is accomplished through thermal treatment of the glassy thermoplastics.[50-54] The objective here is to investigate the changes of fundamental film characteristics, including morphological transformation, after a thermal treatment of sulfonated copolymers, particularly with directly copolymerized poly(arylene ether sulfone) random copolymers.

Materials studied. Dr. Chang Hyun Lee from James E. McGrath's group synthesized copolymerized disulfonated poly(arylene ethersulfone) copolymers containing 2,2'-isopropylidene diphenol units (BisA-XX, XX mean mole percent of hydrophilic moieties), chemical structure shown in Figure 3.9. Then, the cast polymer solution was dried under two different thermal protocols; one set was dried at 60 ℃ in an oven without vacuum for 2 days (BisAXX_60 ℃), while the other set was thermally treated under vacuum at 150 ℃ for an extra 2 days after initially being dried at 60 ℃ for 2 days (BisA-XX_150 ℃).

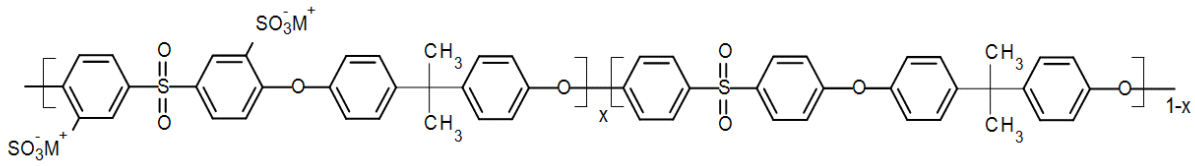

Figure 3.9 Chemical structures of directly copolymerized poly(arylene ether sulfone) random (BisAH-XX) copolymers in metal form (–SO_3Na). Here x means the molar ratio of hydrophilic moieties.

3.4.2 NMR experimental section

Cross-polarization magic-angle spinning (CPMAS) ^{13}C NMR spectra were performed with a Bruker Avance II 300 MHz wide-bore spectrometer operating at Larmor frequencies of 75.47 MHz for ^{13}C and 300.13 MHz for 1H nuclei. Samples (50–60 mg) in thin film forms were cut into small pieces for packing into 4 mm MAS rotors for MAS experiments. Spin-lock pulses of 1 ms duration were applied along both 1H and ^{13}C channels for CP, employing a 50 kHz rf-field at the ^{13}C channel and a ramped rf pulse at the ^{1}H channel whose rf-field strength changes linearly over a 25% range centered at 38 kHz. A pulse technique known as total suppression of spinning side bands (TOSS) was combined with a CP sequence to obtain sideband-free ^{13}C MAS spectra at 6 kHz MAS spinning speed. NMR signal averaging was achieved by co-adding 2048 transients witha 4 s acquisition delay time. ^{1}H and ^{13}C p/2 pulse lengths were 4 ms and 5 ms, respectively. The small phase incremental alternation with 64 steps (SPINAL-64)40 decoupling sequence at 63 kHz power was used for proton decoupling during ^{13}C signal detection.

The centerband-only detection of exchange (CODEX) experiment was used to probe the slow segmental reorientation of the copolymer backbone with time scales in the ranges of 1− 3000 Hz in solids. The CODEX experiment has a special advantage in the signal sensitivity

and resolution because it utilizes only the centerband of a MAS spectrum. The CODEX experiment monitors signals that diphase due to the segmental reorientations of polymer chains that would induce changes in the orientation-dependent chemical shift frequencies. The MAS spinning speed employed in our CODEX experiments was 6.25 kHz.

3.4.3 NMR results and discussion

Figure 3.10 shows (a) motional dynamics and (b) molecular ordering information of sodium ions of BisA-XX, depending on DS and thermal annealing history, studied by solid-state NMR. ^{1}H T_1 data (detected via directly attached ^{13}C signal by employing a short cross-polarization (~ 150 μs)) in Figure 3.10 (a) provides information on the segmental vibrations of protons in BisA-XX aromatic phenylene rings whose frequency range is near the proton's Larmor frequency ($\omega_0 = 3 \times 10^8$ Hz under 7.05 T). Here, the data were obtained in the fully hydrated state at an ambient temperature. ^{1}H T_1 was shortened as the DS value of BisA-XX copolymers increased, because highly absorbed water molecules in high DS BisA-XX systems act as plasticizers softening the polymer chains. The T_1 was much reduced after the thermal treatment at 150 ℃. The T1 difference between BisAXX_60 ℃ and BisA-XX_150 ℃ becomes larger at a high DS. This behavior can be explained by a basic ^{1}H T_1 relaxation mechanism governed by ^{1}H–^{1}H homonuclear dipolar interactions:

$$\frac{1}{T_1} = \langle \mu_{HH} \rangle^2 \left(\frac{\tau_c}{1 + (\omega_0 \tau_c)^2} \right) + \frac{4\tau_c}{1 + (2\,\omega_0 \tau_c)^2} \qquad (3.2)$$

where, $\langle \mu_{HH} \rangle$ and τ_c means the effective ^{1}H–^{1}H dipolar coupling strength and the motional correlation time, respectively. τ_c is not largely different in the polymer systems with the same chemical compositions. T_1 is inversely proportional to $\langle \mu_{HH} \rangle^2$. It indicates that the shortened T_1 after the heat treatment can be attributed to improved effective ^{1}H–^{1}H dipolar interactions

as a result of the formation of compact BisA-XX microstructures. The thermal annealing effects were more observable in BisAXX_150 ℃ samples with a higher DS.

^{23}Na solid-state NMR spectroscopy (Figure 3.10b) was employed to investigate the thermally induced molecular order/disorder in the hydrophilic domains in BisA-XX. For this, all BisA-XX samples were successively treated in boiling 0.5 M H_2SO_4 for 2 h, boiling deionized water for 2 h, 0.5 M NaCl for 3 days, and deionized water for 1 week to convert counter ions to —SO_3^- from K^+ to Na^+ thoroughly. Here, Na^+ ions were used as probes to observe the molecular ordering environment in hydrophilic domains, as Na^+ ions make a complex (–SO_3Na) with –SO_3^-groups in BisA-XX and their quadrupolar interaction (spin 3/2) would be sensitive over the structural and dynamic environments. The characteristic ^{23}Na peak was sharpened as the DS increased, indicating that the packing order or distribution of sodium ions became more uniform. Furthermore, the ^{23}Na peaks of non-annealed BisA-XX_60 ℃ shifted slightly with increasing DS, but their shifted peaks, particularly in BisA-40, returned to positions similar to others, after the thermal treatment. This behavior may be related to the changes of sulfonic acid density in the BisAH-XX matrix after the thermal annealing, which is discussed in volume-based ion exchange capacity.

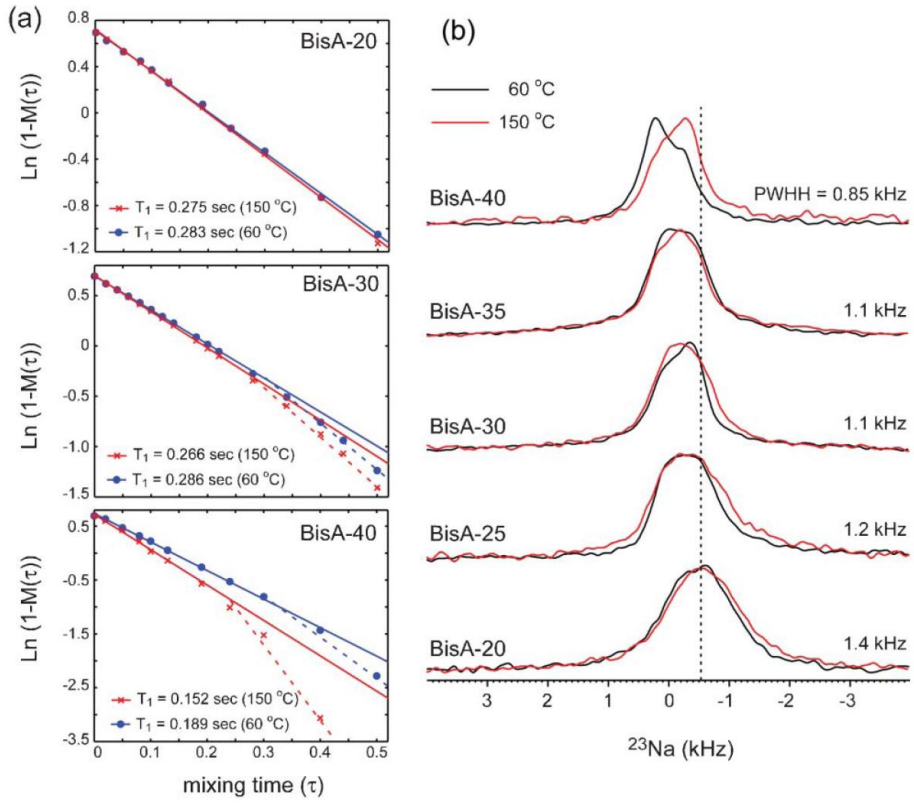

Figure 3.10 (a) $^{1}H–T_1$ plot and (b) ^{23}Na NMR spectra of BisA-XX_60 ℃ and BisA-XX_150 ℃.

3.5 Conclusion

In this chapter, We employed solid-state NMR (SSNMR) spectroscopy to study structure and motional dynamics of three different copolymers. Our results include: 1) The quantified ratios of locally ordered versus disordered components shows that the increased polarity of the hydroxyl substituent diminishes the local compositional heterogeneity of polar and nonpolar phases present in the AVIM homopolymers. 2) The invariance of CSA tensor parameters obtained at the common PAES block regardless of the type of segmented copolymer structures implies that the changes in the crystallinity of the polymeric matrix do not change the local structural and motional environments of aromatic PAES blocks that are

isolated from the aliphatic segments on the nanoscopic scale. Being measured on methine sites in aromatic pheneylene rings, the slow reorientational motions of polymer chains that occur within a few milliseconds regime become slightly faster as the aliphatic segment blocks are introduced in the copolymer sequence. The increased conformational flexibility of the segmented blocks enables rotational reorientations of polymer chains more favorable and faster. 3) Segmental vibrations of protons in BisA-XX aromatic phenyl rings (or ^{1}H-^{1}H dipolar interaction) are enhanced and, thus, their T_1 relaxation values became shorter. The characteristic peak of ^{23}Na solid-state NMR, where Na^+ ions were used as probes to monitor the molecular ordering environment of BisA-XX hydrophilic domains, was also sharpened after the thermal annealing. This implies that the packing order or distribution of sodium ions (in other words, sulfonic acid groups) in BisA-XX became more uniform after annealing. This behavior was more clearly observed in BisA-XX that had a high disulfonation content. In summary, various types of SSNMR spectroscopic methods can provide a wealth of structural and dynamic information complementary to other characterization tools, leading to a better understanding and controlling these copolymer materials.

References

(1) Schmidt-Rohr, K. S., Hans Wolfgang, *Multidimensional Solid-State Nmr and Polymers* Academic Press: London, 1994.
(2) Laws, D. D.; Bitter, H.-M. L.; Jerschow, A. Solid-State Nmr Spectroscopic Methods in Chemistry. *Angewandte Chemie International Edition* **2002,** *41*, 3096-3129.
(3) Cheng, H. N. A., Tetsuo; English, Alan D., *Nmr Spectroscopy of Polymers: Innovative Strategies for Complex Macromolecules*. American Chemical Society: Washington, DC, 2011.
(4) Lee, C. H.; Lee, K.-S.; Lane, O.; McGrath, J. E.; Chen, Y.; Wi, S.; Lee, S. Y.; Lee, Y. M. Solvent-Assisted Thermal Annealing of Disulfonated Poly(Arylene Ether Sulfone) Random Copolymers for Low Humidity Polymer Electrolyte Membrane Fuel Cells. *RSC Advances* **2012,** *2*, 1025-1032.

(5) Zhang, B.; Spano, J.; Chen, Y.; Turner, R.; Wi, S. Crystallinity and Motional Dynamics Study of a Series of Poly(Arylene Ether Sulfone) Segmented Copolymer Analogues. *The Journal of Physical Chemistry B* **2012,** *116*, 7970-7980.
(6) Allen, M. H.; Wang, S.; Hemp, S. T.; Chen, Y.; Madsen, L. A.; Winey, K. I.; Long, T. E. Hydroxyalkyl-Containing Imidazolium Homopolymers: Correlation of Structure with Conductivity. *Macromolecules* **2013,** *46*, 3037-3045.
(7) Stejskal, E. O.; Schaefer, J.; Waugh, J. S. Magic-Angle Spinning and Polarization Transfer in Proton-Enhanced Nmr. *Journal of Magnetic Resonance (1969)* **1977,** *28*, 105-112.
(8) Schaefer, J.; Stejskal, E. O. Carbon-13 Nuclear Magnetic Resonance of Polymers Spinning at the Magic Angle. *Journal of the American Chemical Society* **1976,** *98*, 1031-1032.
(9) Orler, E. B.; Gummaraju, R. V.; Calhoun, B. H.; Moore, R. B. Effect of Preferential Plasticization on the Crystallization of Lightly Sulfonated Syndiotactic Polystyrene Ionomers. *Macromolecules* **1999,** *32*, 1180-1188.
(10) Kotecha, M.; Chaudhuri, S.; Grey, C. P.; Frydman, L. Dynamic Effects in Mas and Mqmas Nmr Spectra of Half-Integer Quadrupolar Nuclei: Calculations and an Application to the Double Perovskite Cryolite. *J. Am. Chem. Soc.* **2005,** *127*, 16701-16712.
(11) Jia, Y.; Kleinhammes, A.; Wu, Y. Nmr Study of Structure and Dynamics of Ionic Multiplets in Ethylene−Methacrylic Acid Ionomers. *Macromolecules* **2005,** *38*, 2781-2785.
(12) Yamamoto, Y.; Murakami, M.; Ikeda, R.; Deguchi, K.; Tansho, M.; Shimizu, T. The Local Structure around Sodium Ions in Poly(Ethylene-Ran-Methacrylic Acid) Ionomers Studied by 23na Solid-State Nmr under a High Magnetic Field, 21.9 T. *Chem. Lett.* **2006,** *35*, 1058-1059.
(13) Lim, J. S.; Lee, Y.; Im, S. S. Influence of Ionic Association on the Nonisothermal Crystallization Kinetics of Sodium Sulfonate Poly(Butylene Succinate) Ionomers. *J. Polym. Sci., Part B: Polym. Phys.* **2008,** *46*, 925-937.
(14) Jerschow, A. From Nuclear Structure to the Quadrupolar Nmr Interaction and High-Resolution Spectroscopy. *Prog. Nucl. Magn. Reson. Spectrosc.* **2005,** *46*, 63-78.
(15) Antzutkin, O. N.; Shekar, S. C.; Levitt, M. H. Two-Dimensional Sideband Separation in Magic-Angle-Spinning Nmr. *Journal of Magnetic Resonance, Series A* **1995,** *115*, 7-19.
(16) Antzutkin, O. N.; Lee, Y. K.; Levitt, M. H. 13c And15n—Chemical Shift Anisotropy of Ampicillin and Penicillin-V Studied by 2d-Pass and Cp/Mas Nmr. *Journal of Magnetic Resonance* **1998,** *135*, 144-155.
(17) Masson, J. F.; Manley, R. S. J. Solid-State Nmr of Some Cellulose/Synthetic Polymer Blends. *Macromolecules* **1992,** *25*, 589-592.
(18) Zhang, X.; Takegoshi, K.; Hikichi, K. Composition Dependence of the Miscibility and Phase Structure of Amorphous/Crystalline Polymer Blends as Studied by High-Resolution Solid-State Carbon-13 Nmr Spectroscopy. *Macromolecules* **1992,** *25*, 2336-2340.
(19) Kishore, A. I.; Herberstein, M. E.; Craig, C. L.; Separovic, F. Solid-State Nmr Relaxation Studies of Australian Spider Silks. *Biopolymers* **2002,** *61*, 287-297.

(20) Wang, J.; Cheung, M. K.; Mi, Y. Miscibility and Morphology in Crystalline/Amorphous Blends of Poly(Caprolactone)/Poly(4-Vinylphenol) as Studied by Dsc, Ftir, and 13c Solid State Nmr. *Polymer* **2002,** *43*, 1357-1364.
(21) Simmons, A.; Natansohn, A. Solid-State Nmr Study of Charge-Transfer Interactions in Polymer Blends. *Macromolecules* **1991,** *24*, 3651-3661.
(22) Huijgen, T. P.; Gaur, H. A.; Weeding, T. L.; Jenneskens, L. W.; Schuurs, H. E. C.; Huysmans, W. G. B.; Veeman, W. S. Carbon-13 Solid-State Nmr Study of the Interfacial Region in Glass-Filled Polyamide 6 Composites. *Macromolecules* **1990,** *23*, 3063-3068.
(23) deAzevedo, E. R.; Hu, W. G.; Bonagamba, T. J.; Schmidt-Rohr, K. Centerband-Only Detection of Exchange: Efficient Analysis of Dynamics in Solids by Nmr. *Journal of the American Chemical Society* **1999,** *121*, 8411-8412.
(24) deAzevedo, E. R.; Hu, W.-G.; Bonagamba, T. J.; Schmidt-Rohr, K. Principles of Centerband-Only Detection of Exchange in Solid-State Nuclear Magnetic Resonance, and Extension to Four-Time Centerband-Only Detection of Exchange. *The Journal of Chemical Physics* **2000,** *112*, 8988-9001.
(25) Matsumoto, K.; Endo, T. Synthesis of Ion Conductive Networked Polymers Based on an Ionic Liquid Epoxide Having a Quaternary Ammonium Salt Structure. *Macromolecules* **2009,** *42*, 4580-4584.
(26) Chen, H.; Elabd, Y. A. Polymerized Ionic Liquids: Solution Properties and Electrospinning. *Macromolecules* **2009,** *42*, 3368-3373.
(27) Bara, J. E.; Carlisle, T. K.; Gabriel, C. J.; Camper, D.; Finotello, A.; Gin, D. L.; Noble, R. D. Guide to Co2 Separations in Imidazolium-Based Room-Temperature Ionic Liquids. *Ind. Eng. Chem. Res.* **2009,** *48*, 2739-2751.
(28) Tang, J.; Tang, H.; Sun, W.; Radosz, M.; Shen, Y. Poly(Ionic Liquid)S as New Materials for Co2 Absorption. *J. Polym. Sci., Part A: Polym. Chem.* **2005,** *43*, 5477-5489.
(29) Tang, J.; Radosz, M.; Shen, Y. Poly(Ionic Liquid)S as Optically Transparent Microwave-Absorbing Materials. *Macromolecules* **2007,** *41*, 493-496.
(30) Weber, R. L.; Ye, Y.; Banik, S. M.; Elabd, Y. A.; Hickner, M. A.; Mahanthappa, M. K. Thermal and Ion Transport Properties of Hydrophilic and Hydrophobic Polymerized Styrenic Imidazolium Ionic Liquids. *J. Polym. Sci., Part B: Polym. Phys.* **2011,** *49*, 1287-1296.
(31) Chen, H.; Choi, J.-H.; Salas-de la Cruz, D.; Winey, K. I.; Elabd, Y. A. Polymerized Ionic Liquids: The Effect of Random Copolymer Composition on Ion Conduction. *Macromolecules* **2009,** *42*, 4809-4816.
(32) Vijayakrishna, K.; Mecerreyes, D.; Gnanou, Y.; Taton, D. Polymeric Vesicles and Micelles Obtained by Self-Assembly of Ionic Liquid-Based Block Copolymers Triggered by Anion or Solvent Exchange. *Macromolecules* **2009,** *42*, 5167-5174.
(33) Vidya, P.; Chadha, A. The Role of Different Anions in Ionic Liquids on Pseudomonas Cepacia Lipase Catalyzed Transesterification and Hydrolysis. *J. Mol. Catal. B: Enzym.* **2009,** *57*, 145-148.

(34) Green, M. D.; Long, T. E. Designing Imidazole-Based Ionic Liquids and Ionic Liquid Monomers for Emerging Technologies. *Polym. Rev.* **2009,** *49*, 291-314.
(35) Hunley, M. T.; England, J. P.; Long, T. E. Influence of Counteranion on the Thermal and Solution Behavior of Poly(2-(Dimethylamino)Ethyl Methacrylate)-Based Polyelectrolytes. *Macromolecules* **2010,** *43*, 9998-10005.
(36) Ye, Y.; Elabd, Y. A. Relative Chemical Stability of Imidazolium-Based Alkaline Anion Exchange Polymerized Ionic Liquids. *Macromolecules* **2011,** *44*, 8494-8503.
(37) Ohno, H. Molten Salt Type Polymer Electrolytes. *Electrochim. Acta* **2001,** *46*, 1407-1411.
(38) Johnson, R. N.; Farnham, A. G.; Clendinning, R. A.; Hale, W. F.; Merriam, C. N. Poly(Aryl Ethers) by Nucleophilic Aromatic Substitution. I. Synthesis and Properties. *Journal of Polymer Science Part A-1: Polymer Chemistry* **1967,** *5*, 2375-2398.
(39) Hale, W. F.; Farnham, A. G.; Johnson, R. N.; Clendinning, R. A. Poly(Aryl Ethers) by Nucleophilic Aromatic Substitution. Ii. Thermal Stability. *Journal of Polymer Science Part A-1: Polymer Chemistry* **1967,** *5*, 2399-2414.
(40) Rose, J. B. Preparation and Properties of Poly(Arylene Ether Sulphones). *Polymer* **1974,** *15*, 456-465.
(41) Zhang, B.; Turner, S. R. Synthesis and Characterization of Poly(Arylene Ether Sulfone)S with Trans-1,4-Cyclohexylene Ring Containing Ester Linkages. *Journal of Polymer Science Part A: Polymer Chemistry* **2011,** *49*, 4316-4324.
(42) Pines, A.; Gibby, M. G.; Waugh, J. S. Proton-Enhanced Nmr of Dilute Spins in Solids. *The Journal of Chemical Physics* **1973,** *59*, 569-590.
(43) Dixon, W. T. Spinning-Sideband-Free and Spinning-Sideband-Only Nmr Spectra in Spinning Samples. *The Journal of Chemical Physics* **1982,** *77*, 1800-1809.
(44) Fung, B. M.; Khitrin, A. K.; Ermolaev, K. An Improved Broadband Decoupling Sequence for Liquid Crystals and Solids. *Journal of Magnetic Resonance* **2000,** *142*, 97-101.
(45) Williams, G.; Watts, D. C. Non-Symmetrical Dielectric Relaxation Behaviour Arising from a Simple Empirical Decay Function. *Transactions of the Faraday Society* **1970,** *66*, 80-85.
(46) Cumbrera, F. L.; Sanchez-Bajo, F.; Guiberteau, F.; Solier, J. D.; Muñoz, A. The Williams-Watts Dependence as a Common Phenomenological Approach to Relaxation Processes in Condensed Matter. *J Mater Sci* **1993,** *28*, 5387-5396.
(47) Li, Q.; Jensen, J. O.; Savinell, R. F.; Bjerrum, N. J. High Temperature Proton Exchange Membranes Based on Polybenzimidazoles for Fuel Cells. *Progress in Polymer Science* **2009,** *34*, 449-477.
(48) Kreuer, K.-D. Proton Conductivity: Materials and Applications. *Chemistry of Materials* **1996,** *8*, 610-641.
(49) Park, C. H.; Lee, C. H.; Guiver, M. D.; Lee, Y. M. Sulfonated Hydrocarbon Membranes for Medium-Temperature and Low-Humidity Proton Exchange Membrane Fuel Cells (Pemfcs). *Progress in Polymer Science* **2011,** *36*, 1443-1498.

(50) Padinger, F.; Rittberger, R. S.; Sariciftci, N. S. Effects of Postproduction Treatment on Plastic Solar Cells. *Advanced Functional Materials* **2003,** *13*, 85-88.
(51) Jo, J.; Kim, S.-S.; Na, S.-I.; Yu, B.-K.; Kim, D.-Y. Time-Dependent Morphology Evolution by Annealing Processes on Polymer:Fullerene Blend Solar Cells. *Advanced Functional Materials* **2009,** *19*, 866-874.
(52) Rowe, B. W.; Freeman, B. D.; Paul, D. R. Influence of Previous History on Physical Aging in Thin Glassy Polymer Films as Gas Separation Membranes. *Polymer* **2010,** *51*, 3784-3792.
(53) Moe, M. B.; Koros, W. J.; Paul, D. R. Effects of Molecular Structure and Thermal Annealing on Gas Transport in Two Tetramethyl Bisphenol-a Polymers. *Journal of Polymer Science Part B: Polymer Physics* **1988,** *26*, 1931-1945.
(54) Liu, J.; Guo, T.-F.; Yang, Y. Effects of Thermal Annealing on the Performance of Polymer Light Emitting Diodes. *Journal of Applied Physics* **2002,** *91*, 1595-1600.

Chapter 4

Humidity-Modulated Phase Control and Nanoscopic Transport in Supramolecular Assemblies

Sections 4.1 – 4.3 and 4.6 are reprinted from the following reference: Ying Chen*, Mark D. Lingwood*, Mithun Goswami, Bryce E. Kidd, Jaime J Hernandez, Martin Rosenthal, Dimitri A. Ivanov, Jan Perlich, Heng Zhang, Xiaomin Zhu, Martin Möller, and Louis A. Madsen (*contributed equally). *J. Phys. Chem. B* **2014**, *118*, 3207. Sections 4.4 – 4.5 are further studies and conclusions based on the published work.

4.1 Introduction

Supramolecular assemblies can arise from molecular building blocks with specifically designed intermolecular interactions, such as hydrogen bonding, ionic interactions, ion-dipolar interactions, π-stacking as well as excluded volume repulsion and shape anisotropy.[1-4] Such assemblies allow for increased degrees of freedom in controlling macroscopic material properties, and currently we are targeting fast ion conduction for batteries, solar cells, and fuel cells. In particular, supramolecular materials show promise for fine control of morphology on many length scales, including the local (few nm) length scale that principally governs ion motion.[5-8] Many studies have explored liquid crystalline (LC) structures formed from supramolecular assemblies for ion conduction applications,[9-14] however the multi-modal characterization of such materials to correlate transport information and structure at the molecular level has been limited. Here we describe a set of subtle mesophase manipulations coupled with sensitive and correlated measurements of structure and transport on a

polymerizable wedge-shaped sulfonate amphiphile. These results represent a new pathway to material control in supramolecular phases composed of amphiphilic molecular building blocks.

Figure 4.1 shows the amphiphile molecular structure as well as a representative supramolecular self-assembly process to form columnar phases. In these novel systems, exposure to humid air drastically alters self-assembly, allowing for sensitive control of phase, as shown in our previous work.[15] Using these manipulations, we can define nanostructures with optimal geometry, dimensions, and dynamics for ion transport.

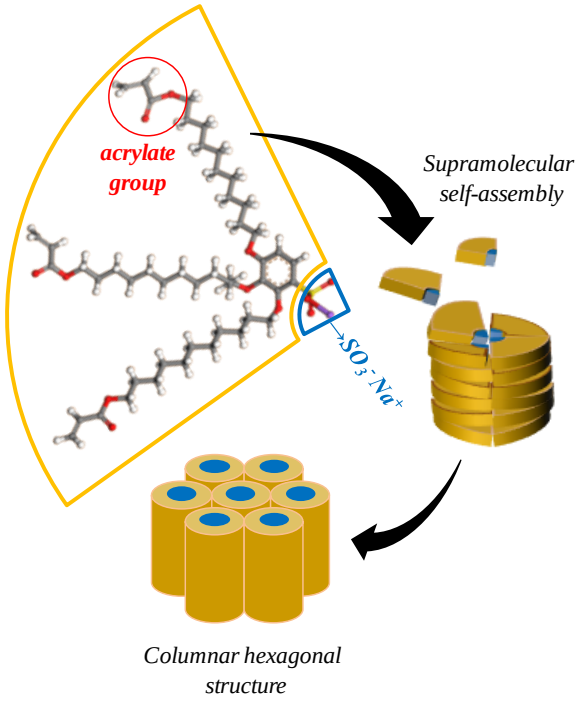

Figure 4.1 Molecular structure of the acrylate sulfonate wedge molecules used in this work. Self-assembly of the mesogen begins with formation of supramolecular disks (tetramers) and continues toward the classical 2D hexagonal columnar structure (at lower humidity values) with ion conducting channels running along the column axes. When exposed to high humidity, this structure readily transforms to bicontinuous cubic structures characterized by fast water transport.[15]

To correlate material structure with ion transport and to understand the mechanisms of ion conduction, it is crucial to combine multiple techniques that probe the structure and dynamics of soft materials. In this paper, we probe supramolecular structure in detail using in situ synchrotron grazing-incidence small-angle X-ray scattering (GISAXS) as a function of relative humidity (RH). We also showcase the use of ^{23}Na solid-state NMR (SSNMR) to reveal drastic RH-dependent structural and ion association changes in these amphiphilic sodium salts. Further, we investigate the transport dynamics using pulsed-field-gradient (PFG) NMR diffusometry, showing that water transport in these materials depends intimately on supramolecular structure. The unique combination of NMR spectroscopy and diffusometry with high resolution X-ray scattering provides new insights into the coupling of structure and morphology with molecular transport.

4.2 Experimental

4.2.1 Acrylated Wedge Molecule Synthesis and Film Preparation

We define the amphiphilic wedge molecules as "**A-Na**" (for acrylated molecule, sodium salt) as shown in scheme 1. Synthesis details were described in our previous work.[15] **A-Na** thin films used in X-ray studies were prepared by spin-coating from solutions in $CHCl_3$ (20 mg.ml^{-1}) over Si substrates. Prior to film deposition, substrates were cleaned by immersion in piranha solution (H_2SO_4:H_2O_2, 3:1) and abundant rinsing with deionized water. **A-Na** salt was used in its pure bulk form as received (a waxy solid) for all NMR studies.

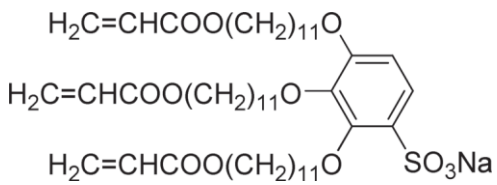

Scheme 1. Chemical structure of sodium 2,3,4-tris(11'-acryloyloxyundecyl-1'-oxy)benzene sulfonate (**A-Na**).

4.2.2 X-ray Scattering Studies

Characterization of the **A-Na** films was carried out by grazing-incidence small-angle X-ray scattering (GISAXS), a powerful technique in structural investigations of thin organic films.[16-17] GISAXS measurements were performed at the BW4 beamline of HASYLAB (Hamburg, Germany); the wavelength used was λ=1.38Å. X-ray patterns were recorded at room temperature using a 2D CCD camera. The norm of the scattering vector **s**(|s|=(2 sinθ)/λ where

is the Bragg angle) was calibrated using a silver behenate standard. Samples were precisely aligned to an angle of 0.4 °with respect to the incident beam. This relatively high value allowed avoidance of the Bragg peaks due to the reflected beam, which is a frequent observation in the GISAXS configuration.[18] Immediately prior to GISAXS measurements, samples were equilibrated at a range of RH-values for at least 1.5 hours, generated by saturated solutions of inorganic salts in D_2O (see Table 1). These various salt solutions create a well-defined RH atmosphere above them due to the different activity of water for the salt solutions.[19] The humidity level was measured using a digital humidity sensor (Sensirion SHT75). The sample is equilibrated above these solutions for controllable and reproducible water uptake. Water uptake, expressed in $\lambda(H_2O/SO_3^-)$, was determined using the following equation:

$$\lambda(H_2O/SO_3^-) = \frac{\text{mass}_{\text{wet}} - \text{mass}_{\text{dry}}}{\text{mass}_{\text{dry}}} \times \frac{\text{MW}_{\mathbf{A-Na}}}{\text{MW}_{H_2O}}$$

Here mass_{dry} stands for the mass of vacuum dried **A-Na** material, mass_{wet} is the mass of wet **A-Na** equilibrated at various salt solutions, while $\text{MW}_{\mathbf{A-Na}}$ and MW_{H_2O} are molecular weight of **A-Na** and water, respectively. To this end, **A-Na** films were placed in a sealed environmental chamber as depicted in Figure 4.2.

Salt	RH (%)
$MgCl_2$	33
$Mg(NO_3)_2$	55
KCl	86
pure D_2O	100

Table 4.1 Inorganic salts used in the GISAXS and NMR experiments and RH conditions obtained above their saturated solutions with D_2O.

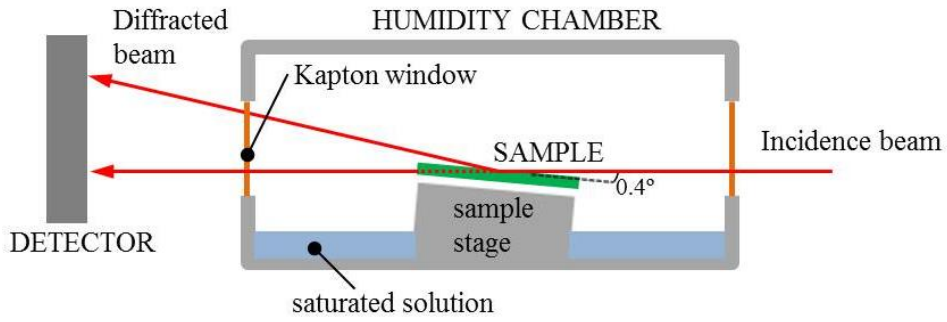

Figure 4.2 Schematic of synchrotron GISAXS setup. The custom-built chamber allows equilibration above humid atmosphere at controlled RH

4.2.3 NMR Studies

All solid-state NMR experiments were performed on a Bruker Avance III 600 MHz (14.1 T) spectrometer using a 3.2 mm HXY probe. **A-Na** salt was packed into a 3.2 mm magic angle spinning (MAS) zirconia rotor, which was then exposed to various hydration levels by placing the rotor over different solutions for ≥ 1 day (Table 1) in sealed chambers. Before measurement, the rotor was removed from the hydration chamber and quickly capped. Experiments were performed at 10 kHz and 18 kHz spinning speeds at the magic angle (54.74 °). No spinning side bands were observed for ^{23}Na MAS spectra with a spinning speed of 10 kHz.

NMR spectra under static conditions were also recorded. Solid NaCl was used as external reference for ^{23}Na, and solid tetrakis(trimethylsilyl)silane was used as an external reference for ^{1}H.[20-22] To achieve uniform excitation, a short single pulse with 2 μs duration corresponding to 30 °tilt angle was used. A total of 1024 and 8 transients with a relaxation delay of 5 s were recorded for ^{23}Na and ^{1}H spectra, respectively. All experiments were conducted at 25 ℃.

For relaxation and diffusion measurements, bulk solid **A-Na** was divided into five samples of 10 – 20 mg each. Each sample was placed into a 1 cm length of 4 mm glass tubing (2 mm inner diameter) with one end sealed, and placed on a vacuum line at 1 mTorr for 2 days. Following evacuation, one sample was transferred into a 5 mm NMR tube and sealed under vacuum. The remaining four samples were held above various solutions (Table 1) at room temperature for ≥ 1 day. Immediately prior to NMR measurements, samples were removed from RH-equilibration tubes and placed into 5 mm NMR tubes along with a length of 4 mm glass rod (to reduce dead volume) and capped.

All PFG NMR diffusion measurements were obtained using a Bruker Avance III wide bore 400 MHz (9.4 T) NMR equipped with a Diff60 diffusion probe and either a 5 mm ^{1}H or 5 mm ^{2}H/^{1}H coil (Bruker Biospin, Billerica, MA). The pulsed-gradient stimulated echo (PGSTE) sequence[23] was used to measure diffusion, with an effective gradient pulse length of δ = 2 ms (the actual pulse length of the sinusoidal pulse was 3.2 ms), a 2 ms gradient stabilization time after each gradient pulse, a gradient pulse spacing of Δ = 50 ms, and gradient strengths varying from g = 20 G/cm to g = 1800 G/cm. 16 to 32 gradient steps were applied, and the number of scans varied from 4 to 64 to yield sufficient signal-to-noise ratio (SNR). Diffusion was measured along the magnetic field (z) direction. The self-diffusion coefficient

D was obtained by fitting the measured signal intensity I as a function of gradient strength g to the Stejskal-Tanner equation[23-24]:

$$I = I_0 e^{-D\gamma^2 g^2 \delta^2 (\Delta - \delta/3)} = I_0 e^{-Db} \qquad (4.1)$$

where γ is the gyromagnetic ratio of the detected nucleus, and the Stejskal-Tanner factor $b = \gamma^2 g^2 \delta^2 (\Delta - \delta/3)$. All PFG NMR experiments were conducted at 25°C. The spin-lattice relaxation time T_1 was measured by the inversion-recovery method. The spin-spin relaxation time T_2 was measured using an incremented echo-train CPMG pulse sequence. Errors in T_1 and T_2 values are $\pm 3\%$, and errors in D are $\pm 5\%$.

4.3 Results and Discussion

Through our coordinated GISAXS and NMR measurements, we present a detailed picture of the supramolecular structure in the **A-Na** material and how mesophase structure, channel dimensions, amorphous character, and domain boundaries influence molecular transport.

4.3.1 X-Ray Scattering

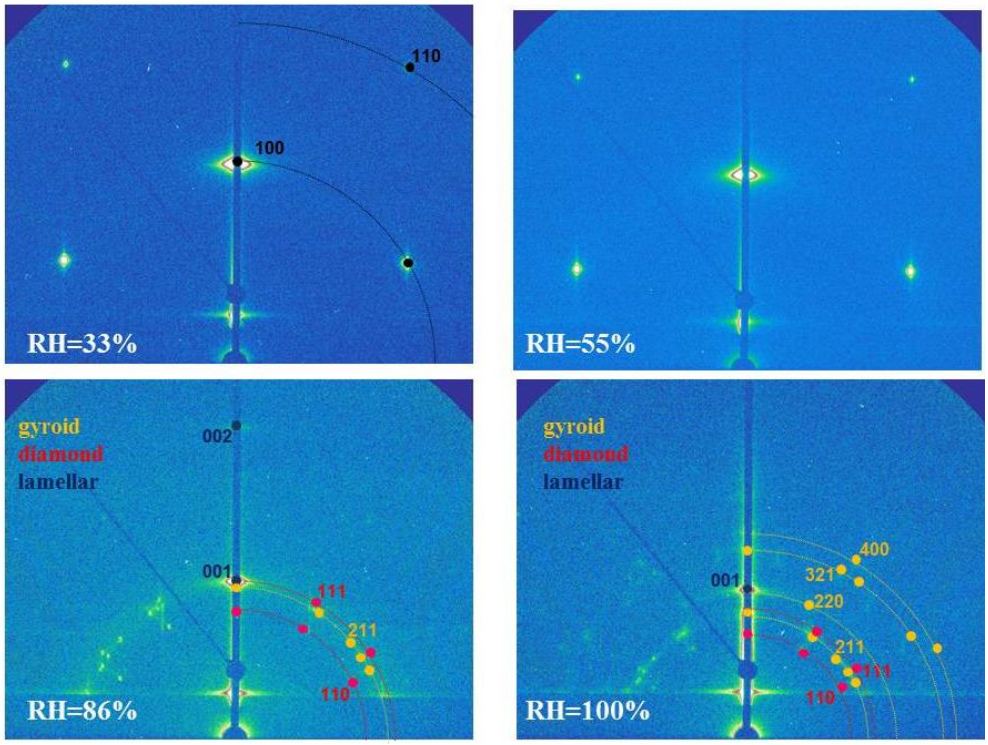

Figure 4.3 2D X-ray patterns vs. RH. At RH ≤ 55%, only the hexagonal columnar phase exists, while at RH ≥ 86% we observe predominantly bicontinuous cubic gyroid and diamond phases together with a lamellar phase. We highlight the main peaks of each phase (see also Table 2).

We show X-ray diffractograms as a function of relative humidity (RH) in Figure 4.3, with Miller indices of the main reflections indicated in each case. Since the patterns are symmetric, we use only one quadrant (Figure 4.3) for peak assignment. The GISAXS patterns show highly oriented film textures. At RH = 33 and 55%, we observe peaks with a ratio of d-spacings of $1:1/\sqrt{3}$. Using the angular positions and d-spacings of the peaks, we assign these peaks to the 100 and 110 reflections of a hexagonal columnar disordered mesophase (Col_{hd}). Importantly, the film exhibits planar orientation, i.e., the column axes lie in the substrate plane.

Water absorption of **A-Na** at RH = 55% results in an increase of the lattice parameter from 39.2 to 40.3Å, i.e., by 3%. At higher RH the mesophase undergoes a phase transition, as inferred from changes in X-ray patterns observed at RH = 86% and 100%. Using the d-spacing ratios (√6: √8: √14: √16 and √2: √3) and the angular positions of the new peaks, we identify two cubic bicontinuous phases (Cub_{bi}), specifically the gyroid (G) and diamond (D) phases. These conclusions are qualitatively similar to those drawn in our previous work,[15] where the phase behavior of thin films of **A-Na** was studied in non-equilibrium conditions in H_2O-saturated atmosphere. However, it is noteworthy that in the present work the phase structure is addressed in quasi-equilibrium conditions using D_2O vapors to match the conditions of NMR experiments. This difference likely accounts for the fact that, in addition to the two bicontinuous cubic phases observed previously, we see an additional pair of peaks with a d-spacing ratio of 1:2, which we assign to a lamellar phase. Table 2 summarizes the hkl-indices of the observed peaks and lattice parameters. Importantly, the new phases grow epitaxially on the parent Col_{hd}, similar to previous reports.[25-27]

RH(%)	Phase	hkl	d_{exp} [nm]	d_{calc} [nm]	Latticeparam. a,b [nm]
33	Col_{hd}	100 110	3.40 1.97	3.39 1.97	a=3.92
55	Col_{hd}	100 110	3.49 2.03	3.49 2.02	a=4.03
86	Cub_{bi}(G)	211	4.49	4.49	a=11.01
	Cub_{bi}(D)	110	5.22	5.25	a=7.43

		200	4.32	4.29	
	Lamellar	001 002	4.31 2.18	4.33 2.16	4.33
100	Cub_{bi}(G)	211 220 321 400	5.54 4.62 3.58 3.32	5.53 4.72 3.62 3.36	a=13.54
	Cub_{bi}(D)	110 111	6.44 5.32	6.47 5.29	a=9.16
	Lamellar	001	4.61	4.61	4.61

Table 4.2 Diffraction peaks pertinent to the different phases formed at different RH-values and the corresponding lattice parameters.

Generally, the diamond and gyroid phases are related by the so-called Bonnet transformation. The Bonnet symmetry implies that the energy of the minimal surfaces of the two structures is degenerate. For this symmetry, the relation between lattice parameters of the unit cells should be $a_G/a_D = 1.57$.[20] In our case, at RH $\geq$ 86% we found this ratio to be constant and equal to 1.49. This difference might be explained by distortions during the G-D transition[28] or as a consequence of confinement imposed by the thin film.

The Cub_{bi} phases appear in the phase diagram of amphiphiles during lyotropic transitions, and are located between the columnar and lamellar structures.[29] The observed co-existence of the G, D and lamellar phases may be thought of as a violation of the classical Gibbs phase rule. One of the reasons for such apparent violation can be the metastable behavior

of the phases in this composition range.[30] Indeed, it is noteworthy that the free energy differences between the cub_{bi} phases can be quite subtle. They are typically introduced into models only in a rather detailed treatment of chain stretching contributions, thermal fluctuations or of van der Waals or electrostatic interactions.[31] Therefore, even a slightly metastable character of the system can bring about phase co-existence. In our case, observation of the usual epitaxial relations such as the equivalence of the 10_{hd} and 211_G peaks means that the phase transitions in **A-Na** operate according to the previously reported mechanisms.[25] However, contrary to the situation described in ref. 25, the films of **A-Na** do not form well-defined optical textures. It is thus possible that the phase transformation process stays incomplete due to pinning of the growing domains at the grain boundaries. Previously, the difficulty to reach equilibrium conditions was mentioned for studies of the phase diagrams of amphiphiles.[30] In particular, the metastable behavior of the cubic phases caused transformation rates significantly longer than the typical experiment duration.

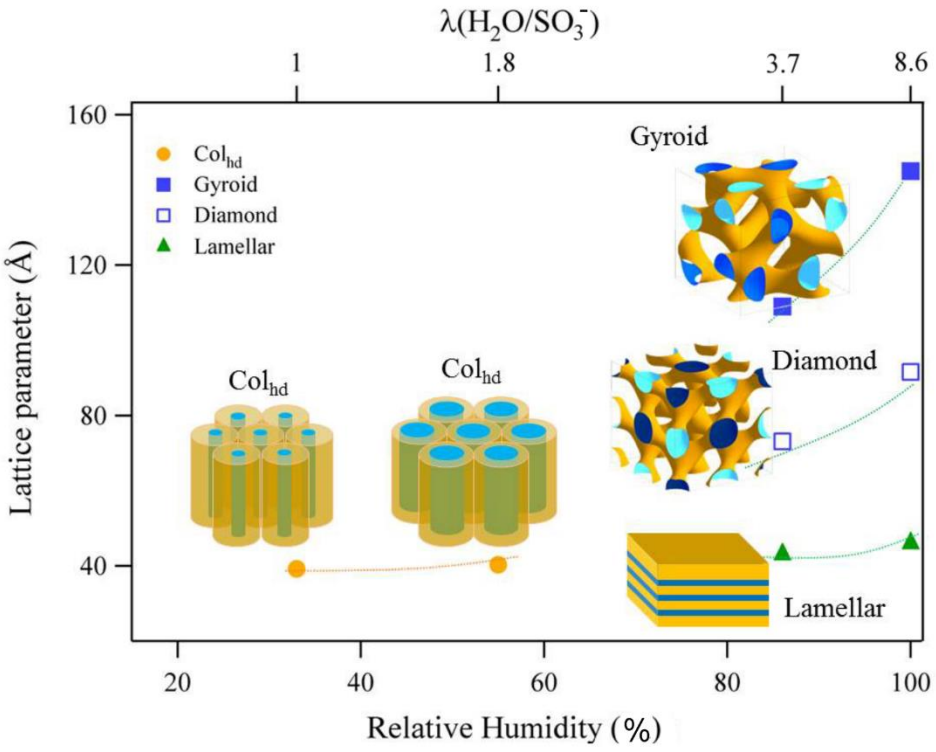

Figure 4.4 Evolution of the lattice parameter as a function of RH (bottom horizontal axis) and water uptake (top horizontal axis) for **A-Na** in different mesophases. Insets: schematic views of the ion channel structural evolution with increasing RH, with hydrophilic channels colored blue.

Figure 4.4 presents the evolution of lattice parameters as a function of RH at room temperature. The columnar phase (Col_{hd}) swells only to a modest degree (3% in linear dimension) when going from RH = 33% to RH = 55%, while increased water uptake induces stronger swelling of the Cub_{bi} structures between 86% and 100% RH (up to 20% swelling). The lamellar structure swells approximately 6% from 86% to 100% RH.

The diamond and gyroidal phases are two of the three known stable bicontinuous cubic phases (primitive cubic being the third).[32] These Cub_{bi} phases contain one single amphiphilic bilayer, which forms a triply periodic minimal surface (TPMS) with cubic symmetry, giving

rise to a 3D continuous ion channel network as depicted in Figure 4.4 and drawn to scale in Figure 4.5. By analyzing the lattice parameters and **A-Na** molecular sizes, we estimate the ion channel dimensions. As detailed in the accompanying electronic supporting information (SI), in this case we estimate the average channel diameter to be 25.7Å. However, we note that the channel diameter is not constant: the channels are thinnest in between the nodes whereas the junctions are much bulkier (see Figure 4.5). In the generated structure, all nodes are interconnected by channels, which means that at this water uptake the channels are not pinched off (as in the gyroid structure below the percolation threshold observed at 11.7%[33]). An analysis of the generated structure makes it possible to estimate the smallest and largest channel diameters of 25.0 and 40.8 Å, respectively. Clearly the cubic phases in these materials are superior for water and ion transport (see conductivity data in Figure S4.1), as these dimensions are much larger than the 15 Å hydrophilic channel in the columnar phase, and the cubic channel dimensions are close to those of established hydrated ion-conducting materials. Indeed, these channel dimensions strongly impact water diffusion, as we discuss below.

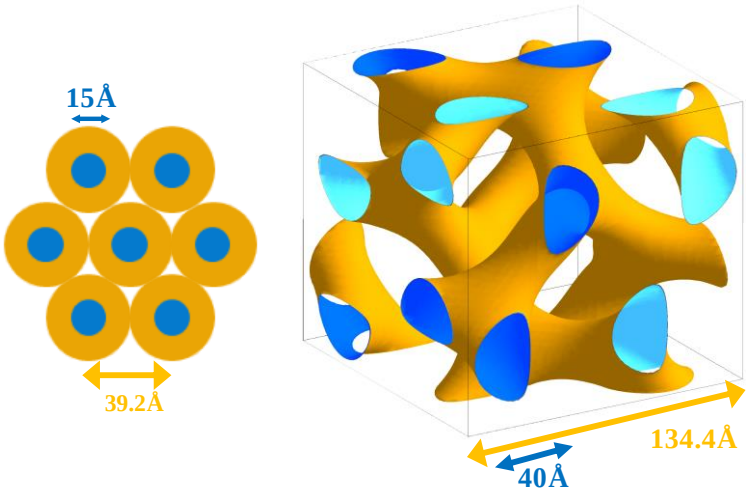

Figure 4.5 Models of Col_{hd} and Cub_{bi} gyroid phases drawn to scale. Ion conducting channels are shown in dark and light blue.

4.3.2 Sodium-23 NMR Measurements

As a quadrupolar nucleus with spin I = 3/2, ^{23}Na has been proven to be a powerful probe of the local environment around the nucleus in various materials,[34-38] as the linewidth and chemical shift of ^{23}Na NMR spectrum are generally determined by the interaction between the electric quadrupole moment (a property of the nucleus) and electric field gradients (a property of the ~ 1 nm scale surroundings).[39] This quadrupolar interaction is very sensitive to atomic bonds of the nucleus, the structure and composition of nearby molecules, and the symmetry of the surrounding charges.[39] Therefore the study of quadrupolar nuclei with solid-state NMR can provide a wealth of information about the local environment of the nuclei.

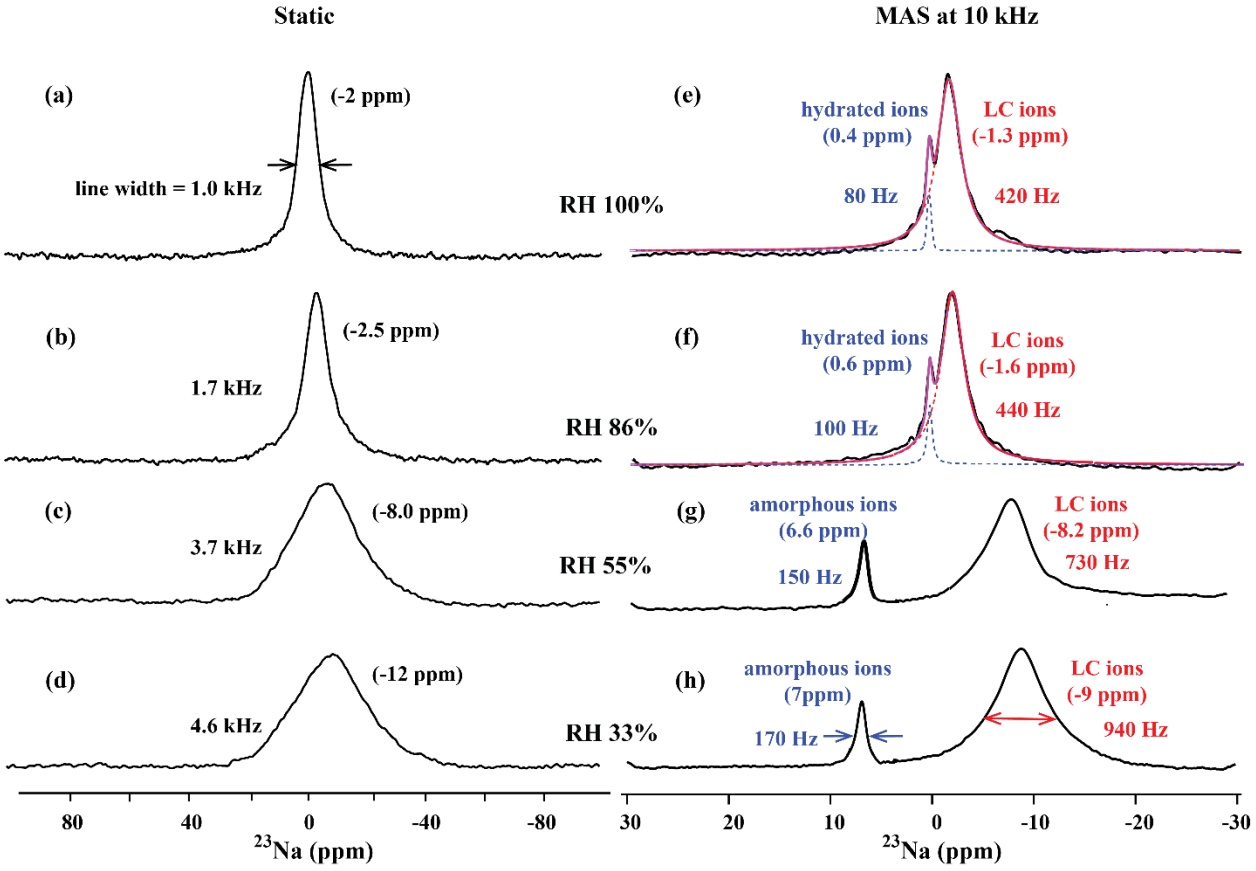

Figure 4.6 ^{23}Na solid-state static (left column, a-d) and MAS (right column, e-h) NMR spectra of **A-Na** salt at different RH. Note that different scales are used for the ppm axis of each column. A clear transition in Na quadrupolar interaction and mobility occurs between 55% and 86% RH, correlated with the phase transition observed by GISAXS. Two separate peaks are observed with MAS at 10 kHz. The sharp peak at 7 ppm at low RH is assigned to Na^+ of amorphous (domain boundary) wedges and contributes to 10 ± 2% of the total signal. The broad peak is assigned to Na^+ of wedges in the LC phases. By increasing RH, all Na^+ ions become completely or partially hydrated. We deconvolute the spectra in (e) and (f) to extract the fraction of each peak using matNMR[40], and the hydrated sharp peak near 0 ppm is 8 ± 1 % of the total signal.

Figures 4.6a–d show the single pulse static ^{23}Na spectra of **A-Na** prepared at varying RH. Overall, the peak linewidth decreases as RH increases. At higher RH, sodium ions become on average more hydrated and the distance between sodium ions increases, reducing the asymmetry in the surrounding electronic environment. This results in decreased electric field gradients (EFGs) at the ^{23}Na nuclei, leading to reduced quadrupolar broadening. In addition, increased motional averaging further reduces the observed EFG. The significant decrease in linewidth from RH 55% to RH 86% indicates a phase change between these two hydration levels, in close agreement with GISAXS observations.

Figures 4.6e–h show the single pulse magic angle spinning (MAS) ^{23}Na spectra of the **A-Na** material with a spinning speed of 10 kHz. The quadrupolar interaction is partially averaged under MAS, resulting in a spectrum that is much better resolved than a static spectrum, allowing us to identify various non-equivalent sodium sites in the system. We observe two

^{23}Na resonances at all hydration levels: a sharp peak at higher chemical shift values (~7 ppm) and a much broader peak at lower chemical values (peak locations and widths specified in Figures 4.6e–h). The narrow line shape at 7 ppm with FWHH = 170 Hz indicates that the quadrupolar coupling is relatively small. Based on published work by E. M. O'Connell et al.[41-44], we can reasonably assume that the sharp peak is the result of an individual Na^+ interacting with an individual RSO_3^- group attached to an isolated ion pair or in similar environments producing very small EFGs. Combined with our discussions below regarding ^{1}H and ^{2}H relaxation and diffusion measurements, we suggest that those individual ion pairs locate predominantly in amorphous regions, or more precisely within domain boundaries of the material. While LC domains consist of well-packed wedge molecules, domain boundaries are much less populated. On the other hand, the chemical shift of the center of the broad peak arises from both isotropic chemical shift σ_{iso} and second-order quadrupolar shift σ_{2QS}, because most other interactions including first-order quadrupolar, dipolar, and chemical shift anisotropy are removed under magic angle spinning. While σ_{iso} is independent of external magnetic field ω_0, σ_{2QS} is inversely proportional to ω_0: $\sigma_{2QS} \propto \omega_Q^2/\omega_0$. In order to confirm the contribution of σ_{2QS}, we also obtained ^{23}Na MAS spectra at 79.2 MHz (data not shown). The broad peak is wider and more upfield shifted at this lower frequency, indicating that the second-order quadrupolar interaction is a major contribution to the broad peak line shape. Therefore, we assign the broad peak to Na^+ ion aggregates inside the ionic channels formed in LC mesophases.

As hydration increases, both peaks in the ^{23}Na MAS spectra shift towards 0 ppm. In ^{23}Na NMR, a single peak at 0 ppm is characteristic of aqueous Na^+ ions, since EFGs approach zero as Na^+ ions become fully hydrated and reside in a symmetric tetrahedral environment.[45]

Therefore, the shift of the hydrated ion peak from 7 ppm at RH 33% to 0.4 ppm at RH 100% shows that Na^+ associated with amorphous wedges becomes increasingly hydrated as RH increases, and that nearly all Na^+ ions of amorphous wedges are hydrated at RH 100%. As RH increases, the broad peak is downfield shifted and narrowed, suggesting a smaller second-order quadrupolar interaction and smaller EFGs as a result of increased hydration of Na^+ ions inside the ionic channels of LC domains. The increased molecular mobility at higher hydration also contributes to the reduction in linewidth. The broad peak at 100% RH appears at -1.3 ppm, which indicates that Na^+ ions inside the ionic channels do not become completely hydrated even under RH 100% with $\lambda(D_2O/SO_3^-) = 8.6$.

^{23}Na NMR can quantify the amount of wedge molecules present as amorphous wedges vs. those within a mesophase. At 33% and 55% RH, the sharp peak contributes to 10 ± 2% of the total NMR signal. At 86% and 100% RH, the two peaks overlap, and deconvolution of the spectra is necessary to find the fraction of each peak. The deconvolution is shown as dotted lines in Figures 4.6e and 4.6f, and we find that the hydrated Na peak at near 0 ppm contributes 8 ± 1 % of the total signal for both 86% and 100% RH. We notice a slight decrease in the fraction of individual wedges at RH ≥ 86% compared to that of RH ≤ 55%, but the small decrease is within measurement error. In short, ^{23}Na MAS NMR spectra provide direct evidence of local structural disorder (the presence of 10% amorphous wedges). We discuss the molecular dynamics and translational motions of these amorphous wedges next.

4.3.3 ^{1}H 1D NMR: Relaxation Measurements and Diffusion-Weighted Spectra

Figure 4.7 shows representative spectra of **A-Na** from several ^{1}H NMR experiments. ^{1}H MAS NMR data are shown at the top of Figure 4.7, static 1D NMR spectra are shown in blue for five humidity values, and diffusion-weighted spectra at the lowest gradient

representative of 2D PGSTE experiments are shown in red. We discuss each measurement below.

The ^{1}H MAS spectrum of **A-Na** at 18 kHz is shown in Figure 4.7 for the purpose of spectral assignment. In addition, Figure S4.2 displays ^{1}H MAS spectra of **A-Na** salt under all RH values with a spinning speed of 10 kHz. In agreement with the ^{23}Na measurements, all proton resonances become sharper and better resolved as RH increases, suggesting faster molecular motion at higher RH. With the help of a simple solution NMR spectrum (not shown), we assign the ^{1}H resonances as shown in Figure 4.7.

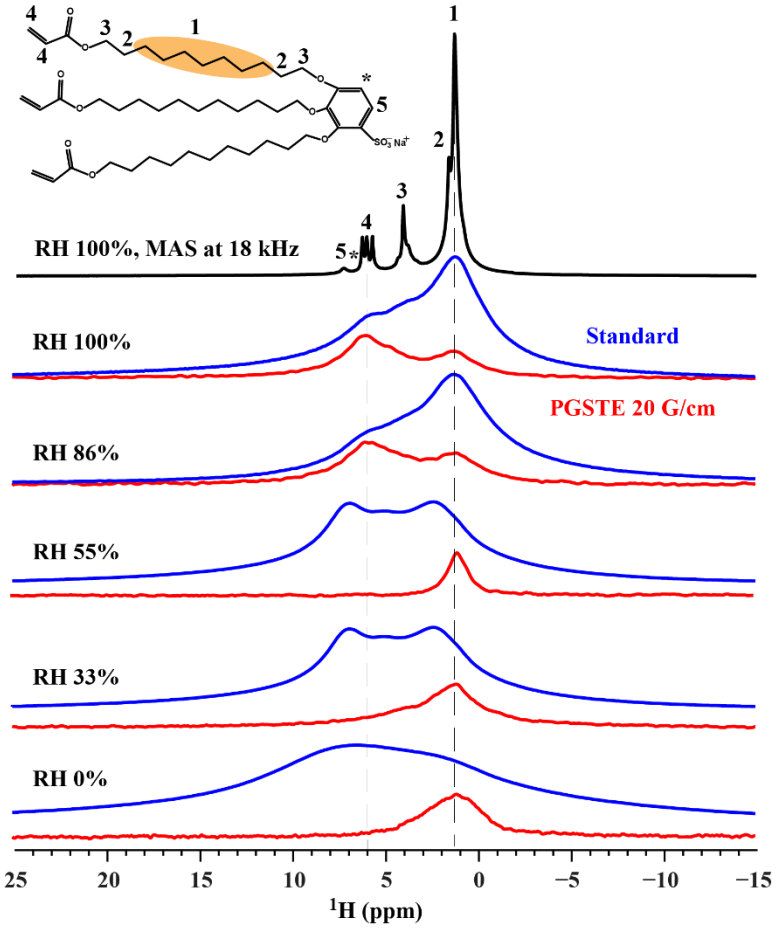

Figure 4.7 ^{1}H NMR spectra of **A-Na**. The ^{1}H MAS spectrum collected at 18 kHz and RH = 100% is at the top (black) for spectral assignment. The proton marked with an asterisk (*) was

not resolved. RH-dependent ^{1}H static 1D NMR spectra (top of each pair, blue) and the first (lowest gradient) spectra of a 2D PGSTE diffusion experiment (bottom of each pair, red) appear below. The 1D spectra (blue) show signal from all protons in the sample, while the diffusion-weighted spectra (red) show only proton signals with faster dynamics (longer T_2) that can be measured by PGSTE. At RH ≤ 55%, only amorphous wedge molecules move fast enough to probe diffusion. At RH ≥ 86%, wedges in LC phases are also accessible due to faster dynamics.

The blue lines of Figure 4.7 are the ^{1}HNMR static spectrum of **A-Na** salt at different RH values. These spectra are broad and nearly featureless due to both inter- and intramolecular static dipolar interactions, which are not averaged on the NMR dipolar coupling timescale (~ 1 ms) due to significantly restricted motion. To gain information on the variety of molecular environments experienced by **A-Na** molecules in the sample, we collect T_2-weighted spectra (Figure S4.3) and measure T_2 decay constants under several RH conditions. For vacuum-dried **A-Na**, about 97% of the proton signal decays rapidly and nonexponentially with $T_2 < 2$ ms, due to the rigidity of the **A-Na** molecules in the Col_{hd} phase, while the remaining resonance centered at 1.3 ppm decays with a single long $T_2 = 45$ ms. We conduct further dynamic studies of spin-lattice relaxation time T_1 and spin-lattice relaxation time in the rotating frame $T_{1\rho}$ (detailed discussions in SI), and these results corroborate our assumption that the long T_2 component at 1.3 ppm is not from the LC structures but from a more mobile amorphous region. Most likely this amorphous component is the domain boundaries separating LC domains. This has dramatic implication for the PGSTE results of the RH ≤ 55% samples, as these diffusion experiments can only measure amorphous wedges, due to the T_2 weighting of these measurements. The T_2 values of all resonances increase with RH, indicating that all protons

become increasingly mobile with water uptake. Considering the spectra at RH ≥ 86%, we notice a significant increase in proton signal intensity centered at 6.1 ppm when comparing these T_2-weighted spectra with τ = 5.6 ms (red lines of Figure S4.3) to the spectra with RH ≤ 55%. This shows that the mobility of protons in the hydrocarbon chains increase from the head to the tail of the chain in the LC structures. Therefore we can observe both wedges in the LC domains (large amount, short T_2) and in the amorphous domain boundaries (small amount, long T_2) at RH ≥ 86%.

We also observe effects of T_2 weighting in the single diffusion-weighted spectra (in red) from the PGSTE diffusion measurements shown in Figure 4.7. In general, PFG-NMR diffusion experiments are conducted by recording successive NMR spectra as a function of gradient strength g, which allows for the display of a single NMR spectrum from the PGSTE experiment. This allows one to determine how much of the total signal available in the sample is probed by the diffusion measurement. Our diffusion measurements only show signals from nuclei with relaxation times long enough to survive the gradient encoding times (2 × 5.2 ms = 10.4 ms), when transverse relaxation (T_2) is active, and the 50 ms diffusion delay , when longitudinal relaxation (T_1) is active. To visualize this, the red lines of Figure 4.7 show the first diffusion-weighted spectra (with the lowest g = 20 G/cm) of the 2D PGSTE experiments at different RH values. These traces closely mimic the T_2-weighted spectra with 5.6 ms spin echo delay in Figure S4.3

As discussed in the previous paragraph, at RH ≤ 55%, protons from the columnar phase do not appear in the PGSTE diffusion experiments due to their short T_2 (< 5 ms), and only the diffusion of amorphous wedges can be measured. At RH ≥ 86%, the dynamical situation changes drastically, and the chain-terminal acrylate protons (at 6.1 ppm) are now visible in the

PGSTE measurements. As discussed above, we use the PGSTE peak at 6.1 ppm to measure the diffusion of the wedges pertinent to both the amorphous and liquid-crystalline regions.

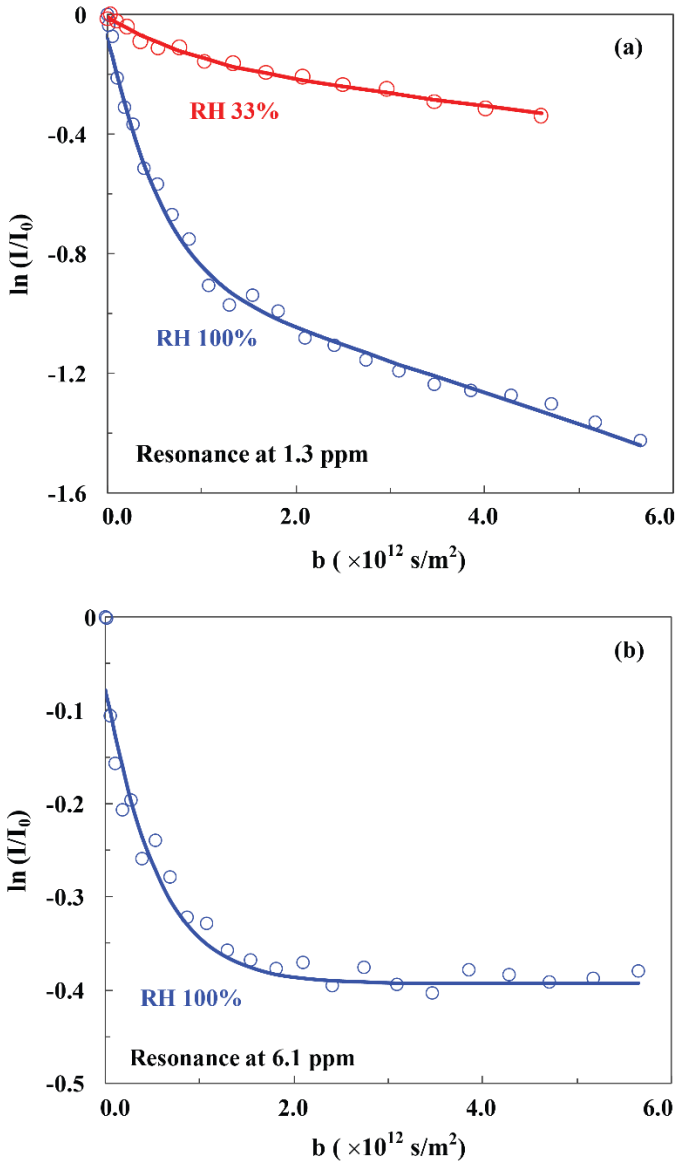

Figure 4.8 PGSTE diffusion experiments on **A-Na** equilibrated over D_2O. (a) Stejskal-Tanner plot of the ^1H resonance at 1.3 ppm from the methylene protons of **A-Na** molecules, showing

fits to obtain two diffusion coefficients at both RH 33% and RH 100%. (b) Stejskal-Tanner plot of the ^{1}H resonance at 6.1 ppm from the chain-terminal acrylate protons of **A-Na** molecules at RH 100%, also fit to obtain two diffusion coefficients. The slow component (< 1×10^{-15} m^2/s) is beyond our detection limit and is assigned to the slow diffusing wedges in the liquid crystal phase. In both plots the x-axis is the Stejskal-Tanner term of Eq. 1, $b = \gamma^2 g^2 \delta^2 (\Delta - \delta/3)$.[23-24]

4.3.4 ^{1}H Diffusion Measurements: Wedge Transport

Figure 4.8 shows Stejskal-Tanner diffusion plots from the ^{1}H PGSTE measurements of **A-Na** salt equilibrated over D_2O. Figure 4.9 presents a summary of all the PGSTE results, including both the ^{1}H measurements on **A-Na** (this section) and the ^{2}H measurements on absorbed D_2O (next section). We conclude that wedges diffuse in two modes, with the fast component in the amorphous boundaries between LC domains and the slow component within the LC domains but existing as individual wedges not participating in LC packing.

At low RH, we observe clear two-component diffusion for the wedge molecules. For example, RH = 33% displays two-component diffusion with $D = 5 \times 10^{-14}$ m^2/s (88% amplitude) and 1.4×10^{-12} m^2/s (12%) for the resonance at 1.3 ppm. As discussed in the previous section, both diffusion coefficients correspond to the methylene protons of amorphous wedge molecules. The I_0 fitting parameter for these components represents the actual population percentage for the amorphous wedge molecules, since a single T_2 value is shared for the two components. The two-component diffusion presents more evidence of structural and dynamic heterogeneity in this supramolecular liquid crystal. We can calculate the diffusion length r using $< r^2 >^{\frac{1}{2}} = \sqrt{(2D\Delta)}$, which represents the statistical average distance a molecule has traveled during the diffusion time Δ.[46] Again using RH = 33% as an example, we find diffusion

length of 70 nm for the slow component and 370 nm for the fast component with $\Delta = 50$ ms. Considering both the ^{23}Na SSNMR and ^{1}H diffusion data, we propose that the 10% of the material present as amorphous wedges exists in interfacial boundaries in between domains of the remaining 90% **A-Na** present in LC structures. We assign the fast component ($D = 1.4 \times 10^{-12}$ m^2/s) to the amorphous wedges diffusing within these domain boundaries, and the slow component ($D = 5 \times 10^{-14}$ m^2/s) to essentially individual wedges (wedge-counterion pairs) diffusing within columnar domains but which do not participate in the columnar packing. Since NMR diffusion measurements reflect transport properties averaged over the entire sample, the existence of two clear diffusion components shows that the individual wedges are not exchanging between LC domains and domain boundaries of the material during the diffusion time of $\Delta = 50$ ms. In other words, wedge molecules are in fast exchange on all length scales smaller than 70 nm, requiring that the LC domains are $\geq$ 70 nm (the diffusion length of the slow component), and that the two different diffusion coefficients for the wedge molecules cannot be caused by differences in local molecular associations (< 1 nm scale).[47]

At high RH (86% and 100%), the diffusion measurements become more complex. Similar to the low RH measurements, we find two diffusion components for the resonance at 1.3 ppm: $D = 1.0 \times 10^{-13}$ m^2/s and 2.1×10^{-12} m^2/s (Figure 4.8a), however we cannot directly relate the I_0 fitting parameters to the percentage of each component due to multiple T_2 values. As above, we assign these D values to wedge molecules diffusing 1) within the mesophase and 2) in the amorphous regions that constitutes the domain boundary. In addition, we notice that the diffusion curve for the resonance at 6.1 ppm (Figure 4.8b) has a very slow and high intensity component that is beyond the detection limit of our PGSTE experiments ($D \leq 1 \times 10^{-15}$m^2/s). To investigate further, we perform another PGSTE measurement with long gradient

encoding times (δ = 8ms), which only reports on the individual wedges with long T_2 components (data not shown). Here we obtain similar diffusion coefficients for both resonances at 1.3 and 6.1 ppm, which match the D values observed at 1.3 ppm with short encoding times (δ = 2ms). This shows that the peak at 6.1 ppm actually consists of three components: two components that are shared across both the 1.3 and 6.1 ppm peaks that are due to individual wedges in both the mesophase and domain boundaries, and one very slow component that is present only at 6.1 ppm. We assign this slowest diffusion coefficient $D \leq 1 \times 10^{-15}$ m^2/s to the slow diffusing wedges in the bicontinuous cubic or lamellar phases. While we are unable to measure the diffusion of the wedges in the columnar phase, it is a reasonable assumption that the Col_{hd} wedge molecules at low RH have even slower diffusion.

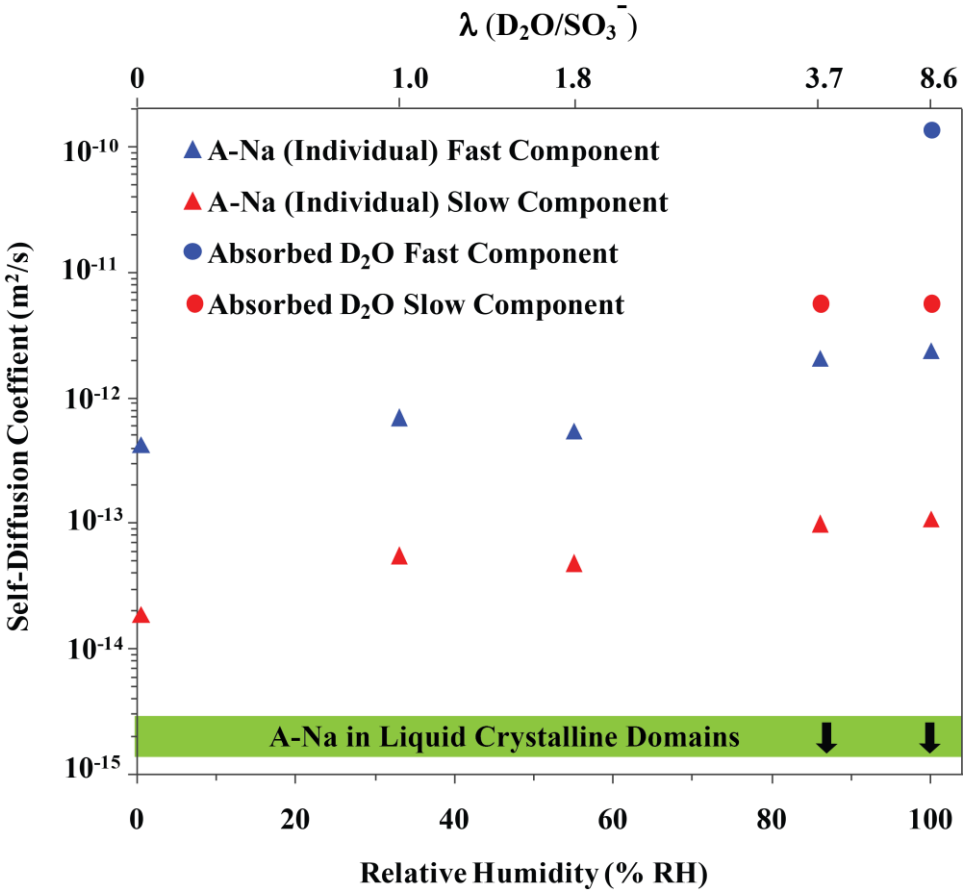

Figure 4.9 Diffusion coefficients of **A-Na** wedge molecules and absorbed D_2O vs. RH and water uptake $\lambda(D_2O/SO_3^-)$.We assign the two diffusion components of the wedges to the individual wedges diffusing within and between LC domains, while the diffusion of the wedges in LC domains is very slow (< 10^{-15} m^2/s) and beyond our detection limit. The slow water diffusion component corresponds to wedges diffusing within amorphous domain boundaries, while the fast component is free water diffusing within the enlarged ionic channels of the bicontinuous phases.

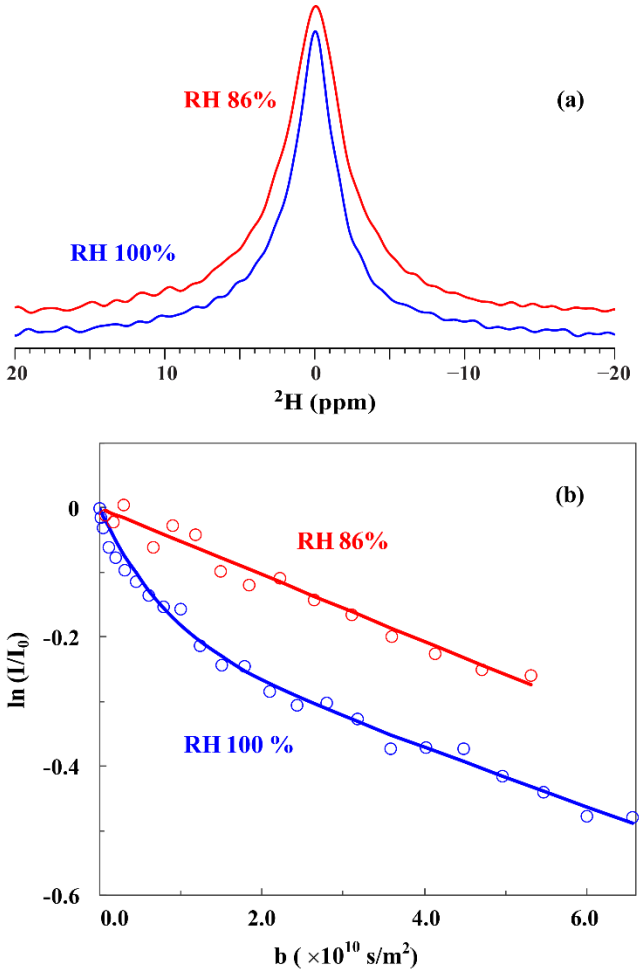

Figure 4.10 (a) ^2H static 1D NMR spectra of absorbed D_2O in the **A-Na** sample equilibrated over D_2O at RH 86% (top) and RH 100% (bottom). (b) Stejskal-Tanner plot of the ^2H peaks

from the absorbed D_2O. We find a single diffusion coefficient ($D = 4.2 \times 10^{-12} m^2/s$) at RH = 86%, and an additional faster component ($D = 1.7 \times 10^{-10} m^2/s$) at RH = 100%.

4.3.5 ^{2}H Diffusion Measurements: Water Transport

In order to perfectly separate water diffusion measurements from wedge diffusion due to ^{1}H NMR spectral overlap from wedge-molecule peaks and to avoid deconvolution inaccuracies, we measure water (D_2O) diffusion by equilibrating samples over salt solutions in D_2O and performing ^{2}H NMR. We observe no detectable ^{2}H NMR signal at RH $\leq$ 55% ($\lambda \leq$ 1.8) due to this small amount of D_2O in the sample being strongly associated with ions in the columnar phase channels. Figure 10 shows ^{2}H 1D static spectra and PGSTE measurements of absorbed D_2O at RH 86% and 100%. Unlike ^{2}H spectra of absorbed D_2O in oriented liquid crystals or Nafion[48], where the quadrupole splitting reveals the degree of LC alignment and order parameter of channel network matrix, here we only observe a broad singlet peak, indicating that no significant macroscopic orientational order of LC structures is present in these bulk samples. Furthermore, the broad peak results from the average signal from D_2O absorbed in both LC structures and amorphous regions. While the linewidth (FWHM) decreases only slightly from 260 Hz to 210 Hz when increasing RH from 86% to 100%, the diffusion behavior is markedly different. The RH = 86% sample shows single component water diffusion ($D = 4.2 \times 10^{-12} m^2/s$), but an additional faster component ($D = 1.7 \times 10^{-10}\ m^2/s$) appears in the RH=100% sample. The slow water component displayed by both the 86% and 100% RH samples has a diffusion coefficient very similar to the fast **A-Na** component, therefore it likely represents D_2O molecules diffusing within domain boundary regions with reasonably strong associations to the sulfonate group of individual **A-Na** molecules. In essence, the D_2O diffuses closely with a wedge-couterion pair. This assignment is supported by the ^{23}Na

measurements, which show that Na^+ ions of individual wedges are nearly completely hydrated at RH ≥ 86%. The fast water component at RH = 100% is only an order of magnitude slower than the diffusion coefficient of pure D_2O[49], suggesting that these D_2O molecules are relatively free to move within the enlarged ionic channels formed at the higher RH. This fast D_2O diffusion coefficient in **A-Na** is also nearly as fast as water diffusion in the benchmark conducting polymer membrane Nafion ($D = 3.5 \times 10^{-10}$ m^2/s) at similar hydration.[48] The fact that we only see the fast water motion in the bicontinuous cubic phase matches the hydrophilic channel dimensions from GISAXS, where the diameter of ionic channels increases from 15.0 Å in the columnar phase to between 25.0 and 40.8 Å in the cubic phase as the RH is increased from 55% ($\lambda = 1.8$) to 100% ($\lambda = 8.6$), as discussed above. Clearly, the cubic phases of **A-Na** are far superior for ion transport, especially at 100% RH.

4.4 Further NMR Studies on Crosslinked Membranes

Stable free-standing membranes based on **A-Na** or similar supramolecular assemblies can be formed by crosslinking acrylic end-groups under appropriated conditions. A set of crosslinked membranes were obtained using UV-induced radical polymerization, with varying counter ions (Li^+, Na^+, and K^+) and relative humidities under which the membranes were crosslinked (RH 100% and ambient). Here we use PFG NMR to measure water transport in these membranes.

4.4.1 Experimental

For diffusion measurements, the five crosslinked membranes, **A-K** (RH 100%), **A-K** (ambient), **A-Na** (RH 100%), **A-Na** (ambient) and **A-Li** (ambient) were immersed in water for 24 hours. After removing surface water rapidly and thoroughly using lint free wipes, each membrane was placed into a capillary of 1.8 mm O.D. × 1.5 mm I.D. and sealed to maintain

water content during NMR measurements. All PFG NMR diffusion measurements were obtained using a Bruker Avance III wide bore 400 MHz (9.4 T) NMR equipped with a Diff60 diffusion probe and a 2 mm ^{1}H solenoid coil. The pulsed-gradient stimulated echo (PGSTE) sequence was used to measure diffusion, with an effective gradient pulse length of $\delta = 2$ ms (the actual pulse length of the sinusoidal pulse was 3.2 ms), a 2 ms gradient stabilization time after each gradient pulse, a gradient pulse spacing of $\Delta = 50$ ms, and gradient strengths varying from g = 20 G/cm to g = 1600 G/cm. 16 to 24 gradient steps were applied, and the number of scans varied from 64 to 256 to yield sufficient signal-to-noise ratio (SNR). Diffusion was measured along the z-direction (static magnetic field direction). The self-diffusion coefficient *D* was obtained by fitting the measured signal intensity *I* as a function of gradient strength *g* to the Stejskal-Tanner equation Eq. 4.1. Errors in D are up to ± 10 % due to fitting of two diffusing components in some cases and slow diffusion in others.

4.4.2 Results and Discussion

Figure 4.11a shows the single-pulse standard spectrum (blue line) compared with a diffusion-weighted spectrum (red line) of the fully-hydrated **A-K** membrane crosslinked at ambient condition, which we denote **A-K**(ambient). The single-pulse spectrum shows the NMR response of all protons in the sample including the signals from crosslinked wedge molecules (broad peak) and signals from absorbed water (sharp peak). The single-pulse spectrum of dried membranes gives only proton signals from wedge molecules (spectrum not shown), the difference between the two spectra of hydrated and dried membranes yields only the water proton signal. Therefore we can obtain water uptake $\lambda(H_2O/SO_3^-)$ directly from the integration ratio of the water peak to the broad peak.

The diffusion-weighted spectrum only shows signals from nuclei with relaxation times long enough to survive the gradient encoding times (2×5.2 ms = 10.4 ms), when transverse relaxation (T_2) is active, and the 50 ms diffusion delay Δ, when longitudinal relaxation (T_1) is active. Therefore, using these diffusion measurements we can only detect the water signal (sharp peak), and we assume that the membrane matrix is immobile. Figure 4.11b shows a ^{1}H Stejskal-Tanner signal attenuation plot for the absorbed water of **A-K** (ambient). We clearly see two diffusion components, a faster component with $D = 1.7 \times 10^{-12}$ m^2/s and a much slower component with $D = 7.1 \times 10^{-14}$ m^2/s. We observe similar two-component diffusion for all five membranes, although with different observed diffusion rates for each membrane. As shown in Figure 4.11c, **A-K** (RH 100%) also exhibits two diffusion components, where the faster component is a factor of 10^2 faster than that of **A-K** (ambient), whereas the slower component is only a factor of 10^1 faster. Similar to our previous study on non-crosslinked **A-Na** salt, we attribute the two diffusion components to free water diffusing inside the ionic channels of the liquid crystalline region (fast component) and water diffusing through the amorphous regions (slow component) in the crosslinked membranes. The presence of the amorphous regions clearly reduces water transport rates in the membranes, although the water in the amorphous region is not a large fraction of the material in the fully hydrated membranes.

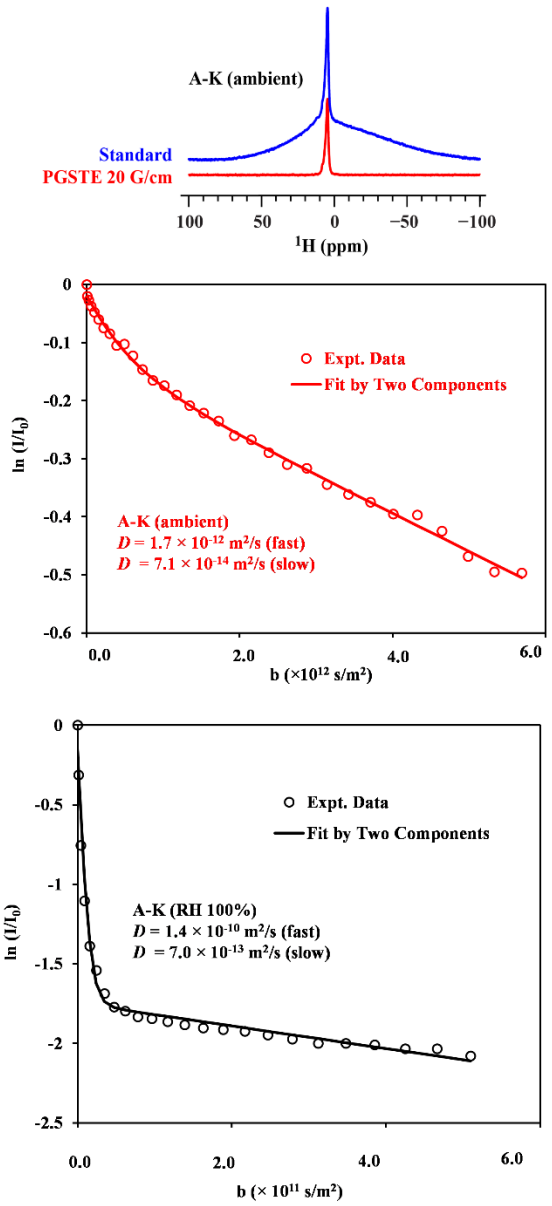

Figure 4.11 (a) Standard static NMR spectrum (blue) compared with a diffusion-weighted spectrum (red) of **A-K** (ambient). The broad peak originates from crosslinked wedge molecules and the sharp peak is from absorbed water. (b) Stejskal-Tanner signal attenuation plot of the absorbed water of **A-K** (ambient), showing fits to obtain two diffusion coefficients. (c) Stejskal-Tanner plot of water signal of **A-K** (RH 100%), again showing fits to obtain two

diffusion coefficients. The x-axis is the Stejskal-Tanner factor from Equation 1, $b = \gamma^2 g^2 \delta^2 (\Delta - \delta/3)$.

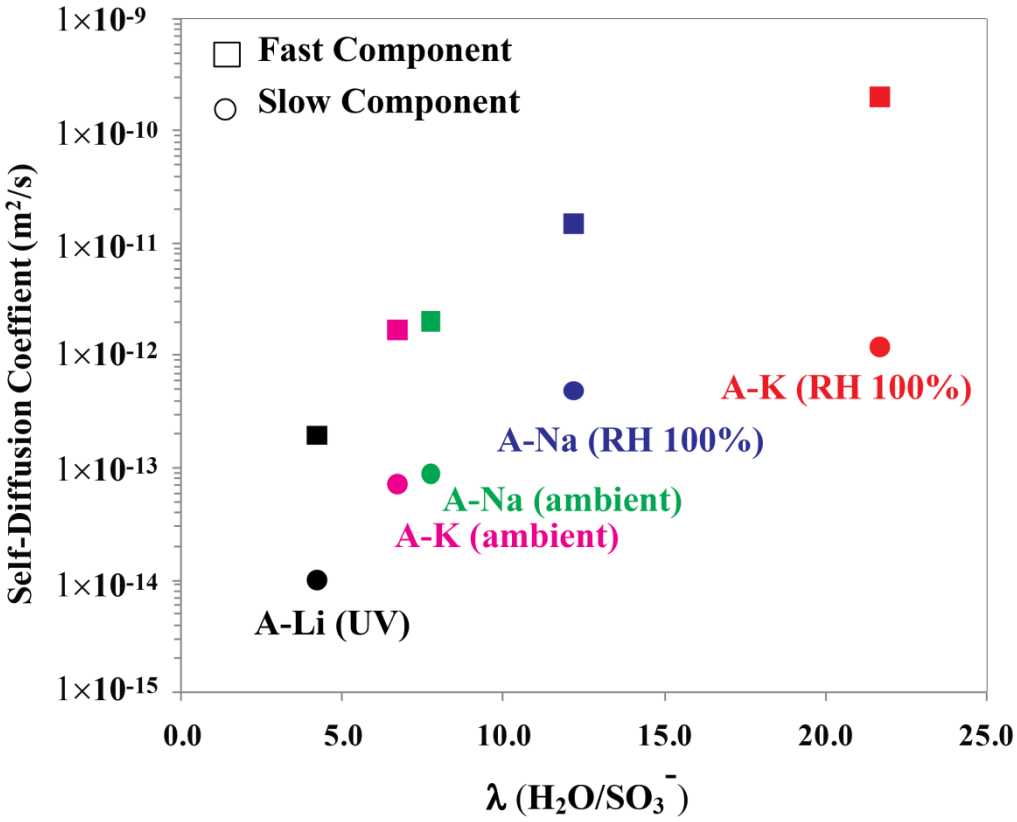

Figure 4.12 Diffusion coefficients of absorbed water vs. water uptake for the crosslinked membranes. Water uptake was calculated from the integration ratio of water proton signal and membrane proton signal. All ^{1}H NMR diffusion measurements show two components, which we attribute to water diffusing inside the ionic channels of the liquid crystalline region (fast) and water diffusing through the amorphous regions (slow) present in the membranes. Both the size of counterion and the relative humidity at which the membranes are crosslinked play a vital role in water uptake and diffusion

Figure 4.12 summarizes the diffusion and water uptake data for all five membranes. The measured diffusion coefficient D monotonically increases as water uptake increases. Clearly, the inclusion of larger counterions and crosslinking under higher RH produce fastest water transport in these membranes. More specifically, we see increased water uptake and diffusion rate for the membranes: 1) crosslinked at RH = 100% > crosslinked at ambient condition, and 2) **A-K** > **A-Na** > **A-Li**. As shown in our previous study,[59] the non-crosslinked **A-Na** salt undergoes a transition from columnar to bicontinuous cubic phases with increased RH, and the bicontinuous cubic phases are far superior for ion transport, especially at RH = 100%. This explains the much higher water uptake and faster water diffusion for the membranes crosslinked at RH 100% than those crosslinked at ambient RH. Compared to **A-Na** salt at RH 100%, where the diffusion coefficients are $D = 1.7 \times 10^{-10}$ m^2/s (fast) and $D = 4.2 \times 10^{-12}$ m^2/s (slow), the **A-Na**(RH 100%) membrane provides a factor of 10^1 slower diffusion components $D = 1.5 \times 10^{-11}$ m^2/s (fast) and $D = 5.3 \times 10^{-13}$ m^2/s (slow). This may be explained by shrinking of the ionic channels and amorphous regions during crosslinking, or introduction of some channel structural defects upon crosslinking. Additionally, we expect that larger counterions will produce larger ionic channels and thus increased free volume in the membranes, which may result in higher water uptake and faster water diffusion. We expect to increase diffusion coefficients further in these materials by casting them with larger counterions, such as tetramethylammonium or those used in ionic liquids (imidazolium and phosphonium derivatives). Notably, the faster diffusion component of the **A-K** (RH 100%) membrane reaches 1.4×10^{-10} m^2/s, comparable to that of Nafion and other ionic block copolymer materials at similar water uptakes.

4.5 **Conclusion**

We have presented a comprehensive picture of rich structural and ion transport behaviors in supramolecular assemblies formed by amphiphilic wedge molecules (**A-Na**). The synergistic combination of GISAXS and multi-modal NMR provides detailed structural and transport properties of a supramolecular material (Figure 4.13).

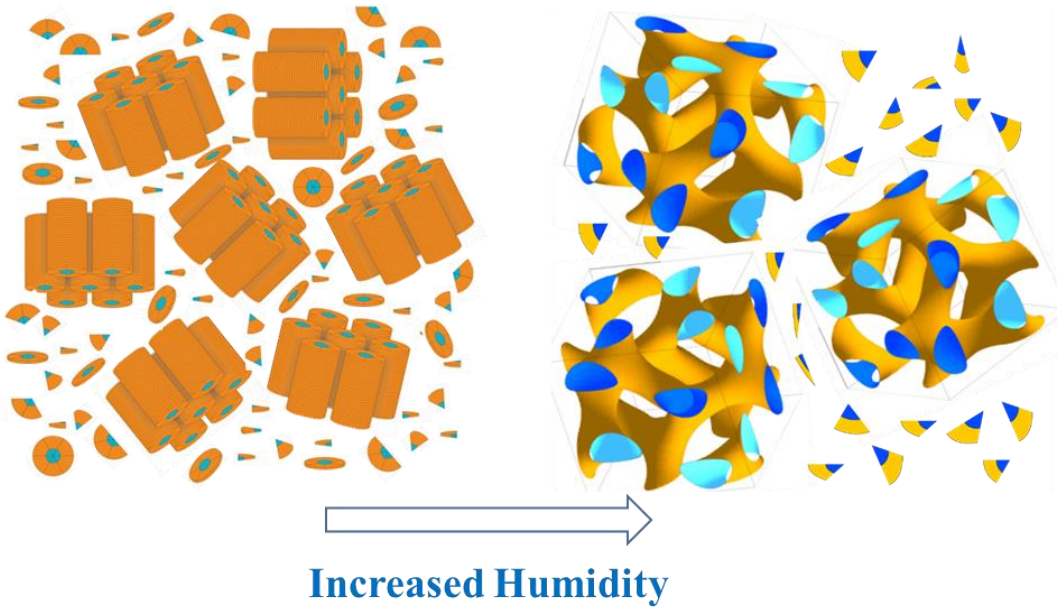

Figure 4.13 Schematic illustration of **A-Na** structural change with increased humidity.

A-Na undergoes a transition from columnar to bicontinuous cubic phases with a simple increase in humidity. GISAXS, ^{23}Na solid-state NMR, and pulsed-field-gradient diffusion NMR all clearly show that the self-assembled **A-Na** material undergoes this change of LC phase, accompanied by drastic increases in ionic mobility at RH $\geq$ 86%. GISAXS measurements describe the hexagonal disordered columnar phase at lower RH and a mixture of gyroid, diamond and lamellar phases at higher RH. In addition, the lattice parameters and the estimated size of the hydrophilic ion channels for each phase increase with relative

humidity; this change is small for the Col_{hd} and lamellar phases and larger for bicontinuous cubic phases. The semi-mesomorphic nature of **A-Na** was quantified with ^{23}Na MAS NMR studies, showing the presence of a significant fraction (~ 10%) of a disordered region at all RH values, which consists of amorphous domain boundary wedge molecules (with Na^+ counterions) that become nearly completely hydrated at RH ≥ 86%.

NMR diffusion studies on the amphiphiles (^1H) show that only amorphous wedges have relaxation times long enough to quantify with PGSTE measurements. We assign the slower PGSTE diffusion component (10^{-14} m^2/s) to individual wedges diffusing through LC phases and the faster component (10^{-12} m^2/s) to individual wedges diffusing within the amorphous boundaries between LC domains. The wedge molecules packed in LC phases are visible in PGSTE measurements only at high RH, but their very slow diffusion($< 10^{-15}$ m^2/s) is beyond our diffusion detection limit. Overall, the domain boundaries of a mesomorphic material must be considered when investigating dynamic properties of the material itself or when measuring the transport of small molecules in the material. In some circumstances, the domain boundaries may be the dominant contributor to an observed property ─ a fact that has received little attention in the literature to date. Similar observations have been made in organic ionic plastic crystals, where domain boundary diffusion can dominate macroscopically measured transport.[50-53] The presence of domain boundaries may also disrupt the continuity of LC domains and thereby reduce water transport and ion conductivity.

NMR diffusion studies on adsorbed water (^2H_2O) show that D_2O molecules are tightly associated to the relatively narrow ionic channels (15.0 Å) in columnar phases at low RH. Two-component D_2O diffusion is observed at higher RH values. We assign the slow diffusion (10^{-12} m^2/s) to D_2O molecules diffusing within domain boundaries. The additional fast

diffusion (10^{-10} m^2/s) obtained at high RH ($\lambda = 8.6$) is a result of relatively free water diffusing within the enlarged and interconnected ionic channels of the bicontinous cubic phases.

Finally, water diffusion (^1H_2O) in five stable membranes polymerized from the supramolecular assemblies shows two-component diffusion for all membranes. We attribute the fast component to free water diffusing inside the ionic channels of LC region and the slow component to water diffusing through the amorphous regions in the crosslinked membranes. The presence of the amorphous regions clearly reduces water transport rates in the membranes by breaking ordered (cubic) transport pathways. Furthermore, we find much higher water uptake and faster water diffusion for the membranes crosslinked at RH 100% than those crosslinked at ambient RH, which we attribute to the phase transition from columnar to bicontinuous cubic phases for the non-crosslinked salt. We also observe higher water uptake and faster diffusion for larger counterions with the order **A-K** > **A-Na** > **A-Li**, which we attribute to the larger ionic channels and thus increased free volume in the membranes with larger counterions. In addition, compared to **A-Na** salts, **A-Na** membranes produced 10-fold slower diffusion coefficients, which we hypothesize is due to shrinking of the ionic channels and amorphous regions during crosslinking, or introduction of some channel structural defects upon crosslinking.

Our combined NMR and GISAXS measurements show that the bicontinous cubic phase is able to facilitate much faster ion transport than the columnar phase, as shown by the channel dimensions from GISAXS and the fast D_2O diffusion of the 100% RH sample. Water diffusion coefficients measured in **A-Na** salt at high hydration and in **A-K** membrane crosslinked at high hydration fall in the range of those measured for benchmark ion conductors such as perfluorosulfonate ionomers at equivalent hydration.[48] These results shows promise

for controlled and informed design of next-generation ion conductors formed from tailored supramolecular building blocks.

4.6 Supporting Information

4.6.1 Conductivity and Water Uptake vs. Relative Humidity

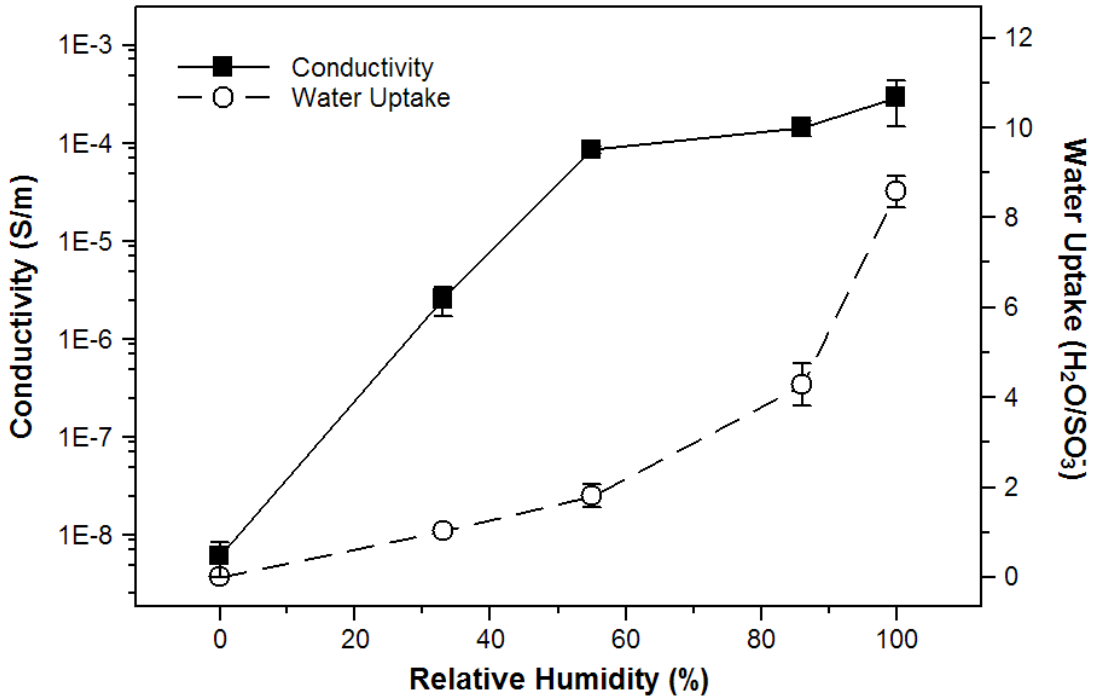

Figure S4.1 Conductivity and water uptake $\lambda(H_2O/SO_3^-)$ as a function of RH.

4.6.2 A-Na Channel Size Analysis

By analyzing the lattice parameters and **A-Na** molecular sizes, we can estimate the ion channel dimensions. For the columnar phase at RH = 55% the column diameter is 39.2 Å. Assuming equal density of ionic channels and hydrophobic periphery of the amphiphiles, the corresponding diameter the Col_{hd} hydrophilic ion channels equals approx. 15Å (cf. Figure 7). For the cubic phases, the lattice parameters together with water uptake values make it possible to estimate the ion channel diameter. For example, it is instructive to calculate the average channel diameter for the gyroid phase observed at RH = 100% with the total volume fraction of channels of 24.4% (from the weight fraction of the RH = 100% sample). For this simple calculation, consider that one unit cell of this phase includes 48 channels connecting the characteristic triple channel junctions (nodes). The total length of channels in one unit cell amounts to ca. 8.5×a. Therefore the average channel diameter in this case can be estimated to be 25.7Å. However, it is clear that this is a very simplified view of the real situation. In fact, it can be easily seen that the channel diameter is not constant: the channels are thinnest in between the nodes whereas the junctions are much bulkier. If one uses the conventional trigonometric expression for the gyroid surface, it is rather straightforward to generate the structure possessing the required fraction (i.e., 24.4%) of one of the phases. In the generated structure all the nodes are interconnected by the channels, which means that at this water concentration the channels are not pinched off (see the gyroid structure below the percolation threshold observed at 11.7%[33]). The analysis of the generated structure makes it possible to estimate the largest and smallest channel diameters. Given the non-circular shape of the channels, one can define the channel diameter from the inscribed circles, resulting in smallest and largest diameters of 25.0 and 40.8 Å, respectively.

4.6.3 NMR Relaxation studies

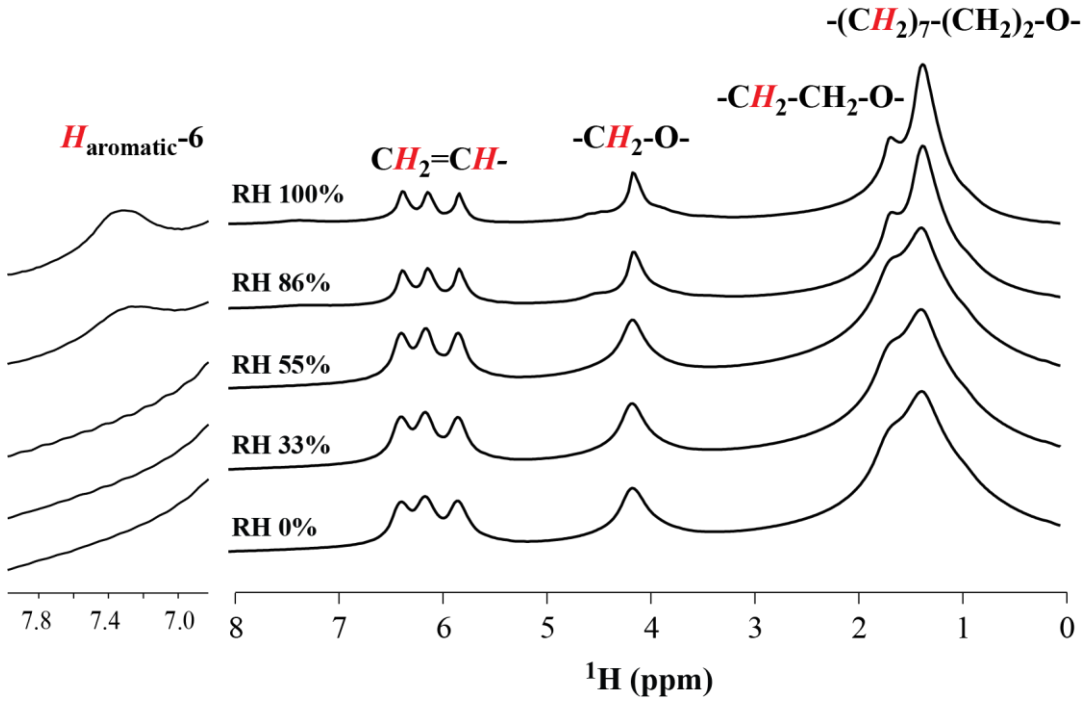

Figure S4.2 ^{1}H solid-state MAS NMR spectra at 10 kHz of the **A-Na** material at different RH. All protons show increased dynamics at higher RH.

We assign the ^{1}H resonances in Figure S4.2 as follows: the resonances between 1 and 2 ppm to the 54 methylene carbon protons, with the peak at 1.30 ppm to the 42 middle methylene protons and the shoulder at 1.63 ppm to 12 protons on the methylenes beta to oxygen. The peak centered at 4.05 ppm with two shoulders at 4.27 ppm and 3.82 ppm corresponds to the 12 protons on the methylenes alpha to oxygen, the resonances at 6.35, 6.12 and 5.82 ppm to the 9 chain-terminal acrylate protons, and the small shoulders at 7.38 ppm to the aromatic proton in the 6 position (**H**$_{aromatic}$-6). We notice **H**$_{aromatic}$-6 only appears with RH ≥ 86%, and **H**$_{aromatic}$-5 (around 6.8 ppm) is missing from all MAS spectra, which means the aromatic protons of the ionic head group are quite immobile even at high RH.

To investigate the structural heterogeneity of this sample, we measure the proton spin-lattice relaxation time (T_1), and spin-lattice relaxation time in the rotating frame ($T_{1\rho}$) as a

function of RH. T_1 is sensitive to fast motions in the MHz regime ($\tau_c \sim 10^{-9}$ to 10^{-10} s), such as single-bond rotations or trans-gauche chain isomerizations,[54-55] while $T_{1\rho}$ is sensitive to slow motions in the kHz regime ($\tau_c \sim 10^{-6}$ to 10^{-7} s), such as chain reorientations.[56-57] Here we obtain a single value for T_1 and $T_{1\rho}$ for the broad static spectrum (T_1 = 580 ms and $T_{1\rho}$ = 5 ms). Based on previous NMR studies on lipid multilayer structures,[58] our result suggests a spin diffusion process that enables all proton spins on molecules in the liquid crystalline phase to relax by a single mechanism. Since the ^{23}Na NMR spectra show that 90% of the material is present in the Col_{hd} phase, we can approximate that these T_1 and $T_{1\rho}$ values represent the T_1 and $T_{1\rho}$ values of the **A-Na** present in the liquid crystalline columnar phase. The presence of different proton T_1 and $T_{1\rho}$ values generally indicates no intimate spin contact or inefficient spin diffusion between different domains of the sample, where each domain or phase has a distinct proton T_1 and $T_{1\rho}$ value. Therefore we can use T_1 and $T_{1\rho}$ to give insight into the structural heterogeneity of this multi-component system. We also obtain T_1 and $T_{1\rho}$ values for the 45 ms T_2 component of the 1.3 ppm peak by adding a spin echo with τ = 2 ms to the regular pulse sequences, which removes the fast decaying signals and measures only the T_1 and $T_{1\rho}$ values that are associated with the long T_2 component. The significantly different relaxation times of this component (T_1 = 990 ms and $T_{1\rho}$ = 80 ms) imply that these protons do not reside in the LC structures, but are in a more mobile amorphous region or part of an individual wedge, as suggested by ^{23}Na MAS spectra. Similar results are seen for **A-Na** at RH = 33% and 55%. The relatively long T_2 at 1.3 ppm is caused by the faster mobility of methylene protons in the middle of the alkyl chains as compared to protons of aromatic head groups and acrylate end groups in individual wedge molecules.

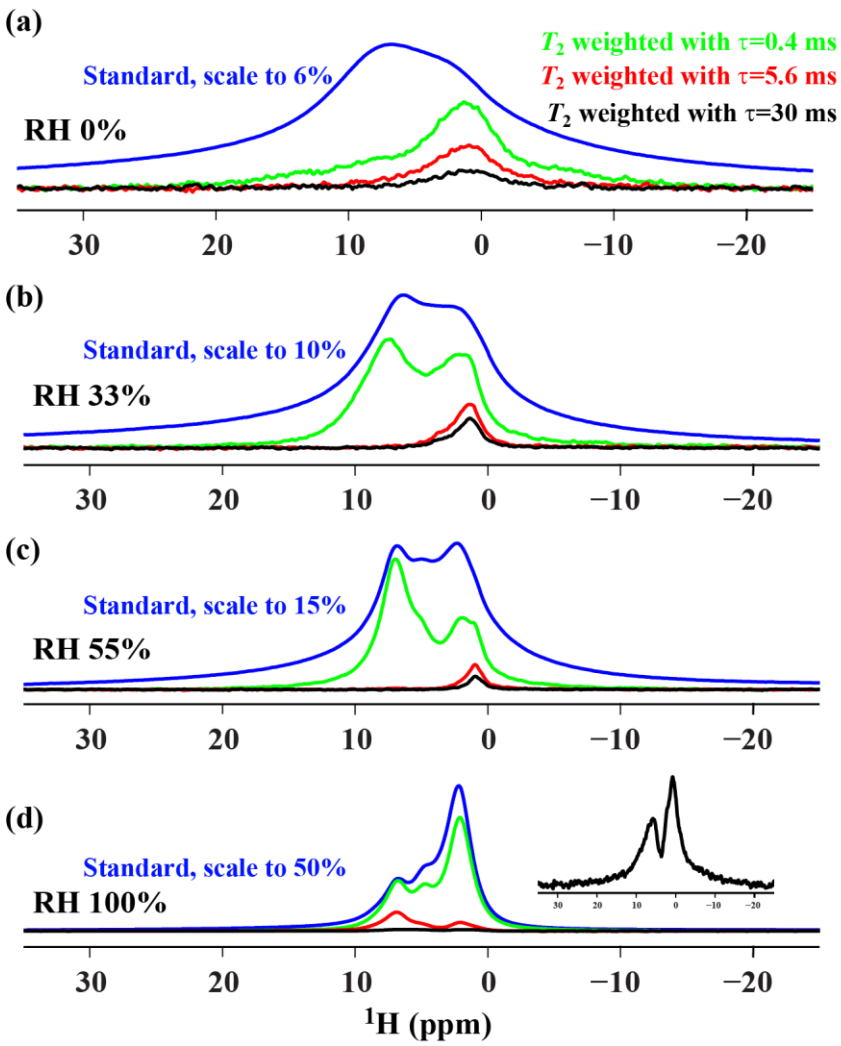

Figure S4.3 The standard static ^{1}H NMR spectrum of **A-Na** salt scaled to different percentages (blue, top of each set), stacked with **T_2**-weighted spectra with various spin echo delay times: τ=0.4 ms (green, second from top), 5.6 ms (red, second from bottom), and 30 ms (black bottom or inset) at different humidity conditions.

Measurements of the spin-spin (transverse) relaxation T_2 give insights into the populations of the heterogeneous sample that are observed by the PGSTE experiments. T_2-weighted spectra are shown in Figure S4.3. Since each diffusion NMR experiment contains two gradient encoding times, each with a duration of 5.2 ms (a 3.2 ms half sinusoid gradient

pulse followed by a 2 ms gradient stabilization time), the T_2-weighted spectra of figure S4.3 with $\tau = 5.6$ ms will appear similar to the diffusion-weighted spectra in Figure 4.7. At low RH values, only a small fraction of the signal survives the spin echoes with and echo delay $\tau = 5.6$ ms. As discussed in the previous paragraph, this long T_2 component is assigned to protons in the amorphous domain boundaries or on individual wedges diffusing independently within liquid crystalline domains. Therefore, the diffusion results at low RH presented in the main paper show only the proton signals of individual wedges. At higher RH, we notice a significant increase in proton signals centered at 6.1 ppm comparing T_2-weighted spectra with $\tau = 5.6$ ms (red lines of Figure S4.3) from RH 0% to 100%. This increase in signal is explained by the increased mobility of the end of the hydrocarbon chain relative to the aromatic head group, an effect that has been previously observed in liquid crystalline phases of amphiphiles.[58] The sharp change between RH 55% and 100% may be explained by the phase transition from the columnar phase to the bicontinuous cubic phase where wedge molecules are not as well-packed and the ionic channels are more interconnected, which can produce more rotational and translational freedom for wedge molecules. We assign the T_2-weighted signal at 6.1 ppm to a combination of signal from both individual wedge molecules and wedge molecules in the LC phases, due to the dramatically increased intensity of the T_2-weighted peak at 6.1 ppm when it appears at high RH (this is shown in Figure S4.3d by scaling the standard 1D spectrum to 50% of its original height). Therefore, the PGSTE diffusion experiments at high RH will observe the diffusion of both individual wedges and wedges packed in the LC phase, especially for the resonance at 6.1 ppm. The fact that the diffusion of LC wedges is only visible at 6.1 ppm and not 1.3 ppm is likely a coincidence, due to the T_2 values of the LC acrylate protons being just long enough to observe with PGSTE while the remaining protons of LC molecules have T_2

values too short to observe with achievable PGSTE pulse sequence parameters. We expect that increasing the mobility of the LC molecules, either by increasing water absorption or altering the molecular structure, will allow NMR diffusion measurements of all components at all chemical shift values.

References

(1) Lehn, J.-M., *Supramolecular Chemistry: Concepts and Perspectives*. Wiley-VCH Verlag GmbH & Co. KGaA: Weinheim, FRG, 1995.

(2) Nakanishi, T., *Supramolecular Soft Matter: Applications in Materials and Organic Electronics*. John Wiley & Sons, Inc.: Hoboken, New Jersey, 2012.

(3) Dong, B.; Sakurai, T.; Honsho, Y.; Seki, S.; Maeda, H. Cation Modules as Building Blocks Forming Supramolecular Assemblies with Planar Receptor–Anion Complexes. *J. Am. Chem. Soc.* **2013,** *135*, 1284-1287.

(4) Ye, X.; Chen, J.; Engel, M.; Millan, J. A.; Li, W.; Qi, L.; Xing, G.; Collins, J. E.; Kagan, C. R.; Li, J.; Glotzer, S. C.; Murray, C. B. Competition of Shape and Interaction Patchiness for Self-Assembling Nanoplates. *Nat Chem* **2013,** *5*, 466-473.

(5) Kato, T.; Mizoshita, N.; Kishimoto, K. Functional Liquid-Crystalline Assemblies: Self-Organized Soft Materials. *Angew. Chem. Int. Ed.* **2006,** *45*, 38-68.

(6) Yasuda, T.; Kato, T., Advanced Systems of Supramolecular Liquid Crystals. In *Supramolecular Soft Matter*, John Wiley & Sons, Inc.: 2011; pp 281-299.

(7) Park, M. J.; Balsara, N. P. Anisotropic Proton Conduction in Aligned Block Copolymer Electrolyte Membranes at Equilibrium with Humid Air. *Macromolecules* **2010,** *43*, 292-298.

(8) Yuan, R.; Teran, A. A.; Gurevitch, I.; Mullin, S. A.; Wanakule, N. S.; Balsara, N. P. Ionic Conductivity of Low Molecular Weight Block Copolymer Electrolytes. *Macromolecules* **2013,** *46*, 914-921.

(9) O'Neill, M.; Kelly, S. M. Liquid Crystals for Charge Transport, Luminescence, and Photonics. *Adv. Mater.* **2003,** *15*, 1135-1146.

(10) Kishimoto, K.; Yoshio, M.; Mukai, T.; Yoshizawa, M.; Ohno, H.; Kato, T. Nanostructured Anisotropic Ion-Conductive Films. *J. Am. Chem. Soc.* **2003,** *125*, 3196-3197.

(11) Yoshio, M.; Mukai, T.; Ohno, H.; Kato, T. One-Dimensional Ion Transport in Self-Organized Columnar Ionic Liquids. *J. Am. Chem. Soc.* **2004,** *126*, 994-995.

(12) Shimura, H.; Yoshio, M.; Hoshino, K.; Mukai, T.; Ohno, H.; Kato, T. Noncovalent Approach to One-Dimensional Ion Conductors: Enhancement of Ionic Conductivities in Nanostructured Columnar Liquid Crystals. *J. Am. Chem. Soc.* **2008,** *130*, 1759-1765.

(13) Ichikawa, T.; Yoshio, M.; Hamasaki, A.; Kagimoto, J.; Ohno, H.; Kato, T. 3d Interconnected Ionic Nano-Channels Formed in Polymer Films: Self-Organization and Polymerization of Thermotropic Bicontinuous Cubic Liquid Crystals. *J. Am. Chem. Soc.* **2011,** *133*, 2163-2169.

(14) Yeh, M.-C.; Su, Y.-L.; Tzeng, M.-C.; Ong, C. W.; Kajitani, T.; Enozawa, H.; Takata, M.; Koizumi, Y.; Saeki, A.; Seki, S.; Fukushima, T. Amphiphilic Design of a Discotic Liquid-Crystalline Molecule for Dipole Manipulation: Hierarchical Columnar Assemblies with a 2d Superlattice Structure. *Angew. Chem. Int. Ed.* **2013,** *52*, 1031-1034.

(15) Zhang, H.; Li, L.; Möller, M.; Zhu, X.; Rueda, J. J. H.; Rosenthal, M.; Ivanov, D. A. From Channel-Forming Ionic Liquid Crystals Exhibiting Humidity-Induced Phase Transitions to Nanostructured Ion-Conducting Polymer Membranes. *Adv. Mater.* **2013,** *25*, 3543-3548.

(16) Rueda, D. R. N., A.; Hernández, J. J.; García-Gutiérrez, M.-C.; Ezquerra, T. A.; Roth, S. V.; Zolotukhin, M. G.; Serna, R. Stacking of Main Chain-Crown Ether Polymers in Thin Films. *Langmuir* **2007,** *23*, 12677-12681.
(17) Müller-Buschbaum, P. Grazing Incidence Small-Angle X-Ray Scattering: An Advanced Scattering Technique for the Investigation of Nanostructured Polymer Films. *Analytical and Bioanalytical Chemistry* **2003,** *376*, 3-11.
(18) Lee, B. P., I.; Yoon, J.; Park, S.; Kim, J.; Kim, K.-W.; Chang, T.; Ree, M. . Structural Analysis of Block Copolymer Thin Films with Grazing Incidence Small-Angle X-Ray Scattering. *Macromolecules* **2005,** *38*, 4311-4323.
(19) Young, J. F. Humidity Control in the Laboratory Using Salt Solutions—a Review. *Journal of Applied Chemistry* **1967,** *17*, 241-245.
(20) Fogden, A. H., S. T. . Continuous Transformations of Cubic Minimal Surfaces. *Eur. Phys. J. B* **1999,** *7*, 91-104.
(21) Earl, W. L.; Vanderhart, D. L. Measurement of 13c Chemical Shifts in Solids. *Journal of Magnetic Resonance (1969)* **1982,** *48*, 35-54.
(22) Morcombe, C. R.; Zilm, K. W. Chemical Shift Referencing in Mas Solid State NMR. *Journal of Magnetic Resonance* **2003,** *162*, 479-486.
(23) Tanner, J. E. Use of the Stimulated Echo in NMR Diffusion Studies. *J. Chem. Phys.* **1970,** *52*, 2523-2526.
(24) Stejskal, E. O.; Tanner, J. E. Spin Diffusion Measurements: Spin Echoes in the Presence of a Time-Dependent Field Gradient. *J. Chem. Phys.* **1965,** *42*, 288-292.
(25) Rancon, Y. C., J. . Epitaxial Relatlonships During Phase Transformations in a Lyotropic Liquid Crystal. *J. Phys. Chem.* **1988,** *92*, 2646-2651.
(26) Renaud, G. L., R.; Leroy, F. Probing Surface and Interface Morphology with Grazing Incidence Small Angle X-Ray Scattering. *Surf. Sci. Rep.* **2009,** *64*, 255-381.
(27) Chvalun, S. N. S., M. A.; Bykova, V.; Blackwell, J.; Percec, V. . Two- and Three-Dimensional Mesophases Formed by Monodendrons Based on Gallic Acid with Partially Fluorinated Alkyl Tails. *J. Polym. Sci. Ser. A* **2002,** *44*, 1281-1289.
(28) Squires, A. M. T., R. H.; Seddon, J. M.; Woenkhaus, J.; Winter, R.; Narayanan, T.; Finet, S. . Kinetics and Mechanism of the Interconversion of Inverse Bicontinuous Cubic Mesophases. *Physical Review E* **2005,** *72*, 011502-011517.
(29) Seddon, J. M. T., R. H., *Polymorphism of Lipid-Water Systems. In Handbook of Biological Physics*. Elsevier Science B.V.: 1995; Vol. 1.
(30) Seddon, J. M.; Templer, R. H., Chapter 3 Polymorphism of Lipid-Water Systems. In *Handbook of Biological Physics*, Lipowsky, R.; Sackmann, E., Eds. North-Holland: 1995; Vol. Volume 1, pp 97-160.
(31) Schwarz, U. S.; Gompper, G. Stability of Inverse Bicontinuous Cubic Phases in Lipid-Water Mixtures. *Physical Review Letters* **2000,** *85*, 1472-1475.
(32) Schwarz, U. S. G., G. . Stability of Inverse Bicontinuous Cubic Phases in Lipid-Water Mixtures. *Phys. Rev. Lett.* **2000,** *85*, 1472-1475.

(33) Shearman, G. C.; Khoo, B. J.; Motherwell, M.-L.; Brakke, K. A.; Ces, O.; Conn, C. E.; Seddon, J. M.; Templer, R. H. Calculations of and Evidence for Chain Packing Stress in Inverse Lyotropic Bicontinuous Cubic Phases. *Langmuir* **2007,** *23*, 7276-7285.
(34) Orler, E. B.; Gummaraju, R. V.; Calhoun, B. H.; Moore, R. B. Effect of Preferential Plasticization on the Crystallization of Lightly Sulfonated Syndiotactic Polystyrene Ionomers. *Macromolecules* **1999,** *32*, 1180-1188.
(35) Kotecha, M.; Chaudhuri, S.; Grey, C. P.; Frydman, L. Dynamic Effects in Mas and Mqmas NMR Spectra of Half-Integer Quadrupolar Nuclei: Calculations and an Application to the Double Perovskite Cryolite. *J. Am. Chem. Soc.* **2005,** *127*, 16701-16712.
(36) Jia, Y.; Kleinhammes, A.; Wu, Y. NMR Study of Structure and Dynamics of Ionic Multiplets in Ethylene−Methacrylic Acid Ionomers. *Macromolecules* **2005,** *38*, 2781-2785.
(37) Yamamoto, Y.; Murakami, M.; Ikeda, R.; Deguchi, K.; Tansho, M.; Shimizu, T. The Local Structure around Sodium Ions in Poly(Ethylene-Ran-Methacrylic Acid) Ionomers Studied by 23na Solid-State NMR under a High Magnetic Field, 21.9 T. *Chem. Lett.* **2006,** *35*, 1058-1059.
(38) Lim, J. S.; Lee, Y.; Im, S. S. Influence of Ionic Association on the Nonisothermal Crystallization Kinetics of Sodium Sulfonate Poly(Butylene Succinate) Ionomers. *J. Polym. Sci., Part B: Polym. Phys.* **2008,** *46*, 925-937.
(39) Jerschow, A. From Nuclear Structure to the Quadrupolar NMR Interaction and High-Resolution Spectroscopy. *Prog. Nucl. Magn. Reson. Spectrosc.* **2005,** *46*, 63-78.
(40) van Beek, J. D. Matnmr: A Flexible Toolbox for Processing, Analyzing and Visualizing Magnetic Resonance Data in Matlab®. *Journal of Magnetic Resonance* **2007,** *187*, 19-26.
(41) Oconnell, E. M.; Root, T. W.; Cooper, S. L. Morphological-Studies of Lightly-Sulfonated Polystyrene Using Na-23 NMR .1. Effects of Sample Composition. *Macromolecules* **1994,** *27*, 5803-5810.
(42) Oconnell, E. M.; Root, T. W.; Cooper, S. L. Morphological-Studies of Lightly Sulfonated Polystyrene Using Na-23 NMR .2. Effects of Solution Casting. *Macromolecules* **1995,** *28*, 3995-3999.
(43) Oconnell, E. M.; Root, T. W.; Cooper, S. L. Morphological-Studies of Lightly Sulfonated Polystyrene Using Na-23 NMR .3. Effects of Humidification and Annealing. *Macromolecules* **1995,** *28*, 4000-4006.
(44) OConnell, E. M.; Peiffer, D. G.; Root, T. W.; Cooper, S. L. Morphological Studies of Lightly Sulfonated Polystyrene Using Na-23 NMR: Effects of Polydispersity in Molecular Weight. *Macromolecules* **1996,** *29*, 2124-2130.
(45) Komoroski, R. A.; Mauritz, K. A. Na-23 Nuclear Magnetic-Resonance Study of Ionic Mobility and Contact Ion-Pairing in a Perfluorosulfonate Ionomer. *J. Am. Chem. Soc.* **1978,** *100*, 7487-7489.
(46) Callaghan, P. T., *Translational Dynamics & Magnetic Resonance: Principles of Pulsed Gradient Spin Echo NMR*. Oxford University Press Inc.: New York, 2011.

(47) Hou, J.; Li, J.; Mountz, D.; Hull, M.; Madsen, L. A. Correlating Morphology, Proton Conductivity, and Water Transport in Polyelectrolyte-Fluoropolymer Blend Membranes. *Journal of Membrane Science* **2013,** *448*, 292-299.
(48) Li, J.; Park, J. K.; Moore, R. B.; Madsen, L. A. Linear Coupling of Alignment with Transport in a Polymer Electrolyte Membrane. *Nature Materials* **2011,** *10*, 507-511.
(49) Holz, M.; Weingartner, H. Calibration in Accurate Spin-Echo Self-Diffusion Measurements Using 1h and Less-Common Nuclei. *Journal of Magnetic Resonance (1969)* **1991,** *92*, 115-125.
(50) Shekibi, Y.; Pas, S. J.; Rocher, N. M.; Clare, B. R.; Hill, A. J.; MacFarlane, D. R.; Forsyth, M. Surprising Effect of Nanoparticle Inclusion on Ion Conductivity in a Lithium Doped Organic Ionic Plastic Crystal. *J. Mater. Chem.* **2009,** *19*, 1635-1642.
(51) Jin, L.; Nairn, K. M.; Forsyth, C. M.; Seeber, A. J.; MacFarlane, D. R.; Howlett, P. C.; Forsyth, M.; Pringle, J. M. Structure and Transport Properties of a Plastic Crystal Ion Conductor: Diethyl(Methyl)(Isobutyl)Phosphonium Hexafluorophosphate. *J. Am. Chem. Soc.* **2012,** *134*, 9688-9697.
(52) Pringle, J. M.; Howlett, P. C.; MacFarlane, D. R.; Forsyth, M. Organic Ionic Plastic Crystals: Recent Advances. *J. Mater. Chem.* **2010,** *20*, 2056-2062.
(53) Kidd, B. E.; Lingwood, M. D.; Lee, M.; Gibson, H. W.; Madsen, L. A. Cation and Anion Transport in a Dicationic Imidazolium-Based Plastic Crystal Ion Conductor. *The Journal of Physical Chemistry B* **2014**.
(54) Dong, R. Y., *Nuclear Magnetic Resonance of Liquid Crystals*. Springer: 1997.
(55) James, T. L., *Nuclear Magnetic Resonance in Biochemistry: Principles and Applications*. Academic Press: 1975.
(56) Klaus Schmidt-Rohr, H. W. S., *Multidimensional Solid-State NMR and Polymers*. Academic Press: San Diego, 1994.
(57) Frank A. Bovey, P. A. M., *NMR of Polymers* Academic Press: San Diego, 1996.
(58) Bocian, D. F.; Chan, S. I. NMR Studies of Membrane Structure and Dynamics. *Annu. Rev. Phys. Chem.* **1978,** *29*, 307-335.
(59) Chen, Y.; Lingwood, M. D.; Goswami, M.; Kidd, B. E.; Hernandez, J. J.; Rosenthal, M.; Ivanov, D. A.; Perlich, J.; Zhang, H.; Zhu, X.; Möller, M.; Madsen, L. A. Humidity-Modulated Phase Control and Nanoscopic Transport in Supramolecular Assemblies. *The Journal of Physical Chemistry B* **2014,** *118*, 3207-3217.

Chapter 5

Diffusion of Drug Delivery Nanoparticles into Biogels Using Time-Resolved MicroMRI

This chapter is adapted and reprinted from the following reference: Xiaoling Wang[*], Ying Chen[*], Lian Xue, Nipon Pothyaee, Rui Zhang, Judy S. Riffle, Theresa M. Reineke and Louis A. Madsen (*contributed equally). *J. Phys. Chem. Lett.* **2014**, *5,* 3825 © 2014, American Chemical Society.

5.1 Introduction

Delivery of small molecules and nanoparticles into cancer cells involves a three step pharmacokinetic process: vascular transport, transvascular transport and interstitial transport.[1-3] These principle steps are relatively efficient for normal tissues, whereas the abnormal physiology of tumors causes transport barriers to the adequate delivery of therapeutic agents to tumors. Specifically, elevated interstitial fluid pressure reduces convective mass transport and hence leaves diffusion as the main mechanism of transport into tumors.[4-6] Moreover, the tumor interstitium hinders diffusion as a result of the dense viscoelastic fiber matrix consisting of collagen and interacting molecules.[7-9] The diffusion rate of a nanoparticle in tumor interstitium correlates with its size, charge, configuration, as well as the content and structure of collagen fibers.[10-14] One advantage of nanoscale therapeutic agents is that they provide potential selective delivery to tumors due to the enhanced permeability and retention (EPR) effect. On the other hand, diffusion of large particles through tumor tissue is decreased due to particle interactions with the interstitial matrix. Therefore optimization of nanoparticle size and surface features (such as charge) for different tumor microenvironments is crucial for sufficient interstitial transport. Fluorescence microscopy techniques such as fluorescence recovery after

photobleaching (FRAP) have been used to study transport of nanoparticles in interstitial matrix as well as tumor-mimetic gels.[12, 15-18] However, these methods are restricted to measurements of diffusion on the sub-mm scale, e.g., into thin gels and into tumor surfaces with limited depth penetration even with the aid of spatial Fourier analysis and multiphoton techniques.[12, 19] Magnetic resonance spectroscopy (MRS) and imaging (MRI) approaches, which are not restricted by material thickness, have been applied for investigating *in vivo* water perfusion,[20] and in recent years time-resolved MRI has been employed in quantitative analysis of blood flow with three dimensional spatial resolution.[21-22] Recent studies report the use of MRI to quantify convective transport of macromolecular contrast agents in hydrogels and tumor tissues.[23-24] Nevertheless, characterization of diffusion-driven nanoparticle transport using time-resolved MRI has not been reported, and a reliable quantitative assessment of three-dimensional diffusion for polymeric nanomaterials is lacking.

In this letter, we describe a non-invasive method for accurate quantitation of diffusion of polymer-based contrast and drug delivery agents, known as theranostic agents, into tumor-tissue-mimetic hydrogels *via* time-resolved MRI. This approach provides three dimensional diffusion rate and concentration distribution of nanoparticles over macroscopic (mm to cm) distances in biological transport media. We examined diffusion of a theranostic polymeric gene-delivery vehicle[25-26] and a block-copolymer-functionalized magnetite drug delivery vector[27-29] into 0.5-2.0 wt.% agarose and into 0.2-1.0 wt.% collagen type I gels. The first theranostic vehicle (Figure 5.1a) incorporates a paramagnetic gadolinium chelate and oligoethyeneamines, so that it offers both transverse and longitudinal relaxivity contrast, as well as the ability to bind and compact nucleic acids for gene delivery.[25] The second vector (shown in Figure 5.1b) is a magnetic block ionomer complex (MBIC) comprised of 8-nm

diameter magnetite nanoparticles in the core surrounded by a double corona structure with a nonionic polyethylene oxide (PEO) shell and anions are bound to nanomagnetite *via* ligand absorption. The unbound negatively charged carboxylates provide binding sites for drug loading through ionic complexation.[28] The superparamagnetic Fe_3O_4 particle core provides primarily transverse relaxivity contrast. Figure 5.1c and 5.1d show the vector nanoparticle size distributions measured by dynamic light scattering (DLS). We also included a clinical contrast agent of sub-nm size, gadopentetic acid (marketed as Magnevist®), for comparative analysis of diffusion into hydrogels.

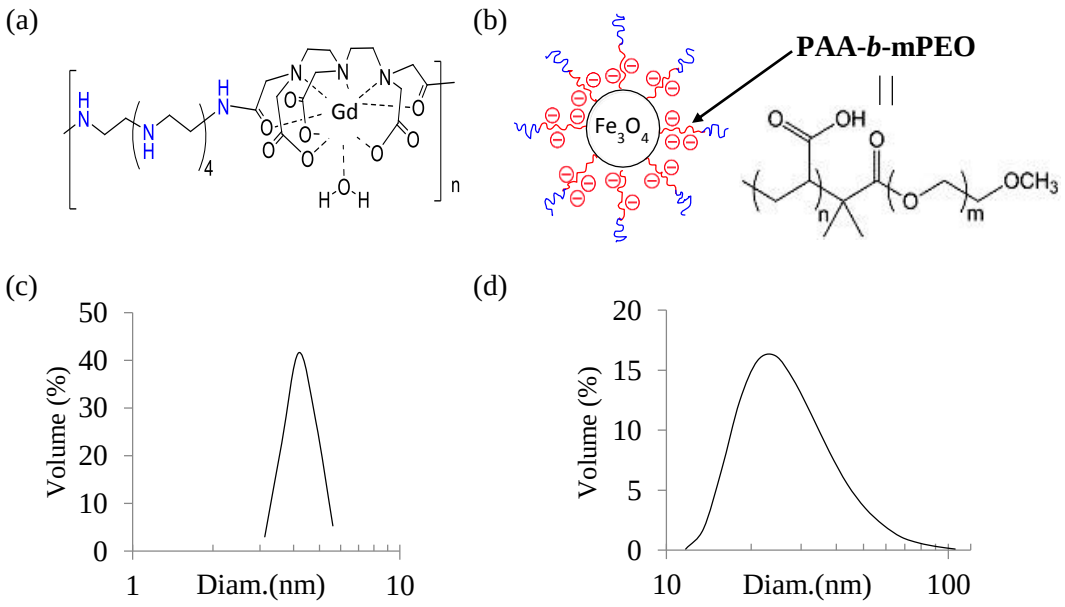

Figure 5.1 Structure of N_4Gd (a) and MBIC (b), as well as DLS size distribution of N_4Gd (c) and MBIC (d).

5.2 Experimental Section

MRI experiments were performed on a Bruker Avance III 400 spectrometer equipped

with a Micro5 imaging probe featuring 5 cm rf coil. Experiments in agarose gels were carried at 25 ℃ and the temperature for experiments in collagen gels were done at 37 ℃. Experimental data were acquired and processed using ParaVision 5.0 (Bruker Biospin, Germany). Data analysis was done with MATLAB R2012a.

For T_2-*weighted* experiments, acquisition parameters for *RARE* pulse sequence are as follows: *TR* (repetition time): 16000 to 20000 msec depending on the T_1 relaxation time of pure hydrogels; *TE* (echo time): 50 to 100 msec depending on the concentration and relaxivities of contrast agent solutions; *FOV*: 1.00 cm; slice thickness: 1.00 mm; and resolution: 0.0078 cm/pixel.

For the T_1-*null-weighted* experiments, in Inversion Recovery (IR) *RARE* pulse sequence, the null time is calculated by

$$t_{null} = T_1 \left[\ln 2 - \ln \left(1 + e^{-\frac{TR-TE}{T_1}} \right) \right] \tag{5.1}$$

Taking acquisition parameters in N_4Gd in 0.5 wt.% agarose gel, for example, *TR*: 2000 msec, *TE*: 8.1 msec, and T_1 in doped gel of reference N_4Gd concentration: 395 msec, hence t_{null} is 271 msec from Equation 5.1. T_1 relaxation time is measured using an inversion recovery NMR pulse sequence.

Inversion time was also determined by running the doped reference gel sample using IR *RARE* MRI pulse sequence and adjusting t_{null} around 271 msec to until lowest signal intensity is observed. t_{null} was set to 280 msec, and the discrepancy between this actual parameter and theoretical calculated value is about 3 %.

Agarose powder was purchased from Sigma-Aldrich. Collagen I, Rat Tail was purchased form Life Technology. Agarose gels were prepared by dispersing agarose powder in water followed by heating solutions of desired concentrations to boil and cooled down in 5

mm NMR tubes at room temperature overnight to allow complete gelation. Collagen gels of low concentration were prepared in phosphate buffered saline (PBS) and left gelling in NMR tubes at pH 7.4 and 37 ℃. The collagen solution was ultracentrifuged at 10 ℃ for 48 hours before use for concentrated gels, and the concentration was determined from volume difference between precentrifugation and supernatant collagen solutions. Preparations were conducted in sterilized environments.

5.3 Results and Discussion

In MR images, contrast is mainly determined by the proton longitudinal relaxation time (T_1) and transverse relaxation time (T_2). MRI contrast agents containing paramagnetic or superparamagnetic centers have the ability to reduce T_1 and T_2 of their surroundings. In a T_1-*weighted* image, shortened T_1 results in positive image contrast (higher signal intensity); while in a T_2-*weighted* image, regions of shortened T_2 show negative contrast and appear darker. Additionally, using a suitable MRI pulse sequence, a null time t_{null} can be determined in which no signal appears in the image due to T_1 relaxation. Thus we can employ a T_1-*null-weighted* image based on the correlation between a chosen concentration of contrast agent solution and its corresponding null point (when $t_{null} \approx \ln 2T_1$) which show near-zero intensity. Hence T_1 null points can be directly encoded into and observed in images as a darkened band or region.

Generally, interference between T_1 and T_2 relaxation processes introduces significant inaccuracy in the determination of the relationship between contrast agent concentration and voxel signal intensity. In common T_1-weighted imaging method for clinical application, the effect of T_2 relaxation cannot be avoided or effectively minimized by manipulating experiment parameters. Moreover, frequently used T_2-weighted imaging of scan repetition time smaller than $5T_1$ can bring serious inaccuracy to the concentration profiles converted from T_2-weighted

images, due to the influence of T_1 relaxation. Thus, we have developed an approach combining time-resolved T_2-*weighted* and T_1-*null-weighted* imaging methods for the accurate quantitative analysis of diffusive transport, and implemented this comprehensive approach to novel polymeric nanoparticles designed for drug deliver for the validation of our methodology. Figure 5.2 shows an illustration of the sample setup and the mathematical model for theranostic vehicle diffusion into hydrogels. In contrast to commonly used T_1-*weighted* images, both of our methods minimize the interference of T_1 and T_2 relaxation on image signal intensity, and consequently ensure the accuracy of diffusion rates determined from time-resolved MRI experiments. T_2-*weighted* images were acquired using the rapid acquisition with relaxation enhancement (*RARE*) sequence[30] with minimized T_1-*weighting* effects by applying adequate repetition time (>$5T_1$). The relationship between voxel signal intensity and concentration is expressed in Equation 5.2, where $S(c_t)$ and $S(c_0)$ are signal intensities at concentrations c_t and c_0 of the diffusing molecule, r_2 is the transverse relaxivity of paramagnetic/superparamagnetic species in the medium, and *TE* is the echo time in the MRI pulse sequence.[31-32]

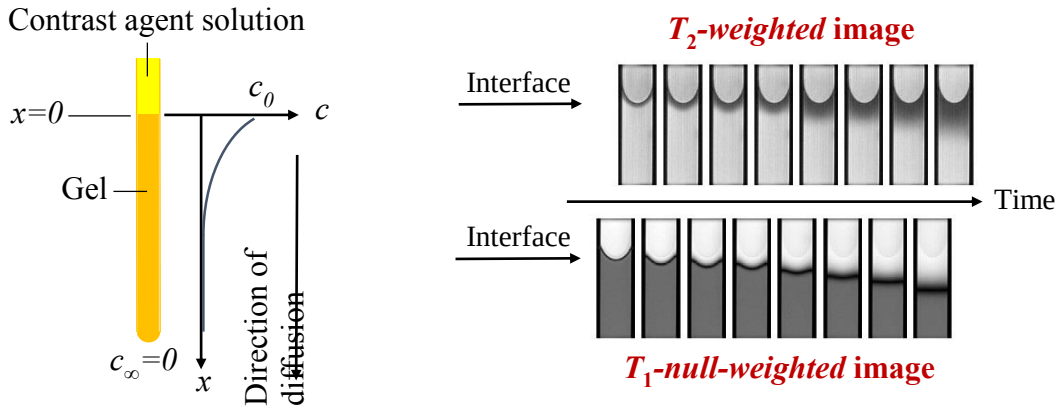

Figure 5.2 Sample setup for MRI measurements and model for one-dimensional diffusion (left), and time-resolved T_2-*weighted* and T_1-*null-weighted* images (right) of N_4Gd diffusing into 0.5 wt.% agarose gel. White-to-black scale represents decreasing signal intensity.

T_1-null-weighted[33] images were obtained using the *RARE* inversion-recovery pulse sequence,[34] yielding a direct measure of nanoparticle concentration over centimeter-scale depth in bulk biogels. The value of t_{null} was determined by testing T_1 of a gel sample doped with a known reference concentration. By setting the inversion time equal to t_{null} in the MRI pulse sequence, the migration of voxels of near-zero signal intensity in time-resolved images then represents the movement of this reference concentration, indicating the diffusion of contrast agent into the gels. Time-resolved *T_2-weighted* and *T_1-null-weighted* images are shown in Figure 5.2.

$$\boldsymbol{c(x,t) = c_0 - \frac{\ln \frac{S(c_t)}{S(c_0)}}{TE \cdot r_2}} \qquad (\mathbf{5.2})$$

$$\boldsymbol{\frac{c(x,t)}{c_0} = \mathrm{erfc}\left(\frac{x - x_0}{2\sqrt{Dt}}\right)} \qquad (\mathbf{5.3})$$

$$\boldsymbol{P(D) = \frac{1}{D\sigma\sqrt{2\pi}} \exp\left(-\frac{\left(\ln(D) - \ln(D_0)\right)^2}{2\sigma^2}\right)} \qquad (\mathbf{5.4})$$

$$\boldsymbol{c(x,t) = \int_0^\infty P(D) c_0 \mathrm{erfc}\left(\frac{x - x_0}{2\sqrt{Dt}}\right) dD} \qquad (\mathbf{5.5})$$

To determine diffusion coefficients (*D*) of polymeric agents through gels *via* *T_2-weighted* MRI, we convert signal intensity to concentration using Equation 5.2. By acquiring images at different time points, we map the variation of concentration as a function of position and time, *c(x, t)* and then fit using Equation 5.3 to extract *D*.

Furthermore, by inserting the lognormal distribution given by Equation 5.4 into Equation 5.3, Equation 5.5 allows us to probe distributions of diffusion coefficients. For comparison, we extracted *D* from *T_2-weighted* images both with and without the use of a distribution. Figure 5.3 shows fitted curves of N_4Gd solution diffusing into different

concentrations of agarose and collagen gels. Fitting of MBIC particle diffusion data can be found in Supplementary Information (Figure S5.1-S5.3).

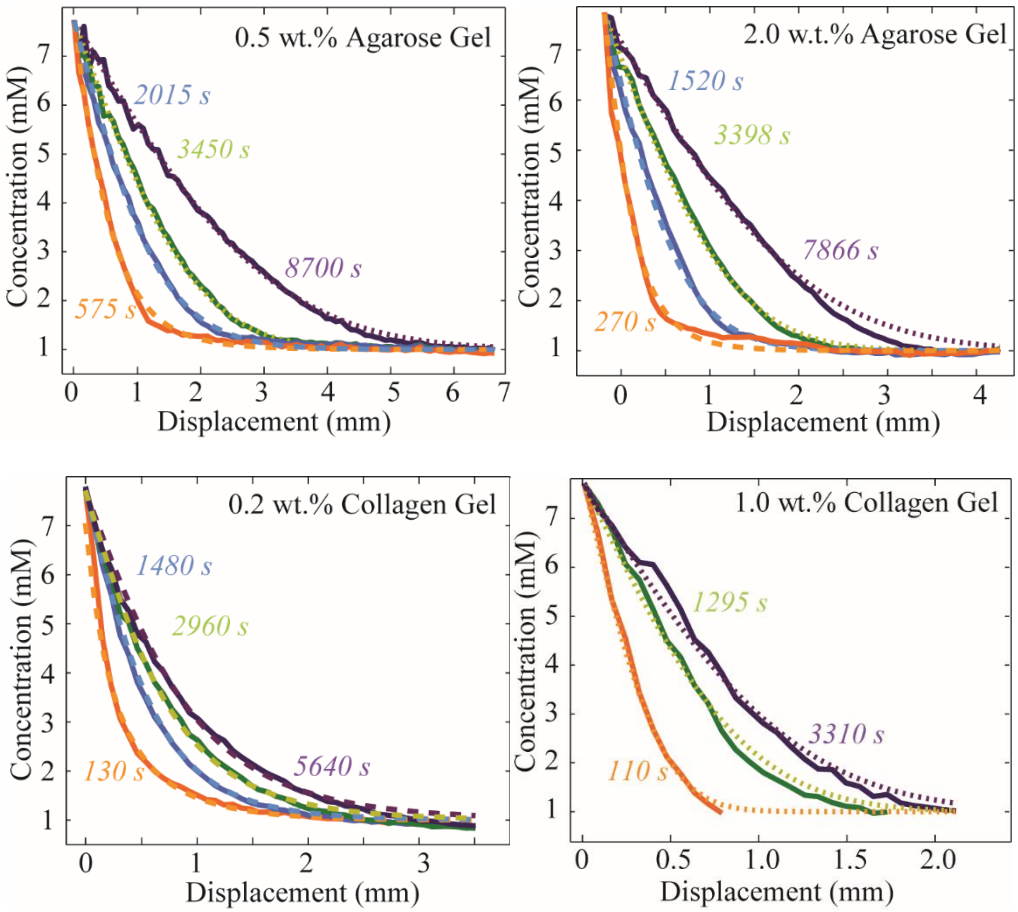

Figure 5.3 N_4Gd ingress into gels measured at progressive time points. Solid lines are concentrations as a function of displacement converted from intensity using Equation 5.2. Dotted lines are fits using Equation 5.3 with no distribution. Dashed lines are fits using Equation 5.5 assuming a distribution of diffusion coefficients *D*. Table S5.1 in SI shows *D* values and distribution widths extracted from each curve.

For analysis of T_1-*null-weighted* images, we plotted signal intensity directly versus displacement *x* for individual images as a function of elapsed time *t* (Figure 5.4). The magnitude of displacements of null points labeling the chosen concentration can then be read

from the near-zero positions on the curves corresponding to every measurement time point. A diffusion coefficient at each time point can be directly calculated using Equation 5.3.

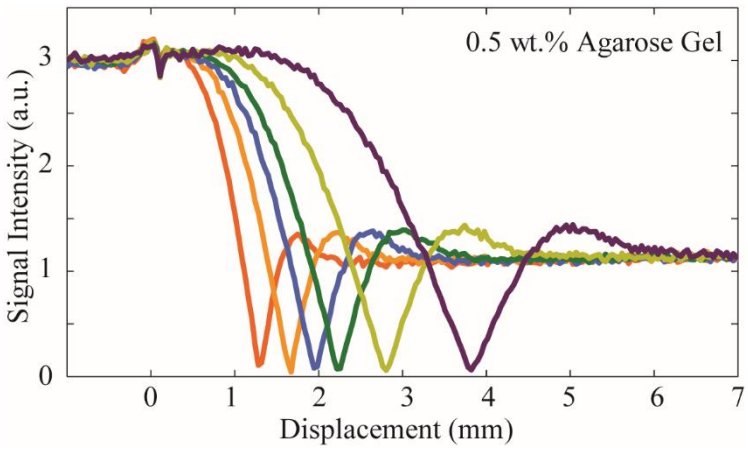

Figure 5.4 Plots of T_1-*null-weighted* data of N_4Gd diffusing into 0.5 wt.% agarose gel measured at different time points (from left to right: 950 s, 1670 s, 2390 s, 3110 s, 4780 s, and 8370 s).

We achieved agreement between diffusion coefficients of N_4Gd particles in 0.5 wt.% agarose gels measured using both methods with a discrepancy < 10% (see Table S5.2, SI). The consistency between the two methods for all particles and diffusing media provides confidence in our approach to measuring *D* for a wide variety of theranostic particles into gels and other biological materials.

All diffusion data obtained using T_2-*weighted* images of the three agents in the four different agarose and collagen gels are listed in Table 5.1. Agarose is a neutrally charged matrix with well-characterized pore size, which provides a measure of steric and hydrodynamic interactions that hinder the movement of nanoparticles in biological media.[35-37] A reduction of median *D* of N_4Gd by 45% is observed with an increase of agarose content from 0.5 to 2.0 wt.%, corresponding to a decrease of ~70% in average gel pore size.[35] The median *D* for N_4Gd into 2.0 wt.% agarose gel agrees well with the *D* for neutral particles of the same size measured

by FRAP.[36] Negligible displacement was observed during the measurement of MBICs diffusing into 2.0 wt.% agarose gel after a 25 hour experiment duration, indicating a $D < 1 \times 10^{-10}$ cm^2/s, set by our spatial resolution of 40 to 80 μm.

Table 5.1 Diffusion coefficients of Gd-DTPA, N_4Gd and MBICs into agarose gels of 0.5 and 2.0 wt.% at 25 ℃, and into collagen gels of 0.2 and 1.0 wt.% at 37 ℃.[a]

Diffusing Medium	Sample	Diffusion Time *t* (s)	Median Diffn. Coeff. *D* ($cm^2 \cdot s^{-1}$)	Distribution Std. Dev. σ
0.5 wt.% Agarose at 25 ℃	Gd-DTPA	all	3.7×10^{-6}	mono
	N_4Gd	**575	3.0×10^{-6}	1.0
		8700	3.5×10^{-6}	mono
	MBICs	**7880	4.5×10^{-8}	1.3
		52650	4.0×10^{-8}	mono
2.0 wt.% Agarose at 25 ℃	Gd-DTPA	all	3.5×10^{-6}	mono
	N_4Gd	**270	1.6×10^{-6}	1.0
		7866	2.0×10^{-6}	mono
	MBICs	all	$<1.0 \times 10^{-10}$	mono
0.2 wt.% Collagen at 37 ℃	Gd-DTPA	all	1.9×10^{-5}	mono
	N_4Gd	**1480	1.2×10^{-6}	0.9
		**5640	0.8×10^{-6}	0.9
	MBICs	all	2.1×10^{-8}	mono
1.0 wt.% Collagen at 37 ℃	Gd-DTPA	all	2.7×10^{-6}	mono
	N_4Gd	all	1.3×10^{-6}	mono
	MBICs	all	3.0×10^{-9}	mono

a Diffusion data (denoted with **) fitted with the Equation 5.4 distribution are listed in the form of the median *D* value and standard deviation of the lognormal distribution.

Pluen and coworkers[36] observed that for 2.0 wt.% agarose gel there is a critical particle hydrodynamic radius (~30 nm) below which *D* decreases drastically. Our observation may also be due to the idea that the mean pore radius reported for 2.0 wt.% agarose gel[35, 37] does not include a distribution of pore sizes, where smaller interconnected pores in a continuous network would limit the transport of particles, though they are larger than the mean pore size. Furthermore, other measurements of pore size may not correspond to what the diffusing MBIC particles experience, when accounting for specific particle surface charge and morphology.

D for MBICs in 0.5 wt.% agarose gel is two orders of magnitude lower than that of the ~8× smaller N_4Gd, due to steric hindrance and the influence of hydrodynamic interactions in porous gels.[38-39] We observe a distribution of *D* for N_4Gd in agarose gels in early time period measurements, as shown in Figure 5.3 and Table 5.1. Moreover, diffusion coefficients detected during later time periods are larger, and the fit better to Equation 5.3 instead of Equation 5.5. This likely results from the larger MBIC particles that move more slowly through the gel and hence contribute less to the image intensity at later times.

Diffusion rates of positively charged N_4Gd particles (ζ-potential +34.1 ± 4.7 mV from DLS measurement) match very closely with the diffusivity of neutrally charged particles of about the same size (~2 nm in radius) reported using FRAP methods[11] in collagen gels of both concentrations. On the other hand, the diffusion of negatively charged MBIC particles (ζ-potential -67.6±4.0 mV) was significantly hindered compared to neutral particles of similar size measured in reference 11. Within 0.2 wt.% collagen gels, the diffusion of MBICs is

approximately 10 times slower than neutrally charged particles, and the diffusivity of MBICs decreases roughly two orders of magnitude compared to neutral particles in 1.0 wt.% collagen gel. This drastic decrease in diffusion rate arises from the electrostatic interaction between the slightly positively charged collagen fibers at neutral pH (ζ-potential ~+4 mV)[40] and negatively charged MBIC nanoparticles. Combined with hydrodynamic and steric interactions, electrostatic effects influence diffusion of nanoparticles of both positive and negative surface charge, owing to their repulsion from or attraction to collagen fibers.[13] Based on Johnson and Deen's model of electrostatic energy between a spherical particle and a fiber[41], the electrostatic interactions increase with the size of diffusing particles as well as the surface charge density of the particle within a given medium. Accordingly, MBICs experience more significant electrostatic interactions than N_4Gd. Our results show that as the particle size and surface charge become larger, collagen gel at tumor relevant concentration (1.0 wt.%) presents a more significant impediment to the diffusive transport of negatively charged nanoparticles, as illustrated in Figure 5.5. Furthermore, our observations support the idea that collagen is the main diffusive hindrance to nanoparticles, and hence determines their transport in tumor interstitium,[11] where collagen is the major component and an electrostatic bandpass is proposed.[14] Our observations thus provide direct and critical information for design of theranostic delivery vehicles to selectively penetrate and permeate tumor tissue, and allow for sensitive optimization of drug delivery and gene therapy agents.

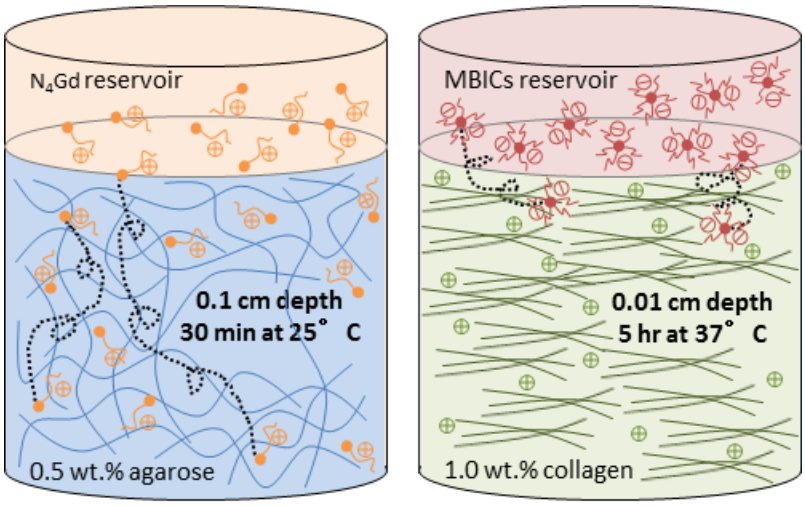

Figure 5.5 Representation of diffusion-driven transport of N_4Gd nanoparticles into 0.5 wt.% agarose gel and MBICs into 1.0 wt.% collagen gel.

5.4 Conclusion

In summary, we have established and validated a simple and accurate approach for quantitative study of nanoparticle diffusive penetration into hydrogels. To the best of our knowledge, this is the first work that combines time-resolved MRI experiments to reliably quantify diffusivity of paramagnetic and superparamagnetic nanoparticles in bulk biological media. Our results agree closely with those obtained from fluorescence techniques, yet the capability of our approach allows the analysis of actual delivery vehicle diffusion through biogels on mm to cm scales during a range of time periods. Accordingly, this method also promises to greatly expand examinations of the transport properties of drug delivery systems into the realm of *in vivo* studies in normal and tumor tissues.

5.5 Supporting Information

Table S5.1 Diffusion coefficients and distribution of N4Gd into agarose and collagen gels.

Diffusing Medium	Diffusing Time/s	Median Diffusion Coefficient / $cm^2 \bullet s^{-1}$	Distribution Standard Deviation σ
0.5 wt.% Agarose at 25 ℃	575	3.0×10-6	1.0
	2015	3.0×10-6	0.5
	3450	3.2×10-6	mono
	8700	3.5×10-6	mono
2.0 wt.% Agarose at 25 ℃	270	1.6×10-6	1.0
	1520	1.6×10-6	0.5
	3398	1.8×10-6	mono
	7866	2.0×10-6	mono
0.2 wt.% Collagen at 37 ℃	130	2.1×10-6	0.9
	1480	1.2×10-6	0.9
	2960	1.0×10-6	0.9
	5640	0.8×10-6	0.9
1.0 wt.% Collagen at 37 ℃	110	2.3×10-6	mono
	1295	1.8×10-6	mono
	3310	1.3×10-6	mono

Table S5.2 Median coefficients of N_4Gd measured by *T_2-weighted* imaging and diffusion coefficients measured by *T_1-null-weighted* imaging of N_4Gd diffusing into 0.5 wt.% agarose gel.

Diffusing Time/s	Median Diffusion Coefficient / $cm^2 \cdot s^{-1}$ measured by T2-weighted	Diffusion Coefficient / $cm^2 \cdot s^{-1}$ measured by T1-null-weighted
575	3.0 ×10-6	
950		3.1×10^{-6}
1670		3.3×10^{-6}
2015	3.0×10^{-6}	
2390		3.4×10^{-6}
3110		3.5×10^{-6}
3450	3.2×10^{-6}	

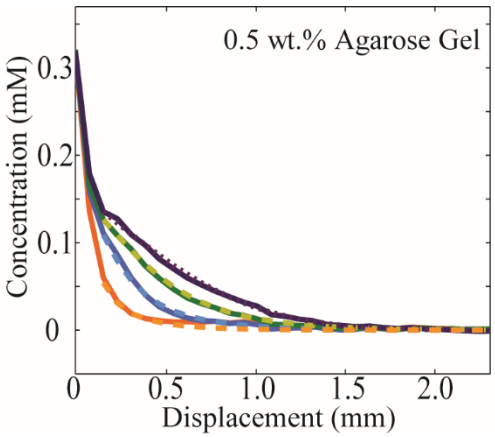

Figure S5.1 Fitting of experimental data (solid line) both with consideration of a diffusion coefficient distribution (dashed line, using Equation 5.5) or with no distribution (dotted line, using Equation 5.2) for diffusing of MBICs into 0.5 wt.% agarose gel.

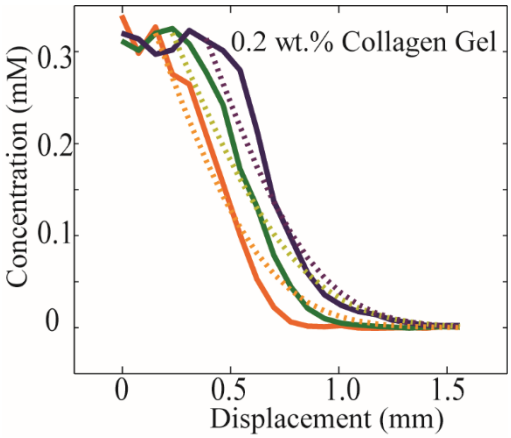

Figure S5.2 Fitting of experimental data (solid line) using Equation 5.2 (dotted line) for diffusing of MBICs into 0.2 wt.% collagen gel.

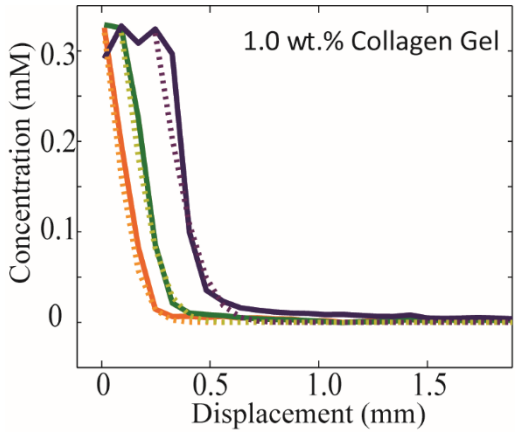

Figure S5.3 Fitting of experimental data (solid line) using Equation 5.2 (dotted line) for diffusing of MBICs into 1.0 wt.% collagen gel.

Reference

(1) Jain, R. K. The Next Frontier of Molecular Medicine: Delivery of Therapeutics. *Nat. Med.* **1998,** *4*, 655-7.
(2) Jain, R. K.; Stylianopoulos, T. Delivering Nanomedicine to Solid Tumors. *Nat. Rev. Clin. oncol.* **2010,** *7*, 653-664.
(3) Chauhan, V. P.; Stylianopoulos, T.; Boucher, Y.; Jain, R. K. Delivery of Molecular and Nanoscale Medicine to Tumors: Transport Barriers and Strategies. *Annu. Rev. Chem. Biomol. Eng.* **2011,** *2*, 281-298.
(4) Boucher, Y.; Baxter, L. T.; Jain, R. K. Interstitial Pressure Gradients in Tissue-Isolated and Subcutaneous Tumors: Implications for Therapy. *Cancer Res.* **1990,** *50*, 4478-4484.
(5) Milosevic, M. F.; Fyles, A. W.; Wong, R.; Pintilie, M.; Kavanagh, M.-C.; Levin, W.; Manchul, L. A.; Keane, T. J.; Hill, R. P. Interstitial Fluid Pressure in Cervical Carcinoma. *Cancer* **1998,** *82*, 2418-2426.
(6) Heldin, C. H.; Rubin, K.; Pietras, K.; Ostman, A. High Interstitial Fluid Pressure - an Obstacle in Cancer Therapy. *Nature reviews. Cancer* **2004,** *4*, 806-13.
(7) Dvorak, H. F. Tumors: Wounds That Do Not Heal. *N. Engl. J. Med.* **1986,** *315*, 1650-1659.
(8) *Cellular Changes Involved in Conversion of Normal to Malignant Breast: Importance of the Stromal Reaction*. 1996; Vol. 76, p 69-125.
(9) Netti, P. A.; Berk, D. A.; Swartz, M. A.; Grodzinsky, A. J.; Jain, R. K. Role of Extracellular Matrix Assembly in Interstitial Transport in Solid Tumors. *Cancer Res.* **2000,** *60*, 2497-2503.
(10) Pluen, A.; Boucher, Y.; Ramanujan, S.; McKee, T. D.; Gohongi, T.; di Tomaso, E.; Brown, E. B.; Izumi, Y.; Campbell, R. B.; Berk, D. A.; Jain, R. K. Role of Tumor–Host Interactions in Interstitial Diffusion of Macromolecules: Cranial Vs. Subcutaneous Tumors. *Proc. Natl. Acad. Sci.* **2001,** *98*, 4628-4633.

(11) Ramanujan, S.; Pluen, A.; McKee, T. D.; Brown, E. B.; Boucher, Y.; Jain, R. K. Diffusion and Convection in Collagen Gels: Implications for Transport in the Tumor Interstitium. *Biophys. J.* **2002,** *83*, 1650-60.
(12) Alexandrakis, G.; Brown, E. B.; Tong, R. T.; McKee, T. D.; Campbell, R. B.; Boucher, Y.; Jain, R. K. Two-Photon Fluorescence Correlation Microscopy Reveals the Two-Phase Nature of Transport in Tumors. *Nat. Med.* **2004,** *10*, 203-7.
(13) Stylianopoulos, T.; Poh, M.-Z.; Insin, N.; Bawendi, M. G.; Fukumura, D.; Munn, L. L.; Jain, R. K. Diffusion of Particles in the Extracellular Matrix: The Effect of Repulsive Electrostatic Interactions. *Biophys. J.* **2010,** *99*, 1342-1349.
(14) Lieleg, O.; Baumgärtel, R. M.; Bausch, A. R. Selective Filtering of Particles by the Extracellular Matrix: An Electrostatic Bandpass. *Biophys. J. 97*, 1569-1577.
(15) Axelrod, D.; Koppel, D. E.; Schlessinger, J.; Elson, E.; Webb, W. W. Mobility Measurement by Analysis of Fluorescence Photobleaching Recovery Kinetics. *Biophys. J.* **1976,** *16*, 1055-69.
(16) Chary, S. R.; Jain, R. K. Direct Measurement of Interstitial Convection and Diffusion of Albumin in Normal and Neoplastic Tissues by Fluorescence Photobleaching. *Proc. Natl. Acad. Sci.* **1989,** *86*, 5385-5389.
(17) Berland, K. M.; So, P. T.; Gratton, E. Two-Photon Fluorescence Correlation Spectroscopy: Method and Application to the Intracellular Environment. *Biophys. J.* **1995,** *68*, 694-701.
(18) Chauhan, V. P.; Lanning, R. M.; Diop-Frimpong, B.; Mok, W.; Brown, E. B.; Padera, T. P.; Boucher, Y.; Jain, R. K. Multiscale Measurements Distinguish Cellular and Interstitial Hindrances to Diffusion in Vivo. *Biophys. J. 97*, 330-336.
(19) Berk, D. A.; Yuan, F.; Leunig, M.; Jain, R. K. Fluorescence Photobleaching with Spatial Fourier Analysis: Measurement of Diffusion in Light-Scattering Media. *Biophys. J.* **1993,** *65*, 2428-2436.
(20) Rosen, B. R.; Belliveau, J. W.; Vevea, J. M.; Brady, T. J. Perfusion Imaging with NMR Contrast Agents. *Magn. Reson. Med.* **1990,** *14*, 249-65.
(21) Markl, M.; Chan, F. P.; Alley, M. T.; Wedding, K. L.; Draney, M. T.; Elkins, C. J.; Parker, D. W.; Wicker, R.; Taylor, C. A.; Herfkens, R. J.; Pelc, N. J. Time-Resolved Three-Dimensional Phase-Contrast MRI. *J. of Magn. Reson. Imaging* **2003,** *17*, 499-506.
(22) Markl, M.; Harloff, A.; Bley, T. A.; Zaitsev, M.; Jung, B.; Weigang, E.; Langer, M.; Hennig, J.; Frydrychowicz, A. Time-Resolved 3d Mr Velocity Mapping at 3t: Improved Navigator-Gated Assessment of Vascular Anatomy and Blood Flow. *J. of Magn. Reson. Imaging* **2007,** *25*, 824-831.
(23) Chen, X.; Astary, G. W.; Sepulveda, H.; Mareci, T. H.; Sarntinoranont, M. Quantitative Assessment of Macromolecular Concentration During Direct Infusion into an Agarose Hydrogel Phantom Using Contrast-Enhanced MRI. *Magn. Reson. Imaging* **2008,** *26*, 1433-1441.

(24) Bernal, G. M.; LaRiviere, M. J.; Mansour, N.; Pytel, P.; Cahill, K. E.; Voce, D. J.; Kang, S.; Spretz, R.; Welp, U.; Noriega, S. E.; Nuñez, L.; Larsen, G.; Weichselbaum, R. R.; Yamini, B. Convection-Enhanced Delivery and in Vivo Imaging of Polymeric Nanoparticles for the Treatment of Malignant Glioma. *Nanomed. Nanotechnol. Biol. and Med.* **2014,** *10*, 149-157.
(25) Bryson, J. M.; Fichter, K. M.; Chu, W.-J.; Lee, J.-H.; Li, J.; Madsen, L. A.; McLendon, P. M.; Reineke, T. M. Polymer Beacons for Luminescence and Magnetic Resonance Imaging of DNA Delivery. *Proc. Natl. Acad. Sci.* **2009,** *106*, 16913-16918.
(26) Wang, X.; Kelkar, S. S.; Hudson, A. G.; Moore, R. B.; Reineke, T. M.; Madsen, L. A. Quantitation of Complexed Versus Free Polymers in Interpolyelectrolyte Polyplex Formulations. *ACS Macro Lett.* **2013,** *2*, 1038-1041.
(27) Pothayee, N.; Balasubramaniam, S.; Davis, R. M.; Riffle, J. S.; Carroll, M. R. J.; Woodward, R. C.; St. Pierre, T. G. Synthesis of 'Ready-to-Adsorb' Polymeric Nanoshells for Magnetic Iron Oxide Nanoparticles Via Atom Transfer Radical Polymerization. *Polymer* **2011,** *52*, 1356-1366.
(28) Pothayee, N.; Pothayee, N.; Jain, N.; Hu, N.; Balasubramaniam, S.; Johnson, L. M.; Davis, R. M.; Sriranganathan, N.; Riffle, J. S. Magnetic Block Ionomer Complexes for Potential Dual Imaging and Therapeutic Agents. *Chem. Mater.* **2012,** *24*, 2056-2063.
(29) Pothayee, N.; Balasubramaniam, S.; Pothayee, N.; Jain, N.; Hu, N.; Lin, Y.; Davis, R. M.; Sriranganathan, N.; Koretsky, A. P.; Riffle, J. S. Magnetic Nanoclusters with Hydrophilic Spacing for Dual Drug Delivery and Sensitive Magnetic Resonance Imaging. *J. Mater. Chem. B* **2013,** *1*, 1142-1149.
(30) Hennig, J.; Nauerth, A.; Friedburg, H. Rare Imaging: A Fast Imaging Method for Clinical Mr. *Magn. Reson. Med.* **1986,** *3*, 823-833.
(31) Abragam, A., *The Principles of Nuclear Magnetism*. Clarendon Press: Oxford,, 1961; p 599 p.
(32) Haacke, E. M.; Brown, R. W.; Thompson, M. R.; Venkatesan, R., *Magnetic Resonance Imaging*. Wiley-Liss New York:: 1999.
(33) Balcom, B. J.; Fischer, A. E.; Carpenter, T. A.; Hall, L. D. Diffusion in Aqueous Gels. Mutual Diffusion Coefficients Measured by One-Dimensional Nuclear Magnetic Resonance Imaging. *J. Am. Chem. Soc.* **1993,** *115*, 3300-3305.
(34) Rydberg, J. N.; Riederer, S. J.; Rydberg, C. H.; Jack, C. R. Contrast Optimization of Fluid-Attenuated Inversion Recovery (Flair) Imaging. *Magn. Reson. Med.* **1995,** *34*, 868-877.
(35) J. Zhou; M. Zhou; Caruso, R. A. Agarose Template for the Fabrication of Macroporous Metal Oxide Structures. *Langmuir* **2006,** *22*, 3332-3336.
(36) Pluen, A.; Netti, P. A.; Jain, R. K.; Berk, D. A. Diffusion of Macromolecules in Agarose Gels: Comparison of Linear and Globular Configurations. *Biophys. J.* **1999,** *77*, 542-552.
(37) Fatin-Rouge, N.; Starchev, K.; Buffle, J. Size Effects on Diffusion Processes within Agarose Gels. *Biophys. J.* **2004,** *86*, 2710-2719.
(38) Deen, W. M. Hindered Transport of Large Molecules in Liquid-Filled Pores. *AIChE J.* **1987,** *33*, 1409-1425.

(39) Johnson, E. M.; Berk, D. A.; Jain, R. K.; Deen, W. M. Hindered Diffusion in Agarose Gels: Test of Effective Medium Model. *Biophys. J.* **1996,** *70*, 1017-1023.
(40) Li, Y.; Asadi, A.; Monroe, M. R.; Douglas, E. P. Ph Effects on Collagen Fibrillogenesis in Vitro: Electrostatic Interactions and Phosphate Binding. *Mater. Sci. Eng. C* **2009,** *29*, 1643-1649.
(41) Johnson, E. M.; Deen, W. M. Electrostatic Effects on the Equilibrium Partitioning of Spherical Colloids in Random Fibrous Media. *J. Colloid Interface Sci.* **1996,** *178*, 749-756.

Chapter 6

Confinement Effects on Structures and Motions of Ions Inside Nafion

6.1 Introduction

Ion conducting materials have played an essential role in electrochemical conversion, storage and transmission in devices ranging from fuel cells, to solar cells, batteries, chemical sensors and artificial muscle actuators. Ionic liquids (ILs) are liquids at or near room temperature consisting solely of ions.[1-4] ILs have been identified as useful, safe and tunable electrolytes due to their unique physicochemical properties, such as high ion conductivity, broad electrochemical window, low vapor pressure, non-flammability, and high thermal stability. Ionic polymers (ionomers) are polymers containing charged and neutral moieties that phase separate into nanometer-scale hydrophilic and hydrophobic domains.[5-7] Ionomers have been studied and used as solid electrolytes based on their ion conductive hydrophilic domains and the hydrophobic domains, which provide mechanical support.[8-10] When absorbed into ionic polymers, ILs may replace classical liquid electrolytes such as water and organic solvents to promote faster ion transport and safety (non-flammability) in ion conducting devices.[11-12] Understanding and optimizing transport of ILs inside ionic polymers is key to obtaining high performance materials and devices and is greatly influenced by many factors including 1) interaction among mobile species, 2) interaction between mobile species and fixed ions in the hydrophilic domains of ionic polymers, 3) local geometry and tortuosity of ionic domains, and 4) mobility of polymer chains.

Tremendous effort has been devoted in experiments and simulations to understand the local liquid structure of ILs, with many ILs based on imidazolium cations. One of the ongoing

mysteries of IL structuring concerns the existence, lifetime, and fraction of ion pairs or larger ion clusters in neat ILs. There is some experimental evidence that supports the existence of ion pairs,[13-14] and their lifetime is estimated to be only a few pico- to nanoseconds.[15-16] An intriguing proposal that has recently attracted attention is the formation of a supramolecular structure of polar and nonpolar domains on the mesoscopic (~ 100 nm) length scale, mainly driven by a 3D cooperative network of hydrogen bonds,[17-19] or more precisely, doubly ionic hydrogen bonds that are bifurcated and chelating.[20] Another model that can be used to help explain ion transport behaviors in ILs is ion clusters. In this model, in addition to ion pairs, ion clusters such as triples, quadrupoles and quintuples also exist and travel as an entity with a short (~ 1 ns or less) lifetime. Our group has been using NMR techniques to map the distribution of these short-lived clusters.[11, 21] In this Chapter, we will use this ion clustering model to explain our NOE and diffusion results.

Developed by DuPont, Nafion® is one of the most studied ionomers and serves as a benchmark material for fuel cell membranes as well as other ion conduction and ion exchange applications. Despite being exposed to extensive and close inspection, a complete picture of the morphology of Nafion remains unresolved.[22] Based on the information gathered from X-ray, neutron scattering, and TEM, a wide range of models have been proposed for the morphology of hydrated Nafion, including an interconnected hydrophilic network of inverted micellar spherical ionic clusters,[23] bundles of elongated rod- or ribbon-like polymeric aggregates in the hydrated matrix,[24-26] long and parallel cylindrical water nanochannels in the hydrophobic matrix,[27] alternating polymer-rich and water-rich lamellar layers,[28] locally narrow and flat water films,[29] and a random nanoscale channel-type bicontinuous network.[30] The difficulties in unraveling a complete Nafion morphology lie in its complexity, non-periodicity

above the nanoscale, and heterogeneity as well as the fact that the sub-micron structures are strongly influenced by pre-treatment.[29] Previous studies of our group supported the existence of sub-micron domains and demonstrated that these sub-micron domains can rotate and realign under macroscopic drawing while the alignment within domains and junctions between domains are not affected.[31] However, little information has been revealed about these domain boundaries and how they affect ion transport.

Our group has previously investigated water and ILs absorbed into Nafion using multiple NMR methods with a highlight on pulsed-field-gradient (PFG) NMR diffusometry.[11, 31-32] Self-diffusion of ILs and water in Nafion reveals non-restricted diffusion behaviors for cations, anions and water at room temperature (25 ℃) when probing experimental diffusion lengths of 0.5 – 3.3 μm. While the cation diffuses slower than the anion at high water content due to its larger size and drag from fixed sulfonate groups in the hydrophilic domains of the ionomer, the anion diffuses 4 × slower at low water content. This reversal in cation/anion behavior was explained by the formation of anion-rich aggregates at low water content inside Nafion.[11] Motivated by these observations, in this chapter we aim to: 1) inspect the formation of ion associations by intermolecular nuclear Overhauser effect (NOE) NMR spectroscopy, 2) explore sample parameter space to explore "free diffusion" regimes, 3) and investigate regimes of "restricted diffusion" where ions encounter geometric barriers to transport. Regarding point 3, we aim to understand the confinement effect of the Nafion nanochannels on ion transport, and utilize restricted ion diffusion behaviors to probe the multi-length-scale geometry of this important ionomer. Since both NOE and PFG NMR experiments are highly dependent on spin relaxation times, we will first discuss the confinement effect on spin relaxation.

6.2 Experimental Section

6.2.1 Sample Preparation

1-ethyl-3-methyl imidazolium tetrafluoroborate ([C_2mim][BF_4]) and 1-ethyl-3-methyl imidazolium trifluoromethanesulfonate ([C_2mim][TfO]) were used to study the confinement effect of ion associations and motions inside ionomers. These ILs were purchased from Solvent Innovation GMBH (Cologne, Germany) with purity >99% and used as received. Extruded Nafion 117 (N117) membranes with equivalent weight of 1100 (grams of dry membrane per mole of sulfonate groups) were obtained from DuPont in the acid form with thickness = 175 μm. Two series of samples were made for different NMR experiments. Series 1 were prepared to fit inside a 5 mm NMR tube and included both [C_2mim][BF_4] and [C_2mim][TfO] simultaneously in N117 with varying water content. N117 membranes were cut into pieces of 3 mm × 7 mm in size and dried in a vacuum oven for 24 hours at 50 ℃ to determine the dry membrane mass (m_{Mem} ~ 60 g) gravimetrically. The membranes were then soaked with a mixture of [C_2mim][BF_4] and [C_2mim][TfO] (with a mole ratio of 1:1), and water (D_2O, 99.9%, Cambridge Isotope Labs) at 60 ℃ for 4-24 hours to achieve different IL uptakes and water content. The wet membranes were blotted carefully to remove surface liquid, wrapped into stacks using Teflon tape and then inserted into our home built sealed polyetheretherketone (PEEK) tube with O.D. 4 mm and I.D. 3.2 mm. These membranes were then used for NMR measurements with temperature decreasing from 50 ℃ to ─ 20 ℃, with ~ 1 hour equilibration at each temperature prior to NMR experiments. The mass of the membranes ($m_{Mem+IL+Water}$) were checked before and after NMR studies to verify no mass change due to water evaporation or absorption during experiments. The membranes were dried in open air or vacuum for a few minutes to achieve different water content at the same IL uptake, and eventually they were

dried in vacuum for > 24 hours at 50 ℃ to remove water and to obtain dried membranes with only ILs ($m_{\mathrm{Mem+IL}}$). The mole ratio of $[C_2mim][BF_4]$ to $[C_2mim][TfO]$ soaked inside membranes, expressed in χ, was determined by multiplying the integration ratio of BF_4^- resonance at -150 ppm to TfO^- ($CF_3SO_3^-$) resonance at -80 ppm in the ^{19}F NMR spectrum by 3/4 (as shown in Figure 6.1b). $\chi = \sim 0.9 - 1.1$ for all our samples. IL uptake $\lambda(C_2mim^+/SO_3^-)$ and water content $\lambda(D_2O/SO_3^-)$ in the membrane were determined using the following equations,

$$\lambda\left(\frac{\mathrm{C_2mim^+}}{\mathrm{SO_3^-}}\right) = \frac{m_{\mathrm{Mem+IL}} - m_{\mathrm{Mem}}}{m_{\mathrm{Mem}}} \times \frac{1100\ \mathrm{g/mol}}{\mathrm{MW_{IL}}} \tag{6.1}$$

$$\lambda\left(\frac{\mathrm{D_2O}}{\mathrm{SO_3^-}}\right) = \frac{m_{\mathrm{Mem+IL+Water}} - m_{\mathrm{Mem+IL}}}{m_{\mathrm{Mem}}} \times \frac{1100\ \mathrm{g/mol}}{\mathrm{MW_{D_2O}}} \tag{6.2}$$

where $\mathrm{MW_{IL}} = (\chi \cdot \mathrm{MW_{[C2mim][BF4]}} + \mathrm{MW_{[C2mim][TfO]}})/(\chi + 1)$, is the weighted average molecular weight of the IL mixture. We note that we neglected any mass change caused by ion exchange between H^+ of the original acid-form Nafion and C_2mim^+.

Series 2 were prepared for 8 mm NMR tubes, using dry N117 pieces of ~ 450 mg soaked in neat $[C_2mim][BF_4]$. The procedures were the same as above, except that membranes were sealed in polyethylene bags, $\mathrm{MW_{IL}} = \mathrm{MW_{[C2mim][BF4]}}$ in Eq. 6.1, and $\lambda(D_2O/SO_3^-) = 0$ throughout all experiments.

Series 1 was used for spin relaxation (Section 6.3.1), intermolecular NOE (Section 6.3.2) and checking free diffusion regions (Section 6.3.3). Series 2 was used mainly for restricted diffusion studies (Section 6.3.4). Spin relaxation and ^1H-^{19}F HOESY experiments were also performed on Series 2 to confirm that the coexistence of TfO^- and BF_4^- may shift the results by $\pm 10\%$, but the trends observed and discussed in the later sections were identical for the two sample series.

6.2.2 NMR Studies

NMR measurements for series 1 were performed on a Bruker Avance III WB 400 MHz (9.4 T) NMR spectrometer equipped with a 5 mm double resonance $^{1}H/^{2}H$ RF coil on a mic probehead where the ^{1}H channel can be tuned to ^{19}F, and a Bruker Avance III 500 MHz (11.8 T) NMR spectrometer equipped with 5 mm double resonance $^{1}H/^{19}F$ coil. NMR measurements for series 2 were performed on the above Bruker Avance III WB 400 MHz NMR equipped with a 8 mm single resonance $^{1}H/^{19}F$ RF coil.

Spin-lattice relaxation T_1 and spin-spin relaxation T_2 of ^{1}H and ^{19}F were measured for both sample series. T_1 was measured using the inversion-recovery method, and T_2 using an incremented echo-train CPMG pulse sequence. Estimated errors in T_1 and T_2 values are $< \pm 2\%$ for single-component fittings.

NOE experiments were performed for free ILs and sample series 1 on the 500 MHz spectrometer. For ^{1}H-^{19}F HOESY, the simplest pulse sequence (no gradients or extra delays) "hoesyqfrv" from the Bruker spectrometer library was used with ^{19}F detection and mixing times varying from 50 to 1700 ms, and $\pi/2$ pulse times of 13.5 μs for ^{1}H and 15.5 μs for ^{19}F. 32 transients with a total of 2k data points in the direct dimension $F2$ (^{19}F) and 96 data points in the indirect dimension $F1$ (^{1}H) were collected, with a spectral width of 25 kHz in both $F2$ and $F1$. The relaxation delay was 4.0 s.

For ILs absorbed in membranes, reduced dynamics leads to much shorter T_1 and T_2 values, therefore any modified pulse sequences with active T_2 decay period longer than a few ms do not produce any signal, such as the commonly used "hoesygp." For ^{19}F-selective 1D NOE, the simple "selno" pulse sequence was employed using Gaussian-shape-selective

excitation on either BF_4^- (-150 ppm) or TfO^- (-80 ppm). Pulse sequences like "selnogp" do not work due to the very short T_2 values. The mixing time was varied from 50 to 1500 ms.

Diffusion measurements were performed on the 400 MHz spectrometer equipped with a DIFF60 (24 T/m at 40 A current) diffusion probe to study diffusion of cation (^{1}H), anion (^{19}F), and water (^{2}H) separately. Again reduced dynamics leads to much shorter T_1 and T_2 values as well as much slower diffusion coefficients for ILs inside membranes, presenting a challenge for diffusion measurements. DIFF60 has a maximum gradient of 24 T/m along the *z*-direction, which allows measuring relatively slow diffusion coefficients (~ 10^{-15} m^2/s). The gradient pre-emphasis was optimized using a dry glycerol sample at 10 ℃. The stability and reliability of our gradient system was confirmed by observing the same diffusion coefficient for dry glycerol when varying effective gradient pulse duration δ from 1 to 3 ms and diffusion time Δ from 10 ms to 1000 ms while keeping a gradient stabilization time of 2 ms and a maximum gradient of 18 T/m.[33] To study IL diffusion in membranes, the pulsed-gradient stimulated echo (PGSTE) sequence[34] was used with an effective δ = 2 ms (actual pulse length of the half sinusoid pulse was 3.2 ms), gradient stabilization time of 2 ms, Δ ranging from 25 – 600 ms, gradient strengths varying from g = 20 G/cm to g = 1800 G/cm, and $\pi/2$ pulse times of 7.5 μs for ^{1}H and 8.5 μs for ^{19}F. 16 to 32 gradient steps were applied, and the number of scans varied from 4×1 to 16×64 to yield sufficient signal-to-noise ratio (SNR). For normal diffusion curves, the self-diffusion coefficient D was obtained by fitting the measured signal attenuation $E(q, \Delta) \equiv I/I_0$ as a function of the reciprocal space vector q using the Stejskal-Tanner equation[34-35]:

$$E(q, \Delta) = \exp(-q^2(\Delta - \delta/3)D). \quad (6.3)$$

Here $q \equiv \gamma g \delta$, γ is the gyromagnetic ratio of the detected nucleus, g is gradient strength, δ is gradient pulse duration, and Δ is diffusion time. Each measurement was done three times to obtain a mean D with an error of $\leq \pm 5\%$.

6.3 Results and Discussion

Figure 6.1 compares single-pulse ^{1}H and ^{19}F NMR spectra of neat IL mixture and the mixture soaked into dry Nafion membranes. Molecular motions are significantly hindered in the nanoporous membrane, resulting in much broader lines. For the cation, spectral resolution is reduced and yet three kinds of protons (aromatic-CH, N-CH_2/CH_3 and β-CH_3) can be resolved for further relaxation, diffusion and NOE studies. For the anion mixture of BF_4^- and TfO^- with molar ratio 1:1, the resonance at -150 ppm for BF_4^- has lower intensity in the free liquid state due to J-splittings by the two boron isotopes (^{10}B and ^{11}B), while the resonance at -80 ppm for TfO^- is lower in intensity for ILs inside membranes due to its larger size and thereby more hindered motion (shorter T_2). Note here ^{19}F spectra width is 50 kHz, while the nutation frequency on the 500 MHz spectrometer is only 20 kHz, so we set on-resonance at either -80 ppm or -150 ppm and perform all ^{19}F experiments twice (one for each anion) to remove the off-resonance pulse excitation effect.

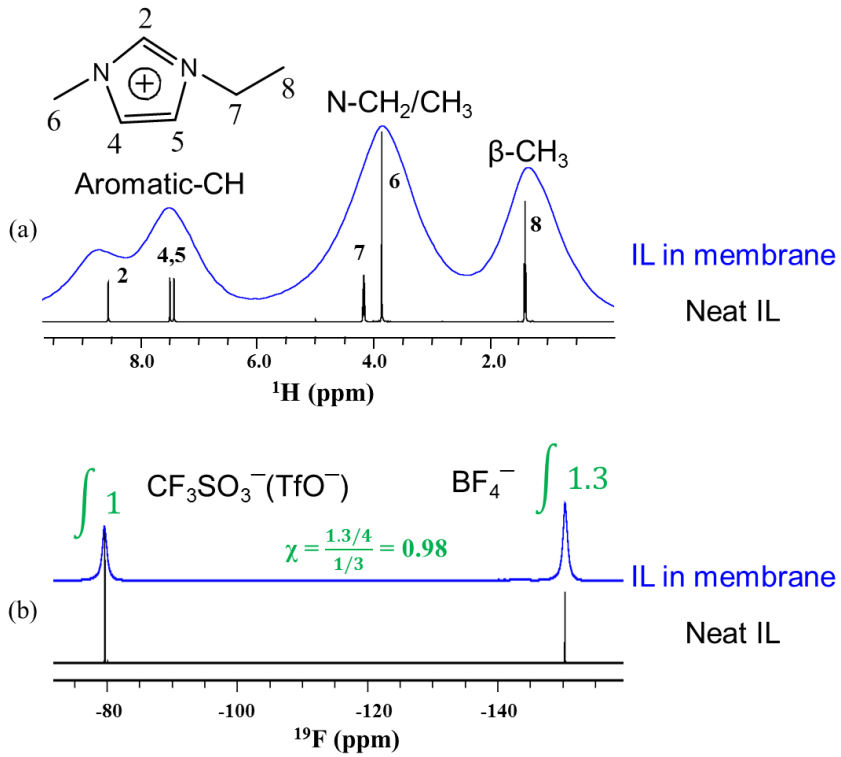

Figure 6.1 ^{1}H (a) and ^{19}F (b) NMR spectra of a mixture of dry $[C_2mim][BF_4]$ and $[C_2mim][TfO]$ in the free liquid state (black lines) and absorbed in membranes (blue lines).

6.3.1 Spin relaxation

Spin relaxation for each chemically distinct spin provides information about molecular dynamics and is heavily influenced by the surroundings of each spin. For molecules dissolved inside a porous solid matrix, spin-spin relaxation T_2 is largely modulated by susceptibility inhomogeneity in the sample, so here we focus on spin-lattice relaxation T_1 in order to better understand the confinement effect on spin relaxation. We measure ^{1}H T_1 of C_2mim^+ and ^{19}F T_1 of BF_4^- and TfO^- as a function of IL uptake $\lambda(C_2mim^+/SO_3^-)$, water content $\lambda(D_2O/SO_3^-)$, and temperature T ranging from -30 ℃ to 50 ℃. Figure 6.2 shows ^{19}F magnetization recovery plotted as a function of the delay time τ, measured at 10 ℃ for $[C_2mim][BF_4]$ at fixed

$\lambda(C_2mim^+/SO_3^-)$ = 0.8 and varying $\lambda(D_2O/SO_3^-)$ = 3.7 (a), 2.2 (b), and 0 (c). The inversion-recovery magnetization curve is given by

$$\{M_0 - M_z(\tau)\}/M_0 = \sum_{i=1}^{N} A(i)\exp(-\tau/T_1^*(i)). \quad (6.4)$$

Here M_0 is the equilibrium magnetization and $M_z(\tau)$ is the magnetization at delay time τ. *N* is the number of components required to fit the data. *A(i)* and $T_1^*(i)$are fitting parameters for the *i*th component. Note that for multi-component relaxation data, the fitting parameter T_1^* is apparent relaxation times involving the effect from exchange or confinement, therefore it does not necessarily represent the true relaxation times of each component. Using Eq. 6.4, a single-component decay fits nicely for Figure 6.2a to obtain T_1^*= 1.25 s, but two components are required to fit Figure 6.2b and 2c. The short T_1^* and long T_1^* values are fitted to be 320 ms and 1.20 s for Figure 6.2b, 21 ms and 1.18 s for Figure 6.2c, respectively. Contrary to the dramatic decrease in the short T_1^* values at lower water content, the long T_1^*values only reduce slightly and the population of the long T_1^* component maintains a similar level (approximately 55%). Figure 6.3 shows the temperature dependence of ^{19}F and ^{1}H T_1^* values at $\lambda(D_2O/SO_3^-)$ = 3.7 (a and b) as well as $\lambda(D_2O/SO_3^-)$ = 2.2 (c and d). It is clear that ^{19}F T_1 of both BF_4^- and TfO^- experiences a transition from single- to multi-component as temperature decreases, while this transition temperature of TfO^- is higher than that of BF_4^-. This may be explained by more hindered motion for TfO^-in the Nafion ionic channels due to its larger size compared to BF_4^-. Similar to the effect of water content, the short T_1^* values decrease significantly at lower temperature, while the long T_1^* values only reduce slightly and reach a plateau at ~263 K. Furthermore, the single-to-multi-component transition temperature increases as $\lambda(C_2mim^+/SO_3^-)$ or $\lambda(D_2O/SO_3^-)$ decreases, corresponding to reduced dynamics as a result of smaller ionic channels at lower IL uptake and water content. Surprisingly, the relative

amplitude of the long T_1^* component only fluctuates modestly with water content, temperature, anion species, and IL uptake, as shown in Figure 6.4. On the other hand, for all different types of ^{1}H in [C_2mim$^+$], we observe single-component T_1^* which becomes shorter at lower temperature. ^{1}H T_1^* also decreases monotonically as λ(C_2mim$^+$/SO_3^-) or λ(D_2O/SO_3^-) decreases, as a result of reduced dynamics.

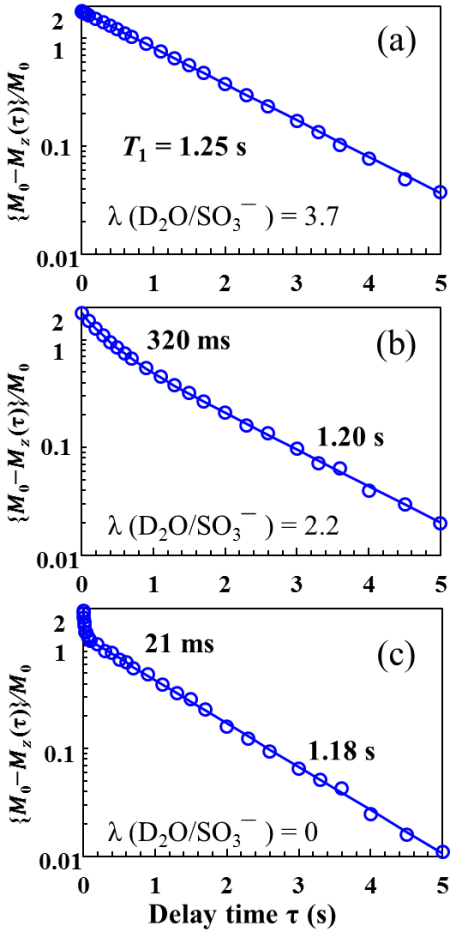

Figure 6.2 ^{19}F magnetization recovery curves measured at 10 ℃ for [C_2mim][BF_4] absorbed in Nafion with 17 wt% IL uptake λ(C_2mim$^+$/SO_3^-) = 0.8 at varying water contents λ(D_2O/SO_3^-) = 3.7 (a), 2.2 (b), and 0 (c).

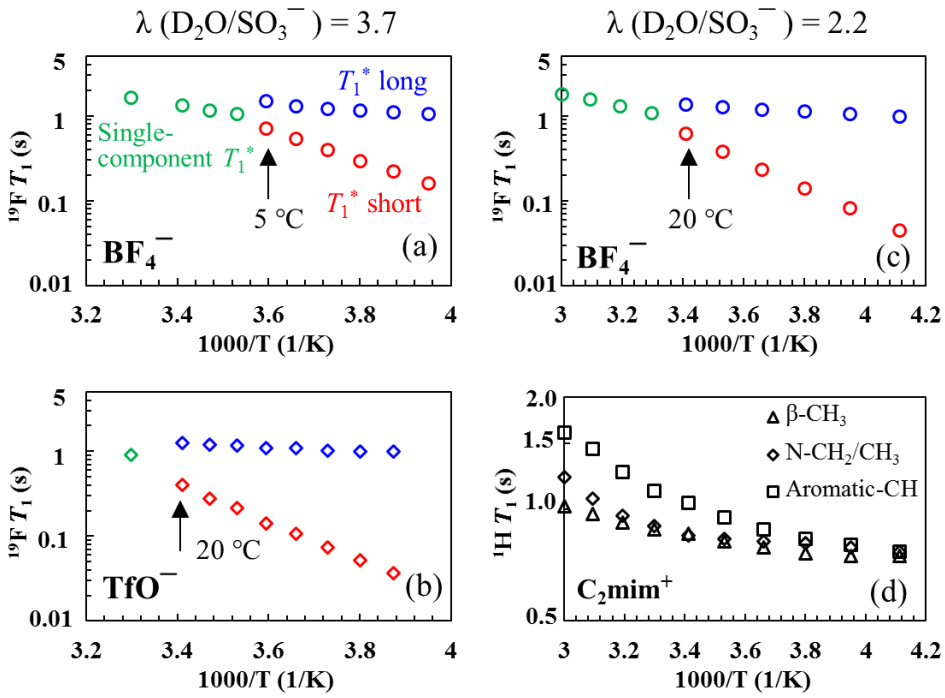

Figure 6.3 Temperature dependence of T_1 for (a) ^{19}F in BF_4^- at $\lambda(D_2O/SO_3^-) = 3.7$, (b) ^{19}F in TfO^- at $\lambda(D_2O/SO_3^-) = 3.7$, (c) ^{19}F in BF_4^- at $\lambda(D_2O/SO_3^-) = 2.2$, and (d) ^{1}H in C_2mim^+ at $\lambda(D_2O/SO_3^-) = 2.2$.

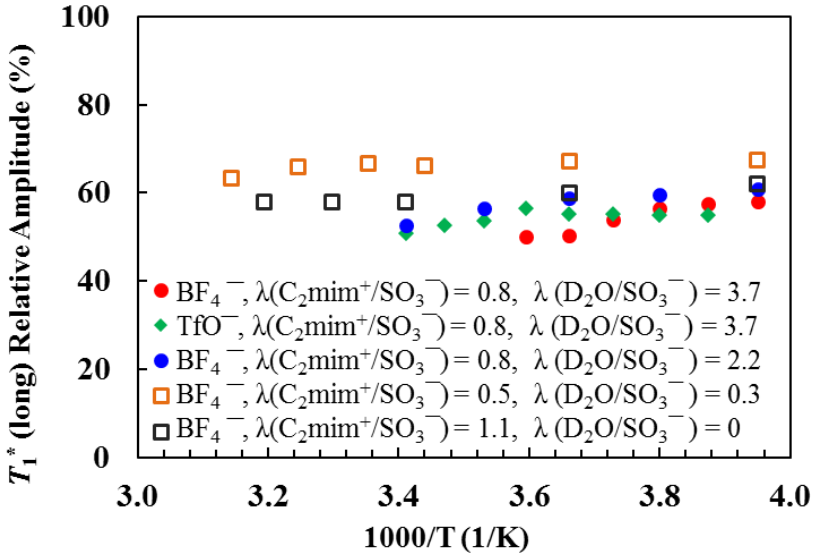

Figure 6.4. Relative amplitude of long T_1^* component vs. IL uptake, water content, and temperature.

Multi-component relaxation can be explained by the exchange between multiple sites with distinguishable local relaxation rates. In the fast exchange limit, a single average relaxation time is obtained by weighting each relaxation site, while in the slow exchange limit, multi-exponential decay is observed with each component representing the population and relaxation rate of each site. In intermediate exchange, the resulting apparent multi-exponential decay is also a function of effective exchange time using the Zimmerman-Brittin treatment.[36] This exchange model has been successfully applied to study "bound" and "free" water states in biological tissues and rocks.[37] In our case, the transition of ^{19}F T_1^* from one to two components is caused by reduced dynamics, and hence can be explained by the transition from the fast exchange limit to the intermediate or slow exchange limit. For a two-site problem, the effective exchange time for intermediate exchange is on the same order as $T_1^{(1)}$ or $T_1^{(2)}$. Although the apparent relaxation times T_1^* obtained using Eq. 6.4 are not true $T_1^{(1)}$ or $T_1^{(2)}$, as one would observe for each population of spins in isolation, we can roughly estimate the exchange time to be ~10 ms to 1 s. However, from PFG experiments (Section 6.3.3), we observe a single-component diffusion coefficient *D* and no significant change in *D* while varying diffusion time from 25 ms to 600 ms under most experimental conditions, which indicates an exchange time between sites of $\leq$ 25 ms. In addition, we obtain the same apparent T_2^* while changing the spacing between refocusing pulses in CPMG experiments from 0.1 ms to 4 ms (Figure 6.5), further indicating an exchange time $\leq$ 0.1 ms.[38] Therefore, the simple exchange model cannot be used to explain the multi-component relaxation we observed in Figure 6.2 and 6.3.

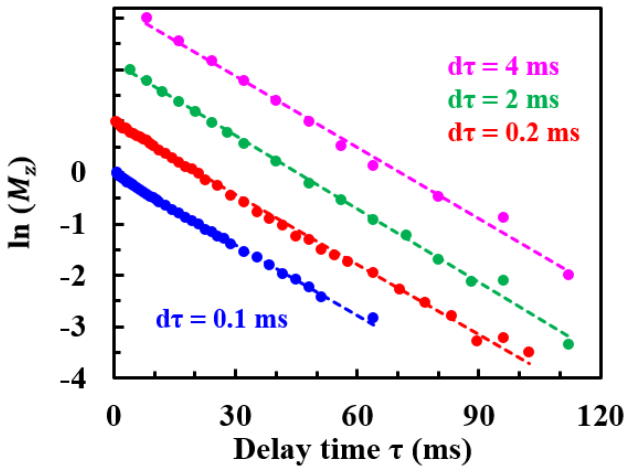

Figure 6.5. ^{19}F magnetization decay curves measured at 10 ℃ for $[C_2mim][BF_4]$ absorbed in Nafion with 17 wt% IL uptake $\lambda(C_2mim^+/SO_3^-) = 0.8$ at water content $\lambda(D_2O/SO_3^-) = 2.2$, and with different timing (echo delay) of refocusing pulses 0.1 ms, 0.2 ms, 2 ms and 4 ms.

For molecules or ions undergoing diffusion in porous media, the pore geometry (boundary conditions and size) as well as pore "surface sink" strength strongly affect spin relaxation.[37] Surface sinks are caused by enhanced intra- or inter-molecular dipolar interaction as the rotational and translational motion are hindered by surface sites (momentarily stronger intermolecular potentials) or the spins are strongly relaxed by the presence of paramagnetic centers at the pore surface. Here we apply the normal-modes solution by Brownstein and Tarr,[39]

$$M(\tau)/M_0 = \sum_{n=0}^{\infty} I_n \exp(-\tau/T_n). \qquad (6.5)$$

T_n are the eigenvalues that satisfy the diffusion equations considering surface or volume sink effects with certain boundary condition on the bounding surface, I_n are the relative intensities of T_n components. T_n and I_n are determined by boundary conditions, pore size, average sink

strength over the surface, and diffusion coefficient. We attempted to fit our data using the four different boundary conditions Brownstein and Tarr employed: planar, cylindrical, and spherical for surface sink, and annular cylindrical for volume sink. Unfortunately, none of these models fit our data well.

To understand our relaxation results, ion diffusion behaviors are crucial. From our diffusion studies below (Section 6.3.5), we conclude that while cations diffuse without geometric restriction in Nafion, anions are partially restricted when crossing domain junctions depending on temperature. In addition, anions experience more restriction from fixed sulfonate groups inside domains than cations. As shown in Figures 6.15a, the pore geometry involves a sub-micron domain (cylindrical or spherical) with a strong surface sink effect and several cylindrical chains with a weak volume sink effect inside the domain. Note that "pore" has a different meaning here than an open pore filled with liquid, and we will discuss this further in Sections 6.3.4 and 6.3.5 below. We are working toward a complete analysis of our relaxation data using this geometry. Here we emphasize that both anomalous relaxation and diffusion behaviors of ions are caused by the interactions between mobile IL ions and the fixed ionic groups of the polymer matrix, but on different time scales. T_1 is sensitive to molecular dynamics of ~ 1 ns, while the time scale for PFG measurement is ~ 100 ms. Comparing Figure 6.3c and 6.9c, T_1 shows deviation from single-component fitting at 20 ℃, while D experiences a transition from free to restricted diffusion at – 20 ℃.

6.3.2 Intermolecular NOEs

NOE spectroscopy has proven to be a powerful technique to obtain distance information between nuclear spins spatially separated within 5 Å and has been used to investigate nanostructural organization in neat ILs and their solutions.[19, 40] ^{1}H-^{19}F HOESY

studies on [C_2mim][BF_4] show strong intermolecular interaction between cation and anion, indicating the presence of a large number of ion clusters (or pairs) with nanosecond lifetimes in neat IL and even in solution.[40] However, a recent model of intermolecular NOEs in solutions proposed that the experimental cross-relaxation rate is dominated by a long range effect rather than short distance dipole-dipole interactions.[16, 41] The authors used [C_2mim][BF_4] as the model system to study the influence of pair dynamics including translational and rotational motions, as well as an "off-center" effect on intermolecular NOE. They found that for neat [C_2mim][BF_4], ions with intermolecular distance up to 15-30 Å can contribute to the NOE, therefore ^{1}H-^{19}F HOESY does not necessarily reveal site-specific local ion pair configuration, but an average of ion orientations over long distance.[41] With this in mind, we focus on the change in the NOE induced by different IL uptakes and water contents for a qualitative analysis, instead of trying to interpret detailed local structures.

Previous studies on neat ILs and their solutions employed phase-sensitive HOESY pulse sequences for signal enhancement. However, in our case, reduced motions for ILs soaked in membranes lead to very short T_2 and any pulse sequence with active T_2 decay period longer than a few ms cannot produce any signal. Hence we use a magnitude-mode HOESY pulse sequence. This pulse sequence produces no detectable cross peak intensities for neat ILs and their aqueous solutions using our experimental parameters with a mixing time of 50 ms. The relatively short mixing time 50 ms is used to minimize problems with spin-diffusion effects. For the IL mixture absorbed inside Nafion, we observe no cross peaks at -150 ppm (BF_4^-) and -80 ppm (TfO^-) with relatively high water content $\lambda(D_2O/SO_3^-) = 5.1$ (Figure 6.6a). However, cross peak intensities increase dramatically at first (Figure 6.6b and 6.6c) then decrease generally (Figure 6.6d) for BF_4^- upon decreasing water content until no cross peaks appear at

$\lambda(D_2O/SO_3^-) = 0$. We observe no cross peaks for TfO^- with all water contents. The decrease in NOE for BF_4^- and the absence of NOE for TfO^- when further lowering water content can be explained by shortened T_2^* (< 1 ms) for these ions such that no signal can survive the pulse sequence. The initial increase in the NOE for BF_4^- may be attributed to the depressed ion translations and rotations according to the pair dynamics model,[41] or to the formation of ion associations between C_2mim^+ and BF_4^-. A complete analysis of the effect of ion motions and configurations on the NOE change requires significantly more experiments and further refinement of the spin relaxation and NOE models to obtain rotational correlation times and to incorporate polymer matrix effects.

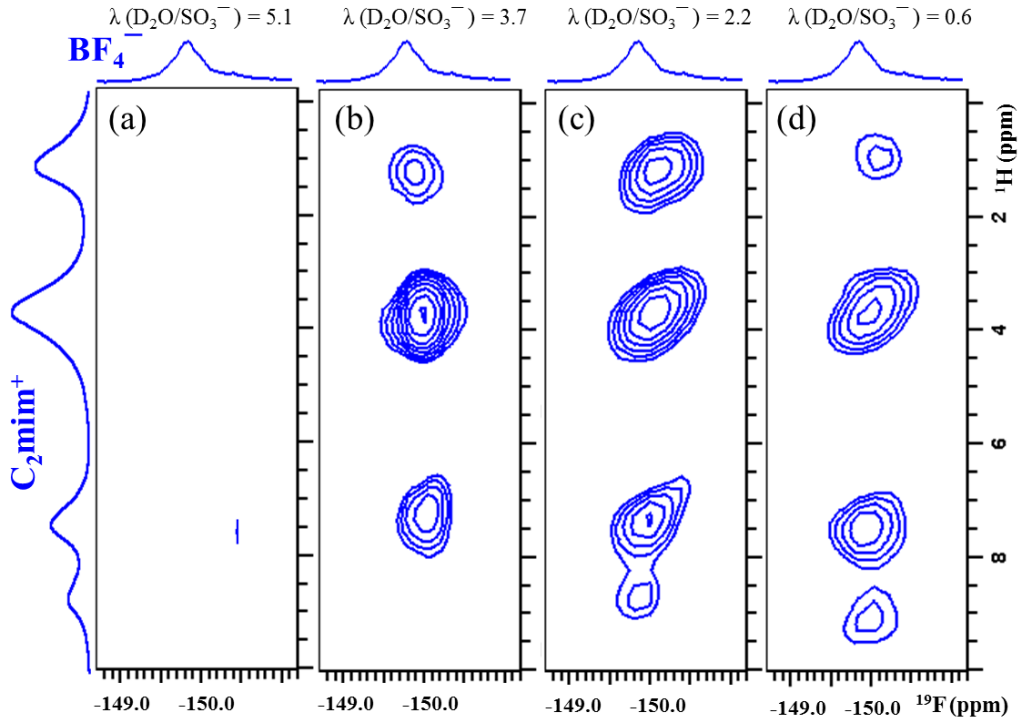

Figure 6.6 ^1H-^{19}F HOESY spectra with a mixing time of 50 ms of a mixture of $[C_2mim][BF_4]$ and $[C_2mim][TfO]$ inside Nafion at $\lambda(C_2mim^+/SO_3^-) = 0.8$ with varying $\lambda(D_2O/SO_3^-) = 5.1$ (a), 3.7 (b), 2.2 (c) and 0.6 (d). No cross peak is observed at -80 ppm (TfO^-) for mixing times

of 50 ms up to 1700 ms, spectra not shown. Note also that we observe no cross peaks for neat ILs with our pulse sequence and experimental parameters.

Here we try to separate the effects of ion motions and configurations by observing the change in NOE intensity with varying sample parameters: water content, temperature and IL uptake. Water molecules screen the electrostatic interactions between ions, therefore lowering water content leads to reduced ion motions due to increased intermolecular interactions. Furthermore, the influence of polymer matrix and the interactions between ions and fixed sulfonate groups increase as IL uptake decreases, resulting in reduced ion motions. In addition, as discussed in the relaxation and diffusion sections, lowering temperature reduces ion motions in a different way from lowering water content. ^{1}H & ^{19}F T_2 decreases as ion motions are slowed, thus reducing ^{1}H & ^{19}F overall signal intensity. As shown in Table 6.1, we observe a decrease in the NOE by lowering temperature and IL uptake, but a significant increase in the NOE by lowering water content. Hence we tentatively attribute this increase in the NOE to closer clustering between cations and anions (increased ion associations) at low water content. This system of ILs absorbed inside a nanoporous medium with varying water content, IL uptake and temperature can also serve as a useful and tunable example system to understand the effects of ion motions and configurations on the NOE.

Table 6.1 Change in ion motions and NOE intensity with varying sample parameters.

Sample parameters	Water content ↓	Temperature ↓	IL uptake ↓
Translation & rotation	↓	↓	↓
^{1}H & ^{19}F spin density	-	-	↓
^{1}H & ^{19}F T_2	↓	↓	↓
^{1}H & ^{19}F signal intensity	↓	↓	↓
^{1}H-^{19}F NOE intensity	↑ ↓	↓	↓
^{1}H-^{19}F distance	↓	-	-

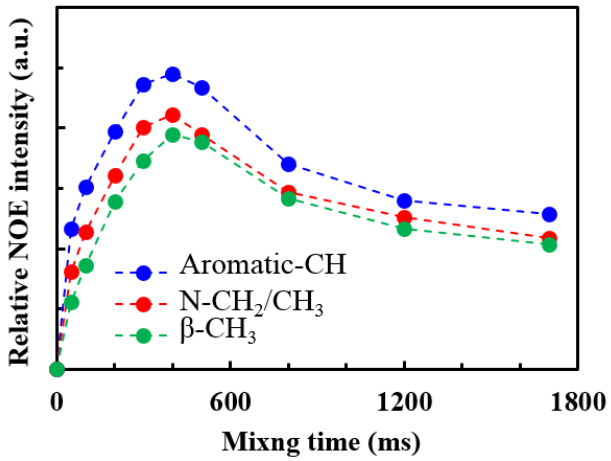

Figure 6.7 ^{1}H-^{19}F HOESY build-up curves for BF_4^- and C_2mim^+ of absorbed IL mixture at $\lambda(C_2mim^+/SO_3^-) = 0.8$ and $\lambda(D_2O/SO_3^-) = 0.6$.

Comparing Figure 6.6b, 6.6c and 6.6d, the preferred mean cation-anion interaction sites become closer to imidazole rings protons rather than alkyl tails when reducing water content.

^{1}H-^{19}F HOESY build-up curves at $\lambda(D_2O/SO_3^-) = 0.6$ (Figure 6.7) suggest a preferential distribution of BF_4^- around aromatic protons, indicating that electrostatic attraction has more influence on cation-anion interactions at lower water content. Furthermore, ^{19}F 1D selective NOESY experiments detect cross peaks for BF_4^- when excited at TfO^- (Figure 6.8a) at very low water content $\lambda(D_2O/SO_3^-) < 1.5$, implying the formation of anion-rich aggregates. This suggestion fits well with our published anionic association model obtained from self-diffusion studies.[11] At high water content, in the swollen hydrophilic domains of Nafion, water significantly screens the electrostatic attraction and repulsion between different ions due to its large dielectric constant, leading to free single ions surrounded by water molecules (Figure 6.8b). Intermolecular interactions become dramatically stronger with decreasing water content. The formation of (momentary) anion-rich associations such as anion-cation-anion triples (Figure 6.8c) can be reasoned by 1) fixed sulfonate groups repel anions, and a large and slow-moving triple works better to reduce the Coulomb energy of the system than two fast moving anions plus a cation or a fast moving anion plus a neutral dipole, and 2) the size, shape anisotropy, charge distribution and conformational flexibility of C_2mim^+, BF_4^- and TfO^- permit specific molecular packing to form anion-rich triples.

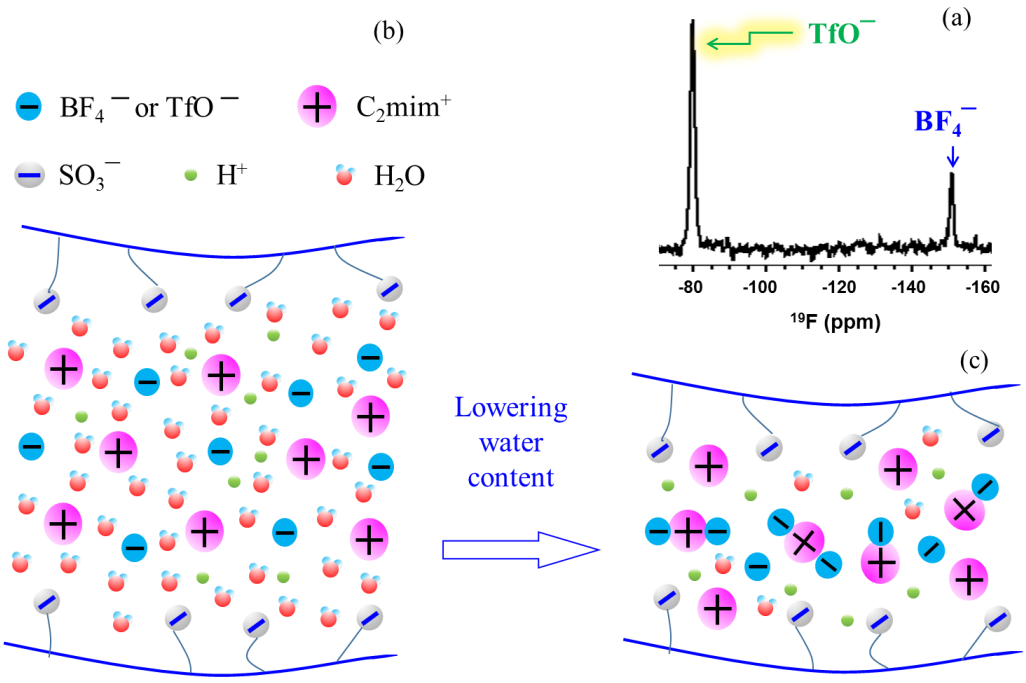

Figure 6.8 (a) ^{19}F 1D selective NOE spectrum for BF_4^- and TfO^- of the absorbed IL mixture at $\lambda(C_2mim^+/SO_3^-)$ = 0.8 and $\lambda(D_2O/SO_3^-)$ = 0.6. Below are schematic illustrations of ILs inside Nafion membranes at (b) high water content, and (c) low water content.

6.3.3 Diffusion: Transition from "free" to "restricted" diffusion regions

Here we vary the sample parameter space (temperature, water content, and IL uptake) to explore "free" diffusion regimes. IL species chemical structure also significantly affects ion transport behaviors, but here we only focus on [C_2mim][BF_4] and [C_2mim][TfO]. The criterion for free diffusion is 1) signal attenuation curves collected from PFG experiments cleanly fit using the Stejskal-Tanner relation Eq. 6.3[35] and 2) diffusion coefficients *D* obtained from the fittings are independent of diffusion time. Surprisingly, cations maintain "free" diffusion under all our measurements, while anions experience a transition from "free" to "restricted" regimes when lowering IL uptake, water content or temperature. For example, with IL uptake $\lambda(C_2mim^+/SO_3^-)$ = 0.8 and T = 313 K, both cation and anion diffusion are non-restricted from

$\lambda(D_2O/SO_3^-)$ = 5.1 to 0.6 with a reverse in the ratio $D_{catoion}/D_{anion}$ when lowering $\lambda(D_2O/SO_3^-$), which was explained by the formation of anion-rich aggregates (Figure 6.9a).[11] When lowering temperature from 313 K to 253 K, at high water content, $\lambda(D_2O/SO_3^-)$ = 5.1 and 3.7, we observe free diffusion and D_{cation}/D_{anion} is nearly independent of temperature (Figure 6.9b and 6.9c). However, at low water content, $\lambda(D_2O/SO_3^-)$ = 2.2 and 0.6, we observe the transition to restricted diffusion at T = 253 K and 303 K (Figure 6.9c and 6.10), respectively. As mentioned earlier, higher IL uptake or water content creates expanded hydrophilic domains in Nafion and thereby reduces the confinement effect due to the polymer-fixed sulfonate groups. On the other hand, higher water content or temperature leads to faster ion dynamics in a different way. Therefore, we expect to observe a transition from free to restricted diffusion when lowering IL uptake, water content or temperature. However, in order to better understand the difference in cation and anion diffusion behaviors and how they are related to Nafion morphology, here we eliminate the parameter water content and study dry membranes with $\lambda(D_2O/SO_3^-)$ = 0 for the following studies.

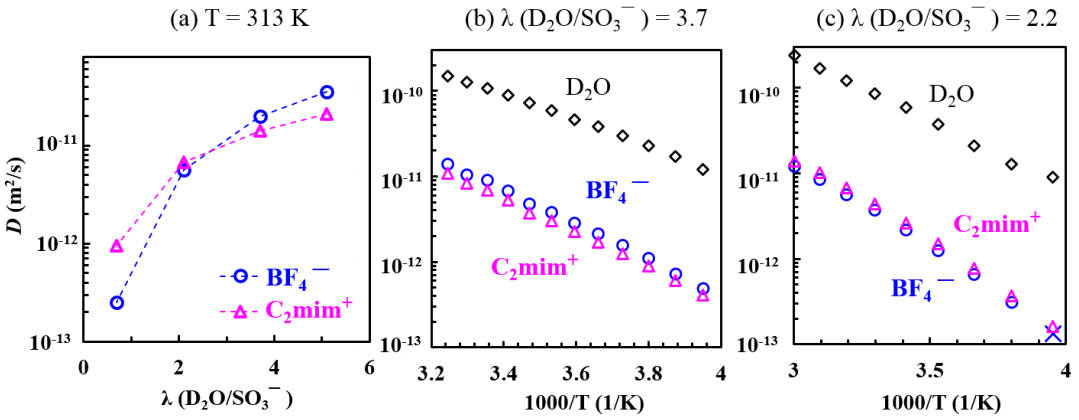

Figure 6.9 Self-diffusion coefficients D of C_2mim^+, BF_4^-, and D_2O at $\lambda(C_2mim^+/SO_3^-)$ = 0.8 vs. $\lambda(D_2O/SO_3^-)$ at T = 313 K (a), and vs. 1000/T at $\lambda(D_2O/SO_3^-)$ = 3.7 (b) and 2.2 (c).

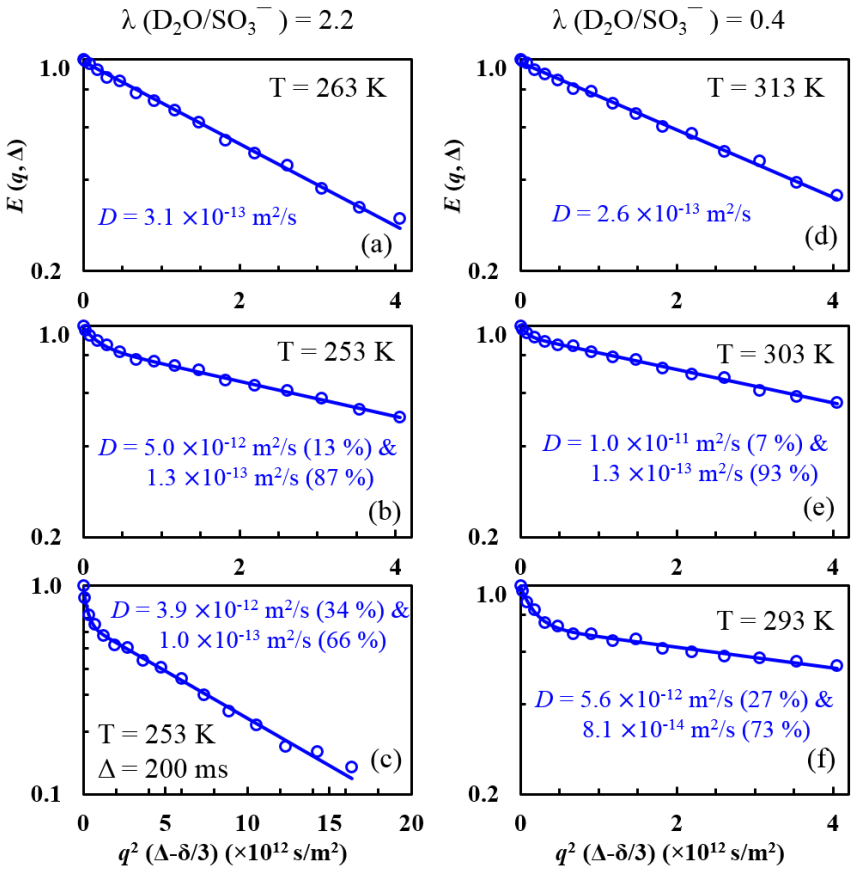

Figure 6.10 Transition from "free" to "restricted" diffusion regimes. Left panel: signal attenuation $E(q,\Delta)$ vs. attenuation parameter $q^2(\Delta - \delta/3)$ for ^{19}F of BF_4^- at $\lambda(D_2O/SO_3^-)$ = 2.2, (a) T = 263 K, (b) T = 253 K, and (c) T = 253 K. Right panel: $E(q,\Delta)$ vs. $q^2(\Delta - \delta/3)$ for ^{19}F of BF_4^- at $\lambda(D_2O/SO_3^-)$ = 0.6, (a) T = 313 K, (b) T = 303 K, (c) T = 293 K. All plots are based on Δ = 50 ms, except (c) is based on Δ = 50 ms.

6.3.4 Diffusion: Dimensional restriction and single-file diffusion

In this section, we focus on restricted ion diffusion by studying $[C_2mim][BF_4]$ absorbed inside Nafion with $\lambda(C_2mim^+/SO_3^-)$ = 1.1 at low water content $\lambda(D_2O/SO_3^-)$ = 0 and at T = 273 – 303 K, where confinement effects in the polymer matrix are enhanced. Figure 6.11 shows surprising differences between cation and anion diffusion in the ionomer. For free diffusion,

according to Eq. 6.3, the slope of $\ln(E(q,\Delta))$ vs. $q^2(\Delta - \delta/3)$ directly gives diffusion coefficient D, which is independent of diffusion time Δ. Cation diffusion behavior (Figure 6.11a) is exactly the same as free diffusion with $D_{\text{cation}} = 2.5 \times 10^{-13}\text{m}^2/\text{s}$ over the experimental diffusion length 0.15 – 0.55 μm, which is remarkable considering the ionic attraction between cation and fixed sulfonate group in the polymer matrix. On the contrary, anion diffusion behaviors (Figure 6.11b and 6.11d) are restricted in three ways. (1) $E(q,\Delta)$ vs. $q^2(\Delta - \delta/3)$ is linear at short Δ (≤ 50 ms), but becomes curved at long Δ (≥ 100 ms). (2) Signal decay is much slower, noting the difference in *x* and *y*-axis scales between cation and anion plots. At $\Delta = 50$ ms, $D_{\text{anion}} = 8.2 \times 10^{-14}\text{m}^2/\text{s}$ obtained using Eq. 6.3, which is 3× smaller than D_{cation}. (3) $E(q,\Delta)$ vs. q^2 collapse onto a single curve at long Δ (≥ 200 ms), indicating a highly restricted or isolated environment.

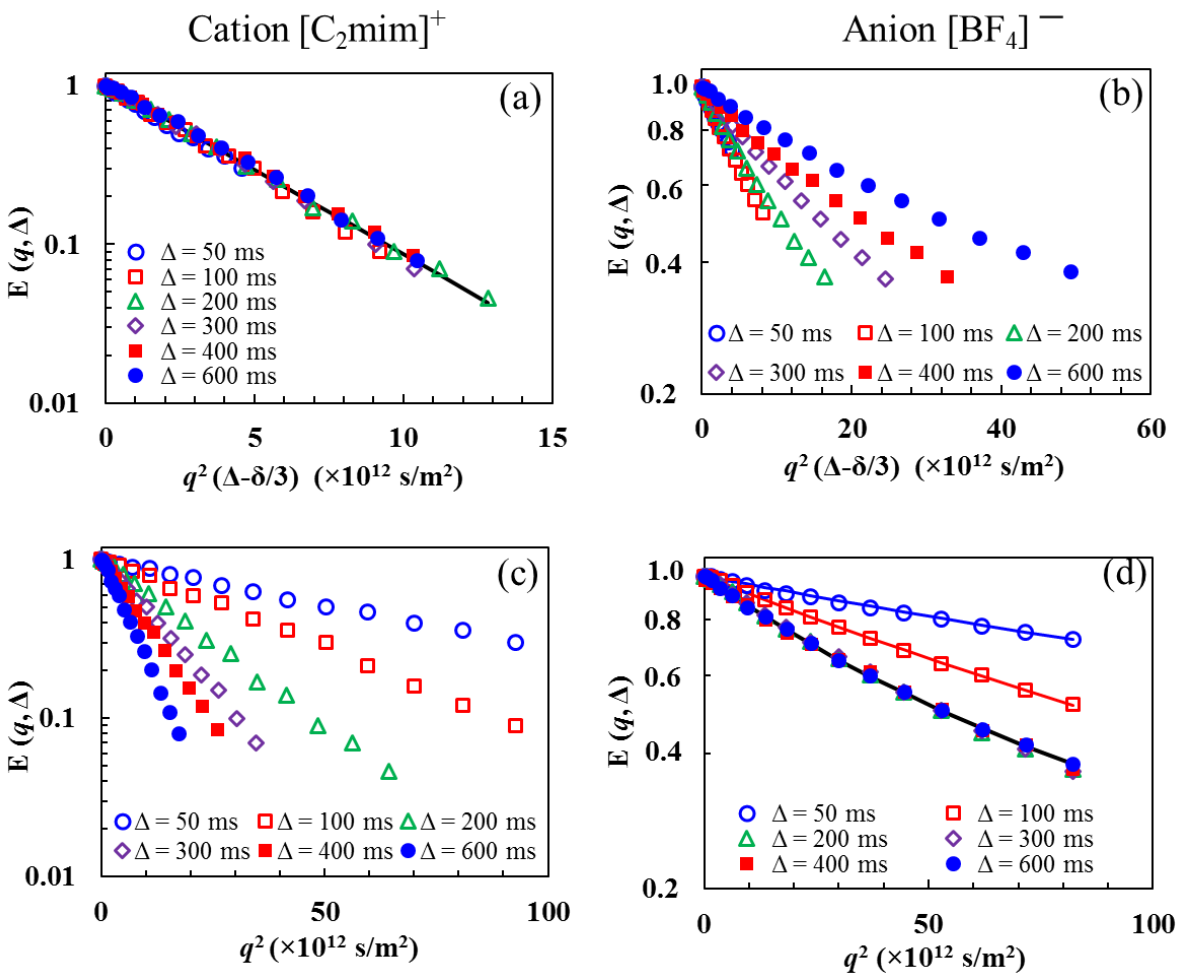

Figure 6.11 Signal attenuation $E(q,\Delta)$ vs $q^2(\Delta - \delta/3)$ for cation (a) and anion (b), and signal attenuation $E(q,\Delta)$ vs q^2 for cation (c) and anion (d), all corresponding to [C2mim][BF4] inside Nafion at λ(C_2mim^+/SO_3^-) = 1.1, λ(D_2O/SO_3^-) = 0, and T = 293 K. Here signal attenuation $E(q,\Delta) \equiv I/I_0$, $q \equiv \gamma g \delta$, γ is the gyromagnetic ratio, g is gradient strength, δ is gradient pulse duration, and Δ is diffusion time. The black line of (a) is the best fit to the data using the Stejskal-Tanner relation $E(q,\Delta) = \exp(-q^2 D(\Delta - \delta/3))$. The lines of (d) show best fits using the dimensionally restricted model Eq. 6.6.

Mitra and Sen demonstrated that the deviation of $E(q,\Delta)$ from quadratic behavior in q in a porous medium contains considerably more valuable information about the medium

microgeometry than enhanced spin relaxation or macroscopic diffusion coefficient.[42] A diffusion model that fits our anion diffusion behaviors well is a collection of randomly oriented cylindrical pores of radius r, as derived by Mitra and Sen[42]

$$E(q,\Delta) = \exp(-D\,\Delta\,q^2)\int_0^1 \exp[q^2\,(D\,\Delta\,-\,\langle r_\perp(\Delta)^2\rangle/4)\,(1-x^2)]dx \qquad (6.6)$$

where $r_\perp(\Delta)$ is the displacement of diffusing species perpendicular to the cylindrical pore axis. A reasonable fitting form of this perpendicular displacement is

$$\frac{r_\perp(\Delta)^2}{4} = \frac{r^2}{4}\left[1-\exp\left(-\frac{4D\Delta}{r^2}\right)\right]. \qquad (6.7)$$

When $D\Delta \ll r^2$, $\langle r_\perp(\Delta)^2\rangle/4 = D\Delta$, $E(q,\Delta) = \exp(-D\,\Delta\,q^2)$, apparent free diffusion is expected. When the product $D\Delta \gg r^2$, $\langle r_\perp(\Delta)^2\rangle/4 = r^2/4$, and diffusion is restricted perpendicular to the cylindrical pore aixs. Therefore in this model, the curvature of $E(q,\Delta)$ vs. q^2 increases as diffusion time increases, which is what we observe for anion diffusion (Figure 6.11).

By fitting the experimental data at 293 K, we obtain radius r of 0.07 μm for all diffusion times. Replacing $D\Delta$ with mean-square displacement $\overline{Z^2}/2$ in Eq. 6.6 we can find the dependence of $\overline{Z^2}$ on Δ. $\overline{Z^2}$ increases nearly linearly with Δ initially, from which we extract $D = 2.1\times10^{-13}\mathrm{m}^2/\mathrm{s}$ (Figure 6.12, left), revealing that anion diffusion is actually comparable to cation diffusion if the geometric confinement effect is removed. Then $\overline{Z^2}$ plateaus at $\Delta \geq 300$ ms, suggesting an isolated geometry with diffusion length L ($L \equiv \sqrt{\overline{Z^2}}$ at plateau) of 0.29 μm at 293 K.

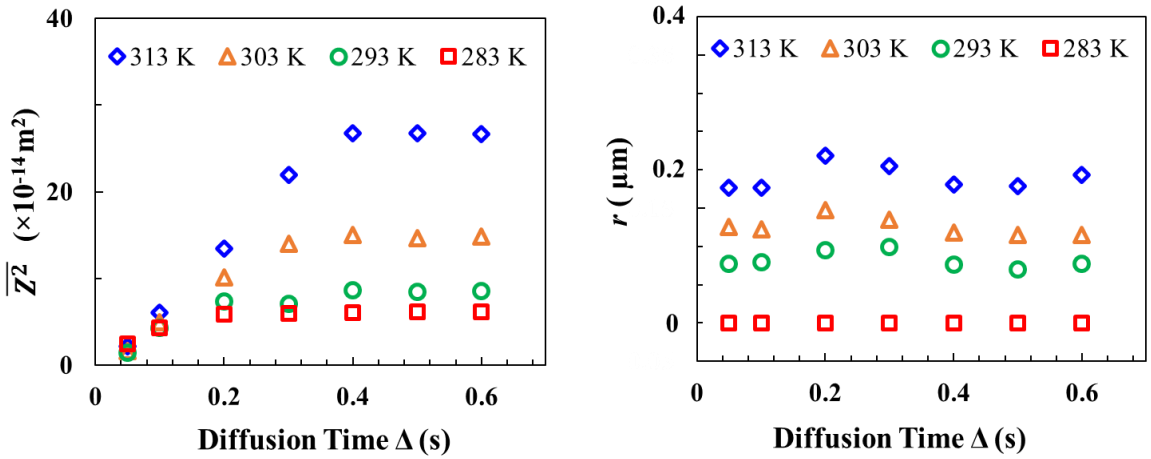

Figure 6.12 Mean-square displacement $\overline{Z^2}$ and restricted domain radius r for diffusing anions obtained by fitting experimental signal attenuation data using Eq. 6.6 at varying diffusion times and temperatures.

Strikingly, both $\overline{Z^2}$ and r change significantly as a function of temperature, as shown in Figure 6.12. By increasing temperature to 303 K, L and r increase to 0.39 and 0.11 μm, respectively. Besides, $\overline{Z^2}$ vs. Δ is linearly dependent at short Δ for T≥ 293 K and the Δ value at which $\overline{Z^2}$ reaches plateau increases with temperature. With this trend, we expect the restriction effect may completely disappear at high enough temperature.

Even more extraordinary is the observation that when reducing temperature to 283 K, the curvature of $E(q,\Delta)$ vs. q^2 increases significantly at short Δ (Figure 6.13a), resulting in $r = 0$ (Figure 6.12b). This is usually referred to a 1D or single-file diffusion model by setting $r_\perp(\Delta) = 0$ in Eq. 6.6

$$E_{1D}(q,\Delta) = \int_0^1 \exp(-q^2\, D\, \Delta\, x^2) dx\,. \qquad (6.8)$$

The resultant $\overline{Z^2}$ vs. Δ is shown in Figure 6.12, left (red square), and $\overline{Z^2}$ vs. $\Delta^{1/2}$ in Figure 6.13b. It is clear that $\overline{Z^2}$ is linearly dependent on $\Delta^{1/2}$ rather than Δ at short Δ ($\leq$ 200 ms), another strong indicator of single-file diffusion. L = 0.24 μm at the plateau in Figure 6.13b where $\Delta \geq 200$ ms. On the other hand, we again observe essentially unrestricted cation diffusion at 283 K with $D_{\text{cation}} = 2.0 \times 10^{-13}\text{m}^2/\text{s}$ at $\Delta = 25$ ms which reduces only slightly to $1.8 \times 10^{-13}\text{m}^2/\text{s}$ at $\Delta = 500$ ms.

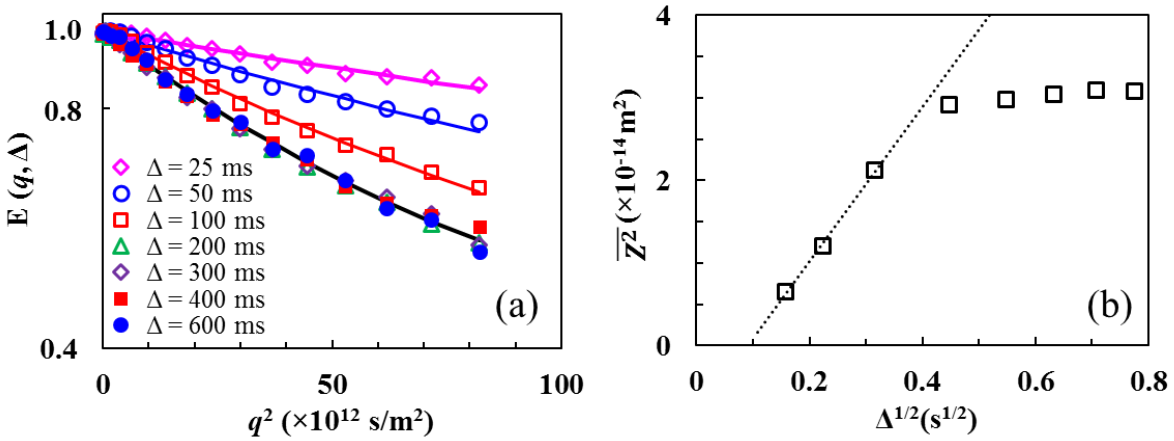

Figure 6.13 (a) Anion diffusion plots $E(q, \Delta)$ vs. q^2 for [C_2mim][BF_4] inside Nafion at λ(C_2mim^+/SO_3^-) = 1.1, λ(D_2O/SO_3^-) = 0 and T = 283 K. The lines show best fits using the single-file diffusion model of Eq. 6.8 (b) The fitting parameter $\overline{Z^2}$ plotted vs. $\Delta^{1/2}$ shows linear dependence at $\Delta \leq 200$ ms.

Figure 6.14 summarizes ion diffusion behaviors of [C_2mim][BF_4] absorbed inside dry Nafion as a function of T. While cations diffuse freely independent of T, the sub-micron restriction length and radius of the anion diffusion increase non-linearly with T (Figure 6.14b). The apparent D_{BF4} obtained from Stejskal-Tanner fitting (Eq. 6.3) at Δ = 50 ms is 4-fold smaller than D_{C2mim}. However, the local anion diffusion D_{BF4} calculated after removing the geometric restriction effect is 3/4 that of D_{C2mim} (Figure 6.14a). Considering the relatively

larger ion size of C_2mim^+ ($r_{C2mim}/r_{BF4} = 1.4$)[11] and the drag effect of polymer-fixed SO_3^- groups on C_2mim^+, the fact that D_{C2mim} is still greater than the local D_{BF4} further indicates the formation of anion-rich aggregates, as we concluded in Section 6.3.2. Here we emphasize that we only observe signals that survive the active T_2 decay and T_1 decay periods. This is particularly important here where molecular dynamics is strongly reduced due to the confinement.

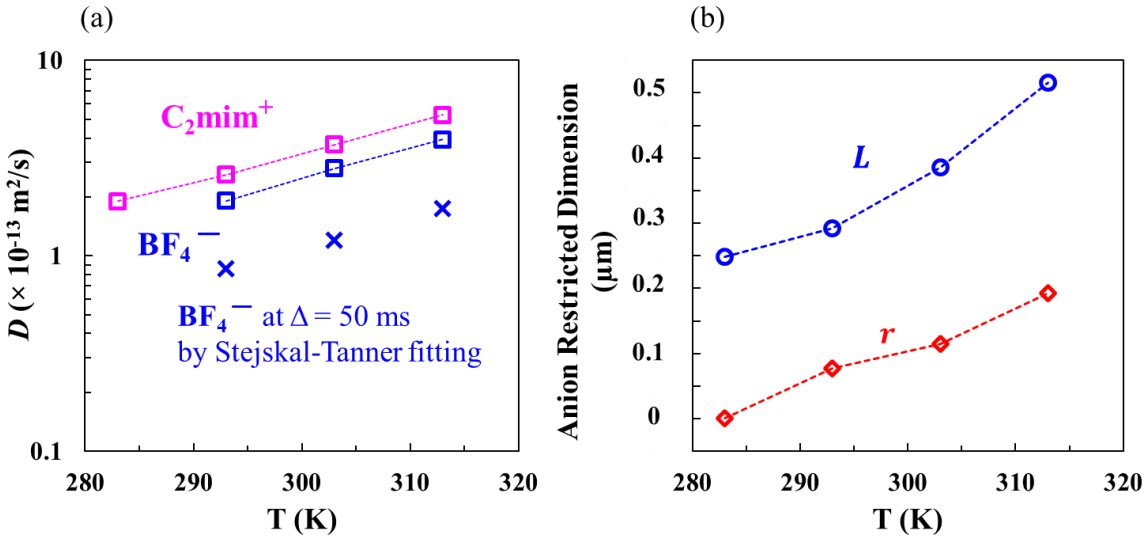

Figure 6.14 Summary of ion diffusion coefficients (a) and anion restricted dimension (b) as a function of temperature. *L* and *r* are the length and radius of the randomly distributed cylindrical pores used to fit anion restricted diffusion, respectively.

Other models may also be used to explain these anomalous diffusion behaviors. We can add diffusion anisotropy into the model by setting $D_\perp$ (diffusion perpendicular to thecylindrical pore axis) different from $D_\parallel$ (diffusion along the cylindrical pore axis), but we observe no significant difference in the fitting results. The reason is in Eq.6.7, in which $\langle r_\perp(\Delta)^2\rangle/4 \sim r^2/4$ as long as $D_\perp \Delta \geq r^2$, which holds for most of our data. Therefore the

geometric confinement contributes more to the anomalous diffusion curves than diffusion anisotropy. Another model is a distribution of isolated spherical pores with different diameters, as discussed in the Ph.D. thesis of our group's previous student Jianbo Hou.[43] For diffusion confined within isolated pores of radius R, if diffusion length is larger than the pore size, then[44]

$$E(q,\Delta) = \exp\left(-\frac{q^2R^2}{5}\right). \tag{6.9}$$

Assuming a Gaussian distribution for the pore size,

$$P(R) = \frac{1}{\sqrt{\pi\sigma}}\exp\left(-\frac{(R-R_0)^2}{\sigma^2}\right) \tag{6.10}$$

we have finally

$$E(q,\Delta) = \frac{1}{\sqrt{1+\frac{q^2\sigma^2}{5}}}\exp\left(-\frac{q^2R_0^2}{5+q^2\sigma^2}\right). \tag{6.11}$$

Using this model, the obtained pore size R_0 is comparable to the diffusion length L obtained using our cylindrical pore model. In this model, the anomalous diffusion is caused by the size distribution of spherical pores, but in our model, shape anisotropy of monodisperse cylindrical pores is the reason for the deviation. Both models have their grounds, but the spherical pore model cannot explain the single-file diffusion curves at short Δ, therefore we prefer the cylindrical pore model.

6.3.5 Multiscale structures of Nafion governing ion diffusion

To understand the dramatic difference between cation and anion diffusion as well as the unusual temperature dependence of anion diffusion, we have to look closely into the multiscale structure of Nafion. As mentioned earlier, several models have been proposed for Nafion morphology. For example, in one model , elongated ribbon-like polymeric aggregates

with length a few hundred nanometers formed from polymer chains backbones are surrounded by the sidechain polymer-fixed sulfonate groups and the counterions.[24-25] These aggregates organize into bundles with preferential orientational ordering so as to construct sub-micron domains that each have random orientations in space.[43-45] In the model of water nanochannels, these sub-micron domains are instead formed by interconnected hydrophilic channels formed from aggregates of sulfonate groups.[46] These models appear to be conceptually distinct, but they are actually compatible by changing perspectives. When the ribbons of polymeric aggregates are close enough, hydrophilic channels are formed between them. So these models are essentially exchangeable depending on the size of and distance between the polymeric aggregates. Here we accept the idea of sub-micron domains that possess intradomain orientational order but are globally orientationally disordered, and we demonstrate the influence of domain boundaries on ion diffusion.

Anion diffusion restricted between sub-micron domains. We attribute the isolated geometry probed by anion diffusion with a length of 0.29 μm and radius of 0.07 μm at 293 K to an average boundary effect due to sub-micron domain boundaries, and this only affects anion diffusion. At domain junctions, we propose that polymeric aggregations from one domain may interact with those from other domains, resulting in a higher density of sulfonate groups, which we call the "SO_3^- boundary", as shown in Figure 6.15. This boundary attracts cations and allows them to migrate through any defects present at the domain boundaries, due to the net attractive electrostatic interaction between the boundary and cations. Although the drag effect of the boundary may temporally trap cations and reduce cation diffusion rates, the relatively small length of the boundary allows for overall free cation diffusion during the experimental diffusion time with a diffusion length of 0.1 – 2 μm. We note that Ohkubo et al. investigated

the presence of a micron-scale structural characteristic inside Nafion using restricted water diffusion (^1H_2O) with the oscillating gradient spin echo (OGSE).[45] However, we repeated some of their measurements without observing any restricted water diffusion under the same experimental conditions.[33] Here we want to emphasize that these sub-micron domain boundaries are not obstacles to neither cation nor water transport during our experimental diffusion time. On the contrary, the boundary restricts only anion transport due to repulsive forces, hence anion motions are confined by the domain boundaries (Figure 6.15).

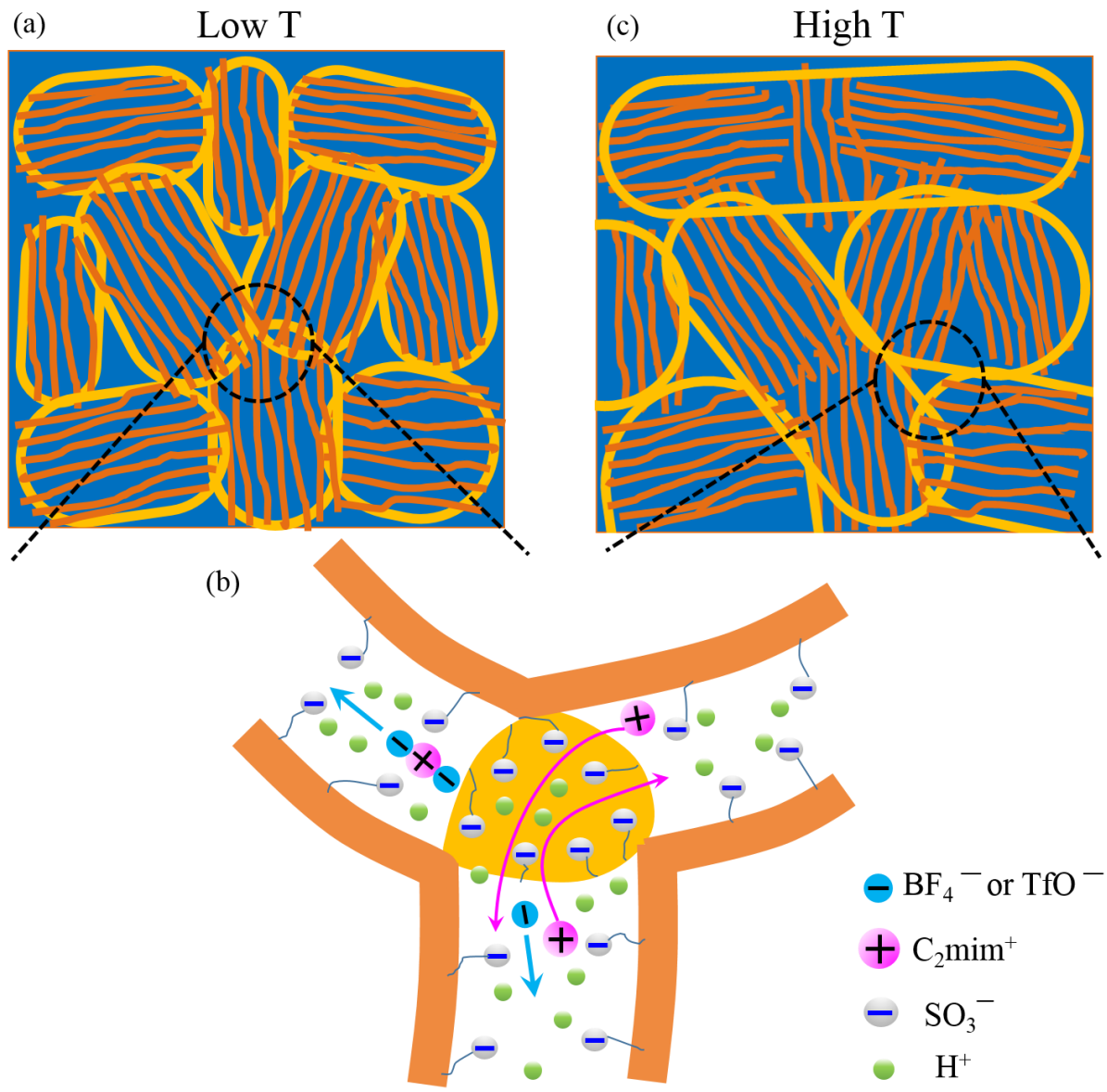

Figure 6.15 The influence of domain boundaries on ion diffusion. Schematic illustration of (a) Nafion structures with sub-micron domains at low T. Orange lines represent polymeric hydrophobic aggregates, yellow curves represent domain boundaries, and the blue background represent hydrophilic transport matrix. (b) Cations can diffuse through domain boundaries, while anions are restricted by the SO_3^- boundaries. (c) The boundary effect is dependent on thermal fluctuations such that the effective domain sizes grow (boundaries disappear) with increasing T.

More important, the SO_3^- boundary effect is not static and varies with temperature (Figure 6.15). When temperature increases, anions may diffuse through domain boundaries if thermal fluctuations of the polymer-fixed SO_3^- groups and anions can overcome the electric potential between them. Therefore the length and radius obtained from fitting anion diffusion data are not necessarily the size of simple structural sub-micron domains as one could determine by, *e.g.*, X-ray scattering, but are the size of detectable confinement boundaries to anion diffusion. The nonlinear increase in the confinement size with temperature signifies the SO_3^- density variation and heterogeneous nature of domain boundaries. According to this trend, at high enough temperature, the boundary effect will disappear and anions will exhibit unrestricted diffusion like cations and water. At low enough temperature, the confinement size will plateau and represent the average domain size that would likely link to a defined polymer structure observable by microscopy or scattering. As shown in Figure 6.14b, the boundary length (and radius) decreases from 0.53 (0.19) μm at 313 K, to 0.39 (0.11) μm at 303 K, 0.29 (0.07) μm at 293 K, and 0.25 (0) μm at 283 K. We can thus notice that the domain size is ~ 0.1 μm, consistent with the characteristic size obtained from SAXS.[24] The sudden decrease in the radius at 283 K involves the confinement effect within domains and we will discussed this next.

Single-file anion diffusion. In the elongated polymeric aggregates model, the distance between aggregates is a few nanometers depending on water content. Here with 19 wt% IL uptake $\lambda(C_2mim^+/SO_3^-) = 1.1$, we estimate this distance is ~ 2 nm. Considering the size of SO_3^-, C_2mim^+, and BF_4^- ions and/or larger ion aggregates s suggested by the NOE studies, up to 2 or 3 moving species can exist in a cross-section (Figure 6.16a). The polymer-fixed SO_3^- groups lining the aggregates serve to attract cations, and the energy required to move a cation

from one negatively charged chain to another is near zero, therefore cations can transport freely between aggregates (Figure 6.16b). On the contrary, the repulsion force between SO_3^- groups and anions push anionic species to the center of diffusing "channels", especially considering the larger anion-rich aggregates. At high temperature, anions may move in 3D due to fast thermal fluctuations, and with a lower diffusion coefficient perpendicular to the long axis. However, at low temperature, anions may not overcome the electric potential and can only transport in the center along the long axis, leading to single-file diffusion behavior (Figure 6.16c). Therefore, it is clear that the "transition" from the polymeric aggregates model to the hydrophilic nanochannel model depends not only on the size of and distance between polymeric aggregates, but also on the dynamics of fixed SO_3^- groups.

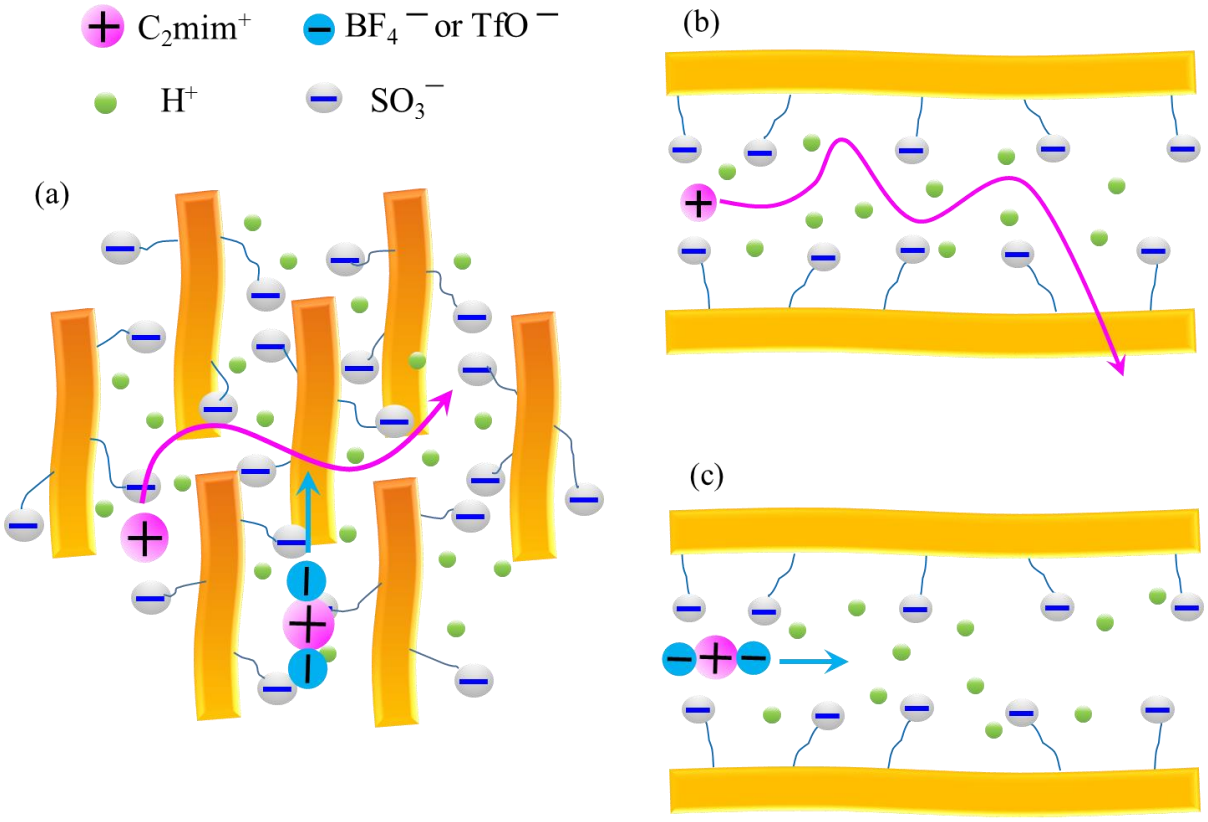

Figure 6.16 (a) Elongated ribbon-like aggregates formed from polymer chains are surrounded with fixed SO_3^- groups and counterions. While cations may diffuse in 3D between

aggregations (b), anions are pushed to the center and can only diffuse in 1D along the "nanochannels" at low temperature (c).

6.4 Conclusion

We employ a combination of NMR techniques to obtain a comprehensive understanding of ion configuration and transport behaviors of ILs inside the benchmark ionomer Nafion. Spin relaxation shows that anion relaxation is more influenced by the fixed sulfonate groups as compared to the cation. ^{1}H-^{19}F HOESY and ^{19}F-^{19}F 1D NOE spectroscopy confirm our assumption of the formation of anion-rich ion aggregates at low water content in the ionomer. While we observe unrestricted diffusion behaviors for cations and anions at high water content, temperature and IL uptake, the full q dependence of signal attenuation $E(q, \Delta)$ in PFG experiments demonstrates that anion diffusion is restricted both between domain boundaries and within domains at low water content. The temperature dependence of this restriction effect further shows that the relative importance of thermal fluctuations and electric potential driven by the polymer-fixed ionic groups plays an essential role in the transport behaviors of ions with like charge.

Reference

(1) Tokuda, H.; Hayamizu, K.; Ishii, K.; Susan, M.; Watanabe, M. Physicochemical Properties and Structures of Room Temperature Ionic Liquids. 1. Variation of Anionic Species. *J. Phys. Chem. B* **2004,** *108*, 16593-16600.

(2) Tokuda, H.; Hayamizu, K.; Ishii, K.; Susan, M. A.; Watanabe, M. Physicochemical Properties and Structures of Room Temperature Ionic Liquids. 2. Variation of Alkyl Chain Length in Imidazolium Cation. *J Phys Chem B* **2005,** *109*, 6103-10.

(3) Tokuda, H.; Ishii, K.; Susan, M. A. B. H.; Tsuzuki, S.; Hayamizu, K.; Watanabe, M. Physicochemical Properties and Structures of Room-Temperature Ionic Liquids. 3. Variation of Cationic Structures. *The Journal of Physical Chemistry B* **2006,** *110*, 2833-2839.
(4) MacFarlane, D.; Forsyth, S.; Golding, J.; Deacon, G. Ionic Liquids Based on Imidazolium, Ammonium and Pyrrolidinium Salts of the Dicyanamide Anion. *Green Chemistry* **2002,** *4*, 444-448.
(5) Galinski, M.; Lewandowski, A.; Stepniak, I. Ionic Liquids as Electrolytes. *Electrochimica Acta* **2006,** *51*, 5567-5580.
(6) Forsyth, S.; Pringle, J.; MacFarlane, D. Ionic Liquids-an Overview. *Australian Journal of Chemistry* **2004,** *57*, 113-120.
(7) Tokuda, H.; Tsuzuki, S.; Susan, M. A. B. H.; Hayamizu, K.; Watanabe, M. How Ionic Are Room-Temperature Ionic Liquids? An Indicator of the Physicochemical Properties. *The Journal of Physical Chemistry B* **2006,** *110*, 19593-19600.
(8) Li, Q.; Jensen, J. O.; Savinell, R. F.; Bjerrum, N. J. High Temperature Proton Exchange Membranes Based on Polybenzimidazoles for Fuel Cells. *Progress in Polymer Science* **2009,** *34*, 449-477.
(9) Geise, G. M.; Cassady, H. J.; Paul, D. R.; Logan, B. E.; Hickner, M. A. Specific Ion Effects on Membrane Potential and the Permselectivity of Ion Exchange Membranes. *Physical Chemistry Chemical Physics* **2014,** *16*, 21673-21681.
(10) Kreuer, K.-D. Ion Conducting Membranes for Fuel Cells and Other Electrochemical Devices. *Chemistry of Materials* **2014,** *26*, 361-380.
(11) Hou, J.; Zhang, Z.; Madsen, L. A. Cation/Anion Associations in Ionic Liquids Modulated by Hydration and Ionic Medium. *The Journal of Physical Chemistry B* **2011,** *115*, 4576-4582.
(12) Park, M. J.; Choi, I.; Hong, J.; Kim, O. Polymer Electrolytes Integrated with Ionic Liquids for Future Electrochemical Devices. *Journal of Applied Polymer Science* **2013,** *129*, 2363-2376.
(13) Tokuda, H.; Hayamizu, K.; Ishii, K.; Susan, M. A. B. H.; Watanabe, M. Physicochemical Properties and Structures of Room Temperature Ionic Liquids. 2. Variation of Alkyl Chain Length in Imidazolium Cation. *The Journal of Physical Chemistry B* **2005,** *109*, 6103-6110.
(14) Gebbie, M. A.; Valtiner, M.; Banquy, X.; Fox, E. T.; Henderson, W. A.; Israelachvili, J. N. Ionic Liquids Behave as Dilute Electrolyte Solutions. *Proceedings of the National Academy of Sciences* **2013,** *110*, 9674-9679.
(15) Weingärtner, H. Understanding Ionic Liquids at the Molecular Level: Facts, Problems, and Controversies. *Angewandte Chemie International Edition* **2008,** *47*, 654-670.
(16) Gabl, S.; Steinhauser, O.; Weingärtner, H. From Short-Range to Long-Range Intermolecular NOEs in Ionic Liquids: Frequency Does Matter. *Angewandte Chemie International Edition* **2013,** *52*, 9242-9246.
(17) Gozzo, F. C.; Santos, L. S.; Augusti, R.; Consorti, C. S.; Dupont, J.; Eberlin, M. N. Gaseous Supramolecules of Imidazolium Ionic Liquids: "Magic" Numbers and Intrinsic Strengths of Hydrogen Bonds. *Chemistry – A European Journal* **2004,** *10*, 6187-6193.

(18) Dupont, J. From Molten Salts to Ionic Liquids: A "Nano" Journey. *Accounts of Chemical Research* **2011,** *44*, 1223-1231.
(19) Corvo, M. C.; Sardinha, J.; Menezes, S. C.; Einloft, S.; Seferin, M.; Dupont, J.; Casimiro, T.; Cabrita, E. J. Solvation of Carbon Dioxide in [C4mim][Bf4] and [C4mim][Pf6] Ionic Liquids Revealed by High-Pressure NMR Spectroscopy. *Angewandte Chemie International Edition* **2013,** *52*, 13024-13027.
(20) Hunt, P. A.; Ashworth, C. R.; Matthews, R. P. Hydrogen Bonding in Ionic Liquids. *Chemical Society Reviews* **2015,** *44*, 1257-1288.
(21) Zhiyang, Z.; Madsen, L. A. Observation of Separate Cation and Anion Electrophoretic Mobilities in Pure Ionic Liquids. *Journal of Chemical Physics* **2014,** *140*, 084204-1-084204-10.
(22) Mauritz, K. A.; Moore, R. B. State of Understanding of Nafion. *Chemical Reviews* **2004,** *104*, 4535-4586.
(23) Gierke, T. D.; Munn, G. E.; Wilson, F. C. The Morphology in Nafion Perfluorinated Membrane Products, as Determined by Wide- and Small-Angle X-Ray Studies. *Journal of Polymer Science: Polymer Physics Edition* **1981,** *19*, 1687-1704.
(24) Rubatat, L.; Rollet, A. L.; Gebel, G.; Diat, O. Evidence of Elongated Polymeric Aggregates in Nafion. *Macromolecules* **2002,** *35*, 4050-4055.
(25) Rubatat, L.; Gebel, G.; Diat, O. Fibrillar Structure of Nafion: Matching Fourier and Real Space Studies of Corresponding Films and Solutions. *Macromolecules* **2004,** *37*, 7772-7783.
(26) Gebel, G.; Diat, O. Neutron and X-Ray Scattering: Suitable Tools for Studying Ionomer Membranes. *Fuel Cells* **2005,** *5*, 261-276.
(27) Schmidt-Rohr, K.; Qiang, C. Parallel Cylindrical Water Nanochannels in Nafion Fuel-Cell Membranes. *Nature Materials* **2008,** *7*, 75-83.
(28) Dura, J. A.; Murthi, V. S.; Hartman, M.; Satija, S. K.; Majkrzak, C. F. Multilamellar Interface Structures in Nafion. *Macromolecules* **2009,** *42*, 4769-4774.
(29) Kreuer, K.-D.; Portale, G. A Critical Revision of the Nano-Morphology of Proton Conducting Ionomers and Polyelectrolytes for Fuel Cell Applications. *Advanced Functional Materials* **2013,** *23*, 5390-5397.
(30) Allen, F. I.; Comolli, L. R.; Kusoglu, A.; Modestino, M. A.; Minor, A. M.; Weber, A. Z. Morphology of Hydrated as-Cast Nafion Revealed through Cryo Electron Tomography. *ACS Macro Letters* **2015,** *4*, 1-5.
(31) Li, J.; Park, J. K.; Moore, R. B.; Madsen, L. A. Linear Coupling of Alignment with Transport in a Polymer Electrolyte Membrane. *Nature Materials* **2011,** *10*, 507-511.
(32) Lingwood, M. D.; Zhang, Z.; Kidd, B. E.; McCreary, K. B.; Hou, J.; Madsen, L. A. Unraveling the Local Energetics of Transport in a Polymer Ion Conductor. *Chemical Communications* **2013,** *49*, 4283-4285.
(33) Hou, J.; Madsen, L. A. New Insights for Accurate Chemically Specific Measurements of Slow Diffusing Molecules. *Journal of Chemical Physics* **2013,** *138*, 054201.

(34) Tanner, J. E. Use of the Stimulated Echo in NMR Diffusion Studies. *Journal of Chemical Physics* **1970,** *52*, 2523-2526.
(35) Stejskal, E. O.; Tanner, J. E. Spin Diffusion Measurements: Spin Echoes in the Presence of a Time-Dependent Field Gradient. *Journal of Chemical Physics* **1965,** *42*, 288-292.
(36) Zimmerman, J. R.; Brittin, W. E. Nuclear Magnetic Resonance Studies in Multiple Phase Systems: Lifetime of a Water Molecule in an Adsorbing Phase on Silica Gel. *The Journal of Physical Chemistry* **1957,** *61*, 1328-1333.
(37) Callaghan, P. T., *Translational Dynamics & Magnetic Resonance: Principles of Pulsed Gradient Spin Echo NMR*. Oxford University Press: Great Clarendon Street, Oxford, 2011.
(38) Bain, A. D. Chemical Exchange in NMR. *Progress in Nuclear Magnetic Resonance Spectroscopy* **2003,** *43*, 63-103.
(39) Brownstein, K. R.; Tarr, C. E. Importance of Classical Diffusion in NMR Studies of Water in Biological Cells. *Physical Review A* **1979,** *19*, 2446-2453.
(40) Lingscheid, Y.; Arenz, S.; Giernoth, R. Heteronuclear NOE Spectroscopy of Ionic Liquids. *ChemPhysChem* **2012,** *13*, 261-266.
(41) Gabl, S.; Schröder, C.; Braun, D.; Weingärtner, H.; Steinhauser, O. Pair Dynamics and the Intermolecular Nuclear Overhauser Effect (NOE) in Liquids Analysed by Simulation and Model Theories: Application to an Ionic Liquid. *The Journal of Chemical Physics* **2014,** *140*, 184503.
(42) Mitra, P. P.; Sen, P. N. Effects of Microgeometry and Surface Relaxation on NMR Pulsed-Field-Gradient Experiments: Simple Pore Geometries. *Physical Review B* **1992,** *45*, 143-156.
(43) Hou, J. Transport and Anisotropy inside Ionic Polymer Membranes, Ph.D. Thesis. Virginia Tech, Blacksburg, VA, 2012.
(44) Price, W. S. Pulsed-Field Gradient Nuclear Magnetic Resonance as a Tool for Studying Translational Diffusion: Part 1. Basic Theory. *Concepts in Magnetic Resonance* **1997,** *9*, 299-336.
(45) Ohkubo, T.; Kidena, K.; Ohira, A. Determination of a Micron-Scale Restricted Structure in a Perfluorinated Membrane from Time-Dependent Self-Diffusion Measurements. *Macromolecules* **2008,** *41*, 8688-8693.

Chapter 7

Summary and Future Work

This dissertation primarily focuses on the investigation and correlation of structure, dynamics and transport properties of soft materials using multiple NMR methodologies, including SSNMR, PFG diffusometry, imaging, and intermolecular NOE. The complicated and dynamic nature of soft materials creates great challenges for their characterization methods. Here, with a variety of NMR techniques, we have demonstrated new and varied aspects of structure, dynamics and transport information gleaned from soft materials.

7.1 Structural characterization by NMR and X-ray scattering

All molecules and atoms undergo motions constantly on different time scales. Hence a "structure" of a material obtained by a certain experimental method indicates the averaged view over the experimental time and length scale. The comparison of solution NMR and X-ray crystallography as methods of structure determination for biomacromolecules such as proteins and DNA has been investigated extensively.[1-3] For soft materials such as polymer membranes with semi-crystalline structures and supramolecular assemblies with semi-mesomorphic structures, NMR spectra are able to distinguish the differences in crystalline and amorphous regions with the highlight on molecules with faster motions in amorphous regions, while X-ray scattering emphasizes crystalline regions where molecules are ordered in periodic crystal lattices. Here we will briefly summarize structural characterization of polymer membranes and supramolecular assemblies using multiple NMR methods (SSNMR, NOE and PFG diffusion) in this thesis, and quickly compare the differences in the information obtained by NMR and X-ray scattering.

In Section 3.2.3, we quantified ratios of locally ordered vs. disordered components present in the alkyl-substituted 1-vinylimidazolium (AVIM) homopolymers using ^{13}C CPMAS NMR.[4] We found that the locally ordered fraction increased from 10% to 68% with increasing alkyl chain length from n = 2 to n = 6, and addition of the hydroxyl group to the side chain terminus decreased the locally ordered fraction from 10% to 0% for n = 2 and from 68% to 23% for n = 6. On the other hand, our collaborators employed X-ray scattering to extract average distance information such as backbone-to-backbone and anion-to-anion distances, and their results showed qualitatively that both decreased alkyl chain length and increased polarity of the hydroxyl substituent diminished the local compositional heterogeneity of polar and nonpolar phases in the AVIM homopolymers.[4] The agreement of these two methods gave us more confidence in our interpretation. The combination of SSNMR and X-ray scattering showed that the reduced locally ordered fraction due to the attachment of a polar hydroxyl group onto the imidazolium homopolymers can explain the 10-fold higher ionic conductivities exhibited by hydroxyalkyl-substituted AVIM homopolymers than the corresponding AVIM macromolecules.[4]

In Section 4.3.2, we quantified the amount of wedge molecules present in the amorphous phase vs. within the ordered liquid crystalline (LC) phases in the supramolecular assemblies formed from sodium 2,3,4-tris(11'-acryloyloxyundecyl-1'-oxy)benzene sulfonate **A-Na** using ^{23}Na MAS NMR.[5] Our result showed that the amorphous domain boundaries between LC domains contribute to ~ 10% of the total wedge molecules and these amorphous wedge molecules became completely hydrated when increasing relative humidity (RH) from 33% to 86%. On the other hand, X-ray scattering did not detect the amorphous phase but focused on LC domains and presented a structural evolution from hexagonal columnar phase

to bicontinuous cubic phases with increasing RH.[5] In addition, NMR relaxation studies (T_1, T_2 and $T_{1\rho}$) showed an significant increase in molecular dynamics as RH increases, especially the mobility of the terminal acrylate groups. Therefore LC structural evolution was facilitated by the dynamics requirement of each part of the wedge molecules, since bicontinuous cubic phases were able to accommodate more mobile terminal groups than hexagonal columnar phases. The combination of SSNMR and X-ray scattering showed that the phase transition within LC domains as well as the presence of the amorphous domain boundaries both contributed significantly to the transport properties of the material.

In Section 6.3.2, we investigated cation-anion and anion-anion interactions in ionic liquids (ILs) [C_2mim][BF_4] and [C_2mim][TfO] absorbed into an ionic polymer Nafion using ^{1}H-^{19}F HOESY and ^{19}F-^{19}F 1D selective NOE. Our results showed that cation-anion distance decreased drastically upon decreasing water content and anion-anion interactions between TFO^- and BF_4^- increased at very low water content. While X-ray scattering does not provide much information for such liquid samples, SAXS and WAXS are the primary techniques for studies of Nafion morphology, and several different models has been proposed for Nafion structures to fit the scattering data.[6-12] In Sections 6.3.3 to 6.3.6, we used restricted ion diffusion inside Nafion to probe multiscale domain structures of Nafion. Our results agreed with some previous models of sub-micron domain structure and we further proposed that a locally higher density of SO_3^- groups – a "SO_3^- boundary," is present in the junctions of sub-micron domains. This boundary facilitates cation diffusion through any defects present at domain junctions due to the electrostatic attraction between the boundary and cations, but it restricts anion transport due to the repulsion force. This boundary effect is temperature-dependent. When temperature increases, anion may migrate through domain junctions if thermal fluctuations of fixed SO_3^-

groups and anions can overcome the electric potential between them. Thus this boundary size is not necessarily the size of static domains obtained by X-ray scattering data, but highly dependent on the dynamics of the fixed SO_3^- groups and reflects the real confinement of anion diffusion.

In summary, SSNMR, intermolecular NOE, PFG diffusometry and X-ray scattering are powerful tools for structural determination for soft materials such as supramolecular assemblies and polymer membranes. While X-ray emphasizes more ordered and static features of the materials, NMR probes more disordered and dynamic nature. Due to the fact that dynamics is highly interwoven with structure in soft materials, the combination of these techniques provide a comprehensive picture for these complicated structures.

7.2 Molecular transport in soft materials

Molecular transport properties of many materials are essential for their applications. In soft materials, transport behaviors of absorbed molecules are strongly influenced or determined by structure and morphology of the porous materials. In this thesis, we have studied multi-component water and wedge molecule diffusion in supramolecular assemblies **A-Na** by PFG diffusometry (Chapter 4),[13] nanoparticle diffusion in biogels by time-resolved MRI (Chapter 5)[14] and cation and ion diffusion in the ionic polymer Nafion (Chapter 6).

In Section 4.3.4, we observed two-component diffusion for individual wedge molecules (^{1}H) present in the amorphous domain boundaries. We assigned the slower PGSTE diffusion component $D \sim 10^{-14}$ m^2/s to individual wedges diffusing through ordered liquid crystal (LC) phases and the faster component $D \sim 10^{-12}$ m^2/s to individual wedges diffusing within the amorphous boundaries between LC domains. The wedge molecules packed into LC phases diffused very slowly $D < 10^{-15}$ m^2/s which was beyond our diffusion detection limit.

Overall, the domain boundaries of a mesomorphic material must be considered when investigating dynamic properties of the material itself or when measuring the transport of small molecules in the material. In some circumstances, behavior of molecules in the domain boundaries may be the dominant contributor to an observed property ─ a fact that has received little attention in the literature to date.

In Section 4.3.5, we observed two-component diffusion for water (^2H_2O) absorbed in **A-Na** at high RH values, while D_2O molecules were tightly associated to the relatively narrow ionic channels of columnar phases at low RH. We assigned the slow diffusion $D \sim 10^{-12}$ m^2/s to D_2O molecules diffusing within domain boundaries, and the fast diffusion $D \sim 10^{-10}$ m^2/s to "free" water diffusing within the enlarged and interconnected ionic channels of the bicontinous cubic phases. Our results showed that the bicontinous cubic phase was able to facilitate much faster ion transport than the columnar phase, and the presence of domain boundaries disrupted the continuity of LC domains thereby reducing overall water transport.

In Section 4.4, we measured water diffusion (^1H_2O) in five stable membranes polymerized from **A-Na** or similar supramolecular assemblies **A-Li** (Li^+ as counterion) and **A-K** (K^+ as counterion) at two relative humidities (RH 100% and ambient). Again we observed two-component diffusion for all membranes and attributed the fast component to free water diffusing inside the ionic channels of the liquid crystalline region and the slow component to water diffusing through the amorphous regions in the crosslinked membranes. The presence of the amorphous regions clearly reduces water transport rates in the membranes by breaking ordered (cubic) transport pathways. Furthermore, we found much higher water uptake and faster water diffusion for the membranes crosslinked at RH 100% than those crosslinked at ambient RH, which we attribute to the phase transition from columnar to bicontinuous cubic

phases for the non-crosslinked salt. We also observed higher water uptake and faster diffusion for larger counterions with the order **A-K** > **A-Na** > **A-Li**, which we attribute to the larger ionic channels and thus increased free volume in the membranes with larger counterions. In addition, compared to **A-Na** salts, **A-Na** membranes produced 10-fold slower diffusion coefficients, which we hypothesize is due to shrinking of the ionic channels and amorphous regions during crosslinking, or introduction of some channel structural defects upon crosslinking.

In Chapter 5, we established and validated a simple and accurate approach for quantitative study of nanoparticle diffusive penetration into biogels using time-resolved MRI.[14] Our results agreed closely with those obtained from fluorescence techniques, yet the capability of our approach allowed the analysis of actual delivery vehicle diffusion through biogels on mm to cm scales during a range of time periods. We observed diffusion of three contrast agents in four different agarose and collagen gels. A reduction of median D of N_4Gd by 45% with an increase of agarose content from 0.5 to 2.0 wt.% corresponded to a decrease of ~70% in average gel pore size.[15] D for MBICs in 0.5 wt.% agarose gel is two orders of magnitude lower than that of the ~8 × smaller N_4Gd, due to steric hindrance and the influence of hydrodynamic interactions in porous gels.[16-17] Within 0.2 wt.% collagen gels, the diffusion of MBICs is approximately 10 times slower than neutrally charged particles, and the diffusivity of MBICs decreases roughly two orders of magnitude compared to neutral particles in 1.0 wt.% collagen gel. This drastic decrease in diffusion rate arises from the electrostatic interaction between the slightly positively charged collagen fibers at neutral pH and negatively charged MBIC nanoparticles. Combined with hydrodynamic and steric interactions, electrostatic effects influenced diffusion of nanoparticles of both positive and negative surface charge,

owing to their repulsion from or attraction to collagen fibers.[18] Our results showed that as the particle size and surface charge became larger, collagen gel at tumor relevant concentration (1.0 wt.%) presented a more significant impediment to the diffusive transport of negatively charged nanoparticles.

In Chapter 6, we explored the sample parameter space (temperature, water content, and IL uptake) of ILs and water in Nafion membrane to assess the "free" and "restricted" diffusion regimes. While cations maintained in "free" diffusion region under all our experimental conditions, anions experienced a transition from "free" to "restricted" regimes when lowering IL uptake, water content or temperature. Due to the SO_3^- aggregates present in the hydrophilic "channels" and the SO_3^- "barriers" with higher SO_3^- density present at sub-micron domain junctions, anion diffusion showed a strong temperature-dependent confinement effect. At low temperature, anions, especially anion-rich clusters, were pushed to the center of diffusing "channels" by the repulsion force between SO_3^- groups and anions, leading to single-file diffusion behaviors. As temperature increased, anions may diffuse freely within domains and even migrate through domain boundaries if thermal fluctuations of SO_3^- groups and anions can overcome the electric potential between them. Therefore the competition between thermal fluctuation and electric potential caused by the fixed ionic groups on the polymer chains plays an essential role in the transport behaviors of mobile ions with opposite charge.

7.3 Future work

NMR methodologies for soft materials studies. As we mentioned in Chapter 2, 4, and 6, one of the main difficulties for NMR applications in soft materials studies is the relatively short T_1 and T_2 of spins present in soft materials caused by the relatively strong partially averaged chemical shift anisotropy, dipolar or quadrupolar interactions remaining in

these systems. These interactions are sometimes very informative and worthy of close inspections, but they do significantly influence signal intensity. For PFG diffusometry and intermolecular NOE, T_1 and T_2 decay during the pulse sequences significantly reduces the final signal intensity. In some cases, no signal can survive the pulse sequences due to an extremely short T_2. For example, we could not measure the diffusion of $[C_2mim][BF_4]$ absorbed in Nafion at 0 ℃ due to the short ^{1}H and ^{19}F T_2 (~ 1 ms). This problem becomes worse for quadrupolar nuclei, like ^{23}Na, with their extremely short T_1 and T_2 caused by strong quadrupolar interactions. For diffusion measurements, several modification of PFG NMR has been suggested to solve this issue, including multiple pulse line-narrowing techniques, such as stimulated echo PFG pulse sequence combined with MREV-8 homonuclear dipolar decoupling and slice selection.[19-21] RF and PFG pulse sequence development can be a direction for our lab's future work. Another technique involves the combination of magic angle spinning (MAS) and PFG.[22-26] A MAS PFG probe could greatly expand our capacity for diffusion measurements in soft materials.

Molecular dynamics (MD) simulations. MD simulations is an intrinsically complementary method for understanding diffusion phenomena. We are beginning to use carbon nanotubes of varying size and charged surfaces as a model for ionic channels of ionic polymers, and to simulate molecular or ion diffusion behaviors inside these channels. This study should provide more visualized and direct evidence about structure-transport relationships. For example, I expect single-file diffusion be observed for anions inside negatively charged channels and cations inside positively charged channels with a certain size while ions with opposite charge may diffuse relatively freely.

Further studies on A-Na supramolecular assemblies. Since higher water uptake and faster diffusion was observed for larger counterions inside these materials, we expect that further increases in diffusion coefficient (and thus ion conductivity) can be achieved in these materials by casting them with larger counterions, such as tetramethylammonium or those cations used in ionic liquids (imidazolium and phosphonium derivatives). Our collaborators may synthesize the supramolecular assemblies with other counterions based on our suggestions, or our lab may conduct ion exchange reactions on existing materials.

Further studies on ion diffusion in ionic polymers. The dramatic difference in the cation and anion diffusion behaviors inside Nafion is intriguing. We propose to utilize more "basic" polymer systems with well-defined structures to distinguish the influences of polymer multi-scale structures and fixed charged groups. More systemic studies including a series of ion containing polymers with positively and negatively charged side groups as well as a variety of ionic liquids can be performed to further investigate these phenomena.

Reference

(1) Fraenkel, E.; Pabo, C. O. Comparison of X-Ray and NMR Structures for the Antennapedia Homeodomain-DNA Complex. *Nat Struct Mol Biol* **1998,** *5*, 692-697.
(2) Krishnan, V. V.; Rupp, B., *Macromolecular Structure Determination: Comparison of X-Ray Crystallography and NMR Spectroscopy*. John Wiley & Sons, Ltd: England, 2001.
(3) Garbuzynskiy, S. O.; Melnik, B. S.; Lobanov, M. Y.; Finkelstein, A. V.; Galzitskaya, O. V. Comparison of X-Ray and NMR Structures: Is There a Systematic Difference in Residue Contacts between X-Ray- and NMR-Resolved Protein Structures? *Proteins: Structure, Function, and Bioinformatics* **2005,** *60*, 139-147.
(4) Allen, M. H.; Wang, S.; Hemp, S. T.; Chen, Y.; Madsen, L. A.; Winey, K. I.; Long, T. E. Hydroxyalkyl-Containing Imidazolium Homopolymers: Correlation of Structure with Conductivity. *Macromolecules* **2013,** *46*, 3037-3045.

(5) Chen, Q.; Wang, Q.; Liu, Y.-C.; Wu, T. The Effect of Hydrogen Bonds on Diffusion Mechanism of Water inside Single-Walled Carbon Nanotubes. *The Journal of Chemical Physics* **2014,** *140*, 214507.
(6) Mauritz, K. A.; Moore, R. B. State of Understanding of Nafion. *Chemical Reviews* **2004,** *104*, 4535-4586.
(7) Gierke, T. D.; Munn, G. E.; Wilson, F. C. The Morphology in Nafion Perfluorinated Membrane Products, as Determined by Wide- and Small-Angle X-Ray Studies. *Journal of Polymer Science: Polymer Physics Edition* **1981,** *19*, 1687-1704.
(8) Rubatat, L.; Rollet, A. L.; Gebel, G.; Diat, O. Evidence of Elongated Polymeric Aggregates in Nafion. *Macromolecules* **2002,** *35*, 4050-4055.
(9) Rubatat, L.; Gebel, G.; Diat, O. Fibrillar Structure of Nafion: Matching Fourier and Real Space Studies of Corresponding Films and Solutions. *Macromolecules* **2004,** *37*, 7772-7783.
(10) Gebel, G.; Diat, O. Neutron and X-Ray Scattering: Suitable Tools for Studying Ionomer Membranes. *Fuel Cells* **2005,** *5*, 261-276.
(11) Schmidt-Rohr, K.; Qiang, C. Parallel Cylindrical Water Nanochannels in Nafion Fuel-Cell Membranes. *Nature Materials* **2008,** *7*, 75-83.
(12) Dura, J. A.; Murthi, V. S.; Hartman, M.; Satija, S. K.; Majkrzak, C. F. Multilamellar Interface Structures in Nafion. *Macromolecules* **2009,** *42*, 4769-4774.
(13) Chen, Y.; Lingwood, M. D.; Goswami, M.; Kidd, B. E.; Hernandez, J. J.; Rosenthal, M.; Ivanov, D. A.; Perlich, J.; Zhang, H.; Zhu, X.; Möller, M.; Madsen, L. A. Humidity-Modulated Phase Control and Nanoscopic Transport in Supramolecular Assemblies. *The Journal of Physical Chemistry B* **2014,** *118*, 3207-3217.
(14) Wang, X.; Chen, Y.; Xue, L.; Pothayee, N.; Zhang, R.; Riffle, J. S.; Reineke, T. M.; Madsen, L. A. Diffusion of Drug Delivery Nanoparticles into Biogels Using Time-Resolved Micromri. *The Journal of Physical Chemistry Letters* **2014,** *5*, 3825-3830.
(15) ZhouZhou; ZhouZhou; Caruso, R. A. Agarose Template for the Fabrication of Macroporous Metal Oxide Structures. *Langmuir* **2006,** *22*, 3332-3336.
(16) Deen, W. M. Hindered Transport of Large Molecules in Liquid-Filled Pores. *AIChE Journal* **1987,** *33*, 1409-1425.
(17) Johnson, E. M.; Berk, D. A.; Jain, R. K.; Deen, W. M. Hindered Diffusion in Agarose Gels: Test of Effective Medium Model. *Biophysical Journal* **1996,** *70*, 1017-1023.
(18) Stylianopoulos, T.; Poh, M.-Z.; Insin, N.; Bawendi, M. G.; Fukumura, D.; Munn, L. L.; Jain, R. K. Diffusion of Particles in the Extracellular Matrix: The Effect of Repulsive Electrostatic Interactions. *Biophysical Journal* **2010,** *99*, 1342-1349.
(19) Dvinskikh, S. V.; Furó, I. Combining Pgse NMR with Homonuclear Dipolar Decoupling. *Journal of Magnetic Resonance* **2000,** *144*, 142-149.
(20) Dvinskikh, S. V.; Furó, I. Cross-Relaxation Effects in Stimulated-Echo-Type Pgse NMR Experiments by Bipolar and Monopolar Gradient Pulses. *Journal of Magnetic Resonance* **2000,** *146*, 283-289.

(21) Dvinskikh, S. V.; Furó, I. Anisotropic Self-Diffusion in the Nematic Phase of a Thermotropic Liquid Crystal by 1h-Spin-Echo Nuclear Magnetic Resonance. *The Journal of Chemical Physics* **2001,** *115*, 1946-1950.
(22) Pampel, A.; Fernandez, M.; Freude, D.; Kärger, J. New Options for Measuring Molecular Diffusion in Zeolites by Mas Pfg NMR. *Chemical Physics Letters* **2005,** *407*, 53-57.
(23) Viel, S.; Ziarelli, F.; Pagès, G.; Carrara, C.; Caldarelli, S. Pulsed Field Gradient Magic Angle Spinning NMR Self-Diffusion Measurements in Liquids. *Journal of Magnetic Resonance* **2008,** *190*, 113-123.
(24) Fernandez, M.; Pampel, A.; Takahashi, R.; Sato, S.; Freude, D.; Karger, J. Revealing Complex Formation in Acetone-N-Alkane Mixtures by Mas Pfg NMR Diffusion Measurement in Nanoporous Hosts. *Physical Chemistry Chemical Physics* **2008,** *10*, 4165-4171.
(25) Romanova, E. E.; Grinberg, F.; Pampel, A.; Kärger, J.; Freude, D. Diffusion Studies in Confined Nematic Liquid Crystals by Mas Pfg NMR. *Journal of Magnetic Resonance* **2009,** *196*, 110-114.
(26) Jenkins, J. E.; Hibbs, M. R.; Alam, T. M. Identification of Multiple Diffusion Rates in Mixed Solvent Anion Exchange Membranes Using High Resolution Mas NMR. *ACS Macro Letters* **2012,** *1*, 910-914.